Electrochemical Applications of Porous Polymeric Materials and their Derivatives

Thesis Submitted to AcSIR

For the Award of the Degree of

DOCTOR OF PHILOSOPHY

In

CHEMICAL SCIENCES

By

Harshitha B A

(Registration Number: **10CC12J26008**)

Under the guidance of

Dr.Sreekumar Kurungot
&
Dr. Rahul Banerjee

Physical & Materials Chemistry Division

CSIR-National Chemical Laboratory

Pune - 411008, India.

September 2016

Certificate

This is to certify that the work incorporated in this Ph.D. thesis entitled **Electrochemical Applications of Porous Polymeric Materials and their Derivatives** submitted by **Ms. Harshitha B A** to Academy of Scientific and Innovative Research (AcSIR) in fulfillment of the requirements for the award of the Degree of **Doctor of Philosophy** in **Chemical Sciences,** embodies original research work under our supervision.

We further certify that this work has not been submitted to any other University or Institution in part or full for the award of any degree or diploma. Research material obtained from other sources has been duly acknowledged in the thesis. Any text, illustration, table etc., used in the thesis from other sources, have been duly cited and acknowledged.

Harshitha B A
Student

Dr. Sreekumar Kurungot
Research Guide

Dr. Rahul Banerjee
Research Co-Guide

DECLARATION

I hereby declare that the matter embodied in this thesis entitled ***"Electrochemical Applications of Porous Polymeric Materials and their Derivatives"*** *is the result of investigations carried out by me in the Physical & Materials Chemistry Division, CSIR-National Chemical Laboratory, Pune, India under the supervision of Dr.Sreekumar Kurungot and Dr. Rahul Banerjee.*

In keeping with the general practice of reporting scientific observations, due acknowledgements have been made wherever the work described is based on the findings of other investigators. The work is original and has not been submitted in part or full, for any degree or diploma to this or to other University.

Date: 15-09-2016

Place: Pune, India

Harshitha B A

ACKNOWLEDGMENT

This thesis owes its existence to the inspiration, guidance and support of several people. I believe that acknowledging their effort could be a humble way of expressing my heartfelt gratitude to all of them as I complete this dissertation.

I would like to foremost thank my research supervisors Dr.Sreekumar Kurungot and Dr.Rahul Banerjee for accepting me into their groups and considering me worthy for their esteemed guidance. I am very much thankful for their contributions in terms of time, energy, ideas, and funding that have made my Ph.D. experience productive as well as stimulating. I will always cherish their support and willingness in allowing me to pursue my research on topics which I am truly passionate about. I am very much grateful for the funding received from UGC towards completion of my doctoral degree. I would like to thank my DAC members: Dr.Ashish Lele, Dr.Ulhas Kharul and Dr. K. Krishnamoorthy for their timely assessment and expert advice which has enormously helped and guided my research works. I thank Prof. Diaz Diaz for all the scientific discussions and his guidance regarding the testing of the photocatalytic activity in COFs. I am very grateful to my course work coordinators: Dr. Rajesh Gonnade, Dr. C. P. Vinod, Dr. Kumar Vanka, Dr. Pankaj Poddar, and Dr. Nithyanandhan for their excellent classes and coursework materials. At this juncture I would also like to thank Dr. Sayam Sen Gupta, Dr. Satishchandra Ogale for their constant encouragement and good wishes.

I wish to thank Prof. Ashwini Kumar Nangia, current Director; Dr. K. Vijayamohanan and Dr. Sourav Pal, former Directors, CSIR-NCL for the instrumental facilities, infrastructure and the academic support provided to carry out my research work at the Institute. I sincerely acknowledge Dr. Chetan Gadgil, Dr. S.M. Shashidhar and the SAC office members for their efforts in ensuring the smooth execution of the AcSIR formalities.

I owe a great debt of gratitude to my colleagues Pritish Wadge, Pandiaraj, Subhadeep Saha, Jayashri Thote and Digamber Shinde for their scientific input in realizing many joint projects. This collaboration would have never been successful without their selfless efforts. I would also like thank my seniors Pradip Pachfule and Sreekuttan Unni for introducing me to the research works in both the groups and for their efforts in helping me during my initial days as a novice researcher. I shall always remain grateful to all the past and present members of both the labs- Beena chechi, Palani anna, Bihag, Vishal, Vrushali, Subhash da,

Chandan da, Tamas da, Arijit, Tanay, Gobinda da, Sujith da, Sushil, Amit da, Manas da, Gargi di, Kanhu, Shouvik, Arghya da, Sarath, Harikrishna, Siddhu, Santosh, Rajith, Roby, Kashyap, Pranav, Vidyanand, Ayasha, Meena, Sachin, Manna, Sharath, Bishnu, Suman, Bikash, Arjun, Saibal, Mohitosh, Suvendu, Himadri, Kaushik, Abdul, Shebeeb for their friendship and the warmth extended to me during my stay in the Institute. I wish to thank the project students Vijitha, Antara, Nivedha, Ishwari, Riya, Akhil and Abin for their help in my work. My stay in this campus has been pleasant with the association of all the research scholars at CSIR-NCL. I would like especially thank Shiva, Ananth, Krishna, Anil, Goudappa Patil, Bhanu, Zenia, Rohini, Monisha, Bipin, Maya, Rajambal, Senthil, Prajitha, Sarabjot, Sushma, Aarthy, Ashwini, Indrapal, Harsha and Sachin Patil, whose friendship shall always be cherished. I personally behold the days spent with Meenal, a great friend, guide and a wonderful senior.

I shall forever remain indebted to my teachers and professors, in particular, Dr. Darshak Trivedi, Dr. Krishna Kumar, Dr. Raghavendra, Dr. Rama Bhat and Dr. Padmaji for their constant support and blessings. Having you both alongside- Reshma and Guddi, I can never ask for anything more. Any words of appreciation cannot make up for my affection for both of you. I thank you Ma, Baba, Subhadeep, Prithvi and Debolina for your continual love and support, which has made me stronger and more confident.

I owe a great part of my achievements to my grandparents (Amma, Poppa, Dada and Avayya) and to my defender, my partner in crime, my little sister, Lavya. Thank you for your limitless love and support despite my idiosyncrasies and calling me creative when I was crazy! Words just cannot describe my salutation to my parents. Thank you daddy- my hero and best friend and Mummy, I can only hope to one day become at least half the woman you are: strong, tough and selfless. Being your daughter is one of the best things in the world to me and I shall promise to live a life that will do justice to all the sacrifices that you all have made.

Though not all may be mentioned but **none** is **forgotten**…….

Harshitha Barike Aiyappa

List of Abbreviations

Abbreviation	Expansion
0-D	Zero-Dimensional
1-D	One-Dimensional
2-D	Two-Dimensional
3-D	Three-Dimensional
AC	Alternating Current
ADT	Accelerated Durability Test
BET	Brunauer–Emmett–Teller
BTC	Benzene-1,3,5-tricarboxylic acid
CCDC	The Cambridge Crystallographic Data Centre
CE	Counter Electrode
CNF	Carbon Nanofibre
CNT	Carbon Nanotube
CO	Carbon Monoxide
COF	Covalent Organic Framework
CV	Cyclic Voltammetry
DC	Direct current
DEF	Diethyl Formamide
DFS	Dynamic Frequency Sweep
DMAc	Dimethylacetamide
DMF	Dimethyl Formamide
DSS	Dynamic Strain Sweep

EDLC	Electric Double Layer Capacitor
EDX	Energy-Dispersive X-ray spectroscopy
emf	Electromotive force
ESR	Equivalent Series Resistance
FESEM	Field Emission Scanning Electron Microscopy
FRA	Frequency Response Analyzer
FTIR	Fourier Transform Infrared Spectroscopy
GC	Gas Chromatography
HR-TEM	High Resolution Transmission Electron Microscopy
ICP-MS	Inductively coupled plasma mass spectrometry
K-L plot	Koutecky-Levich plot
LIB	Lithium-ion Battery
LSV	Linear Sweep Voltammetry
MALDI	Matrix-assisted laser desorption/ionization
MC	Mechanochemistry
MEA	Membrane Electrode Assembly
MOF	Metal Organic Framework
MOM	Metal Organic Materials
NMF	N-methyl Formamide
NMP	N-Methyl-2-Pyrrolidone
NMR	Nuclear Magnetic Resonance
OCV	Open Circuit Voltage
o-DCB	o-dichlorobenzene

OEC	Oxygen Evolving Catalyst
OER	Oxygen Evolution Reaction
ORR	Oxygen Reduction Reaction
ORTEP	Oak Ridge Thermal-Ellipsoid Plot Program
PA	Phosphoric Acid
PBI	Polybenzimidazole
PEMFC	Proton Exchange Membrane Fuel Cell
PTFE	Polytetrafluoroethylene
PVDF	Polyvinylidene difluoride
PXRD	Powder X-ray Diffraction
RDE	Rotating Disk Electrode
RE	Reference Electrode
RRDE	Rotating Ring Disk Electrode
SAED	Selected Area Diffraction
SEM	Scanning Electron Microscopy
SSA	Specific Surface Area
ST	Solvothermal
TEM	Transmission Electron Microscopy
TGA	Thermogravimetric Analysis
WE	Working Electrode
XPS	X-ray Photoelectron Spectroscopy
ZIF	Zeolitic Imidazolate Framework

Table of Contents

Chapter 2

Electrochemical characterization of porous polymeric materials 29-42

Chapter 3

Fe-based coordination polymer gels as proton conductors and their typical transformation into Fe-metal organic frameworks 43-78

Part A

3A. Conversion of Fe-metallogel into Fe-MOFs *via* $PdCl_2$ mediated gel degradation 45-59

Part B

Chapter 4

Covalent Organic Framework (COF) as prototype solid electrolyte in Proton Exchange Membrane Fuel Cells 79-97

Part B

Chapter 7

Summary and Conclusions

PREFACE

A lookout for a combustion-free, clean, safe and sustainable energy system is one of the foremost challenges of the 21st century energy research. In this direction, the renewable energy sources such as solar and wind power encompass huge potential to help reduce the global energy dependency on fossil fuel and thereby curb the greenhouse gas emissions. However, the inconsistency in their incessant availability all round the day and across all seasons makes these resources unrealistic for all time power generation. Thus efforts are on to use alternative electrochemical energy devices like batteries, fuel cells, supercapacitors, etc. which convert chemical energy into electrical energy. The performance of these heterogeneous energy devices depends on the effectiveness of the electrode-electrolyte interface. The electrochemical system operates at its best in the presence of a cordial electron as well as ion movement through and away from the electrode-electrolyte interface. Thus central focus of research is development of materials which can allow facile electron and ion diffusion. The porous carbons have always remained a favorite choice for making electrodes of high energy density devices owing to their good electrical conductivity and high surface area and enormous porosity, which enable easy ion diffusion throughout the bulk of the material. A numerous template based synthesis has been utilized to synthesize carbons with controllable porosity and size. This thesis unravels one such synthetic route, wherein a crystalline Metal Organic Framework (MOF) is used as a self sacrificial template for deriving nanoporous carbons. The as synthesized carbon is observed to provide a facile transport pathway for both ion and electron movement when used as a supercapacitive material. In another instance, the porous polymeric material like metallogel is functionalized with protogenic functional ligand and used as an ion conducting electrolyte for PEM fuel cell fabrication. The material is shown to overpower the conventional H^+ conducting membrane in terms of its ability to conduct protons without any carrier, at anhydrous condition. Lastly, the thesis also discusses ways in which the porous materials could be functionalized to catalyze energy reactions like hydrogen generation from water, electrochemical water oxidation and electrocatalytic oxygen reduction reaction.

The entire thesis spans upto seven chapters and the abstract of each of the chapter is given below:

Chapter 1: This chapter outlines the need to address the electrochemical ways of harnessing energy. It will introduce the porous polymeric materials whose electrochemical properties shall be determined, besides giving a brief insight about the different methods used for their synthesis. The advantages and limitations of the porous materials and the strategies used to implement them in an electrochemical system shall be discussed. The chapter includes a concise state-of-the-art survey of the ways in which the porous polymeric materials, mainly the metal organic frameworks (MOFs), MOF-derived carbons, metal-organic gels and covalent organic frameworks (COFs) are tested as electrode electrocatalysts and ion conductive materials for electrochemical energy devices. The chapter will mainly highlight the strategies used for improving the electronic as well as ionic conductivity of the porous materials, which is very crucial for developing an effective electrode-electrolyte interface, which ultimately determines the performance of any electrochemical device.

Chapter 2: This chapter briefly explains the different types of electrochemical techniques that are utilized inorder to determine the electrochemical behavior of the porous materials in the present thesis work. It intends to familiarize the reader with the electrochemical techniques inorder to analyze the results obtained from characterizations like cyclic voltammetry (CV), charge-discharge study, linear sweep voltammetry, rotating disk electrode (RDE), rotating ring disk electrode (RRDE) Mott-Scottky analysis, AC-impedance analysis techniques etc. It also encloses a brief description of each of the methods used and the nature of the information that could be obtained using these techniques, without pondering into too much detail.

Chapter 3: This chapter discusses the effective ways of utilizing chemically stable Fe-based metallogels. The first part of the chapter explains the conversion of viable Fe^{3+} based metallogels into Fe-MOFs by $PdCl_2$ interceded gel degradation. The oxidation of the metallogel constituents namely, formic acid/formamide by Pd^{2+} is shown to drive the system towards more thermodynamically controlled pathway yielding Fe-MOF crystals. The second part of the chapter describes an ingenious way of entrapping a protogenic acid by way of its gelation with Fe^{3+} ion in DMF. The xerogel obtained from the as synthesised Fe-metallogel is tested for its anhydrous proton conducting ability. The chapter also discusses a way to use the xerogel pellet for fabricating a Membrane Electrode Assembly (MEA) of a Proton Exchange Membrane Fuel Cell (PEMFC).

Chapter 4: This chapter introduces a new way of utilizing mechanochemistry as a judicious, green, and fast synthetic route towards effective synthesis of a bipyridine functionalized covalent organic framework (COF). It describes a unique way in which the as synthesized COF can be used to accommodate the phosphoric acid molecules, a notable proton conducting dopant, and eventually employed as a proton conducting solid electrolyte in a Proton Exchange Membrane Fuel Cell (PEMFC). The open circuit potential study and cell polarization studies are also performed using the single cell fabricated using the COF pellet which unequivocally prove the inherent ability of such materials to conduct protons at dry conditions, which is an immediate requisite for low temperature PEMFCs.

Chapter 5: The chapter discuses the ways in which a catalytic COF can be designed to hold to the veracity of both molecular as well as the heterogeneous catalysts. The first part of the chapter discusses the development of a bipyridine functionalized TpBpy COF as a steady, electrochemical water oxidation catalyst. The chapter highlights the exceptional catalytic activity of the Co-TpBpy, resulting from the intrinsic porosity and the coordinating bipyridinic units imbibed in the COF skeleton. The second part of the chapter illustrates a route in which COFs can be used as effective photocatalysts for generating hydrogen from water. This part presents a way in which a stable COF is used as a substrate to *in situ* synthesize CdS nanoparticles. The investigation of the photocatalytic activity of the as synthesised composite is thereafter discussed.

Chapter 6: This chapter discusses the role of metal organic frameworks (MOFs) as self-sacrificial templates for porous carbon synthesis. The first part of the chapter reports an effective way of converting the less employed non-porous Zn-MOFs into more useful porous carbons without using any additional carbon source. The chapter highlights the influence of ligands in the MOF architecture on the properties of carbons resulting from their direct carbonization. The MOF-derived carbon has been tested for its porosity-dependent gas adsorption properties and electrochemical applications. The second part of the chapter discusses a unique route through which the porous MOF-derived carbons are further activated for Oxygen Reduction Reaction (ORR) in PEMFCs. The chapter presents a way wherein the macro porosity of the MOF carbon is effectively used as a nitrogen reservoir for plugging nitrogen rich g-C_3N_4 units by means of *in situ* polymerization of the melamine. This

route thereby opens a new conduit to design and develop metal-free electrodes with enhanced ORR activity and better mass diffusion characteristics optimal for PEMFC applications.

Chapter 7: The chapter recapitulates the thesis work giving an outline of the main observations and conclusions of each of the chapters. It mainly emphasizes on the outcome of the work presented in each of the chapters. The prospective advantages and limitations of using the porous polymeric materials as electrode, electrocatalyst, and ion conductive materials are discussed. As a final point, the future-directives that could provide some perspectives for the further developments are provided at the end of the discussion of each of the work.

Chapter 1

Introduction

The present chapter will give an overview of the need to look into the electrochemical ways of harnessing energy. It proposes to introduce the porous polymeric materials under study, giving a brief insight about the synthetic strategies used, their structure-property relationship, with special reference to their electrochemical behavior. It will highlight the ways in which the merits and limitations of such porous materials could be exploited in order to implement them in an electrochemical system. It includes a brief literature survey of the applications of such porous materials, mainly the metal organic frameworks (MOFs), MOF-derived carbons, metal-organic gels (MOG) and covalent organic frameworks (COFs) as electrochemical components. This chapter, in particular, accounts for the investigations of the porous materials as electrode materials for supercapacitors; electrocatalysts for fuel cells, metal-ion battery systems and water electrolyzers; as well as proton conductive materials for proton exchange membrane fuel cells. The strategies used for improving the conductivity of the porous materials, both electronic as well as ionic, either by using redox active metals and ligands or by their composite formation with conductive elements are also discussed. The chapter also highlights the ways in which an improvement in the electro responsiveness and the efficiency of such porous materials towards energy conversion can be anticipated.

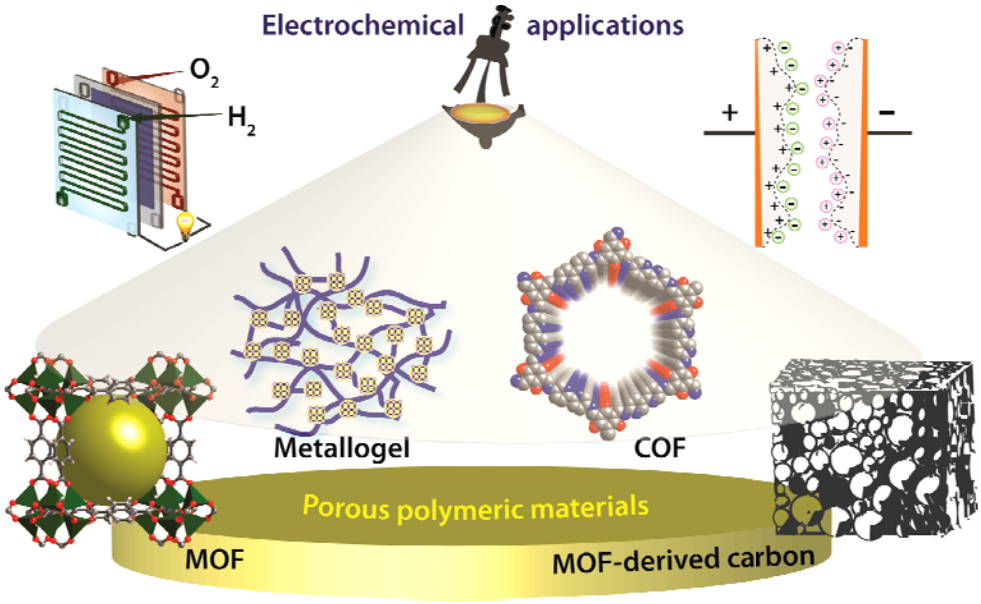

1.1. General Background

In the current energy state, fossil fuels and biomass fulfill most of the global power demands eventually contributing to the undesired CO_2 emission. This calls for an immediate need to recognize cleaner and efficient energy substitutes. Although the solar energy is deemed as the most inexhaustible form of energy, it is also accompanied by several limitations *viz.* absence of sunshine at the night, reduction in the power during the time of cloud covering and fog, inconsistent global availability of sunlight all throughout the year owing to the difference in the geographic terrain and seasons. On the other hand, electrochemical energy devices are one of the conceptually easy pathways which employ electrochemical reactions for implementing effective inter-switching of chemical and electrical energy through bond breaking as well as bond formation. [1] A typical electrochemical cell consists of two electrodes (termed as anode and cathode) dipped in a suitable electrolyte or often separated by an ion conducting membrane which is saturated with an electrolyte.[2] The performance of any electrochemical system, which is heterogeneous in nature, is largely dictated by the efficiency of the electrode-electrolyte interface. An effective electrode-electrolyte interface demands adept movement of both the charges, *i.e.* ions (in the electrolyte part) and charges (in the electrode part) at the phase boundary.[3] Therefore, the components of an electrochemical system must be essentially conductive to the requisite charges besides possessing substantial porosity to furnish maximum surface area for the charge adsorption. This thereby has necessitated the search for porous materials that can be used as electrochemical components inorder to improve the proficiency of the electrode-electrolyte interface. [4]

Among the earlier porous materials, the activated carbon is one of the most extensively tried electroactive materials. [5] In the late 1990's, a major breakthrough is witnessed with the discovery of new porous materials, termed as porous coordination polymers. These unique materials with high structural rigidity and low mass density are found to possess porous microstructure and tunable surface functionality that could be taken advantage of to design them and tailor their potential as effective electrode/electrolyte materials as per the requirement. The first chapter aims to discuss some of the prime electrochemical applications of the porous polymeric materials like metal organic framework (MOF), covalent organic Framework (COF), metal organic gels and their derivatives.

1.2. Porous Materials

The materials which possess pores (also called as voids /cavities/channels/interstices) that can potentially admit gas /liquid molecules through them are termed as 'porous' materials. The typical characteristics of any porous material are mainly decided by the shape, size, and arrangement of the pores, in addition to the amount of the porosity as well as the chemical constitution of the material. The porous materials can be classified either depending on their pore dimensions or on their basic chemical composition.

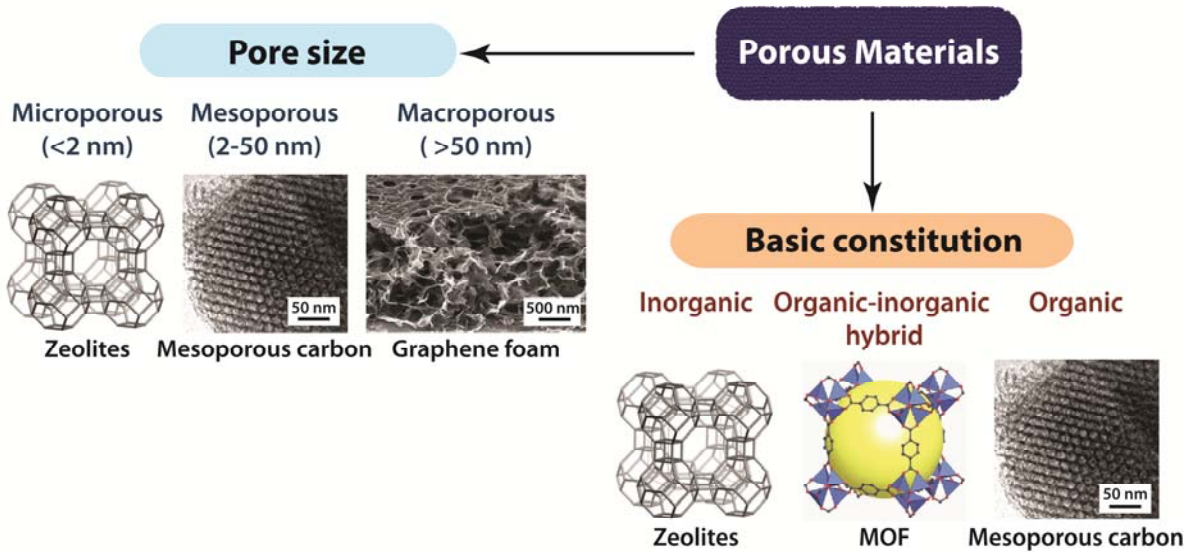

Figure 2.1. *Schematic representation of the classification of the porous materials depending on their pore size and chemical constitution.*

(Image sources: https://en.wikipedia.org/wiki/Mesoporous_material ; https://www.physik.uni-augsburg.de/chemie/Forschungsgebiete/MOFs/; figures of zeolite and graphene foam are reproduced with permission from the American Chemical Society and the Royal Society of Chemistry)

According to the International Union of Pure and Applied Chemistry (IUPAC), the porous materials are classified into three categories depending on the pore size: microporous (< 2 nm), mesoporous (2-50 nm) and macroporous (>50 nm). Some of the prominent microporous materials are naturally occurring crystalline zeolites, most of the metal organic frameworks (MOFs), activated carbons, amorphous glass etc. [6] Owing to their smaller pore dimensions, these materials are extensively used as molecular sieves and size-selective heterogeneous catalysts. These materials show typical Type-I N_2 adsorption isotherm with sharp increase at very low pressures followed by a long and flat saturation plateau.[7]

However, in terms of the electrochemical activity, the mesoporous materials are largely advantageous as they result in the formation of an effective electrical double layer, due to their larger pore volume and high specific surface area. These materials show typical Type-IV isotherm with a steep increase at relatively high pressure. A hysteresis loop, associated with the capillary condensation is often observed in case of mesoporous materials. [8] The main members of this family are mesoporous silica and alumina (used as template for carbon formation). They also include some metal organic frameworks like Cr based-MIL-100, Cr based-MIL-101 etc. [8b,c] These materials are electrochemically important as they possess larger pores that facilitate easier diffusion of ions, in particular, the solvated organic ions, a crucial factor which determines the high power performance of any non-aqueous solvent based electrochemical system. The macroporous materials have pore size greater than 50 nm. The prominent members are polymers, aerogel, graphene foam etc. [9] By the virtue of their large pore dimensions, they are often used as absorbents, catalyst supports etc.

In accordance to their chemical composition, the porous materials can also be classified as inorganic, organic and organic-inorganic hybrid materials. The inorganic porous materials range from the naturally occurring zeolites to the synthetic mesoporous silica and alumina. The members of the organic porous materials include molecular cages, mesoporous carbon, besides the recent class of covalent organic frameworks. [10] The organic-inorganic hybrids contain the distinct characteristics of both the previous classes, such as exceptional mechanical strength, low cost, high thermo stability and easy processability. The classic members of this class are porous coordination polymers, also popular as metal organic frameworks wherein the inorganic units are held along by organic linkers *via* coordination bonds. [11]

1.3. Porous polymeric materials

Porous polymers as defined as polymeric materials enclosing one or more type of pores. Porous polymeric materials constitute of monomer units which repeat themselves, with alongside imbibing porosity during polymerization. The surface area, size and geometry of the resulting pores primarily decide the functionalities of such materials. Determined by the nature of the monomers and the polymerization reaction involved, such porous polymeric materials could possesses varied degree of structural ordering. They can be widely classified

as disordered amorphous and ordered crystalline porous polymers. In general, the amorphous polymers are kinetically controlled products, without any long range periodic order, while the crystalline polymers are thermodynamically favored products, with ordered networks.[11] The later includes the prominent members of the recent class of crystalline porous polymers: MOFs and COFs. Interestingly, most of these materials contain porosity in micro-meso regime, and thereby could be prospectively utilized for the effective development of the electrochemical double layer at the electrode-electrolyte interface.

1.3.1. Metal Organic Frameworks (MOFs)

According to IUPAC, Metal-Organic Framework, abbreviated to MOF, is a coordination polymer (or alternatively a coordination network) with an infinite open framework containing potential voids. These are an extensive class of crystalline inorganic-organic hybrids, first defined by Yaghi and Li in the late 1990's, which consist of metal ions/clusters that are coordination bonded to the organic linkers. [12] They are highly ordered structures with very high and tunable specific surface area, upto 6000 m^2/g enclosing enormous porosity. [13] They are the epitomic beauties resulting from the ingenious and effective amalgamation of the organic-inorganic chemistry. The prevailing MOFs are often synthesised under high pressure, solvothermal conditions using high boiling solvents. However, approaches like ultrasonic, microwave, diffusional and electrochemical means of synthesis have also been explored as well. [14] The aesthetic structural feature in addition to the topological diversity distinguishes the MOFs from many naturally available crystalline materials.

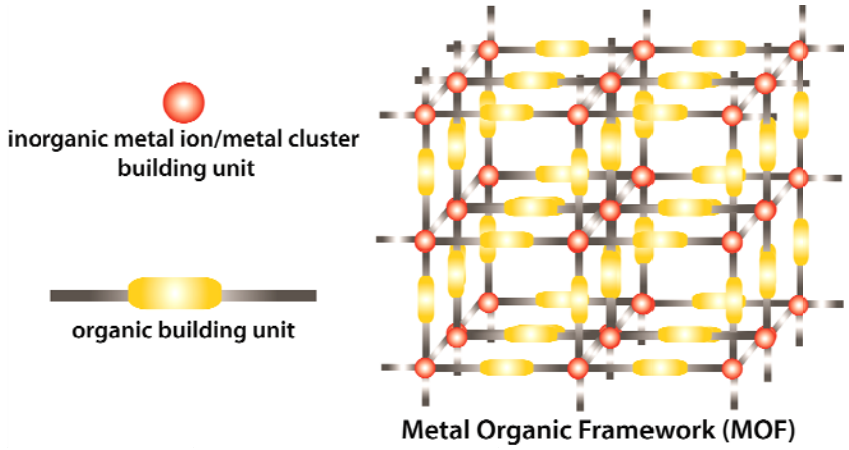

Figure 2.2. *Schematic representation of a typical MOF assembly.*

Till date, these materials are extensively tried for gas adsorption, gas storage and gas separation applications. [15] As these structures could be tailor made according to the need, the molecular building block approach has been often used for assembling the desired functionalities in a MOF. The hallmark porosity of these structures allows facile diffusion of the molecules into and out of the highly ordered frameworks, thereby favoring a good host-guest interaction.

1.3.2. Metal-organic gels/Metallogels

The low molecular weight gels also known as supramolecular gels are distinct 'soft' members of the supramolecular materials group, wherein, the soluble gelator molecules self assemble eventually ensnaring the entire solvent in which they are earlier dissolved, and result in a stable gel. [16] Depending on the nature of the dispersing medium, they are classified as organic gel (organic solvents) and hydrogel (water). In yet another case of metal ion- ligand coordination, in case of metallogels, the interaction results in the formation of a one dimensional gel network unlike the three dimensional crystalline framework in case of the MOFs. Herein the metal-ligand coordination complex is employed as a gelator to immobilize solvent molecules *via* capillary force and surface tension, often guided by non covalent interactions like hydrogen bonding, π-π stacking, van der Waals' and hydrophobic interactions etc. [17] These metallogels have been used as soft materials for applications like magnetism, redox responsiveness, sensing, drug delivery, tissue engineering etc. [18]

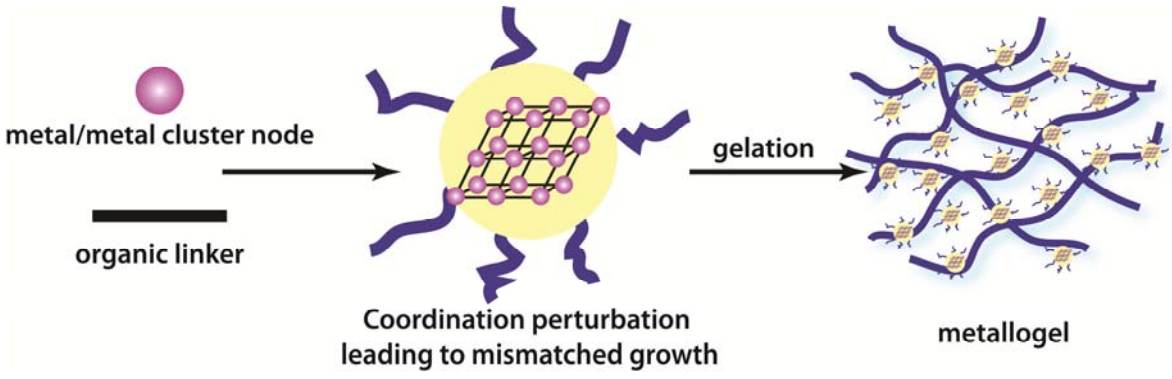

Figure 2.3. *Schematic representation of formation of the metallogel.*

1.3.3. Covalent Organic frameworks (COFs)

Covalent organic frameworks are a class of crystalline, ordered, organic polymeric materials which are made up of an elegant assembly of organic units directionally held by reversible covalent bonds. [19] It is well known that the strong covalent bonds do not leave any room for re-correction/proofing once formed. Therefore such structures are often found to lack long range of ordering and are largely amorphous.[20] Therefore the principles of dynamic covalent chemistry (DCC) have been employed to instill crystallization in the polymerizing systems. In case of COFs, reversible dynamic covalent bond formation is triggered between the reactive groups of the organic units. Several reversible reactions like boronate ester formation, imine formation, hydrazone formation etc. are successfully developed to construct crystalline COF materials.[21] The reversible nature of the above reactions allows bond breaking and reformation, which in turn 'error checks' the polymer to grow into a more thermodynamically favorable crystalline form. As the framework mainly consists of C, H, N, O, B elements, these structures possess relatively low mass density, high thermal stability and permanent porosity. Thus after MOFs, these are the recent class of polymers that are extensively tried for gas adsorption and separation, catalysis, sensing, optoelectronic applications etc.[22] In case of the two-dimensional COFs, the sheets are stacked one above the other by means of π electron cloud interactions. Thus many of the 2-D COFs are tried for their charge carrier ability in photovoltaic cells as well for optoelectronics. [23]

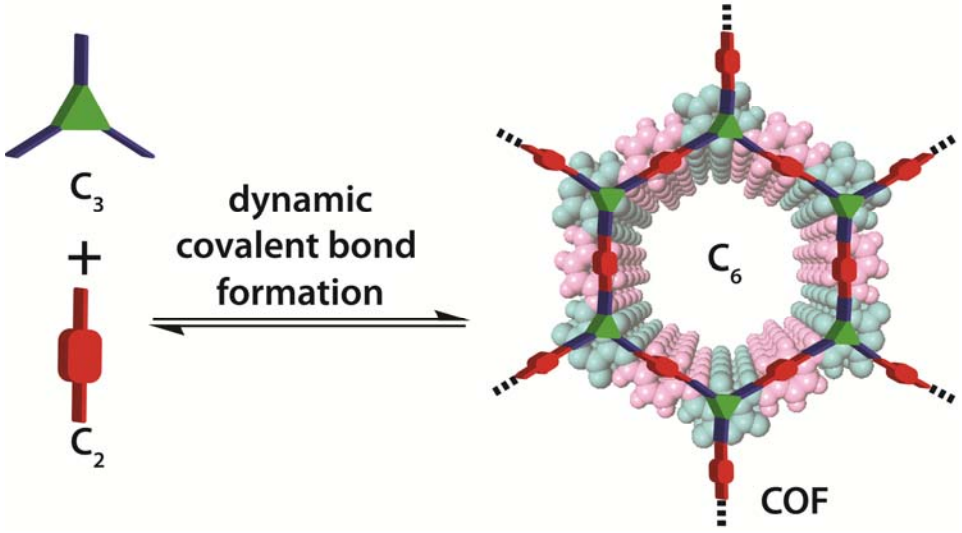

Figure 2.4. *Schematic representation of the COF formation via dynamic covalent bond formation.*

1.4. Porous polymeric materials for electrochemical applications - a brief review

1.4.1. Electrochemical applications of MOFs

1.4.1.1. MOFs as electrode materials for supercapacitors and batteries

In the view of these above discussed merits, MOFs have been extensively tried as heterogeneous catalysts for liquid-phase reactions. [24] They have also been tested as electro sensors for selective ion and molecule detection. Attempts have been made to improve the MOF's electro-responsiveness by introducing redox active groups such as multivariate ions and electroactive ligands. On substituting Zn with more redox active cobalt in Co-MOF-5, pseudo capacitance upto 0.3 F/g at 10 mA/g has been achieved. [25] The redox behavior of Co (II/III) couple also predicted to imbibe electron conducting nature to such MOFs. The presence of such redox centers thus makes them potential electrode materials for fabricating pseudocapacitive electrodes. Besides, the high surface of the MOFs is also potentially capable of physically adsorbing electrolyte ions at the interface, a criterion vital for the formation of electrified double layer. The MOF's high internal surface area and porosity are also used for sheltering pseudo capacitive quantum dots, like SnO_2@ZIF-8, wherein the synergistic effect of both the components is found to result in a high specific capacitance of 931 F/g at 5 mV/s scan rate. [26] However, as most of these structures are poor electrical conductors, they are cannot be directly implemented as electrode materials or as electrocatalysts for fabricating an electrochemical device.

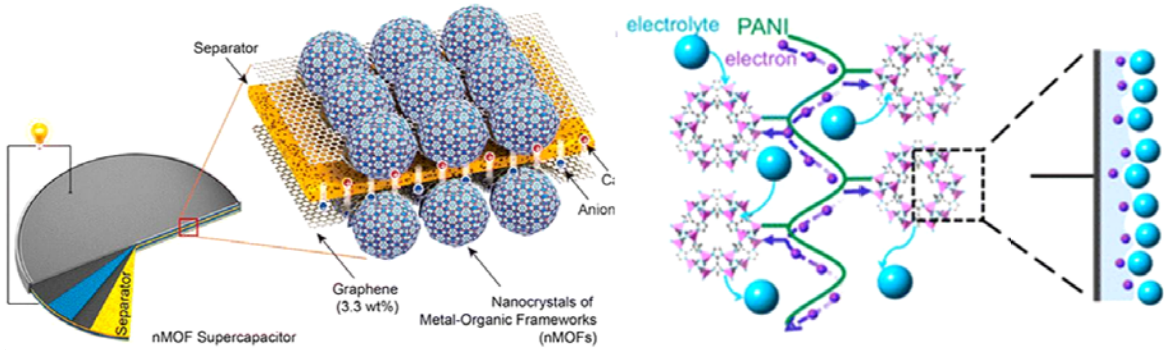

Figure 2.5. *Use of MOF-based composites as electrode materials for fabricating supercapacitors [reproduced with permission from the American Chemical Society (Ref 25(b) and Ref. 28)].*

Henceforth, MOF composites are prepared using electrically conducting phases like activated carbon, CNTs, CNFs etc. which can be seen as a boulder strategy to overcome the poor electron conducting ability of MOFs. [27] However, owing to the smaller sized pores, this approach could only establish electron conduction at the macroscopic level, thereby preventing the complete utilization of the MOFs internal surface area. An attempt in this direction was made by Bo Wang and co workers, wherein the cobalt based ZIF crystals are interwoven using PANI, a conducting polymer and deposited on carbon cloth which was used as a current collector. The material was observed to show a high areal capacitance of 2146 mF/cm^2 at 10 mV/s in a three-electrode configuration system. [28]

In case of Li-ion battery system (LIB), one of the prominent commercial energy storage devices, the Li^+ content and the rate of Li^+ intercalation are believed to be the major limiting factors affecting the energy density of LIBs. In an instance of the MOF utility, the presence of redox active Fe^{3+}/ Fe^{2+} couple in MIL-35(Fe) is found to facilitate easy Li^+ intercalation in the MOF's ordered porous structure. This MOF is found to maintain a reversible capacity upto 70 mAh/g even after 50 cycles.[29] Similarly, another vanadium based MOF, $[Li_2(VO)_2(HPO_4)_2(C_2O_4)]$, containing V (IV)/(V) redox couple, is found to exhibit a high rate LIB performance with a reversible capacity of 47 mAh/g at 500 mA/g. [30] Thus, in addition to the pore functionality, the superior structural integrity and relatively lower gravimetric density of MOFs further promote them as potential electrode materials for lithium-ion and lithium-sulphur batteries.

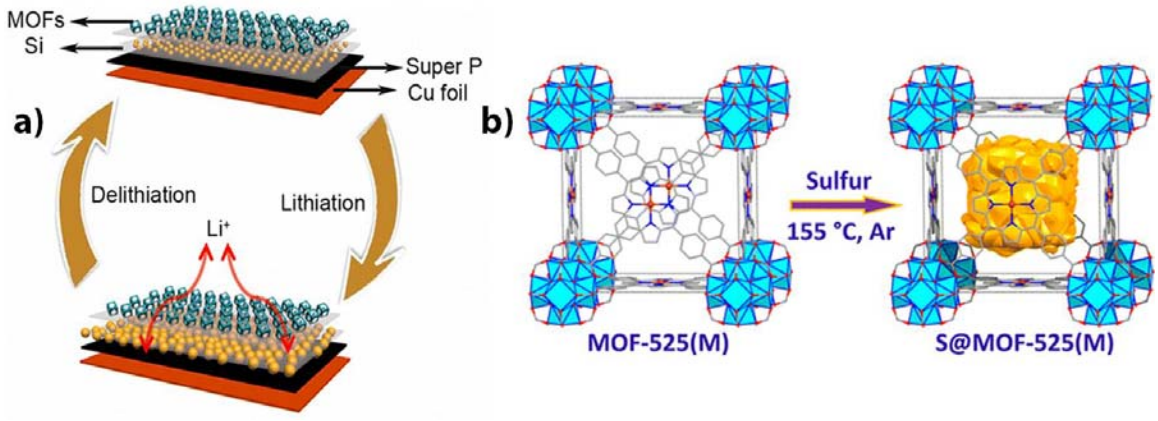

Figure 2.6. *Use of MOF as electrode materials in Li-ion battery and sulphur storage material in Li-S battery [reproduced with permission from the American Chemical Society (Ref 32(b) and Ref. 31)].*

They are observed to assist fast Li^+ intercalation and storage by means of the reversible conversion of their metal centers. In this direction, several multivalent, transition metal based MOFs, e.g. Ni (II), Cr (III) and Fe (III) based MOFs, have also been known to facilitate faster electron release resulting in long range charge delocalization apart from assimilating high Li^+ content in their pores. [31] Besides LIB, the MOFs are also tried as high surface area matrix for confining sulphur in the Li-S battery systems. The mesoporous cages of the MOFs are used for impregnating elemental sulphur up to ~48 wt%. [32] Before use, they are mixed with conductive high surface carbon and then tried as a positive electrode for lithiation process. These are found to possess superior cyclic stability and high capacitance retention ability when compared to the conventional mesoporous silica and mesoporous carbons systems.

1.4.1.2. MOFs as electrocatalysts

As MOFs can be purposely designed to achieve precise and desired functionalities, they have attracted attention as catalysts for various electrochemical reactions like oxygen reduction reaction (ORR), oxygen evolution reaction (OER), hydrogen evolution reaction (HER), oxidation of alcohols etc. [33] The polyoxometalate (POM)-based MOFs, also termed as POMOFs, belong to another class of hybrid framework materials, consisting of POMs (oxyanionic clusters of transition metals) which are connected to each other *via* organic ligands.[34] These materials are reported to show extensive electrochemical activity towards ORR, H_2O_2 oxidation, nitrite reduction, HER reactions etc. In many occasions, pristine MOFs are as such tested for their electrochemical activity, in particular, towards ORR in alkaline medium. [35] However, as discussed earlier, being poor electron conductors, MOFs cannot be directly employed as electrocatalysts. Thereby, a composite of the MOF is made using conductive materials like reduced graphene oxide (r-GO), CNTs etc. For instance, an iron-porphyrin based MOF and reduced GO composite is found to show very high ORR activity in alkaline pH, with an onset potential of just 0.93 V (*vs.* RHE). [36] The presence of high intrinsic porosity and catalytic Fe-N centers are believed to promote ORR activity in the composite. Similarly, a bipyridine containing copper based MOF, Cu–bipy–btc, is found to catalyze ORR at neutral pH at an onset potential of +0.5 V (*vs.* RHE). [37] It is important to note that despite being an efficient ORR catalyst, the commercial platinum (Pt) catalyst is proven to be highly susceptible to poisoning in the presence of strongly adsorbing

intermediates like CO, produced in case of liquid fuel based fuel cells. Thus search is on to look for a non-precious based electrocatalyst for PEM fuel cells. The MOF based structures are also tried as electrocatalysts to catalyze the oxidation of alcohols, another important liquid fuel. A copper based 2-D MOF, $[(HOC_2H_4)_2$d-toaCu] reported by Kitagawa and co-workers is found to catalyze electro oxidation of ethanol at an onset potential of 0.84 V (*vs.* RHE). [38] Recently, the MOFs are also tried for electrochemical reduction of CO_2, a major green house gas. A copper based MOF, capable of generating redox active Cu (II)/ (I) and Cu (I)/ (0) responses is found to effectively reduce CO_2 to useful oxalic acid. [39]

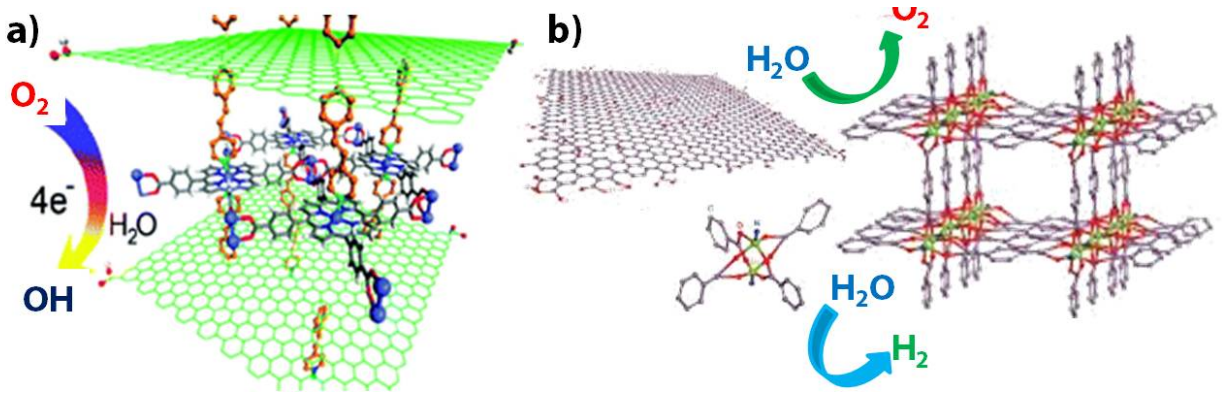

Figure 2.7*. Use of MOF-based composites as multifunctional electrocatalysts for electrochemical energy systems [reproduced with permission from ref. the American Chemical Society and Wiley-VCH Verlag GmbH & Co. KGaA (Ref 36 and Ref. 43)].*

Furthermore, the MOFs constructed using metal ions with oxophilic nature, open metal sites and high M-O bond stability (viz., Mg, Mn, and Co) are used for electrochemical water splitting reactions. [40] Water insoluble, Co-N containing, cobalt based MOFs are recently shown to effect proton-coupled electron transfer mechanism for OER and are thereby tried as anodes for water electrolyzers and rechargeable metal air batteries inorder to catalyze the otherwise sluggish oxygen evolution reaction (OER).[41] In addition, the Ir complex incorporated Zr-based MOF $[Zr_6O_4(OH)_4(bpdc)_6]$ and Fe based MOF (commercially available as Basolite™ F300) are some of the MOF based electrocatalysts [42] known to effect OER at acidic and basic pH conditions, respectively. Many of these electrocatalysts are found comparable to that of the corresponding state of art catalysts: IrO_2 (at low pH) and Pt (at high pH). Some MOFs are also known to show dual catalytic behavior; like the copper based 2-D MOF containing terephthalic acid and triethylene–diamine as

framework units, which was observed to show both HER (with an onset potential of 0.087 V *vs.* RHE) and OER activity (with an onset potential of XX V *vs.* RHE). [43] Thus the MOF's adaptable chemical environment, easily reachable pores and the high accessible internal surface areas could be found beneficial to improve its interaction efficiency with the incoming guest molecules.

1.4.1.3. MOFs as ion conductors for batteries and fuel cells

The commercial PEMFCs operate using Nafion® membrane as the solid proton conducting electrolyte. On hydration, the Nafion® membrane shows proton conductivity of order 10^{-1} S/cm at the PEMFC operating temperature. However, as the ionic conductivity is humidity dependent, the operation temperature is limited to 80 ˚C. [44] This necessitates the need for developing high temperature proton conducting electrolytes that could operate at temperature above 80 ˚C, preferably at anhydrous conditions. The increase in the cell operation temperature would in turn benefit the PEMFC performance by (i) increasing reaction kinetics (particularly the sluggish ORR), (ii) perk up the cell resistance to catalyst poisons like CO, by increasing the rate of its desorption from the catalyst surface and (iii) prevents the undesired flooding of the Pt catalyst besides helping easy water management. Thus, the lookout is on for materials that could conduct protons similar to that of the Nafion® membrane but at anhydrous conditions. [45] In this direction, considering their high thermal stability and ordered pore alignment, MOFs have been tried as proton conducting materials. [46] For the first time, in 2003, a two-dimensional copper based MOF was investigated for its proton conducting ability by Kitagawa and coworkers under 75% relative humidity. [47] It is observed to show a decent conductivity of 10^{-6} S/cm at room temperature. This is followed by another work wherein an iron oxalate MOF containing an ordered array of water molecules is found to show a proton conductivity upto 10^{-3} S/cm at 25 ˚C and 98 % relative humidity. [48] These earlier studies in turn fuelled the testing of many more MOF forms like cobalt, and manganese based MOFs for proton conduction. Further, a highly water stable MOF, containing both sulphonic and phosphoric groups PCMOF-2.5, reported by Kim and coworkers is reported to exhibit a maximum proton conductivity parallel to that of Nafion®, at 2.1×10^{-2} S/cm at 85 ˚C and 90% relative humidity. [49] However, it is noteworthy that most of these MOFs conduct protons at low temperature (<100 ˚C), aided by the presence of water molecules and hydrogen bonding within them inside the framework. Inorder to induce proton

conductivity at higher temperatures, proton conducting organic molecules, with higher melting points and amphiprotic nature like imidazole, triazoles are encapsulated inside the MOF frameworks to render them extrinsic proton conductivity. [50] In this direction, studies have been carried out by Shimuzu and coworkers using β-PCMOF2, wherein a sodium based MOF is observed to show an appreciable proton conductivity of 2×10^{-4} S/cm at 150 ˚C under anhydrous conditions. [51] Further, a membrane electrode assembly is also fabricated using the MOF which shows an open circuit voltage (OCV) of 1.18 V at 100 ˚C, thereby highlighting the potential of the material as a solid electrolyte in PEMFCs.

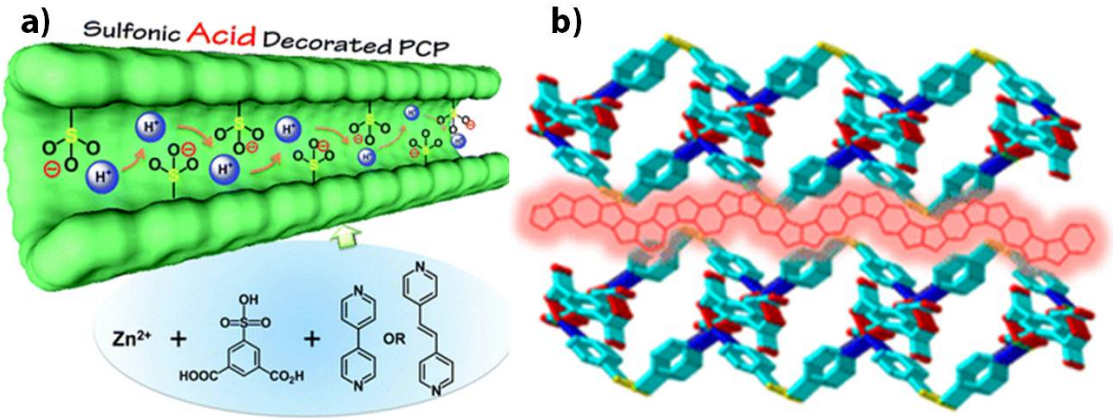

Figure 2.8. *Use of stable MOFs as proton conducting materials for PEM fuel cell applications [reproduced with permission from the Royal Society of Chemistry and the American Chemical Society (Ref 50(b) and Ref. 45(a)].*

Interestingly, some zinc based MOFs like $\{[(Me_2NH_2)_3\text{-}(SO_4)]_2[Zn_2(ox)_3]\}_n$ are also found to conduct protons under both hydrous (4.2×10^{-2} S/cm at 25 ˚C) and anhydrous (1×10^{-4} S/cm at 150 ˚C) conditions.[52] However, as the performance of the commercial Nafion® membranes is still comparably superior in terms of both conductivity and PEMFC performance, there is plenty of scope for improving the proton conducting ability of such MOFs. In addition to the proton conduction, Kitagawa and coworkers have also demonstrated the usefulness of MOFs as potential electrolytes for Li-ion batteries. [53] In an ionic liquid mediated process, a zinc based MOF, ZIF-8 is observed to show conductive pathway for Li^+ ion diffusion *via* solvated $TFSA^-$ anions present in its pores. Another group led by Long and coworkers also report the use of a magnesium based MOF, Mg_2(dobdc) as a solid electrolyte for LIBs.[54] The MOF which is impregnated with a Li^+ source (LiO^iPr)

reportedly displays an ionic conductivity of 3.1×10^{-4} S/cm at 300 K. These advances thereby highlight the potential of the MOFs to be employed in ionic devices.

1.4.1.4. MOFs as corrosion inhibitors

In another instance of exploiting its chemical stability, MOFs have also been tried as corrosion inhibitors to resist oxide formation and metal loss. They are known to combat corrosion by adsorbing onto the metal surfaces, thereby decreasing its exposure to the corroding agents. A typical example of is the silver based $(AgCN)_4.(qox)_2$, which is tested for the carbon steel protection in HCl. [55] The presence of nitrogen atoms in the framework is believed to assist strong adsorption of the MOF onto the carbon steel surface. The efficiency is monitored by calculating the change in the charge transfer resistance before and after the MOF adsorption using the impedance measurements. In another work, about 84% suppression of the corrosion current density is observed in case of Ag (qox)(4-ab).[56] These studies thereby unravel the possibilities of using robust structures like MOFs as anti-corrosive agents to prevent metal dissolution.

1.4.2. MOF-derived nanostructures and their electrochemical applications

Porous carbons are one of the commonly used electrode materials due to their high surface area, good electron conductivity and controllable porosity. However, despite being porous, the MOFs cannot be directly implemented as electrode material owing to their poor electron diffusing ability. Thus in another boulder strategy followed, porous MOFs are pyrolzed and used as 'self-sacrificial templates for deriving very high surface area, electrically conductive carbons.[57] The high surface area of such MOF-derived carbons allows maximum interaction of the active sites with the incoming molecules for effective adsorption/reaction. The first attempt has been made in 2008, by Quiang Xu and co workers, wherein a high surface Zn based MOF, MOF-5, is initially impregnated with furfuryl alcohol (used as a carbon source) and then carbonized at 1000 ˚C under inert conditions.[58] The Zn metal is found to distill out at ~900 ˚C leaving behind pure carbon, with a surface area amounting to ~ 2800 m^2/g. On testing, this MOF-derived carbon is found to result in a very high gravimetric capacitance of 204 F/g at 0.5 mV/s scan rate. In addition, such MOF-derived carbons are also found to be ORR active and are therefore extensively used as cathode electrocatalysts in PEMFCs as a replacement for the costly Pt/C commercial catalysts. In this direction, the cobalt and iron

based MOFs-derived Co/Fe-N-C catalysts are found to perform in par with the Pt/C electrocatalyst in terms of both power and current density under PEMFC operating conditions.[59] Furthermore, inorder to improve their intrinsic activity, the MOF pores are impregnated with different heteroatom containing precursors prior to their carbonization.

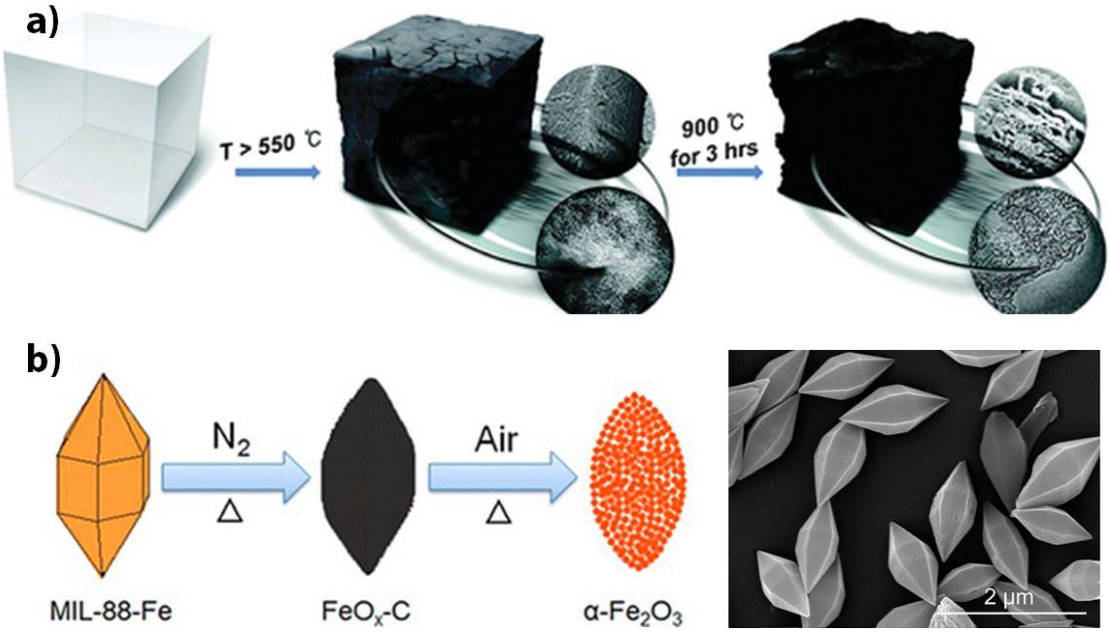

Figure 2.9. *Use of MOFs as 'self sacrificial templates' for deriving a) nanoporous carbon and b) nanostructures metal oxides [reproduced with permission from American Chemical Society (Ref 57(b) and Ref. 60 (b)].*

Besides carbon making, the MOFs are also used as ideal templates for deriving mono dispersed, nanostructured metal oxides (MO), MO/C hybrids, reduced metal nanoparticles, M/C hybrids etc. The double layer hydroxide nanocages derived from the cobalt based ZIF-67 is found to possess a BET surface area of 196 m^2/g. On testing, they are found to display a very high specific capacitance upto 1203 F/g at 1 A/g current density in 1 M KOH solution. [60] Likewise, the Fe_3O_4/carbon composite prepared by Zhi and coworkers is found to show a specific capacitance of 139 F/g at 0.5 A/g current density. [61] As prospective LIB materials, a copper based MOF has been used to obtain mixed valence CuO/Cu_2O nanostructures, which is found to perform superiorly as a LIB anodic material with a capacity of 740 mAh/g at 100 mA/g.[62]

1.4.3. Electrochemical applications of metallogels

The electrochemical property of the metallogels has not been extensively studied except for testing the proton conducting ability of a copper based CuA-Ox xerogel, which is found to exhibit a anhydrous proton conductivity of 1.4×10^{-5} S/cm at 65 ˚C. [63] It is important to note that, on freeze drying, the resulting xerogel retains high porosity and can act as nanoreactors for catalyzing reactions within their pores. Moreover, it is remarkable that, as most of the metallogelators mainly result from the hydrogen bonding along with the metal-ligand coordination interactions, these structures could be generally expected to inherently conduct protons. This invariably leaves huge room for tuning the ion conducting ability of these materials and to be tested as solid electrolytes in electrochemical energy devices.

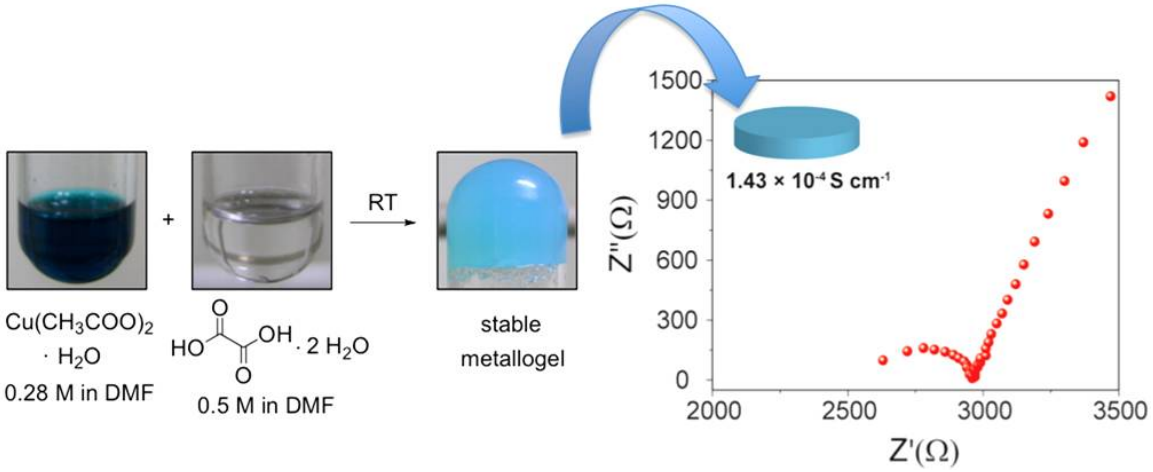

Figure 3.0*. Use of a xerogel-derived from CuA-Ox metallogel as a proton conducting material [reproduced with permission from Wiley-VCH Verlag GmbH & Co. KGaA (Ref 63)].*

1.4.4. Electrochemical applications of COFs

1.4.4.1. COFs as electrocatalysts and electrode materials

COFs being highly porous and crystalline in nature can be modified and built as per the need of the hour. [64] These structures are believed to potentially combine the merits of both the heterogeneous as well as the molecular catalysts. As a demonstration of this fact, Yaghi and coworkers have used metal porhyrin units embedded COFs as catalytic platforms for electro reducing CO_2 to CO. It has been observed that, of all, the cobalt containing COF-367-Co is found to show the highest faradaic efficiency of 90% with an overpotential of -0.55 V (*vs.*

RHE) at neutral pH conditions.[65] It is noteworthy that, like MOFs, the COFs are also poor electron conductors as they lack long range electron delocalization. Therefore, inorder to improve the electron diffusion, Jiang and coworkers report a composite of redox active COFs with CNTs, which is then used as organic electrode for lithium ion battery system.[66] The batteries were found to retain a constant capacity of 74 mAh/g even after 700 cycles with 100% Coulombic efficiency. In an important instance of developing an intrinsically conductive COF, Dinca and coworkers use nickel based Ni_3 $(HITP)_2$ COF as an oxygen reduction reaction (ORR) electrocatalyst in alkaline medium. [67] The material is reported to show appreciable ORR activity with an onset potential of 0.18 V (*vs.* RHE) relative to the standard Pt catalyst. By the virtue of their high intrinsic porosity and robust architecture, some 2-D COFs functionalized with porphyrin units are also tried as host materials for storing sulphur in Li–S battery system. Wang and coworkers report a sulphur loading of 55% sulfur in the as prepared composite, which is observed to deliver a capacity of 633 mA h/g at a rate of 0.5 C, even after 200 charge/discharge cycles. [68]

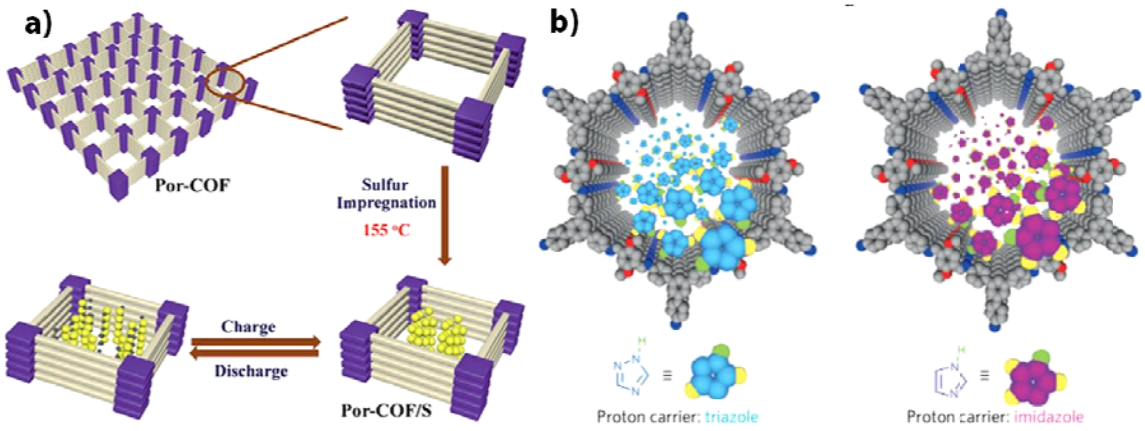

Figure 3.1. *Use of COF as a) sulphur storage material in Li-S battery and b) proton conducting electrolyte for PEM fuel cell system [reproduced with permission from the American Chemical Society and the Nature Publishing Group (Ref 68 and Ref. 69)].*

1.4.4.2. COFs as proton conductors for PEMFCs

Exploiting the robust crystalline architecture of COFs, these structures are used as ionic conductors by incorporating functional groups into the backbone, thereby, improving their efficiency in holding the proton carriers. Depending on the chemical nature of the carrier molecules to be loaded, the functionality of the COF pores is accordingly modified. Jiang and

coworkers report utilization of an acid functionalized COF to load basic heterocyclic proton carriers into the framework. [69] They report a proton conductivity of 4.71×10^{-7} S/cm at 120 °C. Contrary, Zhu and coworkers use a cationic COF to hold anionic POM ($PW_{12}O_{40}^{3-}$) molecules in the COF pores. They report a conductivity of 3.32×10^{-3} S/cm at 97% relative humidity. [70] However, as most of these materials show humidity dependent proton conductivity, it leaves ample room for the development of the COF based anhydrous proton conductors.

1.5. Scope of the thesis work

A critical review on the utilization of the porous polymeric materials and their derivatives reveals that tunable functionality, high accessible surface area and inherent porosity of these materials make them prospective electrode as well as electrolyte materials for fabricating electrochemical devices. However, to be effectively implemented as electrochemical components, there is a real need to improve their electrochemical properties in terms of both electronic as well the ionic diffusion. The survey emphasizes that the nature of the developing electrode-electrolyte interface plays a pivotal role in dictating the electrochemical activity of such materials. It also explains the substantial need to understand the mechanism of the formation of the electrochemical double layer and judges the influence of the material functionalities on the as-formed double layer. The presented literature study mainly highlights the efforts that have been made to improve the effectiveness of the electrode-electrolyte interface in these porous materials. However, considering the plethora of electrochemical devices that are in the energy run, it could also be convincingly understood that the complete potential of such porous materials has not been entirely realized.

The primary purpose of this thesis is to excavate the potential electrochemical applications of the porous materials taking advantage of their highly porous, stable and tunable architecture; mainly as electron and ion conductors. This thesis will mainly focus on the use of metal-organic gels and COFs as anhydrous, proton conducting, solid electrolytes for fabricating proton exchange membrane fuel cell, MOF-derived nanoporous carbon as ORR electrocatalyst for fuel cell plus as charge storage material for supercapacitor and additionally discuss an instance wherein a cobalt-modified COF is tried as a water oxidation electrocatalyst. In addition, the capacity of the COF matrix to harbor CdS nanoparticles and

eventually photo generate hydrogen molecules from water is also illustrated. The thesis comprises of four working chapters which hems in the detailed structural as well as electrochemical characterization of the materials under study.

1.6. Objectives of the thesis work

The specific objectives of the work enlisted in the thesis are as follows:

- To investigate the proton conducting behavior of a metal organic gel network and check its effectiveness as a solid electrolyte for fabricating a membrane electrode assembly (MEA) of proton exchange membrane fuel cell (PEMFC). In particular, the role of a protogenic ligand, namely phytic acid in improving the anhydrous proton conductivity of the metallogel will be studied. A part of the work will also investigate the susceptibility of the metastable metallogel to transform into more thermodynamically favorable crystalline MOF phase.
- To study the ability of a bipyridine functionalized COF to hold proton carriers, *viz*., phosphoric acid within its porous crystalline framework. Further, test its performance as a solid electrolyte in PEMFCs and investigate the gas separation ability of the COF as a function of its crystallinity.
- To check the ability of the COF to catalyze water splitting half-cell reactions and produce H_2 and O_2 from water. Testing the ability of the COF matrix to harbor photoactive nanoparticles and thereby investigate the influence of the COF matrix on the photocatalytic activity of the composite. Further, attempt shall be made to improve the electro-responsiveness of the COF by coordinating active metal ions to the bipyridine units embedded in the COF skeleton. The ability of the material to thereafter catalyze the electrochemical water oxidation reaction shall be examined.
- To validate the self sacrificial nature of the MOF and alongside authenticate the usage of a non porous MOF to obtain porous carbon. The capacitive nature of the as obtained carbons shall be investigated and a correlation of the electrochemical behavior with the carbon properties shall be attempted. Further, the post modification of such carbons shall be attempted inorder to improve their intrinsic catalytic activity for ORR. Thus obtained heteroatom modified carbons shall be tried as electrocatalysts for catalyzing ORR.

1.7. References

[1](a) C. G. Zoski, *Handbook of Electrochemistry,* Elsevier, **2007**.(b) V. S. Bagotsky, *Fundamentals of Electrochemistry*, John Wiley & Sons, Inc., **2005**.

[2] (a) G. Wang, L. Zhang, J. Zhang, *Chem. Soc. Rev.*, **2012**,*41*, 797.

[3](a) M. Winter, R. J. Brodd, *Chem. Rev.*, **2004**, *104*, 4245. (b) P. Simon, Y.Gogotsi, *Nat. Mater.,* **2008**, *7*, 845.

[4](a) D. Wu, F. Xu, B. Sun, R. Fu, H He, K. Matyjaszewski, *Chem. Rev*., **2012**, *112*, 3959.(b) C. Perego, R. Millini, *Chem. Soc. Rev.*, **2013**,*42*, 3956. (c) M. E. Davis, *Nature,* **2002**, *417*, 813.

[5](a) L. Kavan, *Chem. Rev.*, **1997**, *97*, 3061.(b) W. Gu, G. Yushin, *Review of nanostructured carbon materials for electrochemical capacitor applications*, John Wiley & Sons, **2014**, *3*, 424.

[6](a) V. Valtchev, G. Majano, S. Mintova, J. P.Ramírez, *Chem. Soc. Rev.,* **2013**,*42*, 263. (b) A. Walcarius, *Electroanalysis,* **2008**, *20*, 711.

[7] E. Maglara, A. Pullen, D. Sullivan, W. C. Conner, *Langmuir*, **1994**, *10*, 4167.

[8](a) K. Morishige, T. Kawai, S. Kittaka, *J. Phys. Chem. C*, **2014**, *118*, 4664. (b) G. Fe´rey, C. Serre, C. Mellot-Draznieks, F. Millange, S. Surble´, J. Dutour and I. Margiolaki, *Angew. Chem., Int. Ed.,* **2004**, *43*, 6296. (c) G. Fe´rey, C. Mellot-Draznieks, C. Serre, F. Millange, J. Dutour, S. Surble´ and I. Margiolaki, *Science*, **2005**, *309*, 2040.

[9] X. Wang, X. Bu, P. Feng, Porous Inorganic Materials, *Encyclopedia of Inorganic and Bioinorganic Chemistry*, John Wiley & Sons, Ltd., **2006**.

[10](a) S. P. Surwade, S. H. Chai, J.P. Choi, X. Wang, Je S. Lee, I. V. Vlassiouk, S. M. Mahurin, S. Dai, *Langmuir*, **2014**, *30*, 3606. (b) C. Jo, Y. Park, J. Jeong, K. T. Lee, J. Lee, *ACS Appl. Mater. Interfaces*, **2015**, *7*, 11748.

[11] G. K. H. Shimizu, J. M. Taylor, S. Kim, *Science*, **2013**, *341*, 354. (c) S. Sen, N. N. Nair, T. Yamada, H. Kitagawa P. K. Bharadwaj*, J. Am. Chem. Soc.*, **2012**, *134*, 19432.

[12]H. Furukawa, K. E. Cordova, M. O'Keeffe, O. M. Yaghi, *Science*, **2013**, *341*, 12304.

[13]H. C. Zhou, J. R. Long, O. M. Yaghi, *Chem. Rev*., **2012**, *112*, 673.

[14](a) H.-Q. Xu, K. Wang, M. Ding, D. Feng, H.-L. Jiang, H.-C. Zhou, *J. Am. Chem. Soc.*, **2016**, *138*, 5316. (b) H. Al-Kutubi, J. Gascon, E. J. R. Sudhölter, L. Rassaei, *ChemElectroChem*, **2015**, *2*, 462.

[15](a) W.J. Li, J. Liu, Z.-H. Sun, T.F. Liu, J. Lu, S.Y. Gao, C. He, R. Cao, Jun-Hua Luo, *Nat. Commun,* **2016**, *7*, 11830.

[16] (a) D. D. Diaz, D. Kuhbeck and R. J. Koopmans, *Chem. Soc. Rev*. **2011**,*40*, 427. b) P.Terech, R.G.Weiss, *Chem. Rev*. **1997**, *97*, 3133.

[17](a)M.O. M. Piepenbrock, G. O.Lloyd, N. Clarke, J. W. Steed, *Chem. Rev*. **2010**,*110*,1960. (b) G. R. Desiraju, *Angew. Chem. Int. Ed. Engl.* **1995**, *34*, 2311.

[18] A. Y. Y. Tam, V. W. -W. Yam, Chem. Soc. Rev. **2013**, 42, 1540.

[19]Y. Zeng, R. Zou, Z. Luo, H. Zhang, X. Yao, X. Ma, R. Zou ,Y. Zhao, *J. Am. Chem. Soc*., **2015**, *137*, 1020

[20]D. D. Medina, J. M. Rotter, Y. Hu, M. Dogru, V. Werner, F. Auras, J. T. Markiewicz, P. Knochel, T. Bein, *J. Am. Chem. Soc.* **2015**, *137*, 1016.

[21] P. J. Waller, F. Gándara, O. M. Yaghi, *Acc. Chem. Res.* **2015**, *48*, 3053

[22] X. Feng, X. Ding, D. Jiang, *Chem. Soc. Rev*., **2012**, *41*, 6010.

[23] M. Dogru, T. Bein, *Chem. Commun.*, **2014**, *50*, 5531.

[24] J. Liu, L. Chen, H. Cui, J. Zhang, L. Zhang, C. Y. Su, *Chem. Soc. Rev.*, **2014**,*43*, 6011.

[25] (a)R. Diaz, M. Gisela Orcajo, J. A. Botas, G. Calleja, J. Palma, *Mater. Lett.,* **2012**, *68*, 126.(b) K. M. Choi, H. M. Jeong, J. H. Park, Y. B. Zhang, J. K. Kang, O. M. Yaghi, *ACS Nano*, **2014**, *8*, 7451.

[26] Y. Gao, J. Wu, W. Zhang, Y. Tan, J. Zhao, B. Tang, *Mater. Lett.,* **2014**, *128*, 208.

[27]A. Morozan, F. Jaouen, *Energy Environ. Sci.,* **2012**, *5*, 9269.

[28] L. Wang, X. Feng, L. Ren, Q. Piao, J. Zhong, Y. Wang, H. Li, Y. Chen, B. Wang, *J. Am. Chem. Soc.*, **2015**, *137*, 4920.

[29]G. Férey, F. Millange, M. Morcrette, C. Serre, M. L. Doublet, J. M. Grenèche, J.M. Tarascon, *Angew. Chem. Int. Ed.* **2007**, *46*, 3259.

[30]A.S. Hameed, M. Nagarathinam, M. Schreyer, M.V. Reddy, B.V.R. Chowdari,J.J. Vittal, *J. Mater. Chem. A*, **2013**, *1*, 5721.

[31] Z. Wang, B. Wang, Y. Yang, Y. Cui, Z. Wang, B. Chen, G. Qian, *ACS Appl. Mater. Interfaces*, **2015**, *7*, 20999.

[32] (a) R. Demir-Cakan, M. Morcrette, F. Nouar, C. Davoisne, T. Devic, D. Gonbeau, R. Dominko, C. Serre, G. Ferey, J.M. Tarascon, *J. Am. Chem. Soc.* **2011**, *133*, 16154; (b) Y.

Han, P. Qi, J. Zhou, X. Feng, S. Li, Xiaotao Fu, J. Zhao, D. Yu, B. Wang, *ACS Appl. Mater. Interfaces*, **2015**, *7*, 26608.

[33]Y. Xu, X. B. Yin, X. W. He, Y. K. Zhang, *Biosensors and Bioelectronics,* **2015**, *68*, 197.

[34] A. Dolbecq, E. Dumas, C. R. Mayer, P. Mialane, *Chem. Rev.*, **2010**, *110*, 6009.

[35] B. Nohra, H.E. Moll, L. M. Rodriguez Albelo, P. Mialane, J. Marrot, C. M. Draznieks, M. O'Keeffe, R. N. Biboum,J. Lemaire, B. Keita, L. Nadjo and A. Dolbecq, *J. Am. Chem. Soc.*, **2011**, *133*, 13363.

[36] M. Jahan, Q. Bao and K. P. Loh, *J. Am. Chem. Soc*., **2012**, *134*, 6707.

[37] J.J. Mao, L.F. Yang, P. Yu, X.W. Wei, L.Q. Mao, *Electrochem. Commun*. **2012**, *19*, 29.

[38]L. Yang, S. Kinoshita, T. Yamada, S. Kanda, H. Kitagawa, M. Tokunaga, T. Ishimoto, T. Ogura, R. Nagumo, A. Miyamoto, M. Koyama, *Angew.Chem.Int.Ed*., **2010**, *49*, 5348.

[39] R.S. Kumar, S.S. Kumar, M.A. Kulandainathan, *Electrochem. Commun.* 2012, 25, 70.

[40] C. Wang, Z. Xie, K. E. deKrafft, W. Lin, *J. Mater. Chem. A*, **2015**, *3*, 20607.

[41] K. F. Babu, M. A. Kulandainathan, I. Katsounaros, L. Rassaei,A. D. Burrows, P. R. Raithby, F. Marken, *Electrochem. Commun*., **2010**, *12*, 632.

[42] C. Wang, Z. Xie, K. E. de Krafft, W. Lin, *J. Am. Chem. Soc*., **2011**,*133*, 13445.

[43] M. Jahan, Z. Liu, K. P. Loh, *Adv. Funct. Mater.* **2013**, *23*, 5363.

[44](a) H. Steininger, M. Schuster, K. D. Kreuer, A. Kaltbeitzel, B. Bingol, W. H. Meyer, S. Schauff, G. Brunklaus, J. Maier and H. W. Spiess, *Phys. Chem. Chem. Phys*. **2007**, *9*, 1764

[45](a) S. Sanda, S. Biswas, S. Konar, *Inorg. Chem.*, **2015**, *54*, 1218.(b) C. L.-Robert, K. Valle, F. Pereirab and C. Sancheza, *Chem. Soc. Rev*. **2011**, *40*, 961.

[46]A. Horike, D. Umeyama, S. Kitagawa, *Accounts Of Chemical Research*, **2013**, *46*, 2376.

[47] Y. Nagao, R. Ikeda, S. Kanda, Y. Kubozono, H. Kitagawa,Mol. *Cryst. Liq. Cryst.,* **2002**, *379*, 89.

[48] T. Yamada, M. Sadakiyo, H. Kitagawa, *J. Am. Chem. Soc*., **2009**, *131*, 3144.

[49] M. Sadakiyo, T. Yamada, H. Kitagawa, *J. Am. Chem. Soc*., **2009**, *131*, 9906.

[50](a)P. Ramaswamy, N. E. Wong, G. K. H. Shimizu, *Chem. Soc. Rev.,* **2014**, *43*, 5913 (b) P. Ramaswamy, R. Matsuda, W. Kosaka, G. Akiyama, H. J. Jeon, S. Kitagawa, *Chem. Commun.*, **2014**, *50*, 1144.

[51] J. A. Hurd, R. Vaidhyanathan, V. Thangadurai, C. I. Ratcliffe, I. L. Moudrakovski and G. K. H. Shimizu, *Nat. Chem*., **2009**, *1*, 705.

[52] S. S. Nagarkar, S. M. Unni, A. Sharma, S. Kurungot, S. K. Ghosh, *Angew. Chem., Int. Ed.*, **2014**, *53*, 2638.

[53] K. Fujie, R. Ikeda, K. Otsubo, T. Yamada, H. Kitagawa, *Chem. Mater*. **2015**, *27*, 735.

[54] B. M. Wiers, M.L. Foo, N. P. Balsara, J. R. Long, *J. Am. Chem. Soc* .**2011**, *133*, 14522.

[55] S. E.-d. H. Etaiw, A. E.-A. S. Fouda, S. N. Abdou, M. M. Elbendary, *Corros. Sci*., **2011**, *53*, 3657.

[56] S. E.-d. H. Etaiw, A. E.-A. S. Fouda, S. A. Amer and M. M. Elbendary,J. *Inorg. Organomet. Polym. Mater.,* **2011**, *21*, 327.

[57] (a) H.L. Jiang, B.Liu, Y.Q. Lan, K. Kuratani, T. Akita, H. Shioyama, F. Zong, and Q. Xu, *J. Am. Chem. Soc.*, **2011**, *133* , 11854.(b) S. J. Yang, T. Kim, J. H. Im, Y. S. Kim, K. Lee, H. Jung, C. R. Park, *Chem. Mater.*, **2012**, *24*, 464.

[58] B. Liu, H. Shioyama, T. Akita, Q. Xu, *J. Am. Chem. Soc*., **2008**, *130*, 5390.

[59] J. P. Dodelet, *N_4-Macrocyclic Metal Complexes, ed.* J. H. Zagal, F. Bedioui, J. P. Dodelet, Springer, New York, **2006**.

[60] (a)Z. Jiang, Z. Li, Z. Qin, H. Sun, X. Jiao and D. Chen, *Nanoscale,* **2013**, *5*, 11770. (b) X. Xu, R. Cao, S. Jeong, J. Cho, *Nano Lett.*, **2012**, *12*, 4988.

[61] G. Huang, L. Zhang, F. Zhang, L. Wang, *Nanoscale*, **2014**, *6*, 5509.

[62]L. Hu, Y. Huang, F. Zhang, Q. Chen, *Nanoscale*, **2013**, *5,* 4186.

[63] S.Saha, E.M. Schon, C. Cativiela, D. D.Diaz, R. Banerjee, *Chem. Eur. J.* **2013**, *19*, 9562.

[64](a) A. P. Côté, A. I. Benin, N. W. Ockwig, M. O'Keeffe, A. J.Matzger, O. M. Yaghi, *Science*, **2005**, *310*, 1166.

[65] S. Lin, C. S. Diercks, Y.-B. Zhang, N. Kornienko, E. M. Nichols, Y. Zhao, A. R. Paris, D. Kim, P. Yang, O. M. Yaghi, C. J. Chang, *Science*, **2015**, 349, 1208.

[66] F. Xu, S. Jin, H. Zhong, D. Wu, X. Yang, X. Chen, H. Wei, R. Fu, D. Jiang, *Scientific Reports,* **2015**, *5*, 8225.

[67] E. M. Miner, T. Fukushima, D. Sheberla, L. Sun, Y. Surendranath, M. Dinca, *Nat. Commun.,* **2016**, *7*, 10942.

[68] H. Liao, H. Wang, H. Ding, X. Meng, H. Xu, B. Wang, X. Ai, C. Wang, J. *Mater. Chem. A*, **2016**, *4*, 7416.

[69] H. Xu, S. Tao, D. Jiang, *Nat. Mater.* **2016**, 1.

[70] H. Ma, B. Liu, B. Li, L. Zhang, Y.-G. Li, H. -Q. Tan, H.-Y. Zang, G. Zhu, *J. Am. Chem. Soc*. **2016**, *138*, 5897.

Chapter -2

Electrochemical characterization of porous polymeric materials

The electrochemical techniques are powerful and sensitive analytical methods which give a wealth of information on the chemical response of a system when an electric potential is applied to it, at very low detection limits. They are often utilized to determine the concentration, chemical condition, reaction kinetics and mechanism of an electroactive species (could be both inorganic and organic) in the system. They are also used to monitor the redox processes at the electrode-electrolyte interface during the electrical stimulation. The response is usually measured using one of the following parameters: charge (Q), current (i), potential (E) and time (t), as the excitation signal. Depending on the different combinations of the measuring parameters used, a number of electrochemical methods are in practice. Most of these electrochemical techniques classically employ three types of electrodes – the working, the reference and the auxiliary (or counter) electrodes. In a typical experiment, the potential of the working electrode is controlled using a potentiostat and the resulting current is then measured as a function of time. The present chapter gives a brief description about the electrochemical methods used for characterizing the materials and concisely describes the basic working principles of few energy systems involved in the study. The chapter intends to familiarize the reader with the electrochemical techniques inorder to analyze the results obtained from the characterization techniques like cyclic voltammetry (CV), charge-discharge study, linear sweep voltammetry, rotating disk electrode (RDE), rotating ring disk electrode (RRDE), Mott-Scottky analysis, AC-impedance analysis etc. These techniques are utilized in the present study to understand the electrochemical behavior of the materials. It encloses a brief description of each of the methods used and the nature of the information that could be obtained using it, without pondering into too much details.

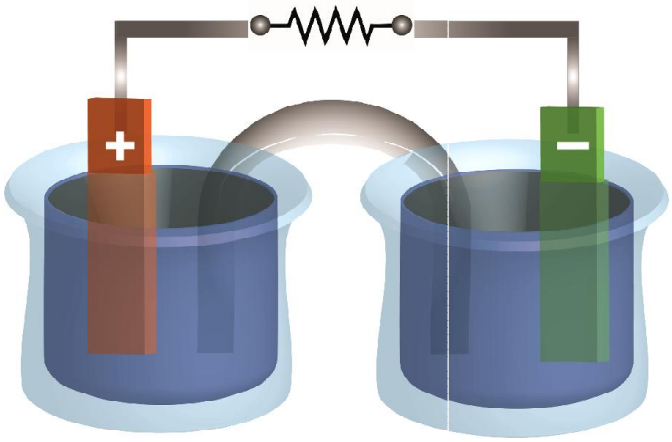

2.1. Electrochemical characterization techniques

2.1.1. Voltammetry: Linear Sweep Voltammetry (LSV) and Cyclic Voltammetry (CV)

Voltammetry is a versatile analytical technique wherein the potential is ramped between the working and reference electrode using a potentiostat and the resulting current is measured.[1] During the potential scan, on reaching a specific potential, the electroactive species (also known as the analyte) undergoes oxidization/reduction at the working electrode. The current resulting from this electrochemical reaction is then measured at the counter electrode. This technique can be used to detect a number of analytes during the same potential scan, which makes it attractive for measuring various chemical species in the given environment at very low detection limits.

Linear Sweep Voltammetry (LSV) is one of the generally applied methods of voltammetry wherein the potential is linearly ramped in either of the directions (negative or positive) and the resulting current is measured as a function of time. [2] This technique is most generally used to measure the electrocatalytic oxygen reduction reaction activity of the species on increasing the amount of dissolved oxygen in the medium. The characteristics of a LSV curve depends on the rate of charge transfer, chemical response of the analyte species and the scan rate used for the potential scan. Cyclic voltammetry (CV), also known as the 'electrochemical spectroscopic equivalent', is another routinely used technique to study the electrochemical property of a chemical species. [3] It is similar to the LSV, except for the back-scanning of the potential which causes the anodic and cathodic scans to repeat alternately for a number of times. In this technique, the potential is scanned between two potentials E_1 and E_2 at a definite scan rate ν, and the resulting current is measured as a function of the changing potential. This technique helps in the preliminary understanding of the rate of a new electrochemical reaction coupled to the electron transfer process at the working electrode. The three-electrode configuration is often used for the CV study. Herein, the potential applied to the working electrode is measured against the reference electrode and the electrical circuit is closed by the auxiliary electrode in turn enabling the current to flow. In the experiment, the combinations of the electrolyte, working electrode, active material and the solvent used determine the potential window that could be applied. **Figure 2.1** illustrates a typical CV for a reversible system. It is important to note that the current bears a negative sign for the cathodic scan (which indicates a decrease in the applied potential), and is positive

for the anodic scan (which indicates an increase in the applied potential). In a reversible process, (i) the potential difference between the two peaks is given by $\Delta E = E_a - E_c = 59/n$ mV, (ii) the peak position remains unaltered with change in the scan rate, (iii) the ratio of the anodic and cathodic peak currents is always one and (iv) the peak currents (anodic and cathodic) are always relative to the square root of the scan rates. The slope of the plot is proportional to the diffusion coefficient (D), as given in the Randles-Sevcik equation at 25 ˚C,

$$i_p = 269\, n^{3/2} A\, D^{1/2} \vartheta^{1/2} C_b$$

where, i_p is the peak current height (in A); n is the number of electrons; A is the area (in cm^2); D is the diffusion coefficient (in cm^2/sec); ν is the scan rate (in V/sec); C_b is the bulk concentration of solution (in M). [4]

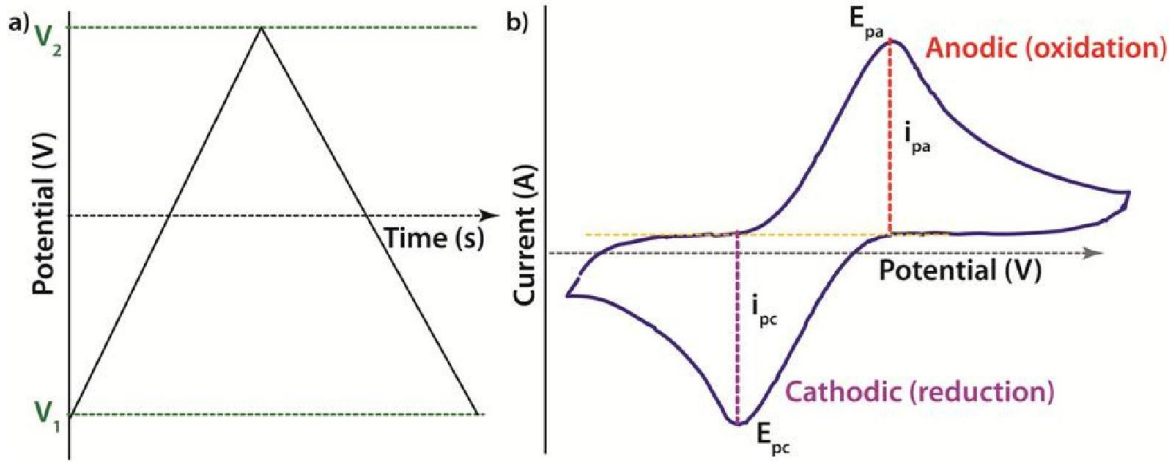

Figure 2.1. *Representation of (a) Waveform of a CV and (b) typical cyclic voltammogram, wherein, E_{pc}, i_{pc} and E_{pa}, i_{pa} are the cathodic and anodic peak potentials and currents respectively.*

2.1.2. Chronoamperometry

The chronoamperometry is a 'current transient technique' in which the potential of the working electrode (which is in the steady state) is changed abruptly from V_1 to V_2 and the resulting changes in the current is measured as a function of time.[5] This technique is widely used to examine the kinetic behavior of an electroactive material. During this potential stepping process, it is supposed that the diffusion of the active species governs the whole process. The kinetics of the interfacial charge-transfer reaction is so facile that it enables the rapid saturation of the active species (equal to its equilibrium concentration) at the electrode

surface. This instant increase/decrease in the active species concentration at the electrode surface is in turn compensated by the ionic supply towards/away from the bulk of the electrolyte, thereby creating a potentiostatic boundary. This technique is often used for quantitatively analyzing the process of nucleation at the electrode-electrolyte interface.

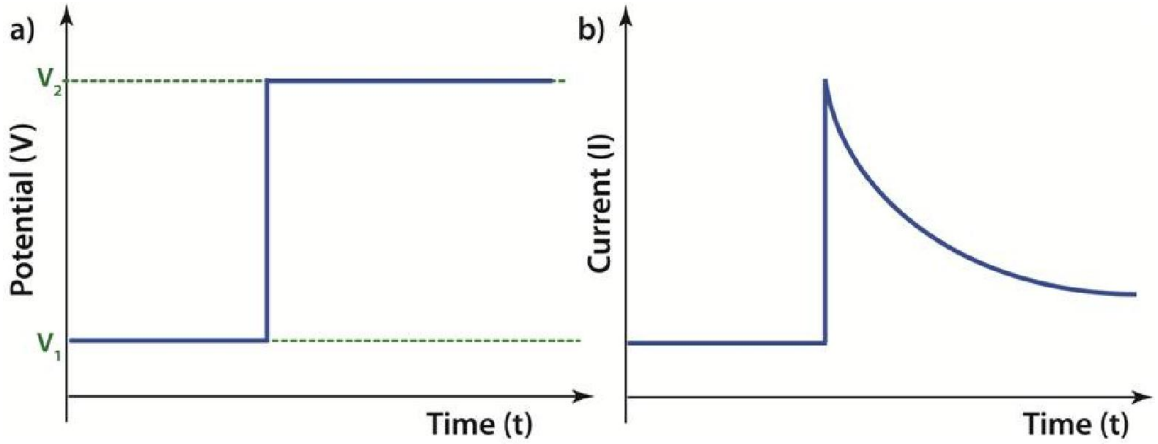

Figure 2.2. *a) Excitation waveform and b) response waveform for a CA.*

2.1.3. Chronopotentiometry

Chronopotentiometry is a powerful technique wherein the current flowing through the working electrode is suddenly stepped up from zero. [6] This results in an abrupt change in the concentration of the electroactive species at the electrode-electrolyte interface and the resulting change in the potential is plotted as a function of time.

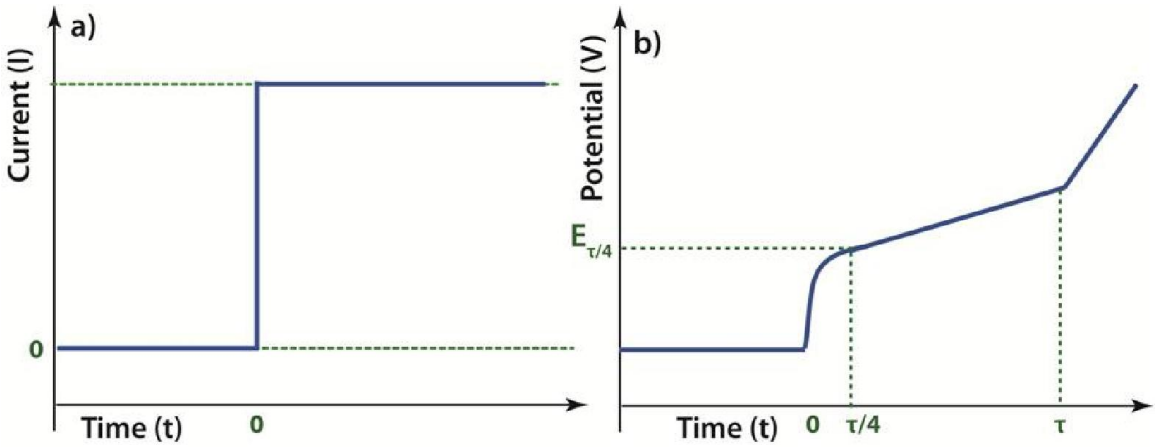

Figure 2.3. *a) Current excitation and b) potential response for CP.*

The overpotential developed at the interface is considered equivalent to the concentration of the reactant is accumulated /exhausted at the electrode surface. During the study, the solution

is left unstirred and a large amount of electrolyte is used to nullify the conventional and migration effects in the system. Thus, the mass transfer is entirely driven by the diffusion factor. **Figure 2.3** illustrates a typical chronopotentiogram for a reversible system.

2.1.4. Rotating Disk Electrode (RDE)

A rotating disk electrode (RDE) is one of the simple, highly accurate hydrodynamic methods used to study the electrode kinetics and mechanisms of reaction at the solid electrode-electrolyte interface. [7] A typical RDE electrode consists of a glassy carbon/platinum disk which is encapsulated inside a rod made up of insulating material like Teflon. The rotation of the RDE electrode is controlled using a motor and rotation is often expressed in terms of frequency, given by, $f = \omega/2\pi$, wherein ω is the angular frequency. During the rotation, the centrifugal forces continually move the electrolyte horizontally away from the RDE centre, thereby replacing the fresh solution towards the electrode surface. The advantages of using RDE are as follows: (i) the thickness of the diffusion layer is same throughout, (ii) minimizes the effect of the double-layer charging on the measurements and (iii) the mass transfer equations could be easily used to relate the experimental factors to the mass transfer of reacting species towards the electrode surface. The number of electrons transferred per O_2 molecule in the ORR process is determined using Koutecky–Levich (K-L) equation. The K-L equation relates the inverse of the current density (1/j) and the inverse of the square root of the rotation speed ($1/\omega^{1/2}$), and can be represented as follows,

$$\frac{1}{j} = \frac{1}{j_k} + \frac{1}{j_d}$$

wherein, j is the measured current density, j_k is the kinetic current density and j_d is the diffusion current density. The measured current density can be further expanded as follows:

$$\frac{1}{j} = \frac{1}{nFKC_{O_2}} + \frac{1}{0.62nFAD_{O_2}^{2/3}C_{O_2}\vartheta^{-1/6}\omega^{1/2}}$$

Or simplified to $\frac{1}{j} = \frac{1}{nFkC_{O_2}} + \frac{1}{B\omega^{1/2}}$; $B = 0.62\, nFC_o\,(D_o)^{2/3}\, v^{-1/6}\, C_{O2}$

where, j_k is the kinetic current density, ω is the angular velocity and B is related to the diffusion limiting current density, also expressed in the above equation (where, F is the Faraday constant (F= 96485 C/mol), C_{O2} is the bulk concentration of O_2 (1.2×10^{-3} mol/l), ν

is the kinematic viscosity of the electrolyte ($\nu = 0.1\ m^2/s$) and D is the diffusion coefficient of O_2 in the electrolyte).

In the present work, the RDE experiments are carried out to understand the fundamentals of the electrocatalytic oxygen reduction reaction (ORR) activity of the catalyst. [8] In the study, all the electrochemical experiments are performed in an Autolab PGSTAT 30 (Echochemie) using a conventional three-electrode system. The glassy carbon (GC) electrode (5 mm diameter) embedded in Teflon is used as the working electrode. This electrode is polished on a polishing cloth using 0.3 μm alumina slurry followed by washing with water and acetone. The sample coating on the working electrode is carried out as follows: 5 mg of the catalyst is dispersed in 1 ml of ethanol in water (3:2) solution by sonication. Then, 10 μl aliquot of the prepared slurry is drop-casted on the GC electrode using a micro syringe. Subsequently, 3 μl of 0.1 % Nafion® solution in ethanol is coated onto the surface as a binder. This electrode is further dried in air for 3 h and is then used as the working electrode.

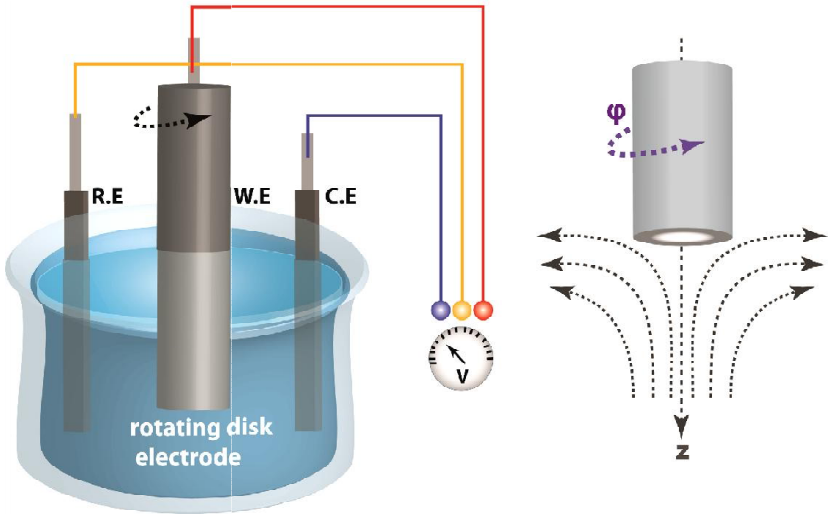

Figure 2.4. *Schematic representation of the hydrodynamic working of a rotating disk electrode.*

2.1.5. Rotating Ring Disk electrode (RRDE)

As the RDE technique is not reversal, the products of the electrochemical reaction are often swept away from the RDE surface. Therefore, the rotating ring disk electrode (RRDE) technique is employed to avail the information equivalent to that from a reversal technique. [9] Herein, an independent ring electrode (made of platinum) is made to surround the disk electrode. It is also important to note that the current–potential characteristics of the disc

electrode is unaffected by the existence of the outer ring. A bipotentiostat is therefore needed to measure the potential of both the disk and ring electrode independently. The information about the electrode reactions occurring at the disk electrode can therefore be obtained by measuring the ring current (I_r).

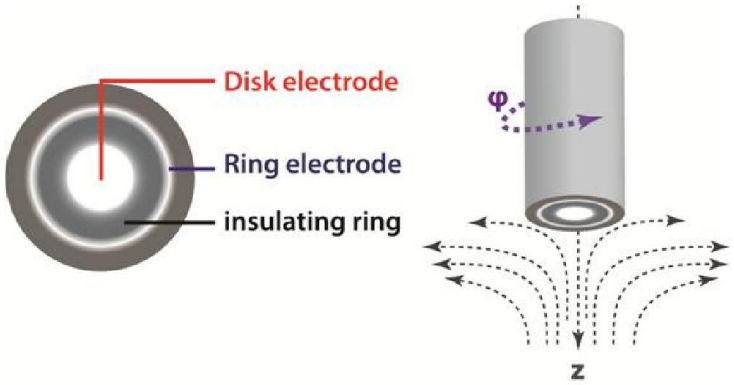

Figure 2.5. *Schematic representation of a rotating ring disk electrode.*

In the present work, the RRDE technique has been employed to understand the nature of the products (*i.e.*, the H_2O_2 yield) generated at the disk electrode. Initially, the collection efficiency of the electrode is determined by using the standard ferrocene redox couple. The collection efficiency (N) is calculated using the ratio of the ring and the corresponding disk current and is found to be 0.37 in the present case. The yield of the H_2O_2 formed during the RRDE analysis is then calculated from the following formula,

$$\mathbf{H_2O_2}\ (\%) = \mathbf{200} \times \frac{\mathbf{I_r/N}}{\frac{\mathbf{I_r}}{\mathbf{N}} + \mathbf{I_d}}$$

Where, I_r is the ring current, I_d is the disc current, and N is the collection efficiency.

2.1.6. Electrochemical Impedance Spectroscopic (EIS) analysis

Impedance refers to frequency dependent resistance to the flow of the alternating current through the circuit elements namely resistor, capacitor, inductor, etc.

Thus, the impedance is given by Z_ω, $\mathbf{Z_\omega} = \frac{\mathbf{E_\omega}}{\mathbf{I_\omega}}$

where, E_ω is the frequency dependent potential and I_ω is the frequency dependent current. It could therefore be understood that the impedance is equal to resistance (Z_ω = R) at the zero frequency limit. In comparison to the direct current (DC) techniques, an alternating current (AC) dependent impedance study provides more information about the electrochemical

reactions. It could be used to distinguish between two or more electrochemical reactions taking place in the reaction system. EIS is a non-destructive technique which provides information about the reactions limited by diffusion and therefore helps to better understand the capacitive behavior of the material under study. [10]

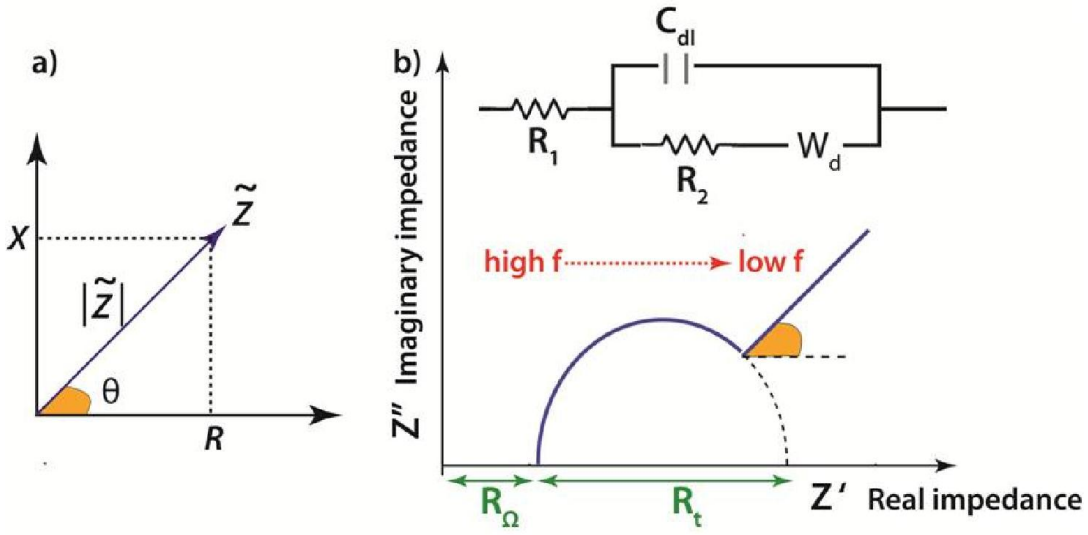

***Figure 2.6**. a) Schematic representation of a complex impedance plane and b) a typical Nyquist plot with its equivalent circuit.*

In the present work, the EIS measurements are carried out to test the components within an assembled membrane electrode assembly (MEA) of a single PEM fuel cell. In the study, a small sinusoidal perturbation (5-15 mV potential) of fixed frequency is applied to the system at a steady state. The system is then scanned across a known frequency range (from MHz to mHz). The response measured at each frequency is then plotted and analyzed. It is important to note that he data obtained is a complex quantity,

$\mathbf{Z_{total} = Z_{real} + Z_{imaginary}}$;

which is defined by the magnitude of the impedance and the phase angle (φ). Using the EIS response, the electrochemical system can be then be modeled as a network of electrical circuit elements called as the 'equivalent circuit'. Depending on the complexity of the system, a number of complex models can be designed. It is important to note that in an equivalent circuit, each element corresponds to some specific element in the electrochemical system. A proper fit would therefore infer proper representation of the elements in the electrochemical system.

2.1.7. Mott-Schottky analysis

Whenever an electrode is brought in contact with an electrolyte, a potential gradient develops at the interface. Depending on the electrical nature of the electrode (conductor/semiconductor) used, the potential drops more on the electrode side or the electrolyte side of the gradient boundary. The Fermi levels of both the systems therefore bend along the interface boundary. The flat band amounts to the band-bending caused by the pinning of the Fermi levels at this semiconductor-electrolyte interface. The Mott-Schottky analysis is thereby used to understand the band-edge positions of the semiconductor at this interface. [11] In the Mott-Schottky analysis, the capacitance at the interface is measured as a function of the potential under the conditions of the depletion of charges at the interface,

$$\frac{1}{C_{SC}^2} = \frac{2}{e\varepsilon\varepsilon_o N}(E - E_{FB} - \frac{kT}{e}$$

wherein, C_{sc} is the capacitance of the space charge region, ε is the dielectric constant of the semiconductor, ε_0 is the permittivity of free space, N is the donor density (electron donor concentration in case of n-type semi-conductor/ hole acceptor concentration for a p-type semiconductor), E is the applied potential, E_{FB} is the flat-band potential, k is the Boltzmann constant and T is the temperature.

The slope of the $1/C_2$ *vs*. E_{we} plot (called as Mott Schottky plot) is often a straight line which is used to calculate the donor density. The flat-band potential is further determined by extrapolating the line to C = 0. The Mott Schottky plot could also be used to determine the property of the semiconductor electrode. In case of an n-type semiconductor, the equation gives a straight line with negative slope, while the equation gives a positive slope for a p-type semiconductor.

2.2. Electrochemical energy systems

2.2.1. Fuel Cell (FC)

The principle of a fuel cell was first defined by a British physicist Sir William Grove in 1839, wherein he utilized cells containing hydrogen and oxygen to generate electric power. Fuel cells are energy conversion devices which convert chemical energy into electrical energy. [12] The fuel cells possess highest energy density among all the electrochemical devices as they operate as long as the reactants are in supply. Depending on

the nature of the reactants used and the type of electrolyte involved in the ionic conduction, the fuel cells are classified into six types. [13]

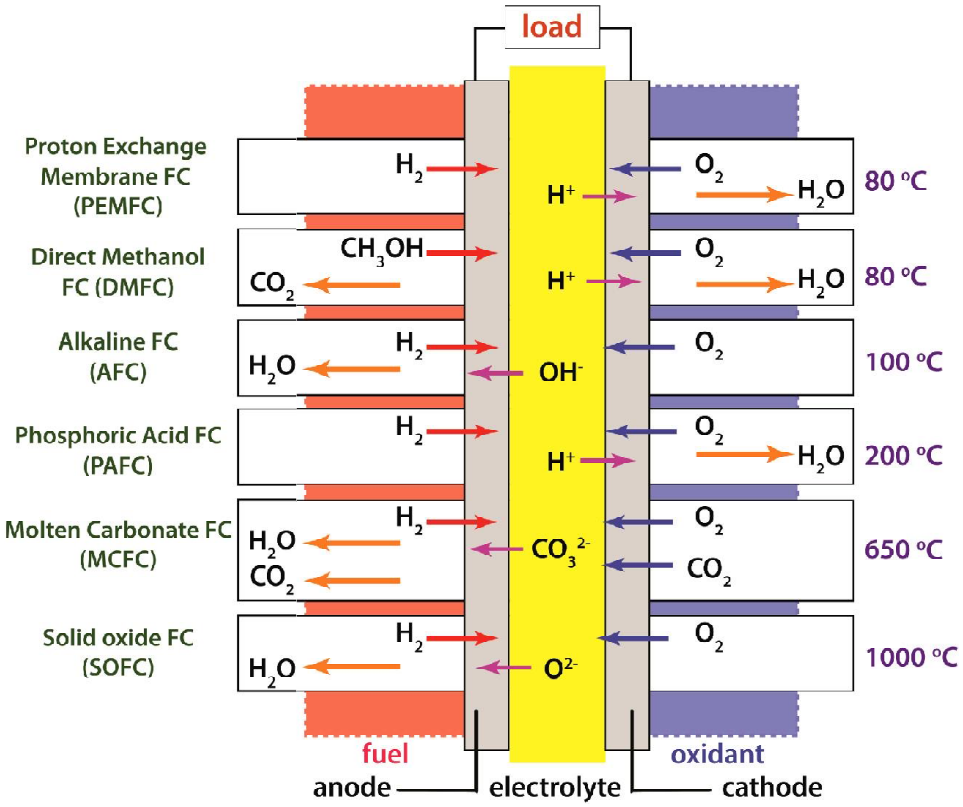

Figure 2.7. Classification of different types of fuel cells.

Among all the fuel cells, the PEMFC is widely used for the low temperature operations (80-160 ^{o}C). It involves a proton exchange membrane which is employed to conduct protons from one face to the other.[14] The commercial PEMFC utilizes Pt based electrocatalyst to drive the half-cell reactions. At the anode, the reactant H_2 gas is oxidized to generate electrons and protons. The as generated electrons travel through the external circuit, which is used for performing electrical work, while the protons pass to the cathode side of the cell through the proton conducting membrane. On reaching the cathode, the reactant O_2 molecules combine with the protons and electrons to produce water.

Anodic reaction (HOR)	**:**	$H_2 + 2\ OH^- \rightarrow 2\ H_2O + 2\ e^-$	$E^o = 0.0$ V
Cathodic reaction (ORR)	**:**	$½\ O_2 + H_2O + 2\ e^- \rightarrow 2\ OH^-$	$E^o = 1.23$ V
Overall reaction	**:**	$H_2 + ½\ O_2 \rightarrow H_2O$	$E^o = 1.23$ V

The Low Temperature PEMFC (LT-PEMFC) uses an acidic, sulfonated tetrafluoroethylene based hydrated ionomer commercially known as Nafion® as

the solid proton conducting membrane. Therefore, the gases must be humidified before being fed. [15] This limits the operation temperature is to 80-90 ˚C, in order to prevent the membrane from drying out. This therefore necessitates a need for an efficient water management system inorder to prevent the undesired flooding near the catalyst surface. Thus, LT-PEMFC needs expert supervision to be operated.

It is observed that the anodic hydrogen oxidation reaction (HOR) is relatively easier compared to the oxygen reduction reaction (ORR). [16] Thus, attempts are made to improve the reaction kinetics by increasing the operating temperature of the fuel cell. This also helps in better water management, which is crucial for the fuel cell performance, besides improving the catalyst resistance to fuel impurities like carbon monoxide (CO) etc. [17] The high temperature variant of PEMFC (HT-PEMFC) utilizes phosphoric acid doped PBI (polybenzimidazole) membrane for conducting protons across the electrodes. Most importantly, as this membrane does not need humidification to conducts proton, the temperature as high as 160 ˚C could be used for operating HT-PEMFCs. The high temperature operation results in better efficiency, higher power density of HT-PEMFC. It also enables relatively easy cooling of the cell and reduces the sensitivity of the platinum catalyst to CO poisoning. [18]

2.2.2. Supercapacitor

An electrochemical double layer capacitor (EDLC) is an energy storage device which stores energy by accumulating charges at the electrode-electrolyte interface, whose capacitance can be defined using the following relation,

$$\mathbf{C = \frac{q}{V}}$$

wherein, C is the capacitance, q is the charge stored and V is the voltage across the electrodes. [19] The capacitance is also related to the area of the electrode (A) and charge separation distance (d) as given by the relation,

$$\mathbf{C = \varepsilon_o \varepsilon_r \frac{A}{d}}$$

wherein, ε_o is the "permittivity" of free space and ε_r is the charge separating material's dielectric constant.

It could be observed that the EDLC is governed by the same basic equations as that of a conventional capacitor except that it utilizes electrodes with higher surface area and with much thinner dielectrics to achieve greater capacitances. [20]

The energy E stored in a capacitor is directly proportional to its capacitance (C) and voltage (V) across the electrodes, given by the relation $\mathbf{E = \frac{1}{2}CV^2}$. The power density is the energy density per unit time, which is represented by the relation: $\mathbf{P = \frac{V^2}{4R}}$, wherein, R is the resistance of the capacitor.

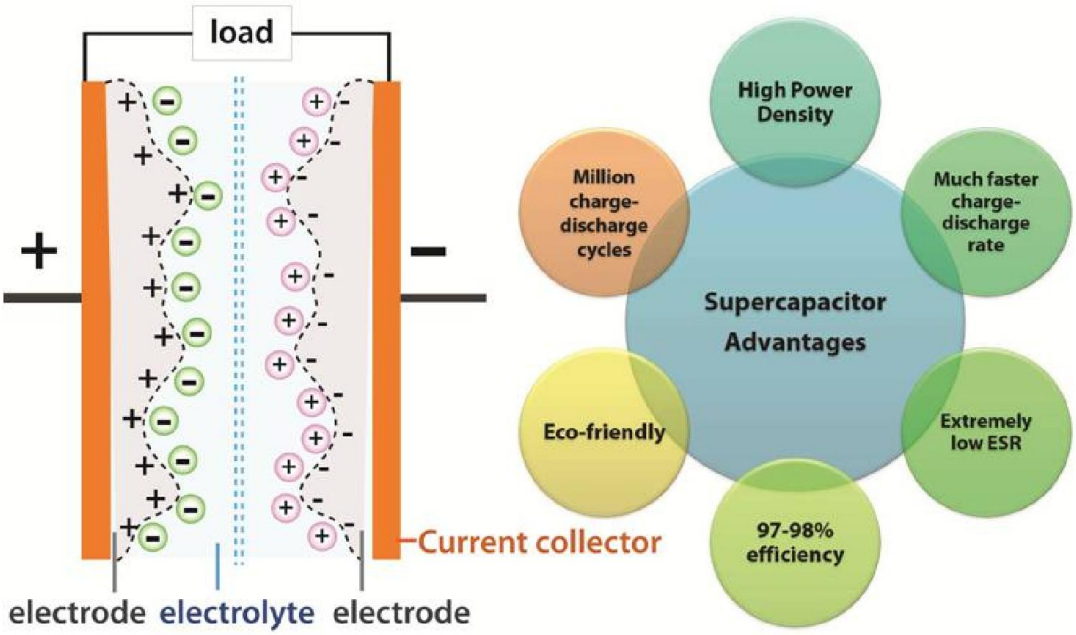

Figure 2.8. *Schematic representation of an electrical double layer capacitor and its advantages.*

By the virtue of their facile reversible ion adsorption way of storing energy, the EDLCs possess the highest power density among all the energy devices. However, these systems suffer from low energy density. [21] Therefore, attempts are made to improve the capacitance by incorporating pseudo-capacitive materials like metal oxides, conducting polymers into these EDLC systems. The pseudo-capacitive materials store charge electrochemically by means of fast reversible redox reactions at the electrode-electrolyte interface. Thus, a material which can store charges both electrostatically (non-faradically via reversible ion adsorption) and electrochemically (faradically via redox reaction) is termed as a 'supercapacitor'. [22] The power and energy density of supercapacitors could be enhanced

by (i) improving the specific capacitance of material, (ii) using high surface area nanostructured electrodes and (iii) employing non aqueous electrolyte, which provides high voltage window for operation. The supercapacitors have several advantages over the conventional battery and fuel cell systems *viz.*, infinite cycle life, rapid charging time, low equivalent series resistance (ESR) compared to batteries and is more environment-friendly, safe and cost effective compared to the other energy devices. [23]

2.3. References

[1](a) A. J. Bard, L. R. Faulkner, *Electrochemical Methods*, Wiley New York, **2001**. (b) B. Speiser, *Linear Sweep and Cyclic Voltammetry, Encyclopedia of Electrochemistry*, John Wiley & Sons Inc., **2007**.

[2](a) G. A. Mabbott, *J. Chem. Educ.*, **1983**, *60*, 697. (b) I. Streeter, R. G. Compton, *J. Phys. Chem. C*, **2007**, *111*, 15053.

[3](a) D. H. Evans, K. M. O'Connell, R. A. Petersen, M. J. Kelly, *J. Chem. Educ.*, **1983**, *60*, 290. (b) J. J. Van Benschoten, J. Y. Lewis, W. R. Heineman, D. A. Roston, P. T. Kissinger, *J. Chem. Educ.*, **1983**, *60*, 772.

[4](a) E. Kätelhön, C. B.-McAuley, R. G. Compton, *J. Phys. Chem. C*, **2015**, *119*, 23203. (b) D. M. Yerga, E. C. Rama, A. C. García, *J. Chem. Educ.* **2016**, *93*, 1270.

[5](a)W. T. Yap, L. M. Doane, *Anal. Chem.*, **1982**, *54*, 1437. (b) E. J. F. Dickinson, I. Streeter, R. G. Compton, *J. Phys. Chem. B*, **2008**, *112*, 4059.

[6](a) C. R. Christensen, F. C. Anson, *Anal. Chem.*, **1963**, *35*, 205. (b) T. Kambara, I. Tachi, *J. Phys. Chem.*, **1957**, *61*, 1405.

[7](a) P. G. Zambonin, *Anal. Chem.* **1969**, *41*, 868. (b) I. Fried, P. J. Elving, *Anal. Chem.*, 1965, *37*, 803; (b) P. Shi, D. A. Scherson, *Anal. Chem.*, **2004**, *76*, 2398.

[8] Y.-H. Shih, G. V. Sagar, S. D. Lin, *J. Phys. Chem. C*, **2008**, *112*, 123. (b) M. Shao, Q. Chang, J.-P. Dodelet, R. Chenitz, *Chem. Rev.* **2016**, 116, 3594.

[9](a) R. Jiang, S. Dong, *J. Phys. Chem.*, **1990**, *94*, 7471. (b) J. Chlistunoff, *J. Phys. Chem. C*, **2011**, *115*, 6496.

[10](a) Y. Aoki, S. Kobayashi, T. Yamaguchi, E. Tsuji, H. Habazaki, K. Yashiro, T. Kawada, T. Ohtsuka, *J. Phys. Chem. C*, **2016**, *120*, 15976. (b) M. E. Orazem, B. Tribollet, *Electrochemical Impedance Spectroscopy*, John Wiley & Sons, Inc., **2008**.

[11](a) A. Mani, Ca. Huisman, A. Goossens, J. Schoonman, *J. Phys. Chem. B*, **2008**, *112,* 10086. (b) T. Kirchartz, W. Gong, S. A. Hawks, T. Agostinelli, R. C. I. MacKenzie, Y. Yang, J. Nelson, *J. Phys. Chem. C*, **2012**, *116*, 7672.

[12](a) W. Vielstich, A. Lamm , H. A. Gasteiger, *Handbook of Fuel Cells: Fundamentals, Technology, Applications*, John Wiley and Sons, Inc., **2003**. (b) E. J. Cairns and H. Shimotake, *Fuel Cell Systems-II*, 30, 392.

[13](a) A. C. Rady, S. Giddey, S. P. S. Badwal, B. P. Ladewig, S. Bhattacharya, *Energy Fuels*, **2012**, *26*, 1471. (b) R. O' Hayre, S.-W. Cha, W. Colell, F. B. Prinz, Overview of Fuel Cell Types, John Wiley & Sons, **2016**.

[14](a) A. Kongkanand, N. P. Subramanian, Y. Yu, Z. Liu, H. Igarashi, D. A. Muller, *ACS Catal.*, **2016**, *6*, 1578.(b) Y. Shao, Y. Cheng, W. Duan, W. Wang, Y. Lin, Y. Wang, J. Liu*, ACS Catal.*, **2015**, *5*, 7288.

[15]M. A. Yandrasits, S. J. Hamrock, *Fuel Cell Chemistry and Operation,* 2, 1040, 15, ACS Symposium Series, **2010**.

[16](a) M. Shao, Q. Chang, J.-P. Dodelet, R.Chenitz, *Chem. Rev.*, **2016**, *116*, 3594. (b) G.G. Asara, L. O. Paz-Borbon, F. Baletto, *ACS Catal.* **2016**, *6*, 4388.

[17](a) J.Y. Tilquin , R. Côté , D. Guay , J.P. Dodelet, G. Denès, *J. Power Sources*, **1996**,*61*, 193 . (b)J. J. Baschuk, X.Li, Int. *J. Energy Res*. **2001**, *25*, 695.

[18](a) M. R. Berber, T. Fujigaya, K. Sasaki, N. Nakashima, *Scientific Reports*, **2013**, *3*, 1764. (b) L. Xiao , H. Zhang , E. Scanlon , L. S. Ramanathan , E.-W. Choe , D. Rogers , T. Apple , B. C. Benicewicz, *Chem. Mater.*, **2005**, *17*, 5328.

[19] M. Winter, R. J. Brodd, *Chem. Rev.*, **2004**, *104*, 4245.

[20] P. Simon, Y.Gogotsi, *Nat. Mater.,* **2008**, *7*, 845.

[21] E. Schmidt, S. Shi, P. P. Ruden, C. D. Frisbie, ACS Appl. Mater. Interfaces 2016, 8, 14879. (b) H. Ji, X. Zhao, Z. Qiao , J. Jung, Y. Zhu, Y. Lu, L. L. Zhang, A. H. MacDonald, R. S. Ruoff, *Nat. Commun.* **2014**, *5,* 3317.

[22](a) G. Wang, L. Zhang, J. Zhang, *Chem. Soc. Rev.*, **2012**,*41*, 797. (b) M. F. El-Kady, Y. Shao, R. B. Kaner, *Nat. Rev. Mater.* **2016**, *1,* 16033.

[23](a) Y. Deng, Y. Xie, K. Zou, X. Ji, *J. Mater. Chem. A,* **2016***,4,* 1144. (b) W. K. Chee, H. N. Lim, Z. Zainal, N. M. Huang, I. Harrison Y. Andou, *J. Phys. Chem. C,* **2016**, *120*, 4153.

Chapter 3

Fe-based coordination polymer gels as proton conductors and their typical transformation into Fe-metal organic frameworks*

The present chapter discusses two effectual ways of utilizing lesser known Fe-based metallogels: one towards effective synthesis of otherwise difficult Fe-MOFs via Pd^{2+} induced gel degradation; second as a proton conducting solid electrolyte by utilizing a protogenic ligand namely phytic acid molecule for gelation with Fe^{3+} ions. The first part of the chapter[#] verbosely explains a simple yet efficient conversion of viable Fe^{3+} based metallogels into Fe-MOFs by $PdCl_2$ interceded gel degradation. The oxidation of the metallogel constituents namely, formic acid/formamide by Pd^{2+}, is believed to be the plausible reason for the disruption of the metallogel network, thereby driving the system towards more thermodynamically controlled pathway yielding Fe-MOF crystals, as elucidated by the Gas Chromatography (GC) and Powder X-Ray Diffraction (PXRD) studies. In the second part of the chapter[##], a xerogel obtained upon slow drying of the phytic acid based Fe-metallogel is tested for its anhydrous proton conducting ability. The xerogel shows high proton conductivity of 2.4×10^{-2} $S.cm^{-1}$. The xerogel pellet is used for fabricating a Membrane Electrode Assembly (MEA) of a Proton Exchange Membrane Fuel Cell (PEMFC) and *in situ* impedance measurements and linear polarization studies are performed on the as fabricated single cell.

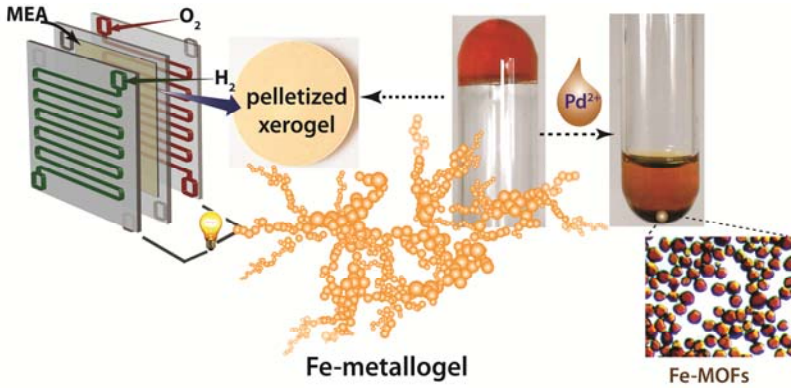

*The content of this chapter has been published in [#]*Cryst. Growth Des.*, **2014**, *14*, 3434 and [##]*Chem. Sci.*, **2015**, *6*, 603.

Reprinted with permission from the [#]American Chemical Society and [##]The Royal Society of Chemistry.

3.1. Introduction

Over past few years, metal organic materials namely metal organic frameworks (MOFs) and metal organic gels/metallogels have emerged as promising materials for multitude of applications namely, gas adsorption, separation and storage, catalysis, sensing, drug delivery etc.[1] due to their tuneable chemical composition, controllable surface area, and pore size. Metallogels belong to an important group of supramolecular materials, whose inherent properties arise from the non-covalent interaction between the metallic entity (metal or metal ion), and the organic connectors (polymeric or other small organic molecules) yielding a stable extended network with capacious immobilization of solvent molecules within. [2] The majority of these metallogels result from non-covalent interactions, mainly hydrogen bonding, apart from metal-ligand coordination. [3] Most of these metallogels therefore do not possess permanent porosity. Henceforth, they cannot be used explicitly for applications like gas adsorption, storage, catalysis etc. like their crystalline MOF counterparts.[4] The literature review reveals that Co, Ni, Cu and Zn based MOFs mainly dominate the list of the most widely studied MOFs, followed by Ca, Mn and Mg based MOFs. [5] Despite being cheap and abundantly available ion, reports of Fe-based MOFs are limited owing to the ready oxidation of Fe^{2+} and easy hydrolysis of Fe^{3+} under hydrothermal conditions. [6] It is important to note that most of the mixtures containing Fe^{3+} ions often gelate in most of the regularly used organic solvents like DMF, ethanol, methanol etc.[7] The sol-gel technique has been one of the well known wet-chemical techniques used for growing crystals.[8] However, this concept has been hardly demonstrated for synthesizing MOFs. The first part of the chapter describes one such proof of concept of use of supramolecular gels as media for the growth of molecular crystals. Herein, chemically induced metallogel degradation results in the transformation of Fe-metallogels into Fe-MOFs.

The second part of this chapter reports the immobilization of a protogenic phytic acid (each molecule contains six phosphate ester ($-H_2PO_4$) groups, and thus, twelve replaceable protons) using Fe^{3+} in N, N'-dimethyformamide (DMF) resulting in a stable metallogel. The FNPA xerogel (obtained upon slow drying of FNPA metallogel) is found to exhibit a high proton conductivity of 2.4×10^{-2} $S.cm^{-1}$ at 120 °C without any assistance of external agent (acid, moisture or any other heterocycle dopants), which establishes it as a distinctive proton conducting supramolecular material.

Part A

3A. Conversion of Fe-metallogel into Fe-MOFs *via* $PdCl_2$ mediated gel degradation

Currently, there exists handful of protocols for the large-scale synthesis of Fe-MOFs, particularly the MIL-n (Fe) series. However, most of these procedures suffer from synthetic constraints like use of toxic HF/HNO_3 and most of their crystal structures are determined from the PXRD patterns owing to the difficulty in the formation of mountable single crystals. [9] This demands a lookout for a facile method to improve the scalability as well as size of such MOFs to make the crystal structure determination easier, essentially needed to understand the MOF structure-property relationship. The sol-gel technique is one of the traditional ways used to improve the crystal size and growth. [8] The technique uses an inert gel matrix to hold the growing crystal nuclei in its position of formation and growth. On attainment of a mountable size, the crystals are recovered on dissolution of the gel matrix, which may be induced by external physical or chemical factors.[10] However, in case of MOFs, which essentially needs an inorganic metal ion along with an organic strut, screening an inert matrix that could be dissolved leaving the MOFs unharmed, would not be easy. It is equally imperative to note that the chemical composition of metallogels is identical to that of the MOFs, except that the latter is a more thermodynamically favored product while gelation is often considered a metastable phase of any transforming system. [11] It is therefore very likely that, if stimulated, such metallogel system could very much act as a reservoir for furnishing the needed metal ions as well as organic linker for *in situ* MOF formation. However, MOF synthesis by means of gel to MOF conversion remains largely unexplored. Moreover, inducing crystallization in such stable metallogel systems would be challenging.

In this part of the chapter, a new strategy for the synthesis of Fe-based MOFs *via* $PdCl_2$ mediated gel-to-crystal transformation from substituted formamide analogues namely NMF (N-Methylformamide), DMF (N, N'-Dimethylformamide) and DEF (N, N'-Diethylformamide) is presented (**Figure 3A.1**).

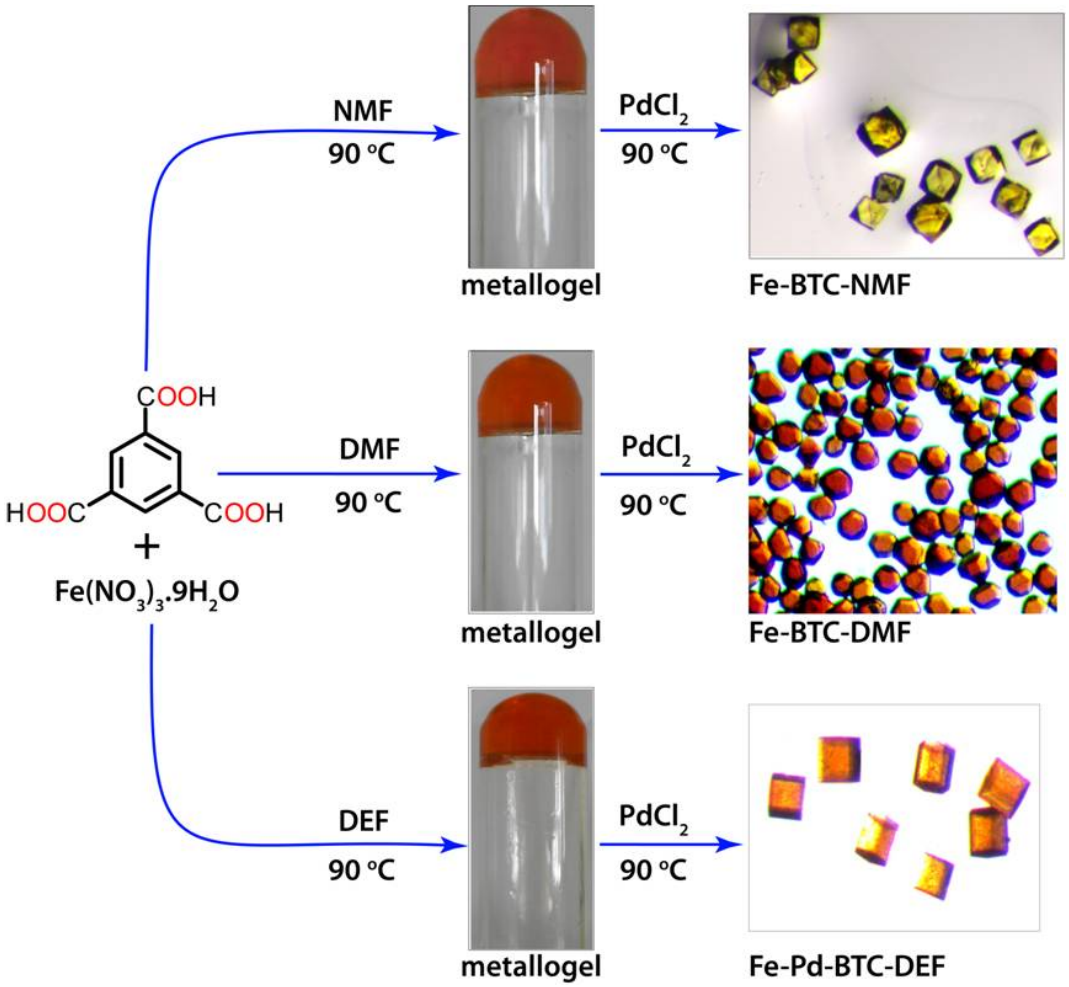

Figure 3A.1. *Schematic representation of conversion of Fe-metallogel into Fe-MOFs via $PdCl_2$ interceded gel degradation.*

3A.1. Experimental Section

In a simple one pot procedure followed, 1 ml of 0.1 mmol of Fe $(NO_3)_3.9H_2O$ and 3 ml of 0.1 mmol of 1, 3, 5-benzene tricarboxylic acid solutions in NMF, DMF and DEF respectively is mixed well and heated. The gelation results within 6 h of heating at 90 ºC, following which, 1ml of 0.1 mmol of $PdCl_2$ (dissolved in each of the corresponding solvent) is added on the top of the metallogel layer. The heating of the vials is continued at 90˚C. The degradation of gel begins after 24 h of $PdCl_2$ addition and the MOF formation results after 48 h (**Figure 3A.1**). Once complete, the crystals are separated by gentle sonication followed by repeated washing with the solvent used for its synthesis. The yield obtained amounts to ~80% in each case.

3A.2. Results and Discussion

3A.2.1. Rheology study

Initially, a simple inversion-tube test is used to verify the gelation of Fe-BTC ligand mixture. The resulting gel is found to be robust with no noticeable weakening observed over weeks. The opaque gels thus obtained are further examined using oscillatory rheology studies.

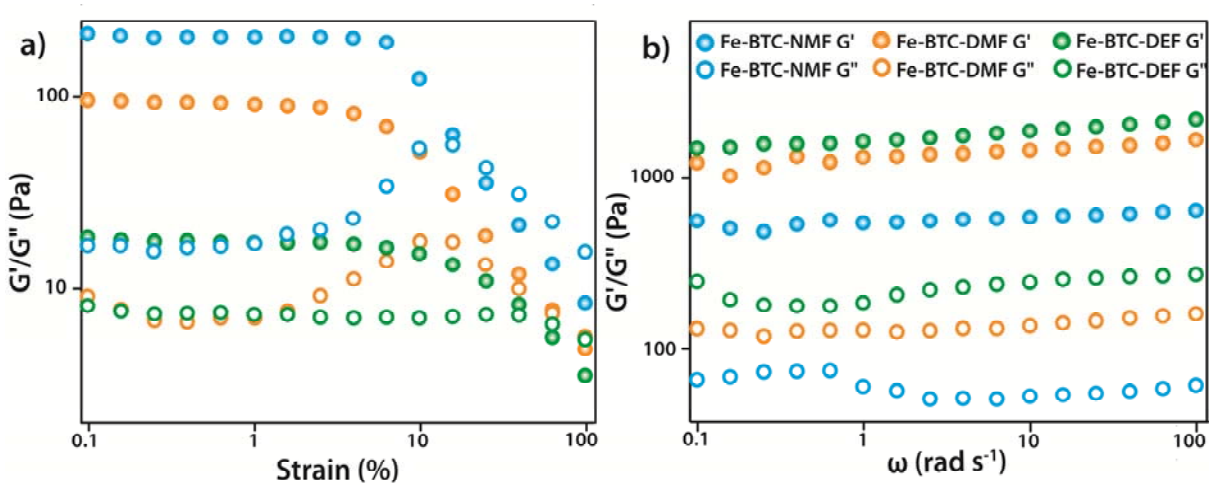

Figure 3A.2. *Combined dynamic strain (DSS) and frequency (DFS) dependent studies of Fe-BTC-DMF, Fe-BTC-DEF and Fe-BTC-NMF metallogels.*

The rheological measurements establish the inherent viscoelastic and fragile nature of the metallogel. The Dynamic Strain Sweep (DSS) and Dynamic Frequency Sweep (DFS) results in **Figure 3A.2** show that the average storage modulus (*G'*) is one order magnitude higher than the loss modulus (*G"*) within the linear viscoelastic regime (for Fe-BTC-NMF and Fe-BTC-DMF gels) and consistent over the whole range of frequency. DFS and DSS results also inform the weaker nature of the Fe-BTC-DEF gel compared to the rest of the two (*i.e.*, Fe-BTC-NMF and Fe-BTC-DMF).

3A.2.2. Electron microscopic studies

The structural morphology of the Fe-metallogels has been studied using environmental SEM (E-SEM). The E-SEM images of the Fe-BTC-NMF gels show the presence of long fibrillar network, while that of Fe-Pd-BTC-DEF and Fe-BTC-DMF exhibited aggregation of thick gel fibers (**Figure 3A.3**).

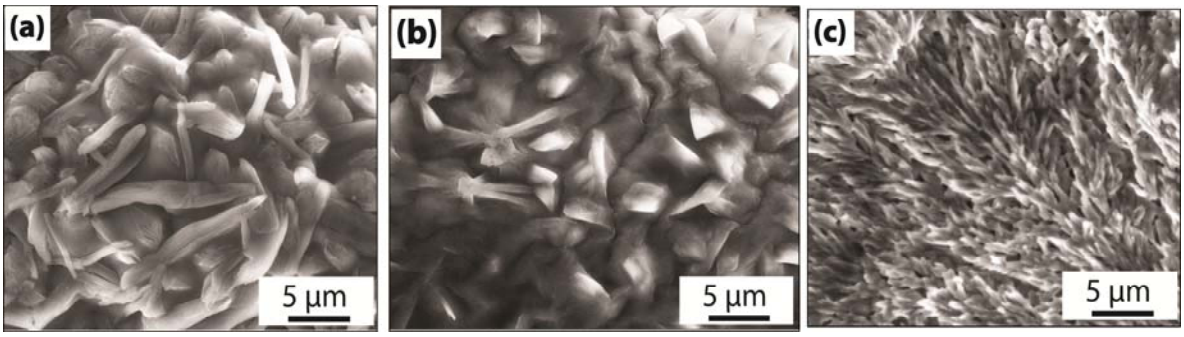

Figure 3A.3*. E-SEM images of (a) Fe-BTC-NMF, (b) Fe-Pd-BTC-DEF and (c) Fe-BTC-DMF metallogels, respectively.*

The SEM images of all the as synthesized Fe-MOFs reveal the formation of crystals with well-defined faces and size varying between 10 to 40 µm (**Figure 3A.4)**.

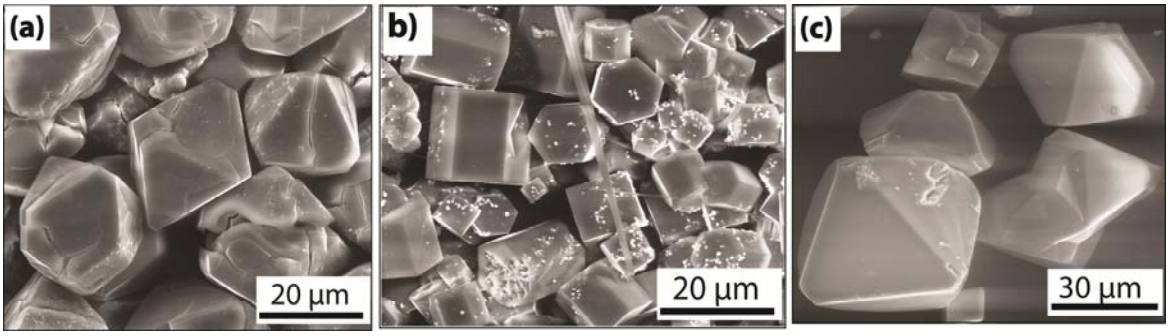

Figure 3A.4. *SEM images of (a) Fe-BTC-NMF, (b) Fe-Pd-BTC-DEF and (c) Fe-BTC-DMF MOF crystals respectively.*

The chemical nature of the residue has been confirmed using the data obtained from spot EDX analysis (**Figure 3A.5**).

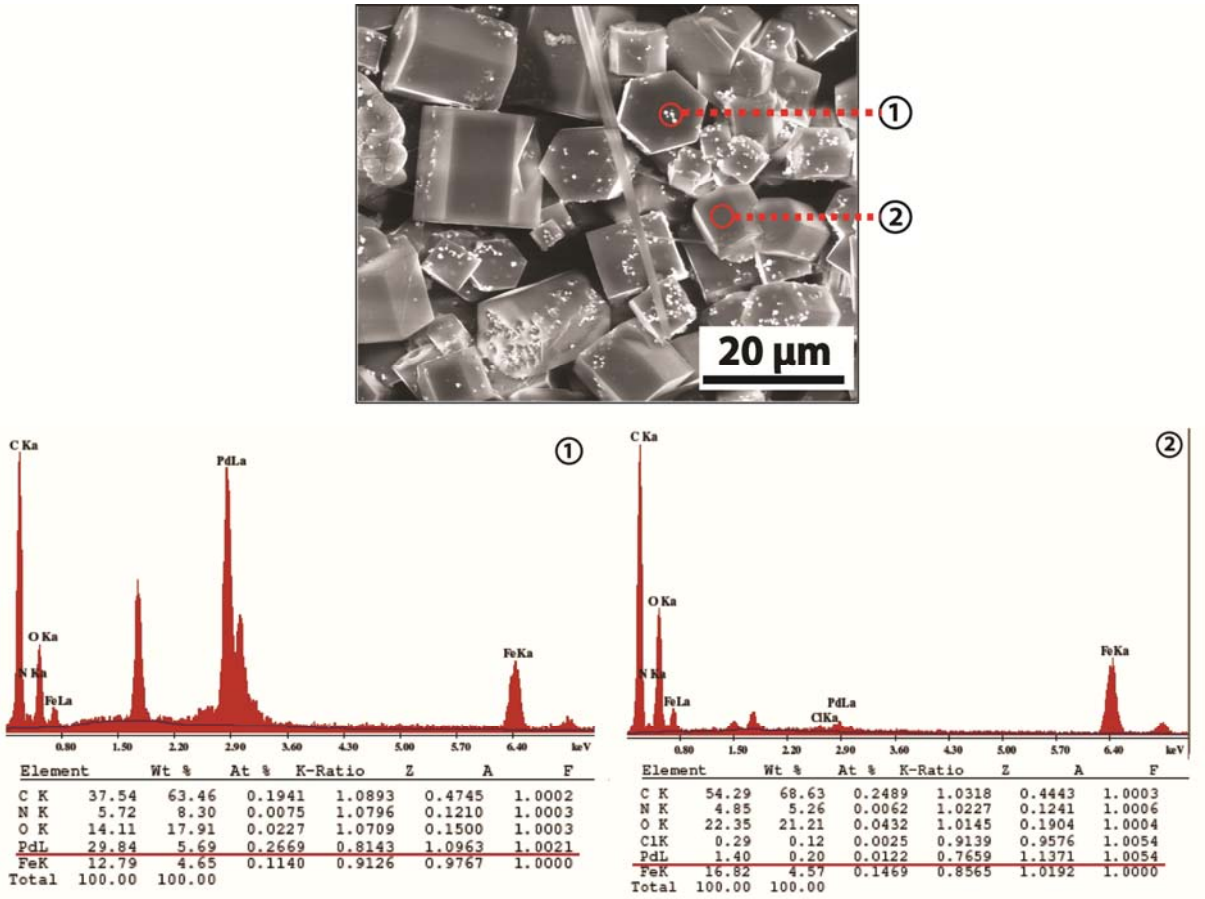

Figure 3A.5*. EDX analysis of the reduced palladium residue on the Fe-Pd-BTC-DEF MOF surface.*

3A.2.3. Single crystal XRD analysis

The Fe-MOFs resulting from the degradation of the metal-organic gel have been investigated using single crystal X-ray diffraction analysis. For the single crystal X-ray diffraction experiment, the as synthesized crystals were taken out of the solution and layered with paratone-N oil. It is then placed in a nylon cryoloop (Hampton research) of 0.7 mm diameter and then mounted in the diffractometer. The data collection was done at 293 K. The crystals were mounted on a Super Nova Dual source X-ray Diffractometer system (Agilent Technologies) equipped with a CCD area detector and operated at 250 W power (50 kV, 0.8 mA) to generate Mo Kα radiation (λ = 0.71073 Å) and Cu Kα radiation (λ = 1.54178 Å) at 298(2) K. The initial scans of each specimen are executed to obtain the preliminary unit cell parameters and to evaluate the mosaicity (*i.e.*, breadth of spots between frames) of the crystal and the required frame width for data collection is selected. CrysAlis^{Pro} program software has

been used suite to carry out the overlapping φ and ω scans at detector (2θ) settings (2θ = 28). Following the data collection, reflections are sampled from all regions of the Ewald sphere to predetermine unit cell parameters for data integration. The resolution of the data set is judged following an exhaustive review of the collected frames. The data is then integrated using CrysAlis^{Pro} software with a narrow frame algorithm. The data is subsequently corrected for absorption by the program SCALE3 ABSPACK scaling algorithm.

In the present work, the crystal structures have been solved using direct method and refined using the SHELXTL 97 [12b] software suite. The atoms are located following an iterative examination of the difference F-maps using the least squares refinements of the previous models. The final model has been refined anisotropically (if the number of data permitted) unless complete convergence is achieved. The hydrogen atoms are placed in their calculated positions (C-H = 0.93 Å) and incorporated as riding atoms with isotropic displacement parameters 1.2-1.5 times Ueq of the attached C atoms. In some cases, the modeling of the electron density within the framework voids did not lead to the identification of recognizable solvent molecules in these structures, most likely due to the highly disordered contents within the large pores in the frameworks. Highly porous crystals containing pores filled with solvents often yield raw data wherein observed strong (high intensity) scattering gets limited to ~1.0 Å at best, with higher resolution data present at low intensity. In addition, the diffused scattering from the highly disordered solvent within the void spaces of the framework and also from the capillary used for mounting the crystal also contributes to the background and towards 'washing out' of the weaker data. The electron density within the void spaces have not been assigned to any guest entity but instead modeled as isolated oxygen and/or carbon atoms. The foremost errors in all the models are believed to lie in the assignment of guest electron density. The structure has been examined using the *ADSYM* subroutine of PLATON[5] to ensure that no additional symmetry could be applied to the models. The ellipsoids in ORTEP diagrams have been displayed at 50% probability level unless noted otherwise. For all structures, it is important to note that the elevated R-values are commonly encountered figures in MOF crystallography for the reasons discussed above. [12]

The CCDC 983264 and **CCDC 983263** contain the crystallographic data for **Fe-Pd-BTC-DEF** and **Fe-BTC-NMF** respectively.

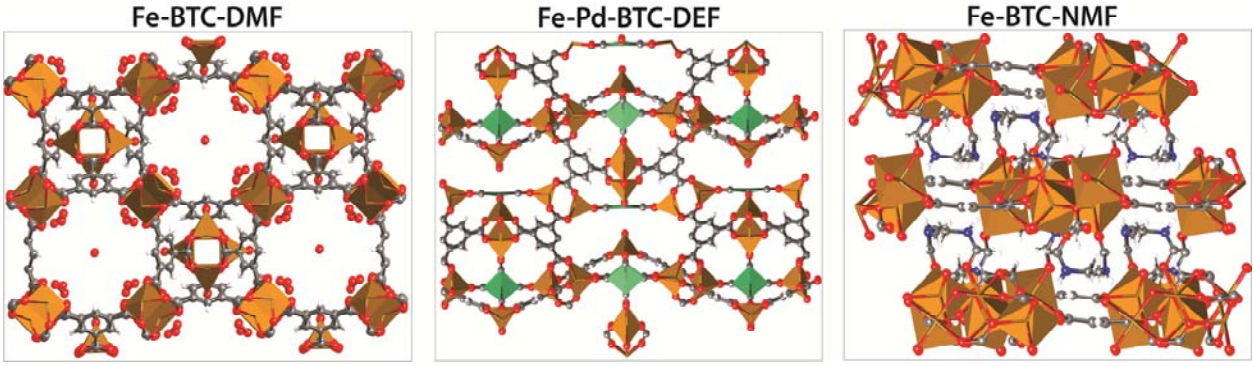

Figure 3A.6. *Single crystal structure of Fe-BTC-DMF, Fe-Pd-BTC-DEF and Fe-BTC-NMF systems, respectively. (Colour code: Fe: orange, O: red, C: grey, N: blue, Pd: green).*

In the study, the data is collected at 293 K. Here, in addition to the known Fe-BTC-DMF [6a], we report two new crystal structures, Fe-Pd-BTC-DEF (3D) and Fe-BTC-NMF (2D).

Crystallographic information of Fe-Pd-BTC-DEF

Fe-Pd-BTC-DEF crystallizes in hexagonal space group $P6_3/mmc$ [a= 19.97, c=26.056Å, $\alpha=90^0$, $\beta=120^0$, V=9001.4 $Å^3$] (see **Table 3A.1** for details). The SBU (Secondary Binding Unit) comprises of two metal centers, Fe (II) and Pd (II) (**Figure 3A.6)**. Of the two Fe centres, one Fe is tetrahedrally coordinated to four O atoms and second Fe is coordinated to five O atoms, thereby effecting a square pyramidal geometry **(Figure 3A.7).** The Pd (II) takes up a square planar geometry and is coordinated with four C atoms of the CO molecules. In the crystal structure, the CO molecules found are possibly produced along the pathway of the presumed formic/formamide oxidation as confirmed from the gas chromatography analysis.

Table 3A.1. Crystal data and structure refinement for Fe-Pd-BTC-DEF:

Empirical formula	C_{22} H_4 Fe_4 O_{17} Pd
Formula weight	870.05
Temperature	293 (2) K
Wavelength	0.71073 Å
Crystal system	hexagonal
Space group	*P* 6_3*/m m c*
Unit cell dimensions	*a* = 19.9724(9) Å α = 90°

	b = 19.9724(9) Å β = 90°
	c = 26.0567(9) Å γ = 120°
Volume	9001.4(7)
Z	6
Density (calculated)	0.963
Absorption coefficient	1.275
F(000)	2536.1
Crystal size	0.34 × 0.29 × 0.12 mm^3
Theta range for data collection	3.13 – 29.11
Index ranges	-23 <= h <= 14, -11 <= k <= 25, -35 <= l <= 30
Reflections collected	19912
Independent reflections	4090
Completeness to theta = 26.02°	91.6 %
Absorption correction	Semi-empirical from equivalents
Refinement method	Full-matrix least-squares on F^2
Data / restraints / parameters	4090 / 0/ 116
Goodness-of-fit on F^2	1.0710
Final R indices [I>2sigma(I)]	R_1 = 0.1344, wR_2 = 0.1231
R indices (all data)	R_1 = 0.1912, wR_2 = 0.1472
Largest diff. peak and hole	0.413 and -0.471 e.$Å^{-3}$

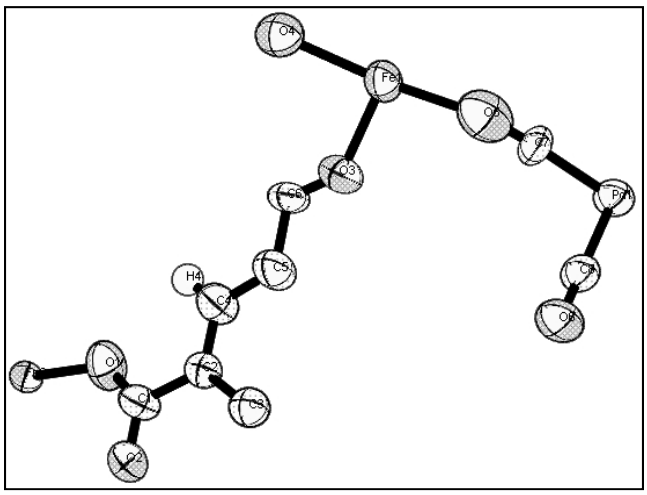

Figure 3A.7. *ORTEP diagram of Fe-Pd-BTC-DEF.*

Crystallographic information of Fe-BTC-NMF

The Fe-BTC-NMF crystallizes in trigonal space group *R*-3 [a=14.03, c=21.27 Å, $\alpha=90^0$, $\beta=120^0$, V=3628.5Å^3] (see **Table 3A.2** for details) into a 2-D network. From the crystal study, it can be established that in the crystal structure of Fe-BTC-NMF, Fe^{3+} assumes an octahedral geometry in which it is coordinated to five oxygens from μ_2-CO_2^-functionalities of one NMF oxygen atom and four BTC molecules (**Figure 3A.6)**.

Table 3A.2. Crystal data and structure refinement for Fe-BTC-NMF:

Empirical formula	$C_6 H_7 Fe N O_5$
Formula weight	228.98
Temperature	293 (2) K
Wavelength	0.71073 Å
Crystal system	trigonal
Space group	*R* -3
Unit cell dimensions	*a* = 14.0339(6) Å α = 90° *b* = 14.0339(6) Å β = 90° *c* = 21.2738(10) Å γ = 120°
Volume	3628.5(3)
Z	18
Density (calculated)	1.886
Absorption coefficient	1.275
F(000)	1788
Crystal size	0.34 × 0.29 × 0.12 mm^3
Theta range for data collection	3.85-27.85
Index ranges	-11<= h <= 17, -16 <= k <= 12, -14 <= l <= 28
Reflections collected	2205
Independent reflections	1841
Completeness to theta = 26.32°	99.76 %
Absorption correction	Semi-empirical from equivalents
Refinement method	Full-matrix least-squares on F^2
Data / restraints / parameters	1841/ 0/ 119

Goodness-of-fit on F^2	0.930
Final R indices [I>2sigma(I)]	$R_1 = 0.0349$, $wR_2 = 0.1150$
R indices (all data)	$R_1 = 0.0478$, $wR_2 = 0.1363$
Largest diff. peak and hole	0.535 and -0.371 e.Å^{-3}

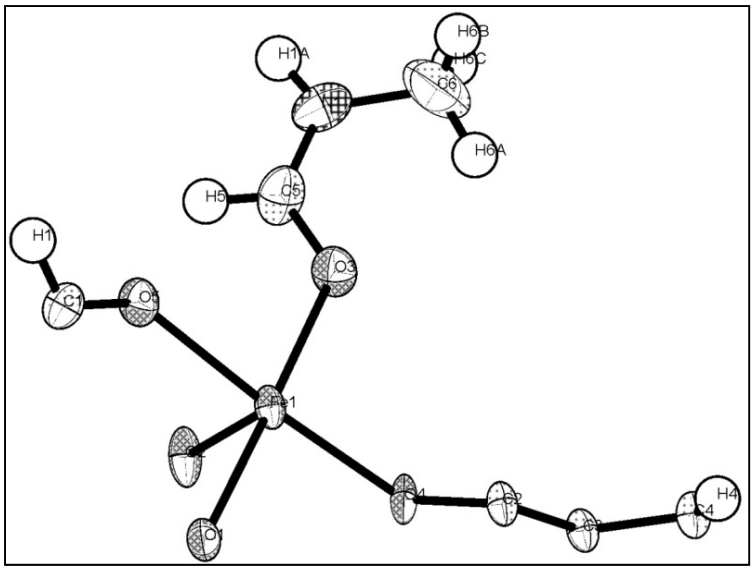

Figure 3A.8. *ORTEP diagram of Fe-BTC-NMF.*

3A.2.4. PXRD analysis

The powder XRD technique has also been employed to determine the bulk purity of the resulting MOF phases. Of the three Fe-MOF synthesized, Fe-BTC-DMF is already reported one, while the other two, *i.e*., Fe-Pd-BTC-DEF and Fe-BTC-NMF, are newly found forms. However, the Fe-Pd-BTC-DEF crystals were found to be very unstable and hence its PXRD pattern could not be obtained. Once taken out of the mother solution, these crystals are observed to immediately transform into unidentifiable precipitates.

The PXRD patterns of the other two MOFs match well with their simulated ones that confirm that the product obtained are in their pure crystalline forms (**Figure 3A.9**).

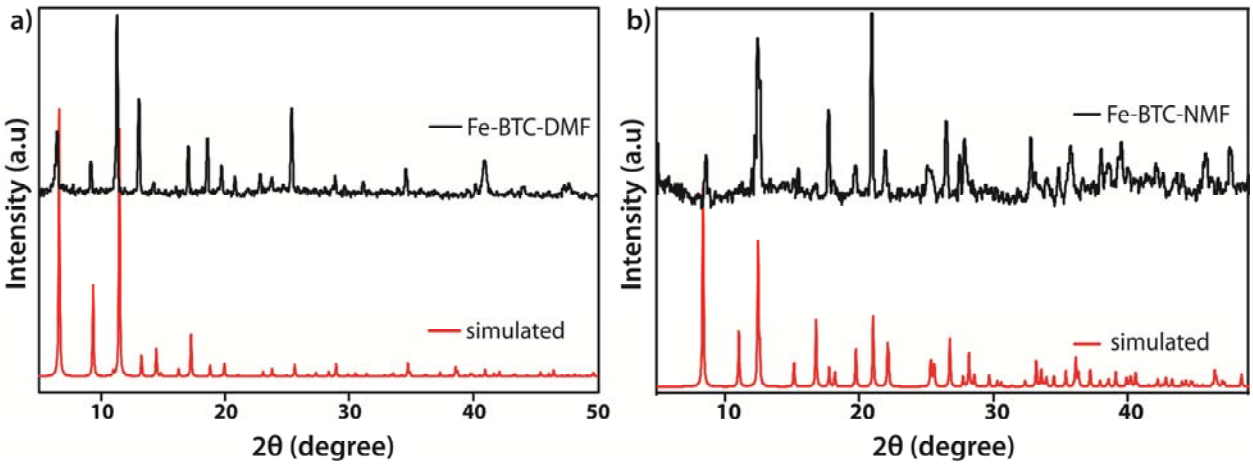

Figure 3A.9. *Simulated and experimental PXRD patterns of a) Fe-BTC-DMF and b)Fe-BTC-NMF.*

The PXRD analysis of the residue left behind after completion of the gel degradation is indicative of the formation of reduced palladium black (**Figure 3A.10**).

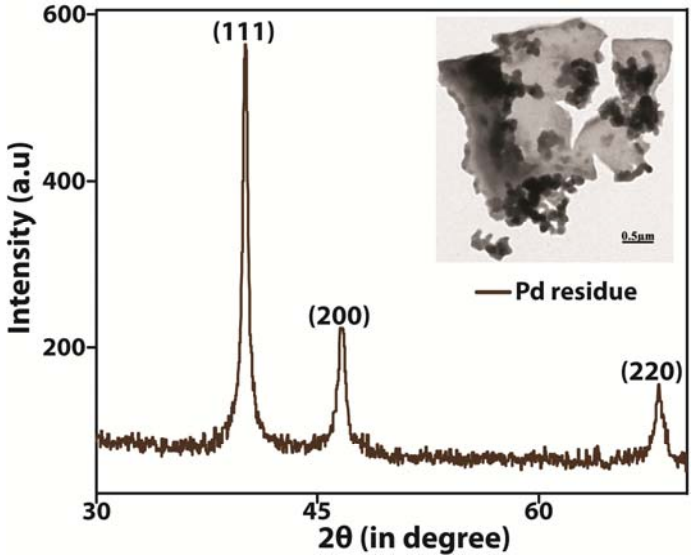

Figure 3A.10. *PXRD of reduced palladium residue isolated after metallogel degradation (JCPDS file no. 87-0638). (Inset) SEM image of reduced palladium residues.*

3A.2.5. FTIR analysis

The presence of Fe^{3+}-ligand coordination during the metallogel formation is confirmed by IR spectroscopic investigation.

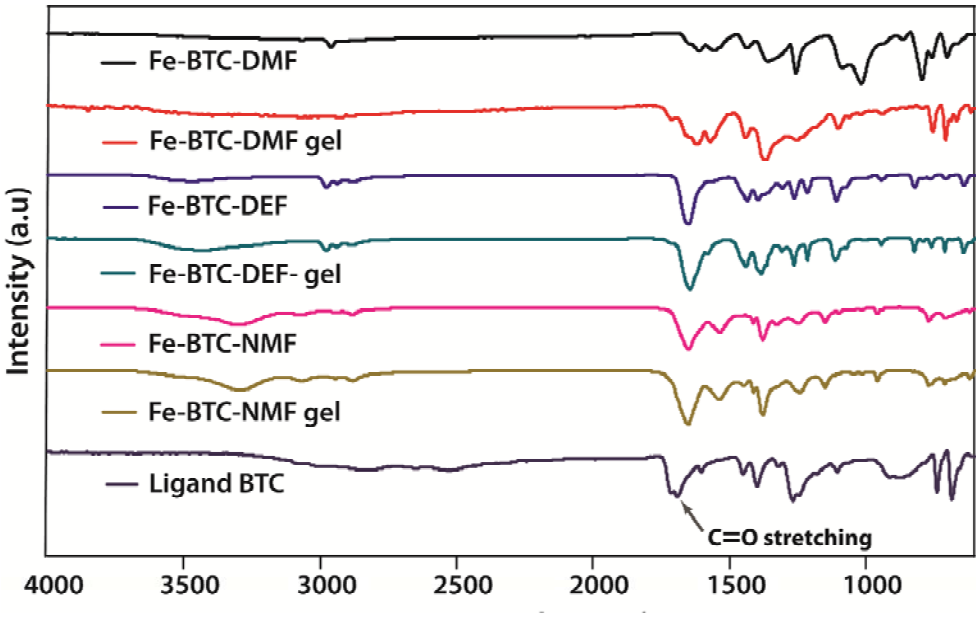

Figure 3A.11*. FT-IR spectra of Fe-metallogels and the resulting Fe-MOFs.*

In the FT-IR spectra of Fe-BTC-DMF metallogel, a red shift in the bond strength of the ligand C=O stretching from 1690 cm^{-1} to 1650 cm^{-1} could be observed which indicates the formation of Fe←C-O bonding during gelation followed by crystallization of MOF (**Figure 3A.11**).

3A.2.6. TGA analysis

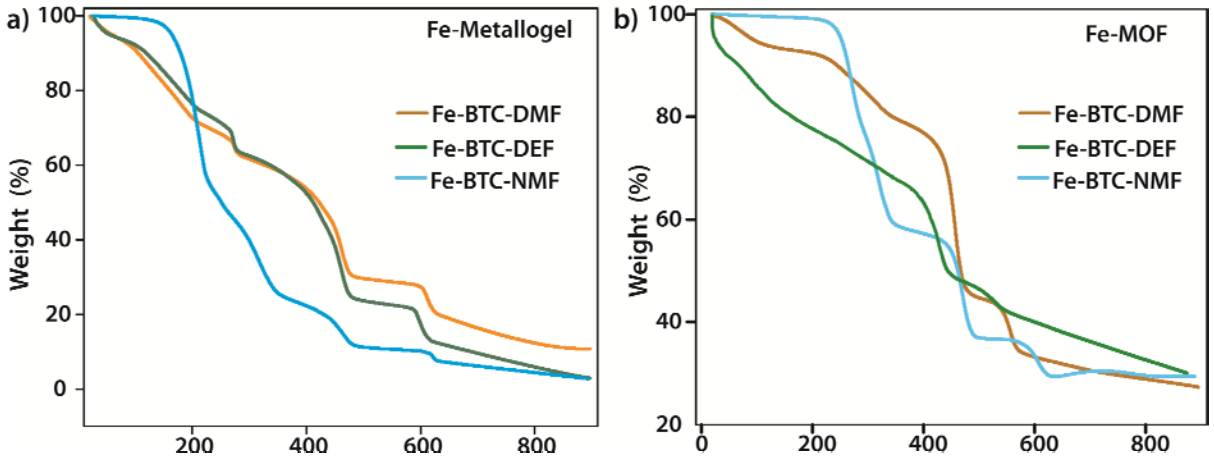

Figure 3A.12. *TGA plots of a) Fe-metallogels and b) the corresponding Fe-MOFs.*

The thermal stability of the Fe-metallogels as well as the resulting Fe-MOFs has been evaluated using the TGA analysis. The TGA curves indicate that the Fe-metallogels possess high thermal stability except for the initial solvent losses observable at 90-160 ˚C (**Figure 3A.12a**). The TGA studies of Fe-MOFs also reveal that, of all, Fe-Pd-BTC-DEF MOF showed relatively poor stability (**Figure 3A.12b**).

3A.2.7. Gas chromatography (GC) study

The metallogel degradation, interestingly, has been observed to produce gaseous products during the course of the transformation. The gas chromatographic study is therefore employed to study the nature of the gaseous products emanating during the course of the transformation from gel-to- crystals. As shown in **Figure 3A.13**, the GC evaluation on the first day (gel phase) did not show the presence of any gaseous product.

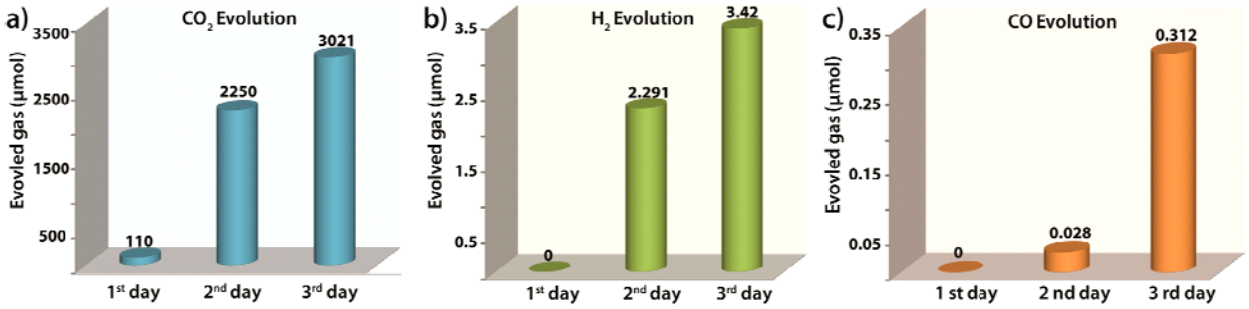

Figure 3A.13. *Bar graphs representing the evolution of a) CO_2, b) H_2, and c) CO gases collected from first to third day during the transformation from metallogel-to-crystals.*

On addition of $PdCl_2$, evolution of CO_2, CO along with traces of H_2 is observed. The rate of evolution is found to increase from second to third day (i.e., during the phases of gel degradation and onset of nucleation) and was found to be steady after that. This is accompanied parallelly by the MOF formation and at the end of the third day; mountable sized MOF crystals could be obtained.

3A.3. Probable mechanism for Fe-metallogel to Fe-MOF transformation

The data interpretation from the PXRD and GC studies is mainly used to derive a probable mechanism for gel-to-crystal transformation event. In the present study, substituted formamide analogues namely NMF, DMF, DEF were chosen as they have always been an attractive preference for MOF synthesis by the virtue of their high boiling point and partial

hydrolytic decomposition into corresponding amines and formic acid at higher temperature. It is also interesting to note that such *in situ* generated amines have proven to deprotonate the ligand, in turn facilitating their coordination to the positive metal ion (Fe^{3+} here) and thereby ruling out the need for an additional base. [13] On the contrary, the role and the fate of the other product, *i.e.,* formate /formic acid, also evidenced to be formed during the course of the reaction have been hardly studied, except in few cases where the formate ion is found coordinated to the metal ion in the crystal structure. [14] An easy way to analyze the formate ion intervention would be its removal from the gelating system. A case study on the formic acid chemistry substantiates the use of precious noble metal ions *viz*., Ag^{+}, Pd^{2+}, Pt^{4+} etc. for its oxidation. On addition of $PdCl_2$, the metallogels have been observed to develop turbidity and later degrade into a sol.

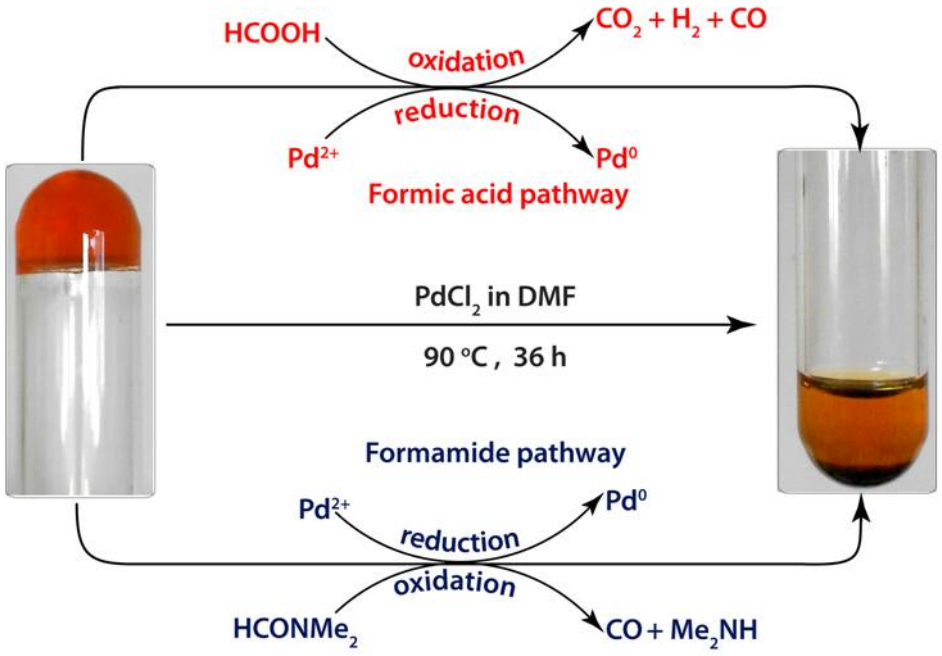

Figure 3A.14*. Schematic representation of mechanism illustrating the conversion of Fe-metallogel into Fe-metal organic frameworks.*

The gel degradation is also accompanied by the alongside formation of palladium black residues. The degradation of gel is observed to complete within 2-3 days following which large sized crystals could be obtained. The presence of formic acid oxidation products CO_2, CO, H_2 [15] along with palladium black confirms that $PdCl_2$ reduces in turn mediating the degradation/oxidation of solvent DMF in the metallogels (**Figure 3A.14**). However, a direct

evidence to detect the presence of formic acid/formate ion in the system failed as DMF also gives positive results to the usually tried test reaction *viz*., the silver mirror test. This is a possible influence of the Lewis acid nature of Ag^{+}, which brings about DMF degradation. The breakdown of DMF results in the *in situ* generation of formic acid that eventually reduces Ag^{+} to Ag. The gel degradation could be observed using all known formic acid oxidation reagents namely Pd $(OAc)_2$, $AgNO_3$ and H_2PtCl_4 addition too. However, it is notable that the quality of the obtained crystals was the best with $PdCl_2$, for reasons unknown. It is remarkable to also observe that the phenomenon did not repeat when tried with chloride salts of other metals namely NaCl, $NiCl_2$. This hints the presence of an oxidative pathway and its involvement in bringing about the degradation of the metallogel (**Figure 3A.14**). It is however intricate to exactly determine the usefulness of formic acid and the role of DMF (apart from being a solvent) in furnishing formic acid in gelation. As noted earlier, the hydrogen-bonding interactions are one of the most important non-covalent forces (apart from metal-ligand co-ordination bonds) in supramolecular gels, a metastable system.[3,16] Thus, the facile formation of Fe-based metallogels could be associated with the presence of formamide along with *in situ* resulting formic acid, which are well-known hydrogen bond donors. The removal of such species *via* oxidation is observed to disrupt the gel network, which consequently results in the complete gel degradation as observed in the present case. This possibly drives the system to follow a more thermodynamically controlled pathway, which eventually results in the formation of MOF crystals, a thermodynamically favored product. [11]

Part B

3B. Fe-phytate metallogel as a proton conducting solid electrolyte for PEM Fuel Cells

Ideally, a PEMFC electrolyte should desirably be able to conduct protons at high temperature (>100 ˚C) under dry conditions besides possessing high mechanical stability. [17] The high temperature performance would essentially improve the fuel cell performance by increasing the cell resistance to fuel impurities like CO, escalate the electrode kinetics along with resolving the water flooding issues, which are of primary concerns of a Nafion® based PEMFC operation. [18] The solid electrolyte often used in case of the commercial High Temperature Proton Exchange Membrane Fuel Cells (HT-PEMFCs) is the phosphoric acid doped-polybenzimidazole (PBI) membrane having high proton conductivity up to 0.1 S/cm at temperatures up to 200 °C. [19] However, during the course of operation, one of the problems affecting the performance of the PA-doped PBI membrane is the leaching of the doped acid thereby decreasing its conductivity. [20] It is important to note that, to be used as a solid electrolyte in a proton exchange membrane fuel cell, the prospective material needs to satisfy two criteria (1) space out the electrode components (mainly the reactant gases) (2) conduct ions (H^+ here) across the electrodes and ultimately complete the electrical circuit. Thus, in order to operate a fuel cell, there is an imperative need of an intrinsically proton-conducting electrolyte, which could perform faster and selective proton transport at preferably 100-200 ˚C and more specifically at anhydrous conditions. It should also alongside be able to separate the anode and cathode components, most importantly prevent the cross diffusion of the reactant gases for an optimal fuel cell performance. [21]

At this outlook, thermally as well as chemically stable metallogels offer a perfect platform to immobilize the proton-conducting entities *via* their coordination to the metal centres. However, one finds very few reports of such metallogels used as proton conductors, one being a CuA-Ox xerogel, which displays a proton conductivity of 1.4×10^{-5} S/cm at 65 ˚C under anhydrous conditions. [22] It is well understood that the proton conductivity depends on the quantity and mobility of the protons present in the system. [23]

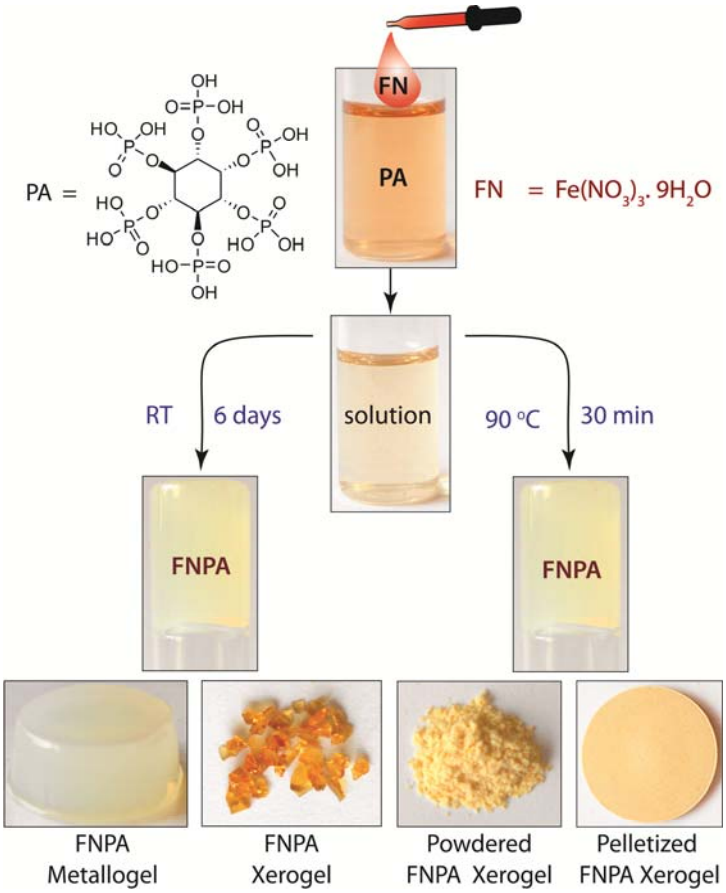

Figure 3B.1. *Schematic representation of the synthesis of FNPA metallogel.*

Among the recognized protogenic molecules, phosphoric acid based phytic acid (inositol hexakisphosphate) contains 12 replaceable protons and is thus competent of easily coordinating to multivalent ions. Furthermore, each phytic acid (PA) molecule contains six phosphate ester ($-H_2PO_4$) groups, recognized for their amphoteric nature that allows proton conduction without any assistance from external proton carriers. [24] This part of the chapter introduces a novel strategy for the immobilization of phytic acid using Fe^{3+} in N, N'-dimethyformamide (DMF) which results in a stable metallogel (FNPA, FN= ferric nitrate nonahydrate; PA = phytic acid).

3B.1. Experimental Section

The synthesis of FNPA metallogel is also performed using a simple one pot procedure at 90˚C, wherein 0.1 mmol of Fe $(NO_3)_3$. $9H_2O$ (FN) and 0.1 mmol of phytic acid (PA) solution (2:1 *v/v*) in DMF were mixed together to form a pale yellow colour solution (**Figure 3B.1**).

The gelation is found to result within 30 min of heating at 90 ˚C, but aging of the metallogel was continued for another 12 h in order to further increase the cross-linking of the gelator fibers. A similar FNPA metallogel is also obtained at room temperature when the pale-yellow colour solution was left undisturbed for ~6 days (**Figure 3B.2**).

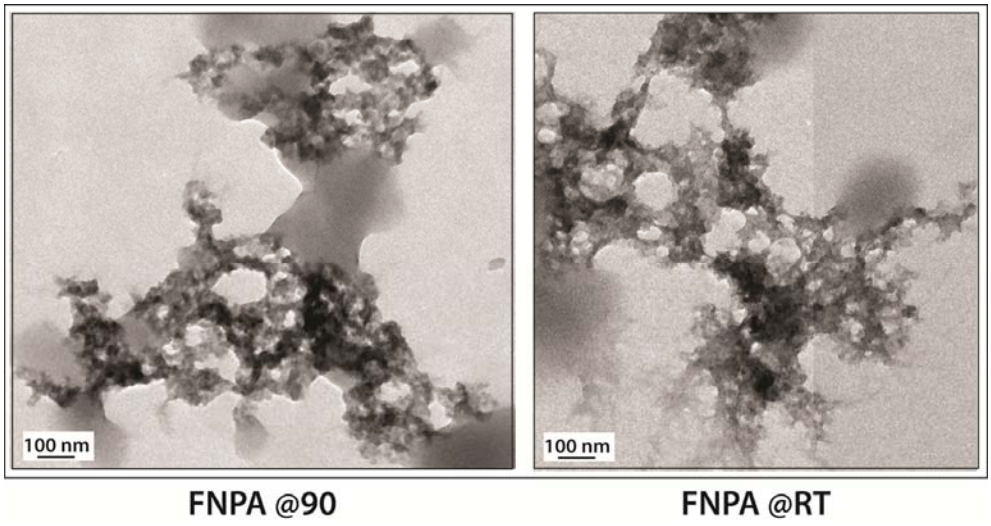

Figure 3B.2*. (a) HRTEM of FNPA metallogel synthesized at (b) 90˚C, (c) RT after 6 days.*

The off-white colour metallogel obtained is slow evaporated at 70-80 °C. The resulting FNPA xerogel is then powdered and later pelletized for proton conductivity studies.

3B.2. Results and Discussion

3B.2.1. Material Characterization

3B.2.1.1. Rheology study

The gel nature of FNPA is at first verified by a simple inversion-tube test (**Figure 3B.1**). The rheological study of FNPA metallogel indicates that the metal-ligand coordination forces are crucial for determining the rate of gelation as the gel strength varied depending on the metal-to-ligand ratio. It is worth mentioning that the precursor solution having metal-to-ligand ratio = 2:1 gelates faster at room temperature and shows better mechanical property (**Figure 3B.3**) compared to the other compositions.

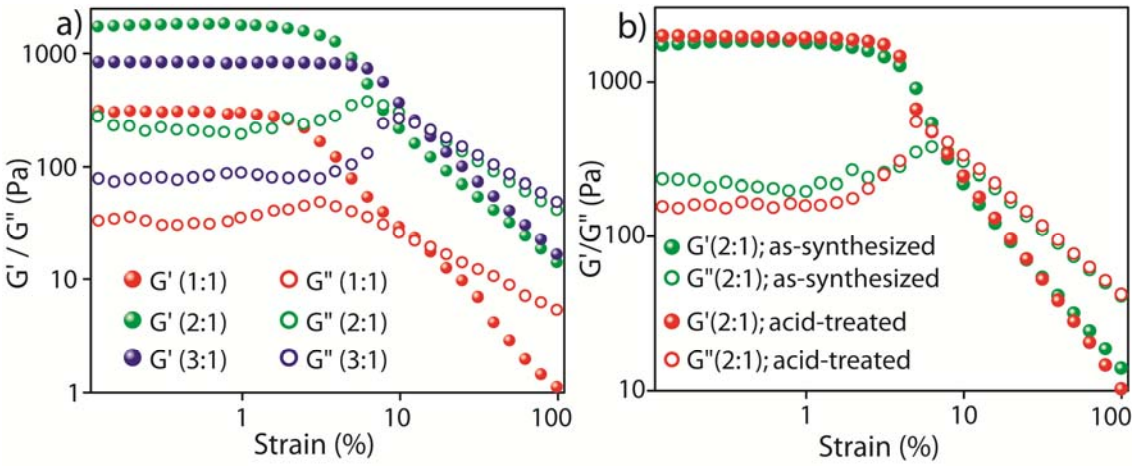

Figure 3B.3. *Combined strain dependent studies of the FNPA metallogel (FN: PA (v/v) in DMF); b) comparative Strain sweep plot of FNPA metallogel after six months and after acid treatment.*

The viscoelastic nature of the opaque metallogel is further measured by oscillatory rheological studies. The dynamic strain sweep (DSS) test carried at a constant frequency of 1 rad/s shows that the average storage modulus (*G'*) was one order magnitude higher than the loss modulus (*G"*) within the linear viscoelastic regime (**Figure 3B.3a**). At a constant strain value of 1%, the storage modulus indicates almost null dependence on the frequency. The FNPA metallogel could be found to be water as well as acid stable, devoid of any observable changes over a period of 6 months (**Figure 3B.3b**).

3B.2.1.2. Electron microscopic studies

The gelation and morphology of the Fe-metallogels is monitored using transmission electron microscopic (TEM) study. The high resolution TEM images of the FNPA metallogel collected within 30 min of mixing of Fe^{3+} and phytic acid solutions indicates the initial formation of the gel nanospheres. The fusion of 20-40 nm-sized spheres into a one-dimensional nanofibre is gradually followed, which finally interweaves into a three dimensional metallogel network **(Figure 3B.4)**. The presence of nanospheres in the early phase of gelation indicates the ready complexation of Fe^{3+} with the multidentate three dimensional phytic acid molecules in DMF. The presence of identical phosphate ester groups in the phytic acid molecules gives all sites an equal opportunity to bind with the metal ion

and initiate a non-directional supramolecular assembly of the gelating components *(viz.* Fe-Phytate complex, DMF, water etc.).

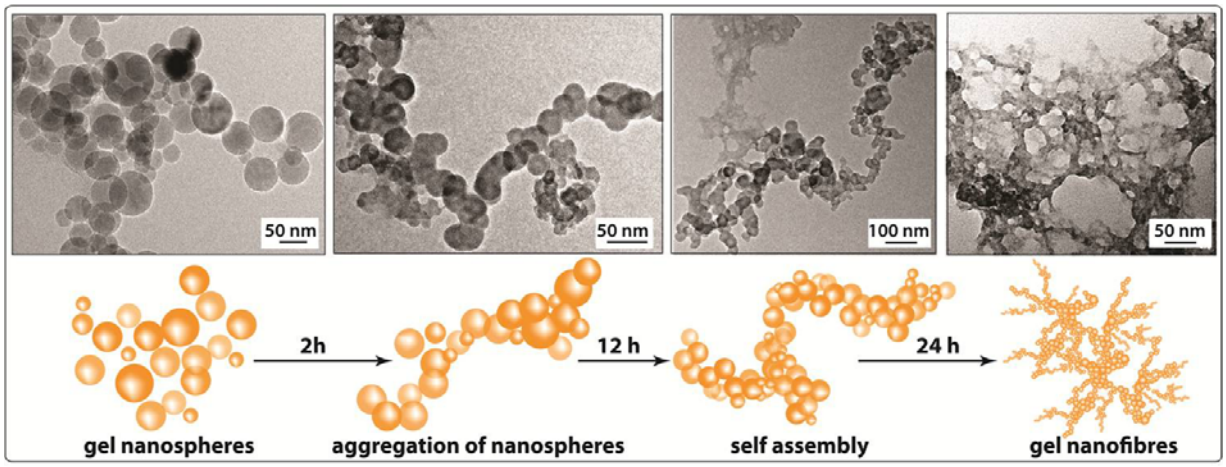

Figure 3B.4*. HRTEM images of the gel collected at different time interval evidencing the formation of the FNPA metallogel nanospheres and their eventual assembly into a 3D metallogel network.*

These amassing of the nanospheres is then driven by the supramolecular forces (H-bonding or coordinate bond) giving rise to nanofibrillar metallogel network structure which eventually results in a monolithic gel structure. [24]

3B.2.1.3. MALDI-TOF study

The MALDI –TOF study is carried out to determine the molecular weight of the possible gelator unit in case of FNPA metallogel (2:1), which is indicated to have the best mechanical strength of all the other FN-PA compositions. The matrix assisted laser desorption ionization-time of flight (MALDI-TOF) is performed using dithranol as the matrix. The sample concentration is ca. 1.0 μM in DMF solvent. 1mg/mL concentration of the matrix solution (in THF) is made and added to the sample solution in 1:1 ratio. The resulting solution has been deposited on a stainless steel sample holder and then dried under vacuum. The sample is then scanned with the N_2 laser (intensity = 4500) at a scan rate of 150 shots/spectrum. The sample is tested under optimized conditions in a positive reflectance mode. The MALDI-TOF spectra of the FNPA metallogel as well as the FNPA xerogel displays many peaks in the low m/z region (m/z < 1000) suggesting non-covalent self-assembly of gelator units (**Figure 3B.5**). However, a prominent peak at m/z = 781.93 (two

Fe^{3+} + one phytic acid + eight H^{+}) strongly hints at the presence of the 2:1 complex (Fe^{3+}: Phytic acid) as the possible gelator unit.

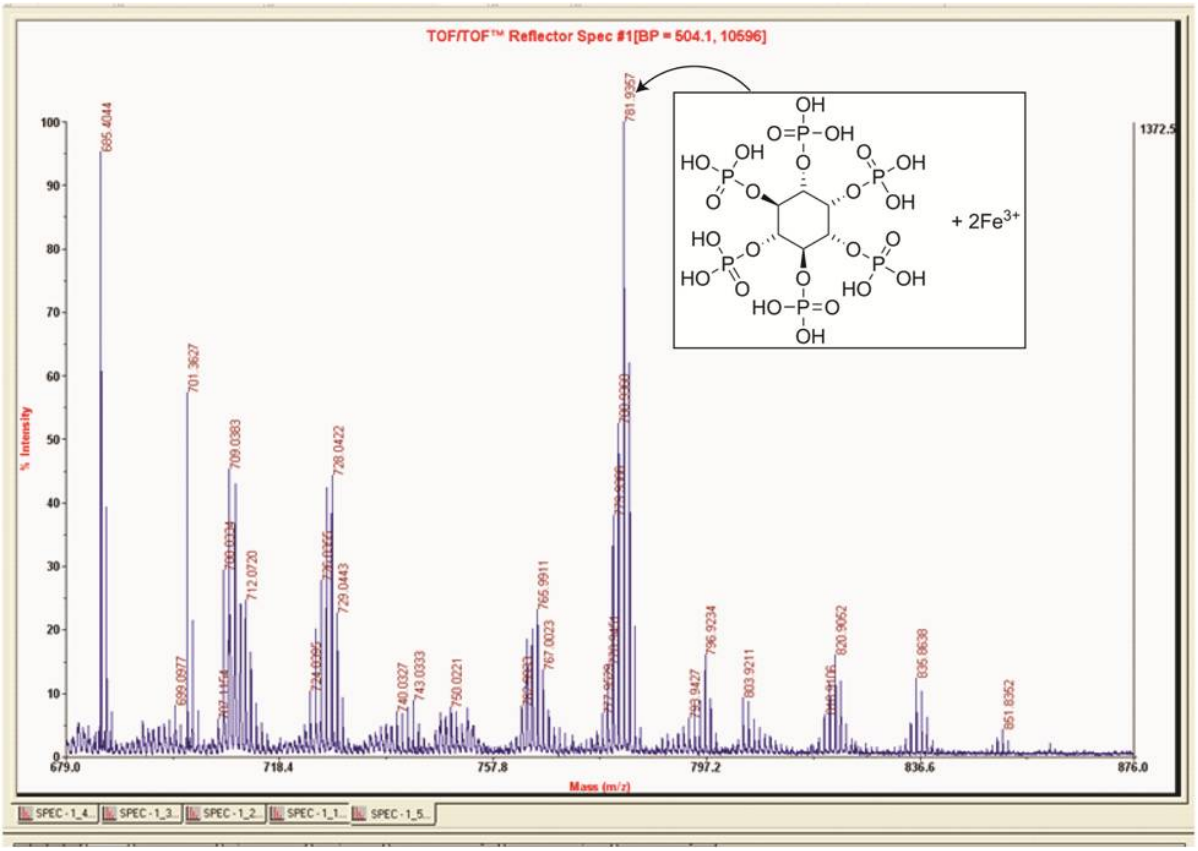

Figure 3B.5. *MALDI-TOF MS spectra of FNPA metallogel indicating presence of prominent peak at m/z value ~781.*

3B.2.1.4. PXRD analysis

The PXRD spectrum of the synthesized FNPA metallogel as well as FNPA xerogel is indicative of the amorphous nature of the material. The spectra showed presence of a broad hump at ~25 ˚, substantiating the absence of long range ordering in the FNPA metallogel (**Figure 3B.6a**).

3B.2.1.5. FTIR analysis

The FTIR study of the xerogel derived after slow drying FNPA metallogel (2:1) indicates the presence of P-OH, P=O, C-O-P, C-C bond stretching frequencies in the spectra (**Figure 3B.6b**).

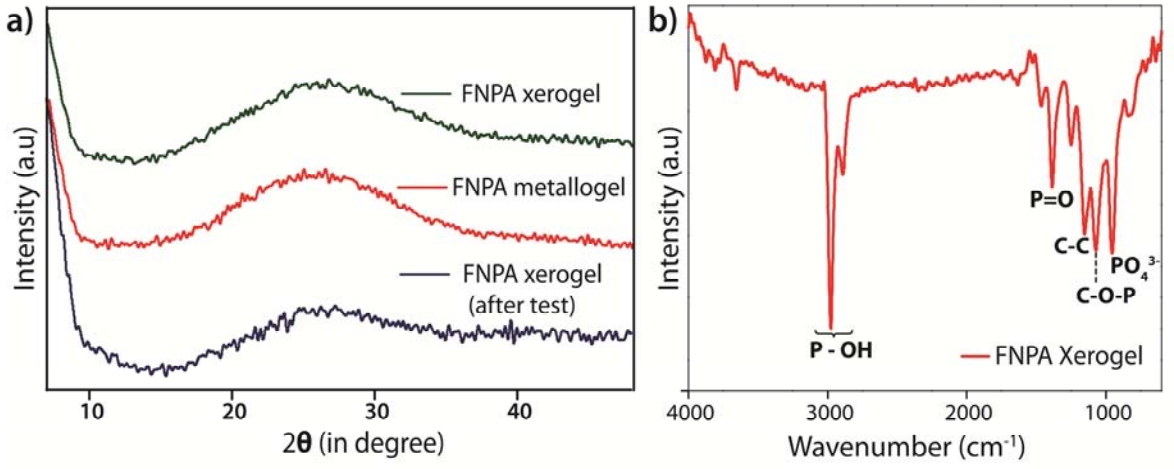

Figure 3B.6. *Combined plots indicating a) PXRD patterns of FNPA metallogel and xerogel, b) FT-IR spectra of FNPA xerogel.*

3B.2.1.6. Surface area analysis

In general, the process of xerogel formation is known to result in the collapsing of the pores, especially in case of soft supramolecular materials like metallogel. However, as one of the desirable features of a solid electrolyte is its ability to prevent gas diffusion across it, in the present work, this pore collapsible process is taken advantage of. The BET (Brunauer, Emmett and Teller) surface area measurements of FNPA xerogel also confirm the poor porosity in the resulting xerogel. The N_2 adsorption isotherm reveals a very low BET surface area of 124 m^2/g (**Figure 3B.7b**) only.

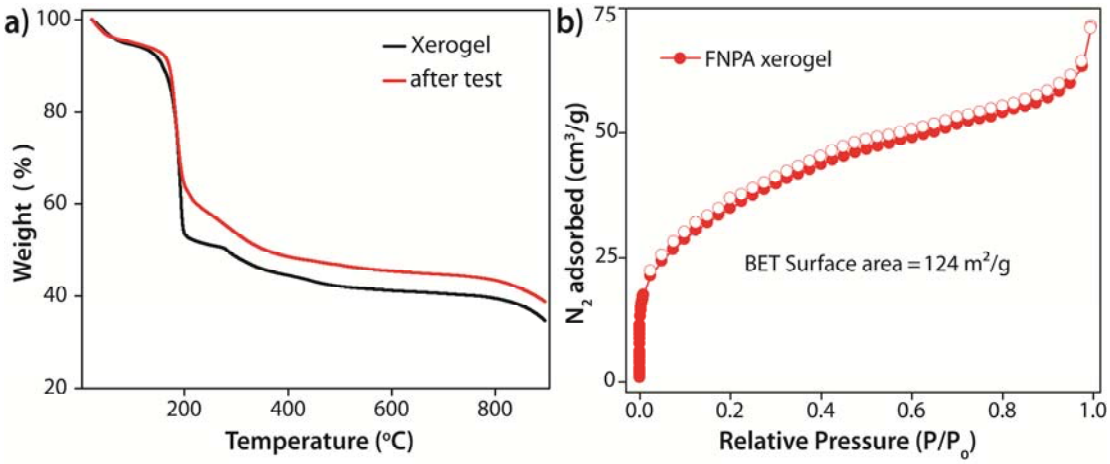

Figure 3B.7. *Combined plots indicating a) TGA curves of FNPA xerogel before and after the proton conductivity test and b) N_2 adsorption isotherm of FNPA xerogel.*

3B.2.1.7. TGA analysis

The thermal stability of FNPA xerogel (dried at 60 ˚C overnight) has been evaluated using the thermogravimetric analysis (TGA). The TGA curve indicates that the xerogel possess high thermal stability up to 150 ^{o}C except for the initial solvent losses observable at 30-80 ˚C (**Figure 3B.7a**). A comparison of the TGA plots of FNPA xerogel before and after proton conductivity measurements is carried to verify the stability of the material. The two TGA curves are observed to overlap very well. However, the loss corresponding to removal of the solvent molecules could also be detected following the comparison.

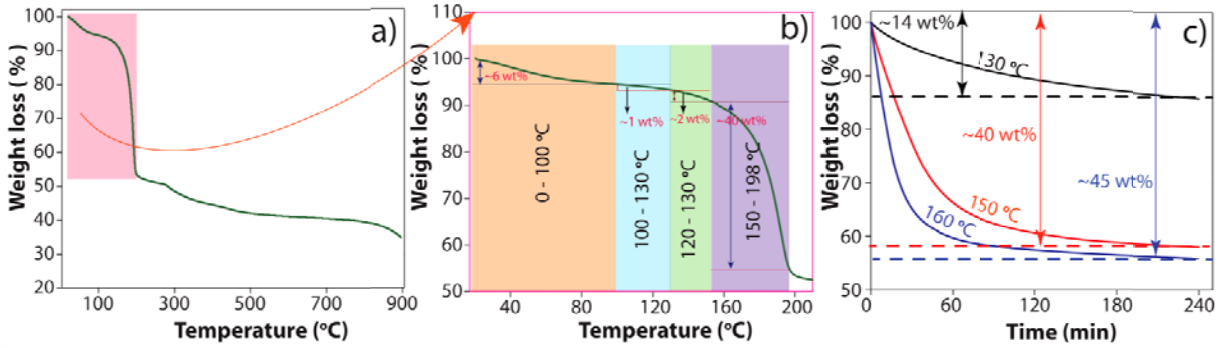

Figure 3B.8. *a) TGA profiles of FNPA xerogel, b) zoomed view of the TGA profile up to 200 °C and c) isothermal TGA thermograms of FNPA xerogel at three different temperatures (130 °C, 150 °C and 160 °C). Quantification of weight loss incurred at each step.*

In order to determine the effect of temperature on the weight loss of the material quantitatively, the isothermal TGA analyses of the xerogel is carried at three different temperatures (130 ˚C, 150 ˚C and 160 ˚C) for 4 h each. A comparative study (**Figure 3B.8**) of the thermograms suggests weight loss of ~14 wt % at 130 ˚C, due to the evaporation of solvent (DMF and water). The framework degradation sets in only after 150 ˚C resulting in a massive weight loss of ~40%, which could thus be found to be the prime reason behind the drop in proton conductivity at operating temperatures above 150 ˚C [weight loss at 150 ˚C = ~ 40%; weight loss at 160 ˚C = ~ 45%].

3B.2.2. Proton conductivity measurements

3B.2.2.1. AC impedance measurements

The quasi-four probe alternate current (AC) impedance measurements have been used to analyze the intrinsic proton conducting ability of the FNPA metallogel in anhydrous

conditions. Initially, the sample is heated at 120 ˚C to eradicate any residual water molecules left behind after the xerogel preparation process. The as obtained xerogel powder is then pelletized. During the preliminary proton conductivity experiments, the xerogel pellet is manually placed between two stainless steel electrodes (**Figure 3B.9**). The set-up is placed inside a sophisticated N_2 flushed, temperature controlled incubator (SH-241, ESPEC Co. Ltd., Japan) connected to the *BioLogic* electrochemical workstation. Prior to each measurement, the sample is allowed to equilibrate for about one hour at each temperature.

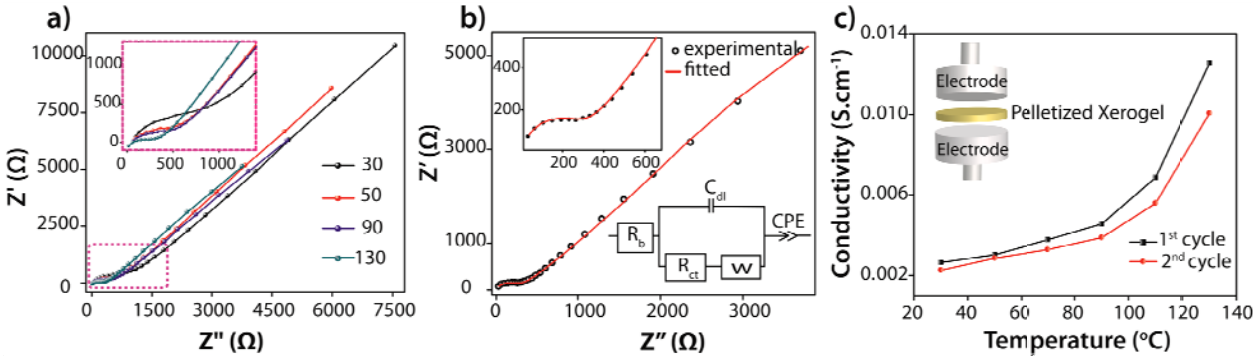

Figure 3B.9. *a) Nyquist plots obtained at different temperatures (in ˚C); b) Nyquist plots obtained at 130˚C and the equivalent circuit used for the fit (inset); c) proton conductivity measured during first and second run and stainless steel electrode assembly (inset).*

The impedance measurements are then executed at frequency ranging from 1 MHz to 100 Hz using 10 mV input voltage amplitude. At high frequency region, the Nyquist plots show a part of semicircle, while at the low frequency region a pronounced tail could be observed. The latter trait is attributed to the diffusion limitations consequential of the blocking effects experienced by the proton at the electrodes [25] (**Figure 3B.9a**). Besides this feature, the two probe Direct Current (DC) conductivity studies also exclude the electronic conduction possibility in the material proving it a poor electrical conductor with resistivity of 6×10^7 Ω/cm. In the study, the proton conductivity of the pelletized xerogel has been determined using the following relation;

$$\sigma = l/(R.A)$$

where, **σ** = proton conductivity (in S.cm^{-1}),

l = pellet thickness (in cm),

R = electrolyte/ pellet resistance (in Ω) and

A = area of the pellet (in cm^{-2}).

From the impedance studies, the material is observed to exhibit high proton conductivity up to 1.2×10^{-2} S/cm at 130 ˚C. However, on continued heating at 150 ˚C, the ionic conductivity decreases to 3.6×10^{-3} S/cm, indicating a change in the material composition thereafter (as indicated by TGA analysis). However, when tried at 130 ˚C, the sample is observed to retain its conductivity on cooling down to 30 ˚C and recycling back (**Figure 3B.9c**).

3B.2.2.2. PEMFC single cell assembly using FNPA as a solid electrolyte

As a validation of the proton conducting nature and its potential as a separating membrane for PEMFC, another set of experiments has been carried out at standard dry H_2/O_2 fuel cell conditions. The direct current measurements are carried out by fabricating a gas tight [2×2 cm^2 MEA] using dry H_2, dry O_2 gaseous reactants, FNPA xerogel pellet as solid electrolyte and Pt-C gas-diffusion electrodes (loading of 1 mg of Pt/cm^2) cold pressed at 1000 kg N for two minutes (**Figure 3B.10**). In the study, standard PEMFC procedure is employed for the MEA fabrication. Initially, about 800 mg of the xerogel powder is added into a 2.5 mm diameter die and then pelletized. The platinized electrodes are prepared by uniformly brush coating the Pt catalyst ink onto the carbon paper support (35CC-SGL with 15% PTFE content). The pellet is placed amid the two platinized carbon electrodes [each containing Johnson Matthey Pt catalyst + Vulcan carbon support (VX 72) + 20% Nafion binder] using Kapton gasket and eventually cold pressed by applying 1000 KgN pressure for 2 min.

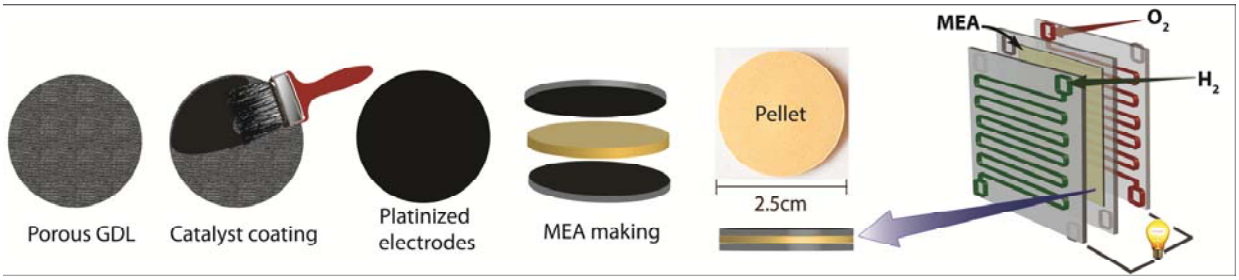

Figure 3B.10. *Schematic representation of the MEA making using pelletized FNPA xerogel as the solid electrolyte.*

The MEA is then arranged onto graphite plates using FRT gasket to enable their single cell assembly (active area = 4 cm^2, Fuel cell Tech).

The single cell test fixture used for the fuel cell polarization study consists of the following components:

- *Aluminium end-plates*
- *Graphite mono polar plates provided with integrated O-ring gasket and serpentine gas flow field*
- *Cathode loading:* 1 mg/ cm^2; N/C: 0.4; electrode thickness: 320 µm
- *Anode loading:* 1 mg/ cm^2; N/C: 0.4; electrode thickness: 324 µm
- *Gas flow:* 0.5 slpm for anode as well as cathode.
- *Operating temperature:* RT-120 ˚C
- *Membrane pellet thickness:* 1615 µm
- *Uncompressed MEA thickness:* 2259 µm
- *Compressed MEA thickness:* 1848 µm
- *% of the compression:* 18 %
- *Thickness of the gasket use :* 714 µm

3B.2.2.3. Electromotive Force (emf) measurement

During the electromotive force (emf) measurements, the cell is fed with 99.999 % pure dry hydrogen at the anode and 99.9 % pure dry O_2 at the cathode. Indicative of the cell being functional, the MEA shows a starting Open Circuit Voltage (OCV) of 0.807 V at 30 ˚C followed by an increment to a maximum of 1.02 V ± 0.02 at 100 ˚C due to the consequential thermal activation of the catalyst.

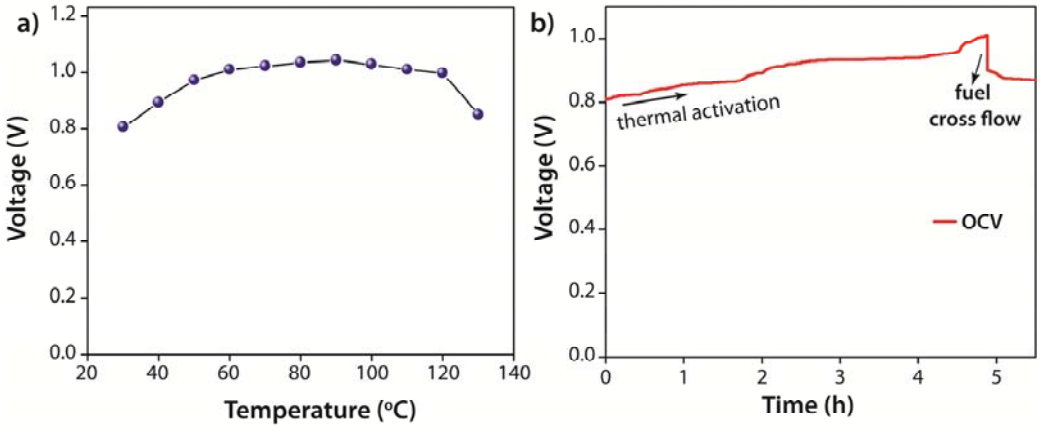

Figure 3B.11. *a) OCV measurement of the fabricated MEA at different temperatures and b) OCV lifetime measurement at 120 ˚C.*

On further rise in temperature, the OCV remained constant thereafter up to 120 °C (**Figure 3B.11a**). The OCV is observed to remain stable for the next five hours, which clearly divulges the denser nature of the pellet. Yet, on further rising the temperature to 130 °C, the OCV decreases rapidly to 0.85 V and thereafter the study has been terminated (**Figure 3B.11b**). The sudden decrease in the OCV is attributed to the cross flow of the reactant gases across the membrane electrolyte. [26]

3B.2.2.4. *In situ* impedance study

The *in situ* impedance measurements are carried out *via* two the electrode arrangement in the frequency range of 1 MHz – 100 Hz using *BioLogic* VPM3 electrochemical work station and 10 mV input voltage amplitude. In the study, O_2 passing cathode is used as the working electrode and H_2 passing anode is employed as the counter and reference electrodes. The results are studied using Nyquist plots obtained at each temperature (from RT to 120 °C). A PEMFC equivalent circuit has been used to fit the plots and the membrane resistance is calculated using the intercept in the complex impedance plane at the high frequency regime. It is important to note that the observed impedance response includes a combination of the responses from the two half-cells: cathode (Pt/C, O_2) and anode (Pt/C, H_2).

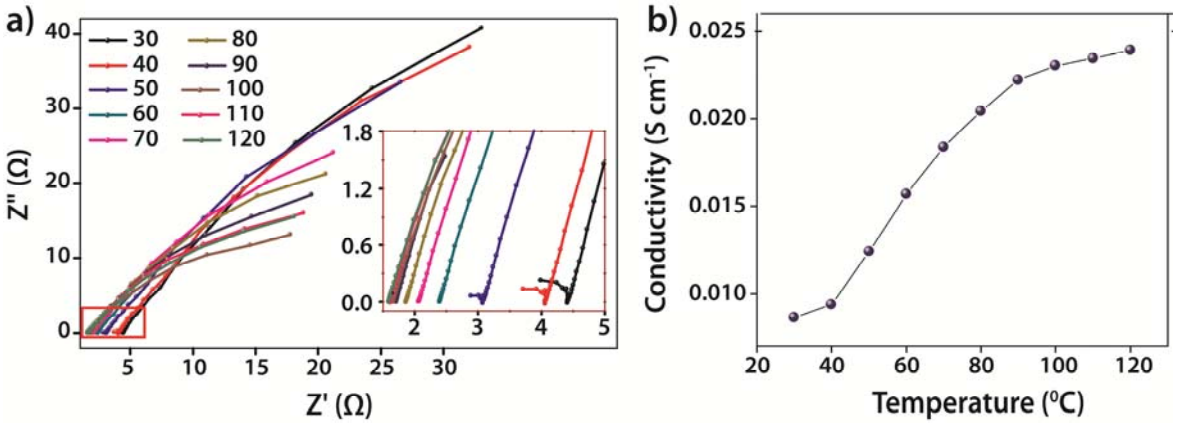

Figure 3B.12*. a) Nyquist plots obtained at different temperatures and b) variation of the MEA membrane conductivity with temperature.*

The presence of a single semicircle is indicative of the comparable time constants (interfacial resistance × capacitance) for the two half-cells (**Figure 3B.12a**). At 30 °C, the Nyquist plot clearly shows the presence of a distinctive charge transfer resistance (R_2) at the low frequency region associated with the catalyst layer. From the high frequency intercept, the

proton conductivity of 8.6×10^{-3} S/cm is measured. With increase in the MEA temperature, an escalation in the interfacial charge transfer could be observed which decreases the time constant, as supported by the disappearance of the semicircle. A high proton conductivity value of 2.4×10^{-2} S/cm is read at 120 °C before the OCV started decreasing due to the fuel cross flow (**Figure 3B.13**). The following equivalent circuit has been used to fit the experimental data:

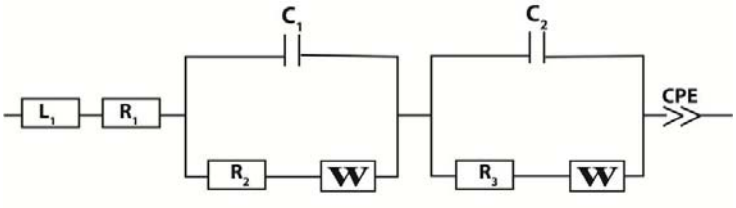

Figure 3B.13*. Equivalent circuit used for fitting the Nyquist plots obtained from the MEA impedance analysis.*

wherein,

L_1 = Inductance

R_1 = Membrane electrolyte resistance,

C_1, C_2 = Double layer capacitance at anode and cathode respectively,

R_2, R_3 = Charge transfer resistance at the anode-electrolyte and cathode - electrolyte interface respectively,

W = Warburg Diffusion impedance,

CPE = Constant Phase Element.

3B.2.2.5. Calculation of Activation Energy (E_a) involved in proton conduction

The activation energy calculated using the following Arrhenius equation,

$$\sigma_T = \sigma_0 \exp(-E_a / k_B T)$$

wherein, σ - proton conductivity (S/cm), σ_0 – pre-exponential factor, k_B - Boltzmann constant,T-temperature (K).

The activation energy was determined using the slope of the straight line obtained using the above equation. In the present work, the E_a is found to be 0.19 eV, indicative of a highly efficient Grotthuss pathway for proton conduction (**Figure 3B.14**). [27]

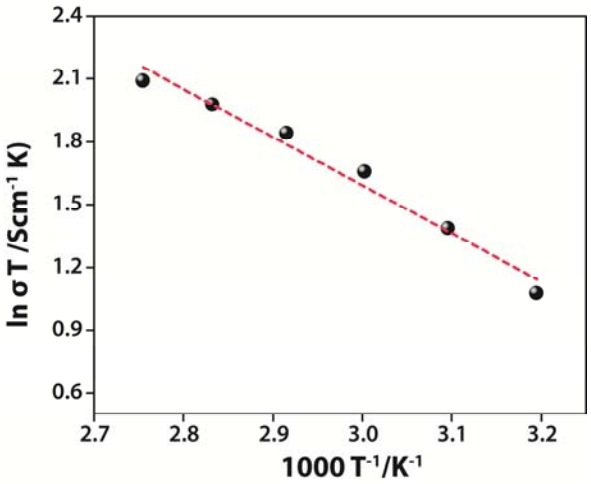

Figure 3B.14*. Arrhenius-type plot obtained at different temperatures.*

3B.2.2.6. Single-cell polarization study

Using FNPA xerogel as the solid electrolyte (with a pellet thickness of 1615 μm) and Pt/C coated porous carbon as electrodes, for the first time, the polarization of the metallogel fabricated PEMFC single cell has been attempted in the present study. The polarization is carried out using the standard PEMFC operating protocol, after passing 35-50 sccm of dry, pure hydrogen and 35-50 sccm dry, pure oxygen gases at the anode and cathode respectively. At 80 °C, a power density of 0.55 mW/cm^2 is achieved at 0.6 V, which happens to be the standard operating potential for a PEMFC fuel cell (**Figure 3B.15a**). A parallel polarization test is also carried out using a pellet with lesser thickness (735 μm). On polarizing it, a power density of 0.94 mW/cm^2 is obtained at 0.6 V, which verifies the decisive role of the electrolyte thickness in influencing the MEA performance (**Figure 3B.15b,c**).

It is thus observed that, for a finest performance, the pellet should be adequately dense to avert the undesired fuel cross flow and alongside be thin enough to maintain the cell resistance at its nominal limit (as Power Density= Current Density × Voltage; V = 0.6 V). Meanwhile, it could also be observed that the FNPA metallogel (without xerogel formation) is itself a good proton conductor and shows conductivity up to 2.5×10^{-3} S/cm at 90 °C. However, the conductivity of the FNPA xerogel is found to be better at least by an order of magnitude than the metallogel as such. This observation demonstrates the effect of the dilution of proton conducting units due to the copious amount of solvent molecules, which decreases the connectivity among the phosphate ester functions inside the metallogel network.

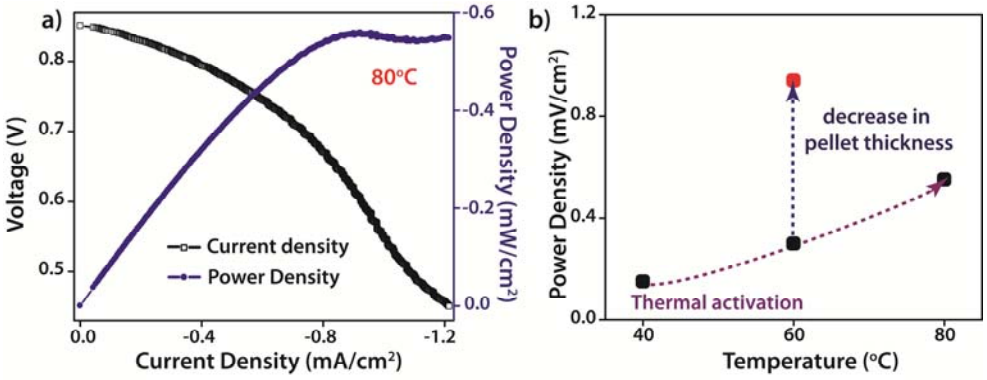

c)

Temperature (°C)	@ 0.6 V	
	C.D (mA/cm²)	P.D (mV/cm²)
60	0.57	0.34
80	0.93	0.55
60	1.56	0.94

Power Density = Current Density X Voltage

Figure 3B.15. *a) Fuel cell polarization plot obtained at 80˚C and b) plot of the power density as a function of temperature indicating the influence of the pellet thickness (thicknesses of the two pellets used are 1615 µm and 735 µm).*

3.2. Conclusion

The present chapter deals with the effective utilization of the otherwise laid back Fe-based metallogels; firstly, as self sacrificial precursors for one-pot synthesis of single crystalline Fe-MOFs *via* Pd^{2+} tempted metallogel degradation; secondly, as potential proton conducting solid electrolytes in PEMFC application.

In the first part of this chapter, a simple and competent route for the synthesis of single crystalline Fe-based MOF crystals *via* $PdCl_2$ mediated gel degradation is discussed. The study hints at the possible conversion of Fe-based metallogel into Fe-MOFs instigated by the oxidation of formic acid/DMF. This route demonstrates a classic example for a sol-gel technique based synthesis of single crystal structures. Most importantly, the study highlights the use of a Fe-metallogel as self-sacrificial precursor for effectively synthesizing Fe-MOFs that are otherwise hard to make and insist high-resolution powder X-ray diffraction data for determining their structure through the cumbersome Rietveld refinement techniques.

The second part of the chapter presents a directed proposal for the synthesis of a highly proton conducting PEMFC solid electrolyte by immobilizing protogenic, phosphate ester based ligand *via* gelation with Fe^{3+} ion using high boiling solvent namely, DMF. The FNPA metallogel carries distinct proton conducting ability due to the presence of one-dimensional nanofibrillar structure, which favors proton propagation using minimum activation energy. The xerogel obtained from slow drying of the metallogel is then tested for its gas separating capacity and proton transport ability in dry PEMFC fuel cell operating conditions. At 120 ˚C, the solid electrolyte constituted MEA results in an OCV of 1.02 V ± 0.02 with an inherent proton conductivity of 2.4×10^{-2} S/cm. Most convincingly, the present work is believed to mark an opening bid to understand the performance of such metallogel-derived solid electrolyte using fuel cell polarization studies. The electrical circuit completion of the PEMFC single cell is confirmed on achievement of 0.94 mW/cm^2 power density at 0.6 V. Although further enhancement in the power density could be still anticipated with the optimization of the pellet thickness, these studies undeniably prove the intrinsic ability of the metallogel derived materials to transport protons at high temperature under anhydrous conditions, which is an urgent requisite for high temperature PEMFC's.

3.3. References

[1] (a) A. Carne, C. Carbonell, I. Imaz, D. Maspoch, *Chem. Soc. Rev*., **2011**, *40*, 291. (b) J.Y. Lee , O. K. Farha , J. Roberts , K. A. Scheidt , S. T. Nguyen, J. T. Hupp, *Chem. Soc. Rev.*, **2009**,*38*, 1450.

[2](a) D. D. Diaz, D. Kuhbeck and R. J. Koopmans, *Chem. Soc. Rev*. **2011**,*40*, 427. b) P.Terech and R.G.Weiss, *Chem. Rev*.**1997**, *97*, 3133. c) A. Y.-Y. Tam and V.W. -W. Yam,Chem. Soc. Rev.**2013**,42, 1540. d) G. Yu, X. Yan, C. Han and F. Huang, *Chem. Soc. Rev*. **2013**, *42*, 6697.

[3](a)M.O. M. Piepenbrock, G. O.Lloyd, N. Clarke and J. W. Steed, *Chem. Rev*. **2010**,*110*,1960. b) G. R. Desiraju, *Angew. Chem. Int. Ed. Engl.* **1995**, *34*, 2311.

[4](a) H. Furukawa, K. E. Cordova, M. O'Keeffe, O. M. Yaghi, *Science*, **2013**, *341*, 1230444.(b) G. K. H. Shimizu, J. M. Taylor and S. Kim, *Science*, **2013**, *341*, 354. (c) S. Sen, N. N. Nair, T. Yamada, H. Kitagawa P. K. Bharadwaj, *J. Am. Chem. Soc.*, **2012**, *134*, 19432.

[5](a) S. Henke, R. Schmid, J.D. Grunwaldt, R. A. Fischer, *Chem. Eur. J.*,**2010**, *16*, 14296. (b) U.Stoeck, S. Krause, V.Bon, I.Senkovska, S. Kaskel, *Chem. Commun*., **2012**, *48*, 10841.

[6](a) L. Xie, S. Liu, C.Gao, R. Cao, J. Cao, C. Sun, Z. Su, *Inorg. Chem*.,**2007**, *46*,7782.(b) T. R. Whitfield, X. Wang, L. Liu, A. J. Jacobson, *Solid State Sci.,* **2005**, *7*,1096. (c) C. Serre, F. Millange, S. Surble, G. Ferey, *Angew. Chem. Int. Ed*., **2004**, *43*, 6286.(d) C. Serre, F. Millange, S. Surble J.-M. Greneche, G. Ferey, *Chem. Mater.,* **2004**, *16*, 2706.

[7](a) R. C. T. Howe, A. P. Smalley, A. P. M. Guttenplan, M. W. R. Doggett, M. D. Eddleston, J. C. Tanb , G. O. Lloyd, *Chem. Commun*., **2013**, *49*, 4268. (b) M. R. Lohe, M. Rose , S. Kaskel, *Chem. Commun*., **2009**, 6056. (c) J. Nanda, A. Biswas, B. Adhikari, A. Banerjee, *Angew. Chem. Int. Ed*., **2013**, 52, 5041. (d) P. Sahoo, R. Sankolli, H.-Y. Lee, S. R. Raghavan and P. Dastidar, *Chem. Eur. J*.,**2012**, *18*, 7965-8244. (e) D. K. Kumar, D. A. Jose, A. Das and P. Dastidar. *Chem. Commun*.,**2005**, 4059.

[8](a) O. M. Yaghi, G. Li, H. Li, *Chem. Mater*.,**1997**, 9, 1074.(d) C. D. Jones, J. Chong Tan , G. O. Lloyd, *Chem. Commun*., **2012**, *48*, 2110. (b) Desiraju, G. R., Curtin, D. Y. & Paul, I. C. *J. Am. Chem. Soc.*,**1977**, *99*, 6148.(c) V. R. Thalladi, S. Brasselet, H.-C. Weiss, D. Bläser, A. K. Katz, H. L. Carrell, R. Boese, J. Zyss, A. Nangia, G. R. Desiraju, *J. Am. Chem. Soc*.,**1998**, *120*, 2563.

[9](a) P. Horcajada, S. Surble, C,Serre, D.Y. Hong, Y.K. Seo, J.S Chang, J.M. Greneche, I. Margiolaki , G. Ferey, *Chem. Commun*., **2007**, 2820.(b) K. Kongpatpanich, S. Horike, M.Sugimoto, S. Kitao, M. Setoc , S. Kitagawa, *Chem. Commun*., **2014**, *50*, 2292.

[10](a) L. Meazza, J. A. Foster, K. Fucke, P. Metrangolo, G. Resnati, J. W. Steed, *Nature Chem.* **2013**, *5*,42.(b) J. A. Foster, M.O. M. Piepenbrock, G. O. Lloyd, N. Clarke, J. A. K. Howard, J. W. Steed, *Nature Chem*.,**2010**, *2*,1037.

[11](a) Desiraju, G. R., *Nat. Mater*., **2002**, *1*, 77. (b) Mondal, R., Howard, J. A. K.; Banerjee, R., Desiraju, G. R. *Chem. Commun*. **2004**, 644. (c) Bilton, C., Howard, J. A. K., Madhavi, N. N. L., Nangia, A., Desiraju, G. R.; Allen, F. H. *Acta Crystallogr.B*, **2000**, *56*, 1071. (d) Allen, F. H., Howard, J. A. K., Hoy, V. J., Desiraju, G. R., Reddy, D. S., Wilson, C. C., *J. Am. Chem. Soc.*, **1996**, *118*, 4081.

[12](a). CrysAlisPro, Version 1.171.33.66; Oxford Diffraction Ltd.: Abingdon, U.K., **2010**. (b). G. M. Sheldrick, **1997**, SHELXS '97 and SHELXL '97. University of Göttingen,

Germany. (c). A. L. Spek, **2005**, PLATON, A Multipurpose Crystallographic Tool, Utrecht University, Utrecht, The Netherlands. (d). L. A. Dakin, P. C. Ong, J. S. Panek, R. J.Staples, P. Stavropoulos, *Organometallics*, **2000**, *19*, 2896. (e). S. Noro, R. Kitaura, M. Kondo, S. Kitagawa, T. Ishii, H. Matsuzaka, M. Yamashita, *J. Am. Chem. Soc.* **2002**, *124*, 2568. (f). M. Eddaoudi, J. Kim, D. Vodak, A. Sudik, J. Wachter, M. O'Keeffe, O. M. Yaghi, *Proc. Natl. Acad. Sci. U.S.A.* **2002**, *99*, 4900.

[13]A. D. Burrows, K. Cassar, R. M. W. Friend, M. F. Mahon, S. P. Rigbyb, J. E. Warren, *Cryst Eng Comm*., **2005**, *7*, 548.

[14] L. Rajput, D. Kim, M. S. Lah, *Cryst Eng Comm*., **2013**,*15*, 259.

[15](a)Y. Qin, J. Wang, F. Meng, L. Wangac , X. Zhang, *Chem. Commun.,* **2013**, *49*, 10028-10030.(b) N.Miyaura , A.Suzuki, *Chem. Rev*. **1995**, *95*,2457. (c) Z. L. Wang, J. M. Yan, Y. Ping, H.L. Wang, W. T. Zheng, Q. Jiang, *Angew. Chem. Int. Ed.,* **2013**, *52*, 4406.

[16](a)I. P.Santos , L.M. Liz-Marzan, *Nano Lett*., **2002**,*2*,903.(b) I. Kapoor, E.-M. Schön, J. Bachl, D. Kühbeck, C.Cativiela, S.Saha, R. Banerjee, S. Roelens, J. J Marrero-Tellado, D. D. Díaz, *Soft Matter*, **2012**, *8*, 3446. (c)A.Mallick, E. M. Schön, T.Panda, K. 100 Sreenivas, D. D. Díaz, R.Banerjee*, J. Mater. Chem*., **2012**, *22*, 14951 (d) B. Xing, M.F. Choi, B. Xu, Chem. Eur. J.,2002, 21,8. (e) A. Y.-Y. Tam,V. W.-W. Yam, *Chem. Soc. Rev*., **2013**,*42*, 1540.

[17](a) H. Steininger, M. Schuster, K. D. Kreuer, A. Kaltbeitzel, B. Bingol, W. H. Meyer, S. Schauff, G. Brunklaus, J. Maier and H. W. Spiess, *Phys. Chem. Chem. Phys*. **2007**, *9*, 1764.(b) M. F. H. Schuster, W. H. Meyer, M. Schuster and K. D. Kreuer, *Chem. Mater.* **2004**, *16*, 329.

[18](a) M. Schuster, C. C. de Araujo, V. Atanasov, H. T. Andersen, K.D. Kreuer and J. Maier, *Macromolecules*, **2009**, *42*, 3129. (b) C. L.-Robert, K. Valle, F. Pereirab and C. Sancheza, *Chem. Soc. Rev*. **2011**, *40*, 961.

[19](a)L. Xiao, H. Zhang, E. Scanlon, L. S. Ramanathan, E.-W. Choe, D. Rogers, T. Apple and B. C. Benicewicz, *Chem. Mater.* **2005**, *17*, 5328. (b) S.-I. Lee, K.-H. Yoon, M. Song, H. Peng, K. A. Page, C. L. Soles and D. Y. Yoon, *Chem. Mater*., **2012**, *24*, 115.

[20](a) Y.Oono, T. Fukuda, A. Sounai and M. Hori, *J. Power Sources*, **2010**, *195*, 1007.(b) Y.Oono, T. Fukuda and M. Hori, *J. Power Sources*, **2009**,*189*, 943.

[21](a)K. A. Page, B. W. Rowe, *ACS Symposium Series,* **2012**, *9*, 147.(b) G. Girishkumar , M. Rettker , R. Underhile , D. Binz ,K. Vinodgopal , P. McGinn , P. Kamat, *Langmuir*, **2005**, *21*, 8487.

[22] S.Saha, E.M. Schon, C. Cativiela, D. D.Diaz, R. Banerjee, *Chem. Eur. J.* **2013**, *19*, 9562.

[23](a) S. Beyazyildirim, K. D. Kreuer, M. Schuster, A. J. Bhattacharyya and J.Maier, *Adv. Mater.* **2008**, *20*, 1274. (b) K. Miyatake, E. Shouji, K. Yamamoto, E. Tsuchida, *Macromolecules*, **1997**, *30*, 2941.

[24](a)T.D. Hamilton, D.-K. Bučar, J. Baltrusaitis, D. R. Flanagan, Y. Li, S. Ghorai, A. V. Tivanski, and L. R. MacGillivray, *J. Am. Chem. Soc*. **2011**, *133*, 3365. (b) S. Varghese, N. S. S. Kumar, A. Krishna, D.S. S. Rao, S. K. Prasad and S. Das, *Adv. Funct. Mater.* **2009**,*19*,2064.

[25] (a) J. M. Taylor, K. W. Dawson and G. K. H. Shimizu, *J. Am. Chem. Soc*. **2013**, *135*, 1193. (b) S. Horike, D. Umeyama and S. Kitagawa, *Acc. Chem. Res*. **2013**, *46*, 2376. (c) J. A. Hurd, R. Vaidhyanathan, V. Thangadurai, C. I. Ratcliffe, I. L. Moudrakovski and G. K. H. Shimizu, *Nat. Chem*. **2009**, *1*, 705.

[26] (a) N. Agmon, *Chem. Phys. Lett*. **1995**, *244*,456. (b) T.Yamada, M. Sadakiyo and H. Kitagawa, *J. Am. Chem. Soc*. **2009**, *131*, 3144.

Chapter 4

Covalent Organic Framework (COF) as prototype solid electrolyte in Proton Exchange Membrane Fuel Cells*

Mechanochemistry is often deemed as a judicious, green, and fast synthetic route for effective realization of a waste-free environment. However, the poor physical properties *viz*., low specific surface area, poor crystallinity etc. of the as synthesised materials has been a major bottleneck for their realistic applications. This chapter[#] introduces a new way of using such mechanochemically synthesized covalent organic framework (COF) to fabricate Membrane Electrode Assembly (MEA) of Proton Exchange Membrane Fuel Cell (PEMFC), a concept rarely realized using such materials. Herein a less porous mechanochemically synthesized COF (TpBpy-MC) is used to accommodate phosphoric acid molecules, a notable proton conducting dopant. On integrating such proton conducting functionalities into the less porous COFs, they could be readily employed as gas separators and solid electrolytes in a real fuel cell. Accordingly, the mechanochemically synthesized COF inhibits the undesired fuel crossover and makes up a stable OCV of 0.93 V at 50 °C, besides exhibiting a high proton conductivity of 1.4×10^{-2} S cm^{-1}. Most importantly, the COF backbone remains intact upon acid doping, thereby permitting a long time PEMFC operation. These studies unequivocally prove the inherent ability of such materials to conduct protons at dry conditions, which is an immediate requisite for low temperature PEMFCs.

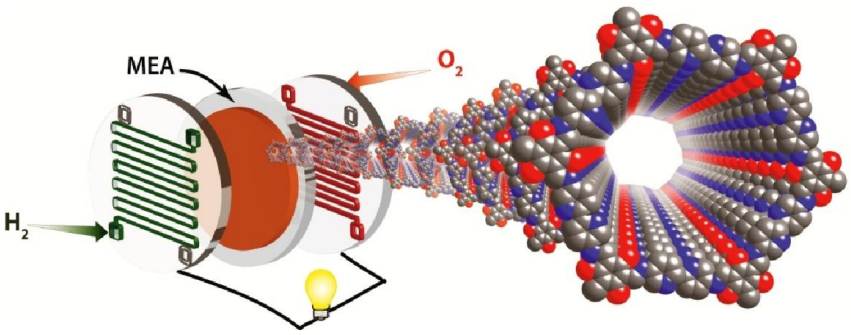

*The content of this chapter has been published in [#] ***J. Mater. Chem. A, 2016***, *4,* 2682 and is reprinted with permission from [#]The Royal Society of Chemistry.

4.1. Introduction

The mounting need of regular chemicals and synthetic materials has led to a startling rise in the production of perilous trade contaminants. [1] This has instigated the researchers to bring in newer synthetic routes with cheaper, cleaner, and proficient protocols to be used in the contemporary day processes. Amongst all the greener methods, mechanochemistry has received outspread response from the time it has been recognized to effect metal-metal bond formation in metal alloys.[2] This procedure usually entails use of nominal amount of reaction solvents, with alongside being time efficient, when compared with the other conventional used techniques. Recently, momentous steps have been taken to mechanochemically effect the formation of coordination bonds and thereby synthesize industrially significant materials like the microporous zeolites.[3] The mechanochemical approach is also extended to realize multiple bond formation between metal ions/clusters and organic linkers and construct open framework structures like MOFs.[4]

Covalent organic frameworks (COFs) are structured, lightweight, organic, open frameworks containing intrinsic porosity and crystallinity that make them functional for applications such as gas adsorption and storage, sensing, catalysis etc. [5] These materials can be functionalized as per the requirement, which they are needed for. Most importantly, the COFs are chemically robust and are have been proven to retain their chemical stability up to 12 M H_3PO_4 loading, unlike their other porous component, the MOFs, which fail to endure such chemical stress. Yet, unlike the MOFs, which are easily synthesised using simple scalable methods *viz*., simple mixing (at room temperature), solvothermal, microwave, etc., the COF synthesis is challenging.[6] It involves use of cumbersome sealed tube method, which is time consuming and demanding need of profuse amount of solvents for processing them. This necessitates an imperative need for a simpler, quicker, and neater route of COF synthesis from both energy expending and environment taxing point of view. Although, there are reports of covalent bond formation using mechanical energy in polymers and 0-D organic cages [7], their use towards construction of multiple covalent bonds like in case of the ordered COFs is not well explored. [8] Moreover, COFs synthesized in this way are bound to suffer from low porosity and poor crystallinity considering to the limitations of the technique. [9] Therefore, the solvothermal method has always been chosen over the mechanochemical route for synthesizing COFs with practical applications.

It is noteworthy that although many MOFs are recognized for their proton conducting ability, but strikingly, there exist very few examples of proton conducting COFs. [10] In fact, the performance of such materials under real fuel cell operating conditions has not been demonstrated till date. The present chapter highlights the usefulness of such mechanochemically derived bipyridine functionalized COF (TpBpy-MC) as a solid electrolyte for Proton Exchange Membrane Fuel Cell (PEMFC). The work shows a pioneering way to integrate COFs into the PEMFC assembly and *in situ* monitor its proton conducting ability. The less porous, mechanochemically synthesized TpBpy-MC is found to effectively separate the reactant gases, besides showing high intrinsic proton conduction under the PEMFC operating conditions (**Figure 4.1**).

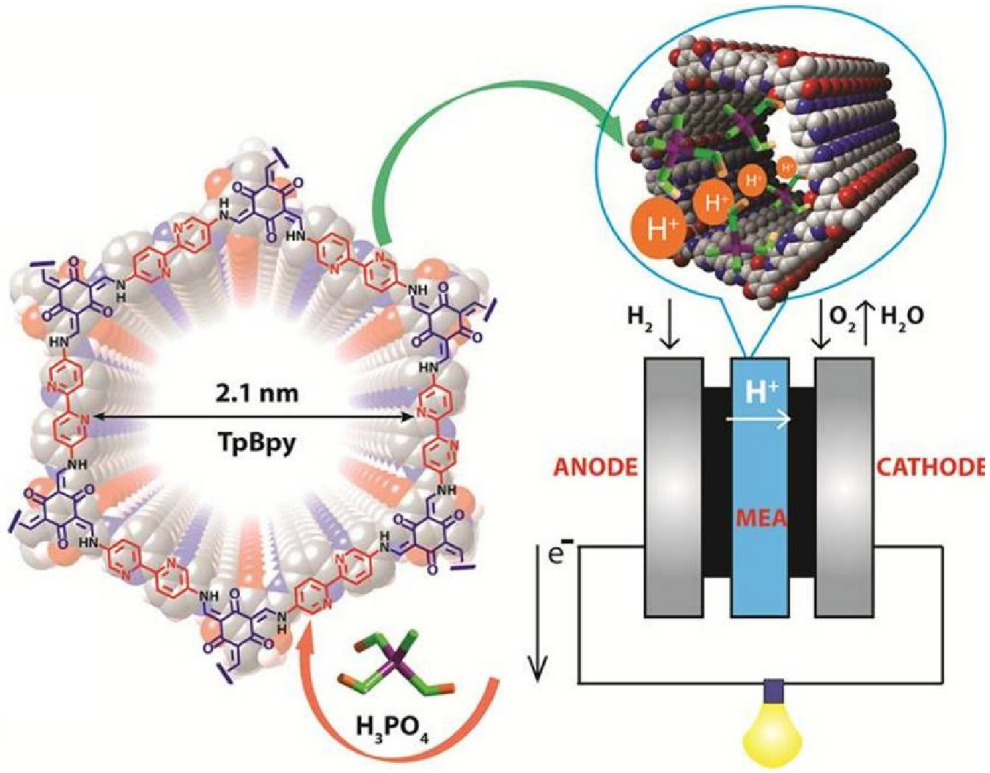

Figure 4.1*. Schematic representation of the loading of phosphoric acid (PA) into TpBpy COF and later its integration as a solid electrolyte in PEMFCs.*

4.2. Experimental Section

4.2.1. Synthesis of TpBpy-MC by mechanochemical route: 1,3,5-triformylphloroglucinol Tp (63 mg, 0.3 mmol) and 2,2'-bipyridine-5,5'-diamine Bpy (83.7 mg, 0.45 mmol) are taken in a 5 mL stainless steel jar (containing one 7 mm diameter stainless steel ball) holding a

solvent mixture of 60 µL of DMAc + 30 µL of *o*-DCB + 15 µL of 6 M acetic acid. The procedure is optimized with respect to the reaction time and milling frequency. In the typical procedure followed, the reaction mixture is ground for 90 min. at 30 Hz. Then the resulting TpBpy-MC powder is washed using minimal amount of DMAc, water and acetone successively. (Isolated yield= ~84 %).

4.2.2. Synthesis of TpBpy-ST by solvothermal route: The solvothermal synthesis of TpBpy-ST is achieved by charging a pyrex tube with 1,3,5-triformylphloroglucinol (Tp) (63.0 mg, 0.3 mmol) and 2,2'-bipyridine-5,5'-diamine(Bpy) (83.7 mg, 0.45 mmol) in a solvent combination containing 4.5 mL of dimethylacetamide (DMAc), 1.5 mL of o-dichlorobenzene (o-DCB) and 0.6 mL of 6 M aqueous acetic acid (AcOH). This mixture is sonicated for 10-15 min. for homogenous dispersion of contents. The tube is sealed off and then heated at 120 °C for 3 days.

4.2.3. Loading experiment of phosphoric acid into TpBpy-MC: The phosphoric acid is loaded into the bipyridine functionalized COFs by soaking a known amount of TpBpy-MC/ TpBpy-ST powder (300 mg) of in 50 mL of 12 M H_3PO_4 for 2 h. The as treated material is filtered, washed with water, and finally dried under vacuum for 4 h at room temperature.

4.3. Results and Discussion

4.3.1. Material Characterization

4.3.1.1. Electron microscopic study

The SEM and TEM images of TpBpy-ST point at the interwoven fiber like morphology with visible signs of crystallite aggregation and size ranging between 100-300 nm (**Figure 4.2a**). On the other hand, the microscopic images of TpBpy-MC reveal sheet-like morphology with particle dimensions lesser than the solvothermally derived one. The decrease in the particle dimension is a characteristic result of the mechanochemical delamination process (**Figure 4.2a**). [11]

The SEM imaging of the pellets used for the proton conduction test is also performed to understand the effect of pelletization on the COF morphology. In case of PA@TpBpy-MC, the cross section of the COF pellet reveals compact packing of the crystallites, while in case

of the solvothermally synthesized PA@TpBpy-ST; the pellet seems to be fluffily packed (**Figure 4.2c**).

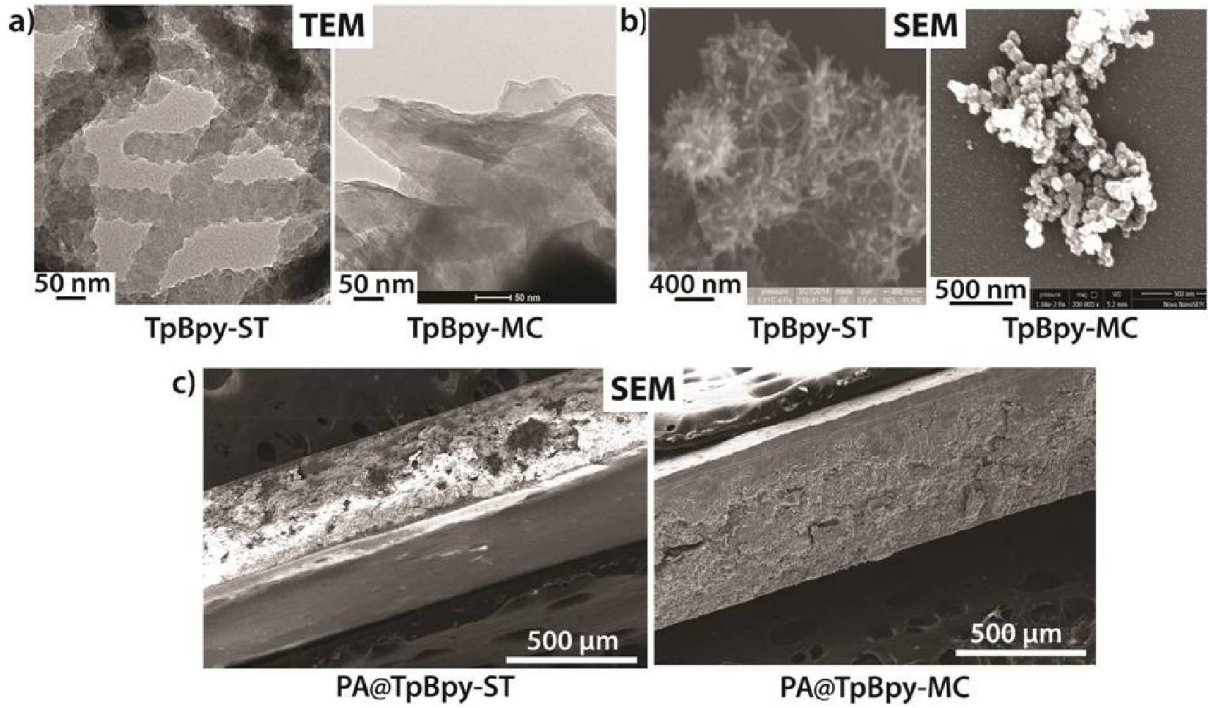

Figure 4.2. *Corresponding a) TEM images, b) SEM images of TpBpy-ST and TpBpy-MC and c) SEM images of PA@TpBpy-ST and PA@TpBpy-MC pellets.*

4.3.1.2. PXRD analysis

The PXRD spectrum of TpBpy-MC shows a prominent first peak corresponding to the characteristic (100) plane of the 2-D COF. However, the intensity of this peak is less compared to the solvothermally synthesized TpBpy-ST (**Figure 4.3**). This is a result of the haphazard displacing of the COF layers enforced by the mechanical energy applied to COF during its synthesis. This favors the partially eclipsed configuration of TpBpy-MC, with poorly accessible pore features. This diffuses the reflections from the (100) plane thereby weakening the peak intensity.

The peak at ~26° corresponds to the (001) plane, whose broadening indicates the irregular π–π stacking of the COF layers.

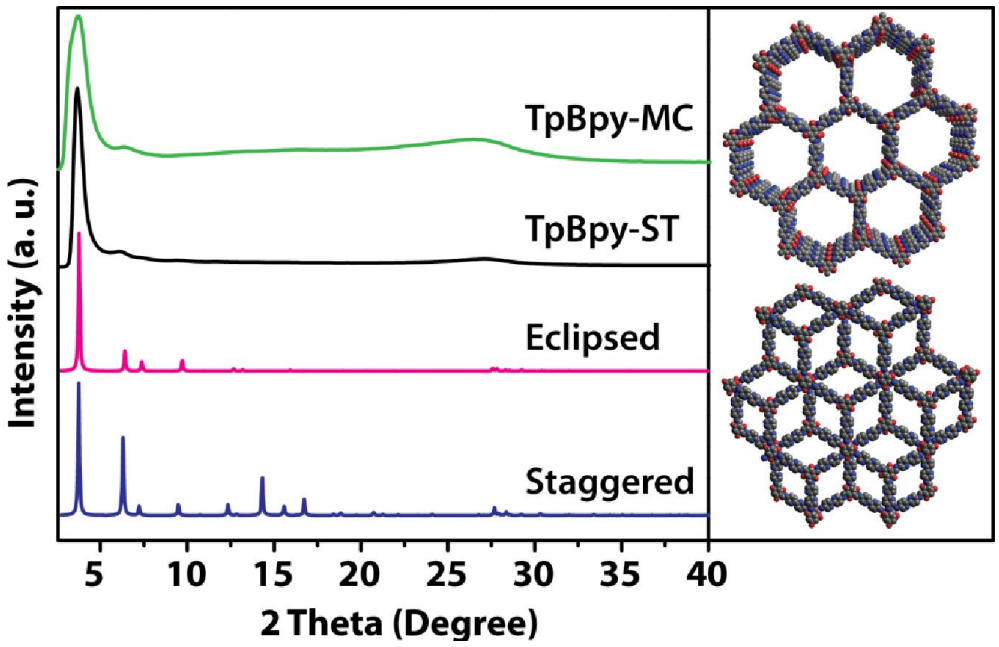

Figure 4.3. *Comparative PXRD patterns of the as-synthesized* ***TpBpy-ST*** *(Black) and* ***TpBpy****-MC (Green) COFs.*

4.3.1.3. FTIR analysis

The FTIR spectra of both the COFs indicate no left over traces of the starting materials.

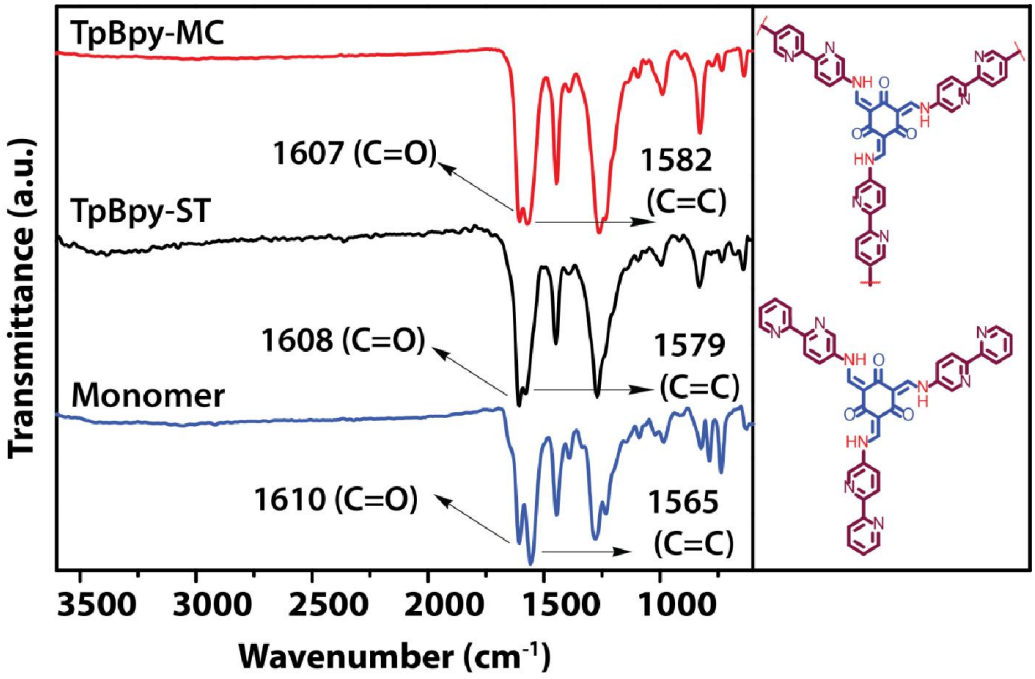

Figure 4.4. *Comparative FTIR spectra of TpBpy-MC, TpBpy-ST and the monomer.*

It also confirms the removal of the N–H stretching bands (3112-3317 cm^{-1}) (corresponding to Bpy) and the C=O stretching frequency (1637 cm^{-1}) (corresponding to Tp) (**Figure 4.4**) which are otherwise clearly observed in case of the starting materials. Additionally, the spectra show introduction of two new, strong peaks corresponding to the C=O (1607 cm^{-1}) and C=C (1579 cm^{-1}) stretching frequencies, thereby confirming the keto form of the COFs.

4.3.1.4. TGA analysis

The Thermogravimetric Analysis (TGA) of the activated TpBpy-ST and -MC indicates the high thermal stability of the frameworks up to 350 °C. After 360 °C, a gradual weight loss of 30-40% is observed, indicative of the frameworks' decomposition after that (**Figure 4.5**).

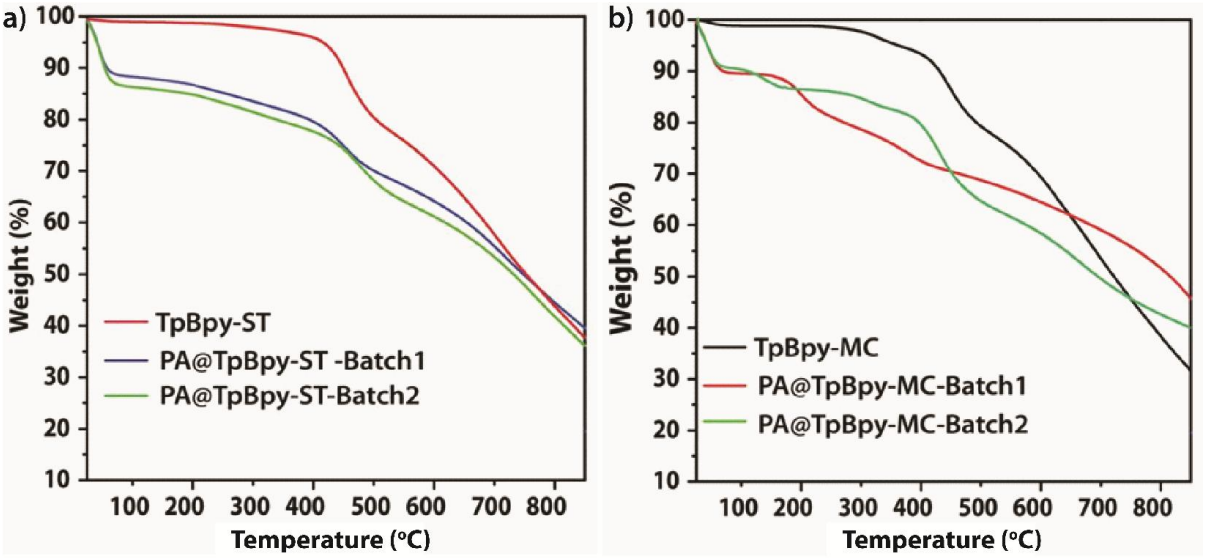

Figure 4.5. *Combined TGA profiles of a) TpBpy-ST and PA@TpBpy-ST; b) TpBpy-MC and PA@TpBpy-MC.*

4.3.1.5. Surface area analysis

The surface area of the COFs is calculated using BET model. The activated TpBpy-ST and TpBpy-MC are found to possess BET surface areas of 1746 and 293 m^2g^{-1}, respectively (**Figure 4.6**). The lower surface area of TpBpy-MC compared to its solvothermal equivalent is most likely due to the decreased particle dimensions and sheet-like structure, contrasting the TpBpy-ST's fiber like morphology. This accordingly obstructs the long-range ordering of the pores in TpBpy-MC, which eventually limits the adsorption to the reachable pores in the framework.

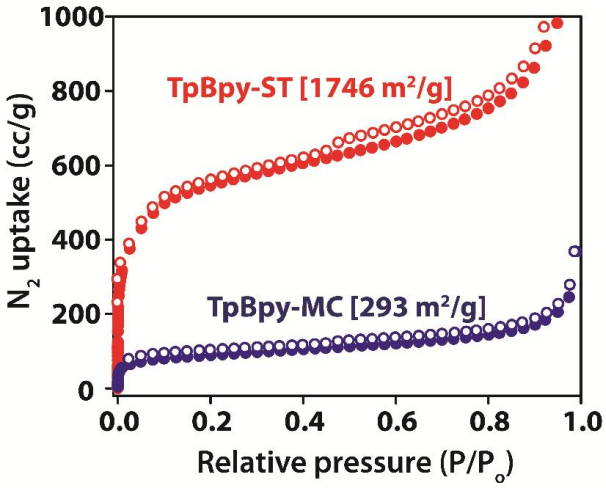

***Figure 4.6**. N_2 adsorption isotherms of TpBpy-ST (red) and TpBpy-MC (blue).*

4.3.2. Chemical Stability test post acid doping

4.3.2.1. PXRD analysis

The PXRD spectra of the COF pellet post conductivity study matches well with that of the fresh one, which confirms the chemical stability of the material (**Figure 4.7**).

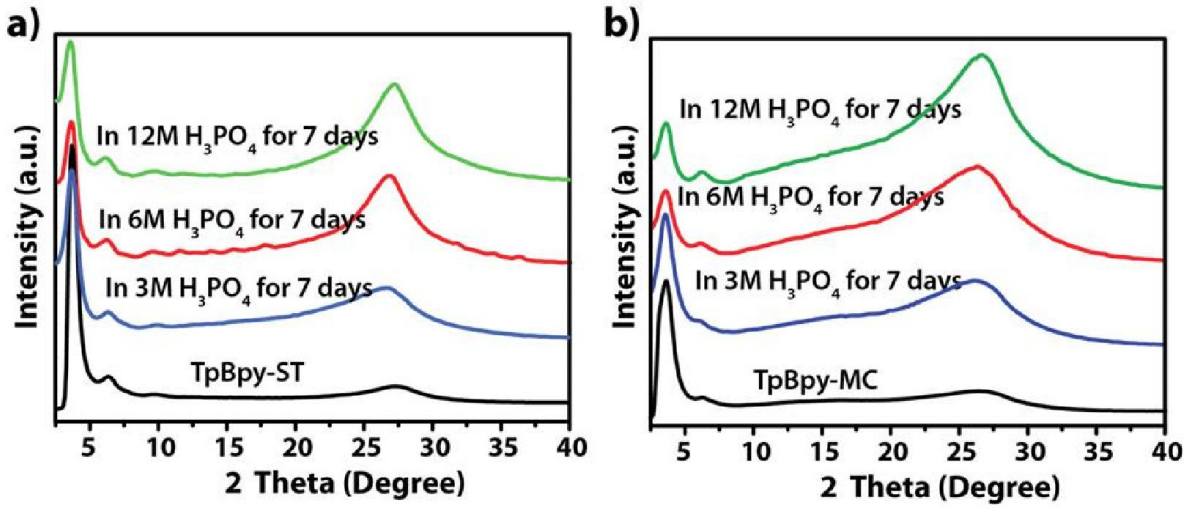

***Figure 4.7.** Comparative PXRD spectra of TpBpy-ST and TpBpy-MC before and after the phosphoric acid loading.*

4.3.2.2. FTIR analysis

The comparative FTIR spectra of the COFs post acid treatment also confirm the chemical stability of the material (**Figure 4.8**).

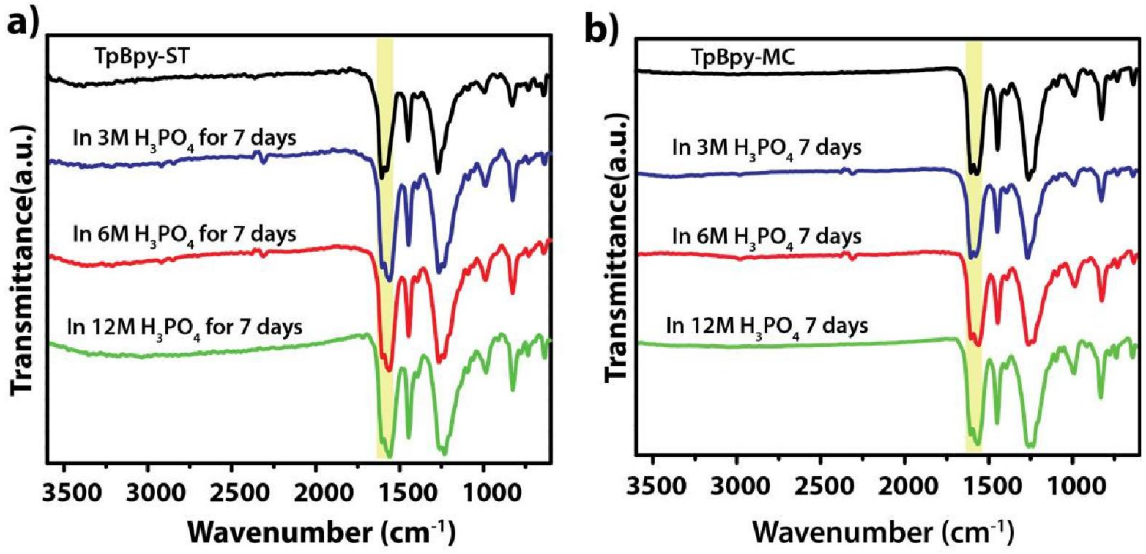

Figure 4.8. *Comparative FTIR spectra of TpBpy-ST and TpBpy-MC before and after the phosphoric acid loading.*

4.3.2.3. Surface area analysis

The surface area of the COFs has been found to decrease drastically up to 80 m^2 g^{-1} on loading phosphoric acid (**Figure 4.9**). This predominantly hints at the blockage of the COF pores by the incoming phosphoric acid molecules.

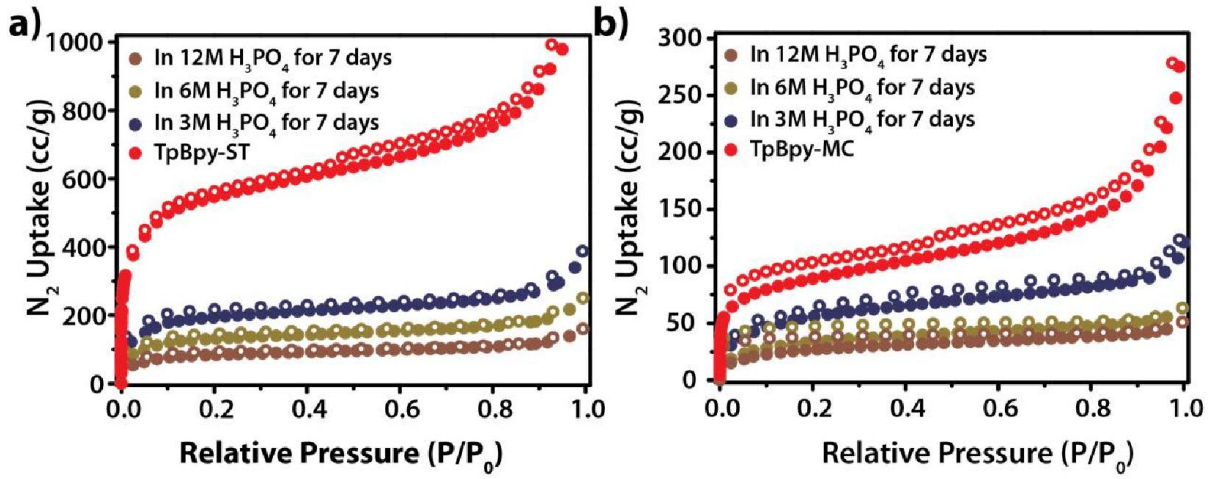

Figure 4.9. *Comparative N_2 adsorption isotherms of TpBpy-ST and TpBpy-MC before and after phosphoric acid loading.*

4.3.3. Proton conductivity study

4.3.3.1. AC impedance measurements

The proton conduction ability of the bare and phosphoric acid loaded COFs is measured using quasi-four-probe configuration, using the Frequency Response Analyzer equipped Solartron 1286 Electrochemical Interface, under anhydrous environment. Each time, the conductivity value is determined using the semicircle in the Nyquist plot, in which the high frequency intercept is considered as the contribution from the pellet resistance. The pristine COF as such does not exhibit any proton conducting behavior. This verifies the role of the COF as the support matrix, and the necessity to add the proton carriers' in order to conduct protons across it.

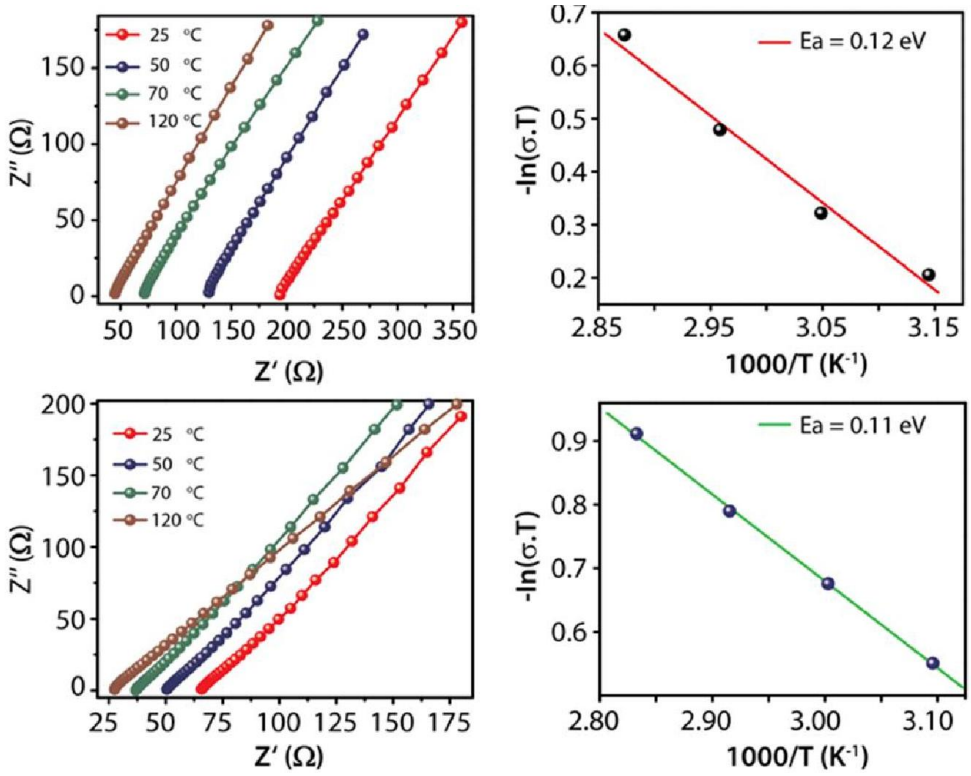

Figure 4.10. *Temperature dependent Nyquist plots and corresponding Arrhenius plots of PA@TpBpy-ST and PA@TpBpy-MC.*

The conductivity study further reveals that the proton conducting ability of the phosphoric acid doped COF improves with increasing temperature from 233 to 393 K (**Figure 4.10**). At 393 K, a highest proton conductivity of 1.98×10^{-3} and 2.5×10^{-3} S cm^{-1} is measured for PA@TpBpy-ST and PA@TpBpy-ST-MC, respectively (**Figure 4.10**). The

performance of the present phosphoric acid doped COFs is equivalent to their MOF counterpart, *i.e.,* PA@MIL-101 (1.3 x 10^{-3} S cm^{-1} at 120 °C, 0% RH). [12] It is also important to note that comparatively, the conductivity of the phosphoric acid doped COF reported here is at least two orders of magnitude higher than the reported PA@Tp-Azo (6.7 x 10^{-5} S cm^{-1} at 120 °C and 0% RH).

4.3.3.2. Calculation of Activation Energy (E_a) involved in proton conduction

The activation energy is calculated using the following Arrhenius equation:

$$\sigma_T = \sigma_0 \exp(-E_a / k_B T)$$

wherein, σ is the proton conductivity (S/cm), σ_0 is the pre-exponential factor, k_B is the Boltzmann constant and Tis the temperature (K).

The activation energy is determined using the slope of the straight line obtained using the above equation. In the present work, the activation energy value is calculated to be 0.12 and 0.11 eV for PA@TpBpy-ST and –MC, respectively (**Figure 4.10**). This verifies the operating of Grotthuss proton hopping mechanism in both the materials. [13] The structural resemblance and similar activation energy in both PA@TpBpy-ST and -MC hints that the proton conduction results from the structural diffusion of protons along the phosphoric units that are held to the bipyridine units *via* hydrogen bonding.[14]

4.3.3.3. Membrane Electrode Assembly (MEA) fabrication using PA@TpBpy-MC as a solid electrolyte

The proton conducting ability of the phosphoric acid doped COFs is further verified by utilizing these materials as solid-state electrolytes under H_2/O_2 fuel cell operating conditions (**Figure 4.11**). [15] Initially, the electrodes are prepared by spraying 40 wt. % Pt/C catalyst ink onto the porous carbon paper (35 CC-SGL containing 15% PTFE).Then COF pellet is prepared using *ca*. ~250 mg of powder and 2.5 mm diameter die. The pellet is placed in between the two platinized electrodes [Pt catalyst (Johnson Matthey) + Vulcan carbon support (VX 72) + 20% Nafion binder] using Kapton gasket. The entire assembly is then cold pressed applying 1000 KgN pressure for 2 min. The MEA is then arranged onto the graphite plates using an FRT gasket for single cell assembly (active area = 4 cm^2, procured from Fuel Cell Tech., USA).

The single cell test fixture used for fuel cell polarization study consists of the following components:

Aluminium end plates

Graphite mono polar plates provided with integrated O-ring gasket and serpentine gas flow field

Cathode loading: 1.0 mg/cm^2; N/C: 0.4; electrode thickness: 349 μm

Anode loading: 1.0 mg/cm^2; N/C: 0.4; electrode thickness: 351 μm

Gas flow: 0.5 slpm for anode as well as cathode.

Operating temperature: RT-50 ˚C

Membrane pellet thickness: 850± 5 μm

MEA thickness: 1558 ± 5 μm

Thickness of Gasket used: 630 μm

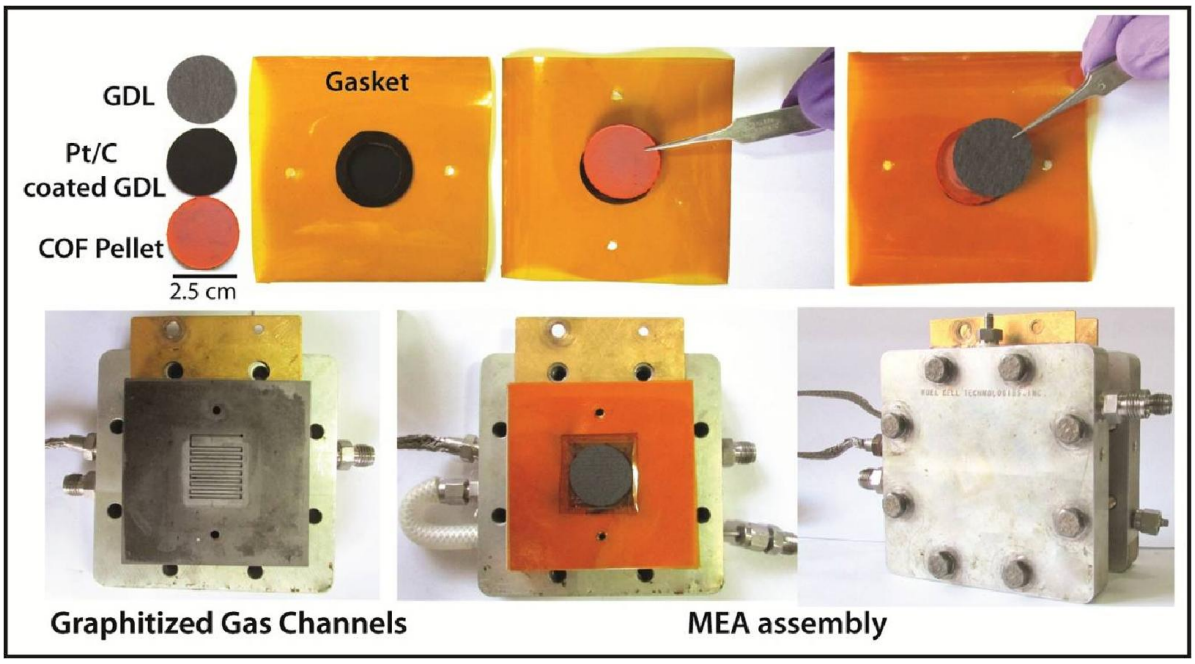

Figure 4.11. *Optical photograph of the fuel cell assembly using the fabricated MEA with pelletized PA@TpBpy COF as the solid electrolyte.*

4.3.3.4. Open Circuit Voltage (OCV) measurement

Initially, the flow rate of the H_2 and O_2 reactant gases is optimized to maximize the OCV build up. It is observed that the OCV initially increases with increase in the flow rate up to a maximum of 80 sccm. A rapid decrease in the OCV results thereafter, possibly due to the

mechanical breakdown of the pellet. Thus, the OCV lifetime test is performed at 50-sccm flow rate for both H_2 and O_2 to maximize the OCV lifetime (**Figure 4.12**).

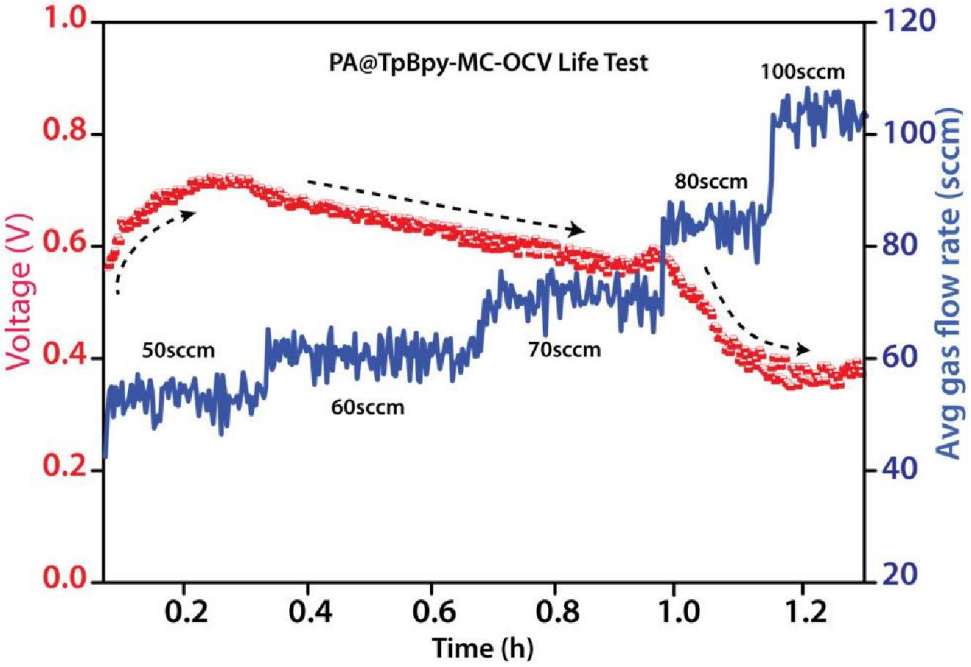

Figure 4.12. *Study of the effect of flow rate on OCV of the* ***PA@TpBpy-ST*** *constituted MEA at 50 °C.*

During the OCV measurement, the cell is fed with pure dry H_2 (99.999%) at the anode and pure dry O_2 (99.9%) at the cathode. In case of solvothermally synthesized COF derived pellet, the cell is found to show a starting OCV of 0.66 V at 30 °C. On increasing the temperature to 50 ˚C, the OCV increased slightly to 0.68 V, before decreasing rapidly thereby forcing the operation shut down (**Figure 4.13**). On the other hand, in case of the mechanochemically derived COF, the cell is found to show a starting OCV of 0.86 ± 0.02 V at 30 ˚C (**Figure 4.13**). On further increasing the temperature, OCV shoots up to 0.92 ± 0.02 V at 50 ˚C and remained constant thereafter.

The OCV is observed to remain stable for the next 2.5 h, which confirms the denser nature of the mechanochemically synthesized COF pellet.

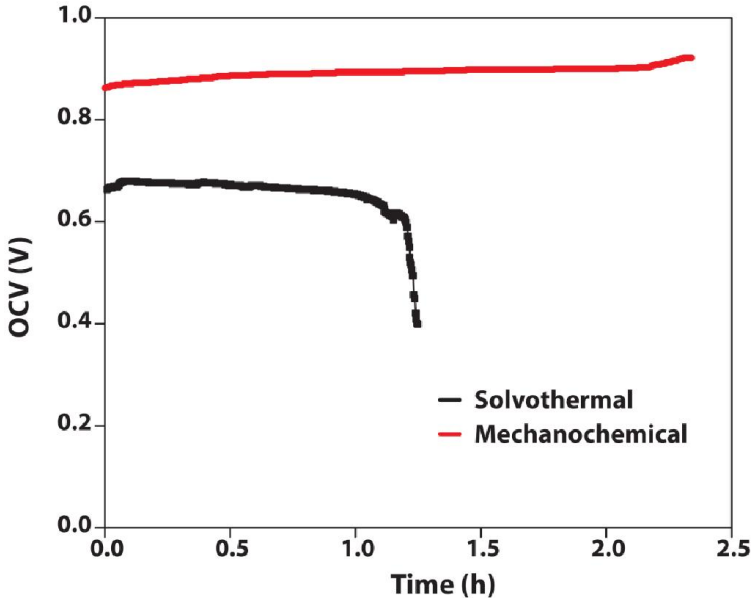

Figure 4.13. *Lifetime measurement of OCV obtained using the fabricated MEA.*

4.3.3.5. H_2 crossover study

The hydrogen gas crossing over from the anode to cathode, because of the fuel leak, has been estimated by analyzing the *in situ* Linear Sweep Voltammogram (LSV) profile of the PA@TpBpy-ST constituting single cell (**Figure 4.14**).

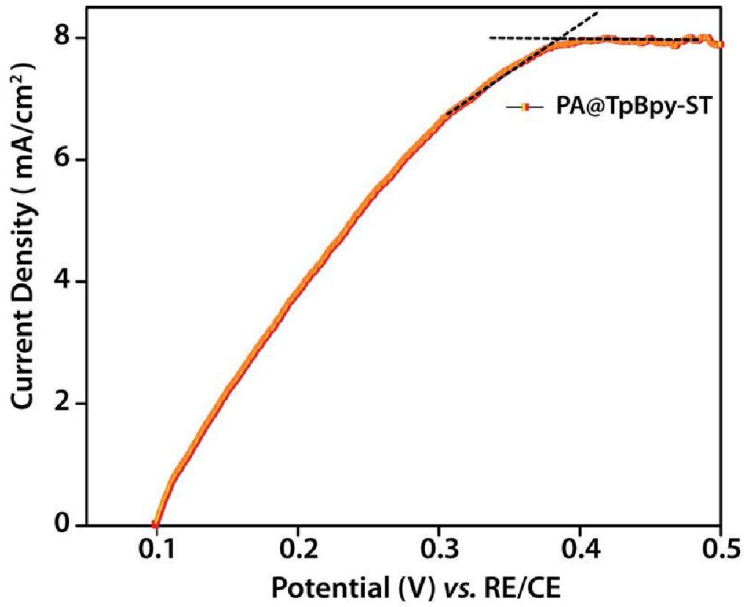

Figure 4.14*. LSV profile for the hydrogen crossover in the PA@TpBpy-ST constituted PEMFC after 1.2 h of OCV life test measurement.*

In the study, the cathode potential is scanned linearly from its OCV (found to be 0.10 V) at 2 mV/s scan rate of until 0.5 V. This scan enables instant oxidization of the H_2 molecules that could have probably diffused from the anode under the limited mass transfer conditions. At 50 ^oC, the cell is found to exhibit a mass transfer limited current density (J_{lim}) of 8 mA/cm^2. This limiting current is proportional to the rate of H_2 crossover from the anode to cathode as given by the relation,

$$\mathbf{J_{x\text{-}over,\ H2} = J_{lim} / nF}$$

where, n = 2 for the H_2 oxidation reaction and F is the Faraday's constant (96485 C/electron-mole).

Using this relation, the H_2 crossover flux at the cathode is calculated to be 4.1 X 10^{-8} mol cm^{-2} s^{-1} at 50 ºC. This value is found to be nearly one order higher than that reported for the pristine MEAs derived from Nafion as the proton conducting membrane (normally, in the order of 10^{-9} mol cm^{-2} s^{-1}).

4.3.3.6. *In situ* Impedance study

The *in situ* impedance measurements are carried out *via* two-electrode configuration in the frequency range of 1 MHz – 100 Hz and 10 mV input voltage amplitude, using O_2 passing cathode as the working electrode and H_2 passing anode as the counter and reference electrodes. The results are studied using Nyquist plots obtained at each temperature (from 30-50 ˚C).

The plots are fitted using a PEMFC fuel cell equivalent circuit and the electrolyte resistance is calculated by determining the intercept made on the real axis at the high frequency regime in the complex impedance plane (**Figure 4.15**). On measuring, the Nyquist plot reveals a high frequency resistance corresponding to a solid-state electrolyte conductivity of 1.4×10^{-2} S cm^{-1} along with a distinctive catalyst charge-transfer resistance (R_2) at the low frequency region (**Figure 4.15**). With further increase in temperature, the R_2 is found to decrease, due to the possible thermal activation of the catalyst. However, the solid-state electrolyte resistance is found to remain largely unaffected by the rise in the cell temperature.

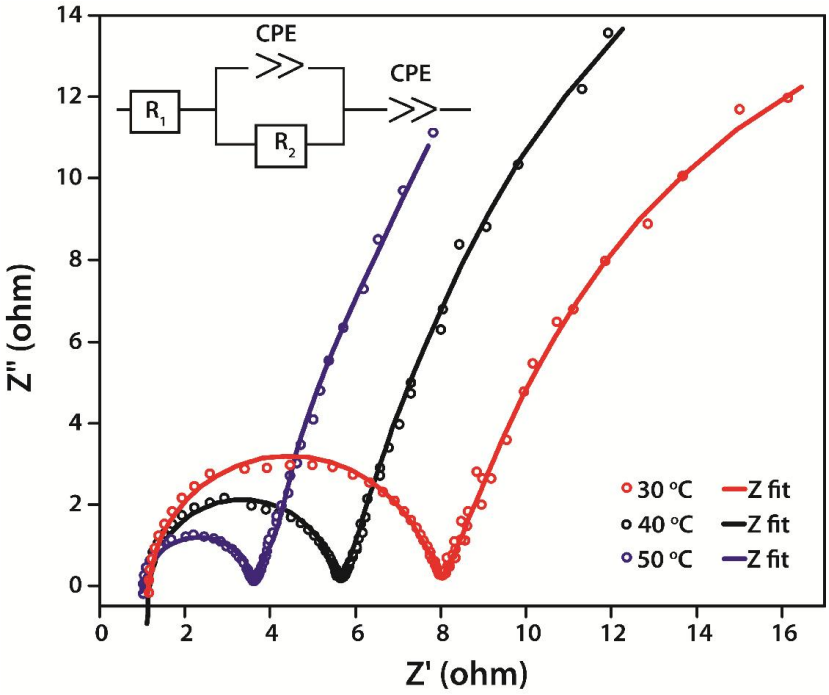

Figure 4.15*. Nyquist plots obtained at different temperatures (in ˚C) with the equivalent circuit used for fitting (inset).*

4.3.3.7. Single-cell polarization study

Using PA@TpBpy-MC as the solid electrolyte, the PEMFC fuel cell reaction is driven by carrying out the single cell polarization study. It is noteworthy that as the OCV lifetime test of the MEA fabricated pellet indicated the effective reactants gas separation only till 50 ^{o}C, the temperature in the present operation has been limited to 50 ^{o}C. Prior to the polarization, the H_2 and O_2 flow rates have been increased to prevent the MEA from fuel starving under this stress. This fortuitously incites increase in the OCV from 0.90 to 0.92 V. Once achievement of a steady OCV, the MEA polarization is initiated. The single cell is observed to provide a maximum current density of 29 mA cm^{-2} and a maximum power density of 7 mW cm^{-2}. This study ascertains the fuel cell circuit completion besides validating the proton conducting ability of the phosphoric acid loaded COF (**Figure 4.16**). It is important to note that though the performance of PA@TpBpy-MC pellet is lesser than the conventional Nafion® membrane, the difference could be seen as a consequence of the massive disparity in the thickness of the electrolyte used in both the cases (50 μm in Nafion *vs.* 900 μm in COFs).

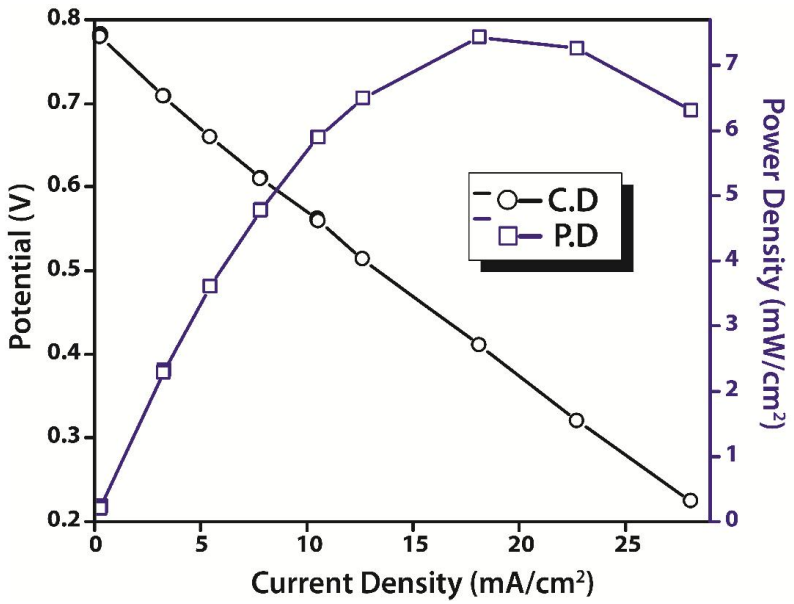

Figure 4.16. *Fuel cell polarization plot obtained at 50 ˚C using dry H_2, Pt, C/COF pellet/Pt, C, dry O_2 electrochemical cell.*

4.4. Conclusion

In summary, the present chapter introduces covalent organic frameworks (COFs) as proton conducting solid electrolytes for anhydrous PEMFC operation. By integrating proton-conducting functionalities into stable mechanosynthesized COFs, a unique way is hereby demonstrated to enable effective utilization of such less porous COFs as solid electrolytes in PEMFC. In the work, a bipyridine functionalized covalent organic frameworks (TpBpy) is used for loading phosphoric acid molecules. The acid doped COF is found to retain its crystallinity and stability, which makes it a prospective candidate for proton conduction applications. On acid doping, the mechanochemically derived COF backbone is found to outperform its solvothermal counterparts in terms of gas separation efficacy under real fuel cell operating conditions. Interestingly, although the bare COFs are found to exhibit negligible proton conductivity, on phosphoric acid loading, the COFs drastically show the onset of proton conducting activity at anhydrous conditions. This demonstration is thus believed to unravel more avenues to employ such mechanochemically synthesized materials for acute applications such as ion conductors in high temperature fuel cells and batteries.

4.5. References

[1](a) K. Tanaka, Wiley-VCH, Weinheim (2003).(b) S. L. James, C. J. Adams, C. Bolm, D. Braga, P. Collier, T. Friščič, F. Grepioni, K. D. M. Harris, G. Hyett, W. Jones, A. Krebs, J. Mack, L.Maini, A. G. Orpen, I. P. Parkin, W. C. Shearouse, J. W. Steed, D. C. Waddell, *Chem. Soc. Rev.*, **2012**, *41*, 413.

[2](a) L. R. MacGillivray, J. L. Reid, J. A. Ripmeester, *J. Am. Chem. Soc*., **2000**, *122*, 7817.(b) T. Friščić, Chem. Soc. Rev., **2012,** *41*, 3493.

[3](a) M. K. Beyer, H. Clausen-Schaumann, *Chem. Rev*., **2005**, *105*, 2921. (b) R. E. Morris, S. L. James, *Angew. Chem. Int. Ed.*, **2013**, *52*, 2163.

[4](a) T. Friščić, D.G. Reid, I. Halasz, R. S. Stein, R. E. Dinnebier, M. J. Duer, *Angew. Chem. Int. Ed.*, **2010**, *49*, 712. (b) T. Friščić, L. R. MacGillivray, Chem. Commun., **2003**, *11*, 1306. (c) K.Tanaka, F. Toda, *Chem. Rev*. **2000**, *100*, 1025. (d) T. Friščić, I. Halasz, P. J. Beldon,A. M. Belenguer, F. Adams, S. A. J. Kimber, V. Honkimäki ,R. E.Dinnebier, *Nat. Chem*., **2013**, *5*, 66.

[5](a) A. P. Côté, A. I. Benin, N. W. Ockwig, M. O'Keeffe, A. J.Matzger, O. M. Yaghi, *Science*, **2005**, *310*, 1166. (b) X. Feng, X. Ding, D. Jiang, *Chem. Soc. Rev.*, **2012**, *41*, 6010. (c) C. J. Doonan, D. J. Tranchemontagne, T. G.Glover, J. R. Hunt ,O. M. Yaghi, *Nat. Chem.,* **2010**, *2*, 235. (d) Y. Zeng, R. Zou, Z. Luo, H. Zhang, X. Yao, X. Ma, R. Zou ,Y. Zhao, *J. Am. Chem. Soc*., **2015**, *137*, 1020. (e) D. D. Medina, J. M. Rotter, Y. Hu, M. Dogru, V. Werner, F. Auras, J. T. Markiewicz, P. Knochel, T. Bein, *J. Am. Chem. Soc.* **2015**, *137*, 1016.

[6](a) N. Stock, S. Biswas, *Chem. Rev*., **2012**, *112*, 933. (b) M. Eddaoudi, D. F. Sava, J. F. Eubank, K. Adil ,V. Guillerm, *Chem. Soc. Rev*., **2015**, *44*, 228. (c) A. Carné-Sánchez, I.Imaz, M. Cano-Sarabia ,D. Maspoch, *Nat. Chem*., **2013**, *5*, 203.

[7](a)B. Icli, N. Christinat, J. Tönnemann, C. Schüttler, R.Scopelliti, K. Severin, *J. Am. Chem. Soc.*, **2009**, *131*, 3154. (b) A. Orita, L. Jiang, T. Nakano, N. Ma, J. Otera, *Chem. Commun.,* **2002**, 1362. (c) J. Huang, J. A. Moore, J. H. Acquaye, R. B. Kaner, *Macromolecules*, **2005**, 38, 317.

[8] S. Chandra, S. Kandambeth, B. P. Biswal, B.Lukose, S. M. Kunjir, M. Chaudhary, R. Babarao, T. Heine, R. Banerjee, *J. Am. Chem. Soc.*, **2013**, *135*, 17853.

[9](a) B. P. Biswal, S. Chandra, S. Kandambeth, B. Lukose, T.Heine, R. Banerjee, *J. Am. Chem. Soc.*, **2013**, *135*, 5328.

[10]S. Chandra, T. Kundu, S. Kandambeth, R. BabaRao, Y.Marathe, S. M. Kunjir, R. Banerjee, *J. Am. Chem. Soc.,* **2014**, *136*, 6570.

[11]G. Das, D. B. Shinde, S. Kandambeth, B. P. Biswal, R. Banerjee, *Chem. Commun*., **2014**, *50*, 12615.

[12]V. G. Ponomareva, K. A. Kovalenko, A. P. Chupakhin, D. N. Dybtsev, E. S. Shutova, V. P. Fedin, *J. Am. Chem. Soc*., **2012**, *134*, 15640.

[13] N. Agmon, *Chem. Phys. Lett*., **1995,** *244*, 456.

[14](a) J. Zaccaro, M. Bagieu-Beucher, A. Ibanez, R. Masse, *J. Solid State Chem*., **1996**, *124*, 8.(b) J. Oueslati, A. Oueslati, C. Ben Nasr ,F. Lefebvre, *Solid State Sci.,* **2006**, *8*, 1067.

[15]H. B. Aiyappa, S. Saha, P. Wadge, R. Banerjee, S. Kurungot, *Chem. Sci.,* **2015**, *6*, 603.

Chapter 5

Covalent Organic Framework (COF) as catalysts for water splitting half-cell reactions*

The covalent organic frameworks (COFs) have tunable porosity and large specific surface area, in view of which, they can be designed to hold to the veracity of both molecular as well as the heterogeneous catalysts. The first part of the chapter[#] discusses the development of a steady, proficient Oxygen Evolution Reaction (OER) catalyst for water oxidation. In this work, a bipyridine functionalized COF (TpBpy) is used as an electrochemical water oxidation catalyst by assimilating Co (II) ions into its framework. Co-TpBpy shows high OER activity and excellent stability even after 24 h of activity and 1000 OER cycles at neutral pH. This exceptional catalytic constancy of Co-TpBpy comes from the collegial effect of the intrinsic porosity and coordinating bipyridinic units imbibed in the COF skeleton. The second part of the chapter[##] illustrates a route in which COFs can be used as effective photocatalysts for generating hydrogen from water. In the study, CdS nanoparticles are *in situ* grown on a stable COF (TpPa-2) substrate and the resulting photocatalytic activity of the as synthesised composite is investigated. The π conjugated skeleton, high surface area, and abundant two-dimensional hetero interfaces furnished by the COF are believed to stabilize the generated photoelectrons high photocatalytic activity of the composite.

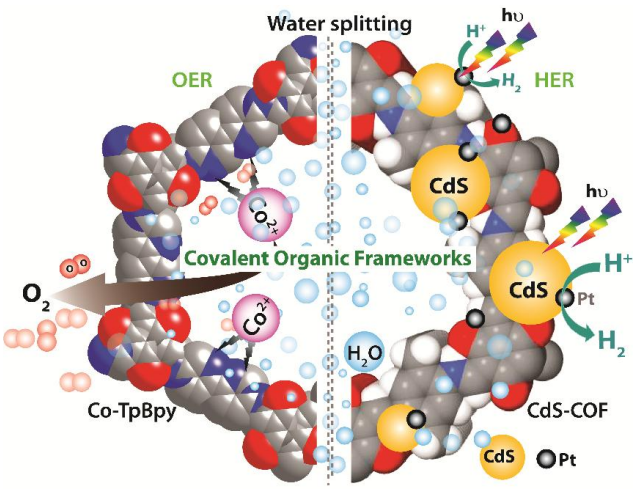

*The content of this chapter has been published in [#]***Chem. Mater.,*** 2016, *28*, 4375 and [##]***Chem Eur. J.,*** 2014, *20*, 15961**.**

Reprinted with permission from the [#]American Chemical Society and [##]Wiley-VCH Verlag GmbH & Co. KGaA, Weinheim.

5.1. Introduction

Covalent Organic Frameworks (COFs) belong to the topical class of crystalline organic polymers having well defined molecular structures involving atomic level assembly of organic structural units through strong covalent bonds.[1] This structure, also termed as 'organic zeolite', is an explicit 'brainchild' of the reticular chemistry. They can be ingeniously constructed in order to precisely control the nature, quantity, and spatial organization of the active sites in the porous framework. The COFs derived *via* modified Schiff base reaction are stabilized by the proton tautomerism and are found to be thermally as well as chemically stable. [2] The liberty to tune the porosity and functionalities in the framework renders them the potential to be employed for various applications *viz*., gas adsorption, and storage, as substrate for organic catalysis, optoelectronics, proton conduction etc. The development of a stable, efficient Oxygen Evolution Reaction (OER) catalyst capable of oxidizing water is one of the premier challenges in the conversion of solar energy to electrical energy, owing to its poor kinetics. [3] An easy way of improving the catalytic ability of COFs is introduction of heteroatom rich, in particular, N-type monomers such as bipyridine containing units, which would improve their interaction with the metal centers, which are considered to form vital active sites in many molecular OER catalysts. [4] Herein, a bipyridine functionalized covalent organic framework (TpBpy) is employed as a heterogeneous OER catalyst by coordinating active Co (II) ions into its porous framework. The high water oxidation activity, catalytic constancy, and strong durability of Co-TpBpy arise from the concerted effect of the inherent porosity and functional bipyridine units in the COF matrix.

The presence of high density of heteroatoms apart from high stability makes COF a suitable support for anchoring the nanoparticles. The second part of the chapter discusses another efficient way of utilizing a highly stable COF, TpPa-2, as a support matrix for the *in situ* deposition of photocatalytic CdS nanoparticles. The CdS-COF hybrid is found to show enhanced absorption of the visible photons in comparison to that of bulk CdS, indicating its superior visible light harvesting ability. The high surface area, in addition to its crystallinity, stability and light absorption ability, is found to increase the photo stability of the hybrid apart from suppressing the recombination of the generated photoelectrons thereby resulting in a remarkably high photocatalytic activity.

Part A

5A. Co (II) modified COF as a robust electrocatalyst for Oxygen Evolution Reaction (OER)

Water electrolysis forms a dependable link connecting the primary renewable energy and stable hydrogen economy. Electrochemical reactions are one of the conceptually easy pathways for implementing effective inter-switching of chemical and electrical energy through bond breaking as well as bond formation. This in particular has been successfully realized in mining power capital like water by means of its splitting into hydrogen (H_2) and oxygen (O_2) and their ultimate revival into water itself, rendering the whole process renewable, green and clean. [5] Although about 97% of the water available in the earth is saline, very few oxygen evolution reaction (OER) catalysts are known to operate in neutral water under ambient conditions. The development of an earth-abundant, stable catalyst operating at neutral conditions at low overpotential thus remains a deep-seated chemical challenge. Amidst the two half-cell reactions, the reductive hydrogen evolution reaction is quicker while the oxidative oxygen evolution reaction is held back by the intricacy brought by its mechanistic complexity. This reaction demands four-electron assisted oxidation of two water molecules coupled with the elimination of four protons to form energy intensive oxygen-oxygen bond.[3,6] As the above process inevitably involves the mediation of many electrons and protons, the transition metal ions with variable valences are successfully tried as Oxygen Evolving Catalysts (OECs). Amongst all, RuO_2 and IrO_2 are listed as the most effective OECs catalyzing water oxidation. [7] However, being expensive and limitedly available, they cannot be commercially employed for larger scale development of OECs. This sets an upsurge research interest to develop inexpensive catalysts that can effectively catalyze water oxidation with minimum overpotential. The water splitting reaction customarily engages two half-cell reactions; a proton reduction reaction, which is favored at low pH, and a water oxidation reaction, which is favored at higher pH. Thus, an ideal integrated water-splitting device should be capable of working in neutral pH medium with the purpose of harmonizing the effects of these opposing reaction conditions.[8] Until now, owing to the sluggish kinetics, very few OER catalysts are reported to catalyze water oxidation at neutral pH conditions. Of late, the earth abundant cobalt containing molecular

OECs particularly their phthalocyanine, porphyrin, salophen, phosphonate complexes are extensively tested for water oxidation activity.[9] A key drawback of molecular WOCs is their eventual solubilization as homogeneous species during the course of the catalytic process. [10] Among the cobalt based OECs, electrodeposited Co-Pi films, Co-Fe Prussian blue polymers etc. have been verified to effect water oxidation in neutral medium.[11] These OECs belong to the group of heterogeneous catalysts and are thereby advantageous compared to their homogeneous counterparts. However, one of the limitations of such catalysts is the imperative necessity to impart structural control inorder to realize their optimal activity. Moreover, as the water oxidation reaction involves liberation of molecular oxygen, continuous catalytic cycles often result in the leaching out of the catalyst.[12] This instates a need to develop highly porous, large specific surface area catalyst substrates to aid easy passage of evolving O_2 molecules and improve their long term stability. The studies on metal containing OECs reveal that the active site is centered on coordination entities, wherein the metal is coordinated to organic molecules often ligated to it *via* heteroatoms like nitrogen. Utilizing the inherent high surface area and tunable electronic structure, the COFs could be designed to combine the advantage of both heterogeneous as well as molecular OECs. [13] In the present work, a cobalt coordinated bipyridine based covalent organic framework (Co-TpBpy) is designed and examined for its performance as an OEC under neutral pH conditions (**Figure 5A.1**).

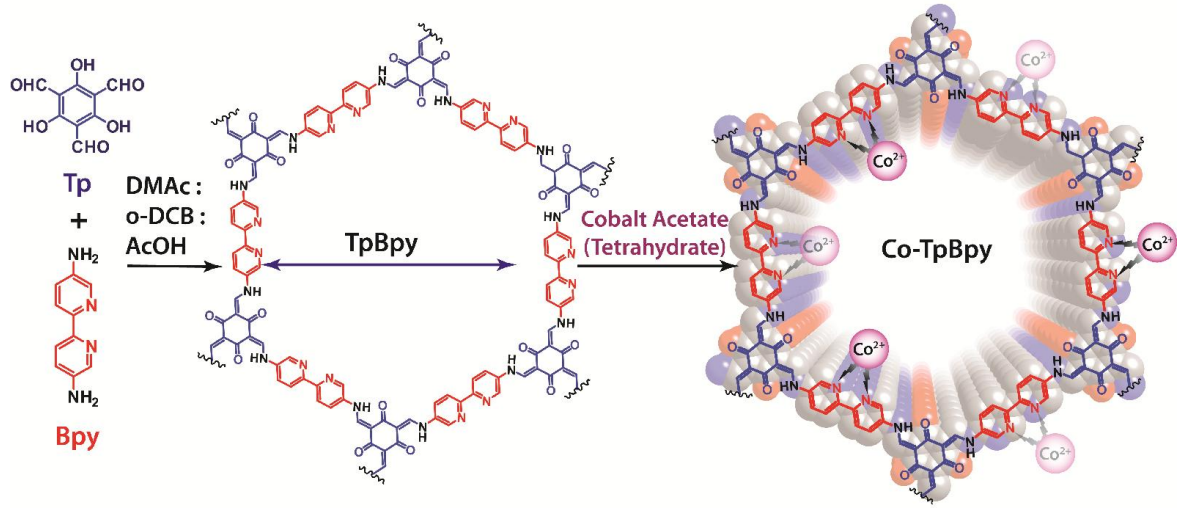

Figure 5A.1. *Schematic representation for the synthesis of TpBpy and Co-TpBpy via Co (II) impregnation.*

5A.1. Experimental Section

5A.1.1. Synthesis of TpBpy

In this work, a previously described reaction protocol is employed to synthesize bipyridine functionalized TpBpy COF.[2b] The synthesis is carried out *via* Schiff-base condensation of 0.06 mmol of 1, 3, 5, triformylphloroglucinol (Tp) and 0.06 mmol of 2,2‘ bipyridyl 5,5‘ diamine in DMAc: DCB (3:1) solvent mixture using 0.5 ml of 6 M acetic acid. The mixture is transferred into using a Teflon lined autoclave. The mixture is homogenized using sonication and then heated at 120 °C for 3 days. Once the reaction time is complete, the as obtained COF is washed using copious amount of 3M acetic acid (to remove any un-reacted amines), water and finally with warm ethanol.

5A.1.2. Co (II) loading into the TpBpy framework

In a typical procedure followed, 50 mg of the TpBpy COF powder is treated with an estimated amount of $Co(OAc)_2.4H_2O$ (varied from 5-30 mg), which is solubilized in 20 ml of dry methanol. The mixture is stirred for about 4 h at RT, and subsequently washed using dry methanol. The as obtained material (termed as Co-TpBpy) is vacuum dried overnight at 60 ˚C. As expected, the amount of cobalt (II) content in the COF matrix is found to increase with the increasing amount of $Co(OAc)_2.4H_2O$ taken. However, the cobalt content coordinating into the COF matrix remains constant when treated with 20 mg and 30 mg of the cobalt salt (as observed from the TGA spectral analysis, Figure XX). This highlights the saturation of the COF coordinating sites with cobalt (II) ions after 20 mg loading of cobalt acetate. The optimized synthetic protocol is further used for synthesizing Co-TpBpy and for the subsequent characterizations and catalytic study.

5A.2. Result and Discussion

5A.2.1. Material Characterization

5A.2.1.1. Electron microscopic study and EDX analysis

The transmission as well as the scanning microscopic image of TpBpy reveals the 103ibrillary nature of the COF. On cobalt impregnation, the 103ibrillary morphology is found to be largely preserved (**Figure 5A.2**). In addition, the TEM images further do not indicate the formation of any metal nanoparticles or oxide residues in the COF framework

(**Figure 5A.2c**). The TEM and SEM images of Co-TpBpy after the OER stability test reveal that the matrix is largely intact. However, a slight increase in the surface roughness is also observed (**Figure 5A.2d**).

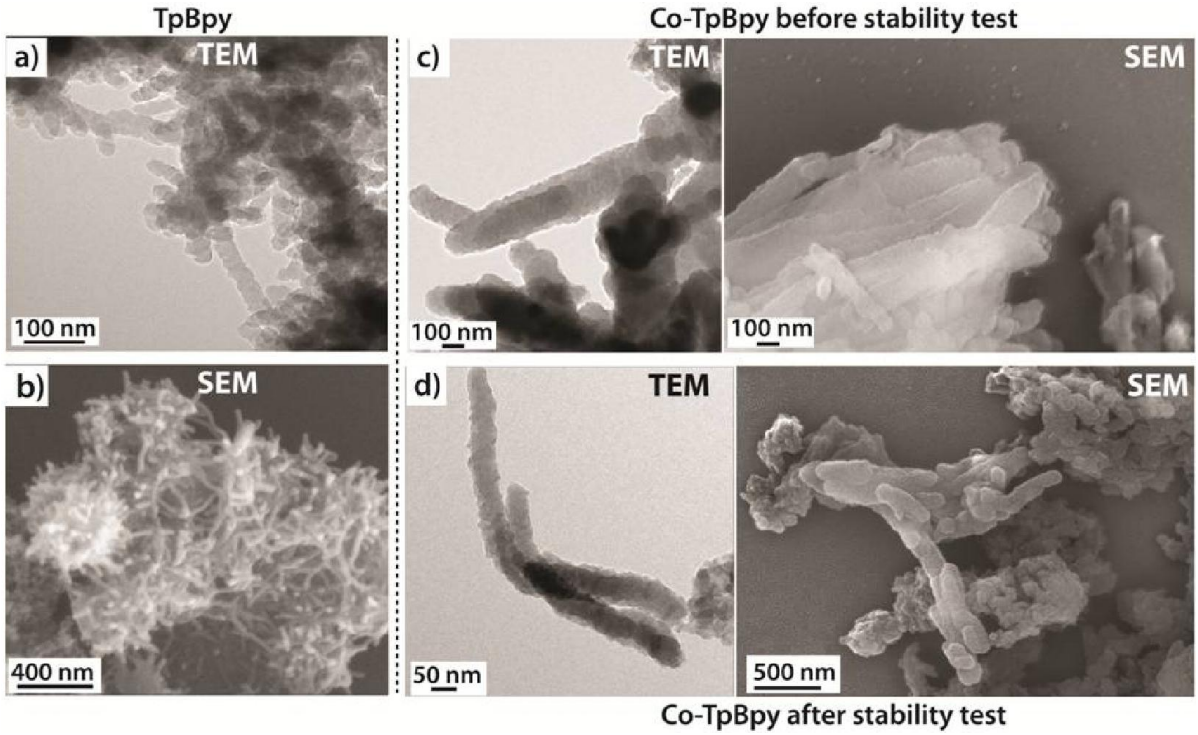

Figure 5A.2. *SEM and TEM images of (a, b) TpBpy and (c, d) Co-TpBpy.*

However, the spot EDX mapping verifies the homogeneous distribution of Co and N content within the Co-TpBpy matrix (**Figure 5A. 3**).

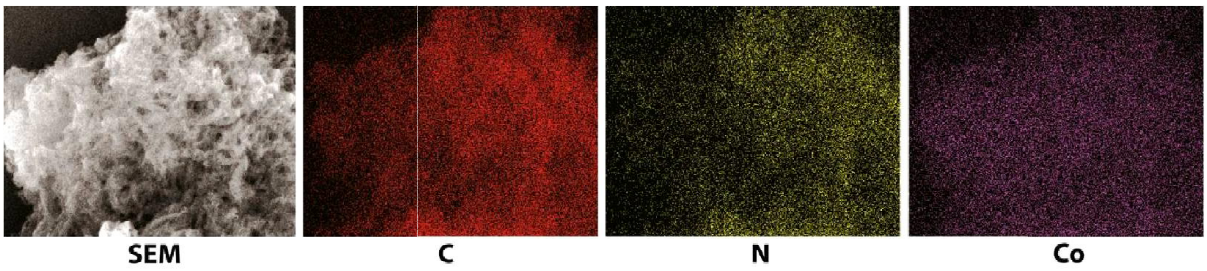

Figure 5A.3. *Elemental mapping of Co-TpBpy showing uniform impregnation of cobalt into the TpBpy matrix.*

5A.2.1.2. PXRD analysis

The PXRD spectrum of Co-TpBby reveals the presence of an intense first peak at 2θ ~3.6°, which corresponds to the 100 plane reflections of TpBpy besides indicating the retention of

the other peaks as found in the pristine COF matrix (**Figure 5A.4a**). The similar PXRD pattern with no extraneous peaks intimates the absence of any undesired moieties in the cobalt-modified TpBpy. It thereby highlights the retention of the robust TpBPy framework after cobalt impregnation. It also rules out the formation of any undesirable moieties (like starting metal precursor salt, metallic Co or cobalt oxide residues) in the cobalt-modified TpBpy framework.

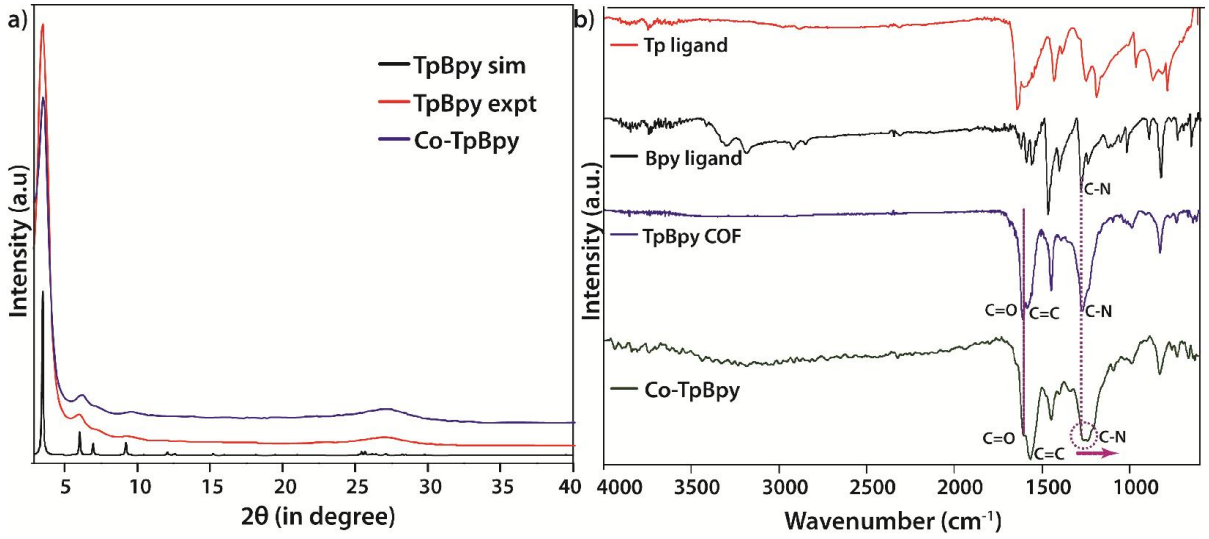

Figure 5A.4. *Comparative (a) PXRD and b) FTIR spectra of TpBpy and the cobalt modified TpBpy (Co-TpBpy).*

5A.2.1.3. FTIR analysis

The FTIR spectrum of TpBpy notably indicates the disappearance of bands corresponding to the ν_{N-H} stretching (3112-3317 cm^{-1}) of the Bpy ligand and $\nu_{C=O}$ stretching (1637 cm^{-1}) of the Tp ligand (**Figure 5A.4b**). Conversely, the spectrum indicates the presence of strong peaks corresponding to the stretching frequency of $\nu_{C=O}$ (1607 cm^{-1}) and $\nu_{C=C}$ (1579 cm^{-1}), thereby verifying the existence of the COF in the stable keto-form. On cobalt modification, the FTIR spectrum of Co-TpBpy indicates a red shift in the $\nu_{C=N}$ stretching frequency (from 1579 to 1563 cm^{-1}). The pronounced broadening in the ν_{C-N} peak indicates the coordination of the cobalt ions to the bipyridinic nitrogen atoms in the COF framework. In addition, after ther cobalt modification, the $\nu_{C=O}$ peak at 1608 cm^{-1} remains unaffected implying that Co(II) ion does not bind to the -C=O bond present in the COF, which also happens to be one of the potential sites for ion coordination (**Figure 5A.4b**).

5A.2.1.4. TGA analysis

The cobalt content in Co-TpBpy is analyzed using TGA under oxidizing conditions (in O_2 atm.). The PXRD pattern of the deposit left behind is found to be largely Co_3O_4 phase (~15.5 %), which accounts to an estimate amount of ~12 % cobalt content (the molar mass of Co_3O_4 being 240.7972 g/mol) (**Figure 5A.5a**). The TGA analysis of Co-TpBpy in air thereby reveals that the framework contains ~12% cobalt content. The loading estimation matches well with the Inductively Coupled Plasma (ICP) analysis result (13% cobalt content).

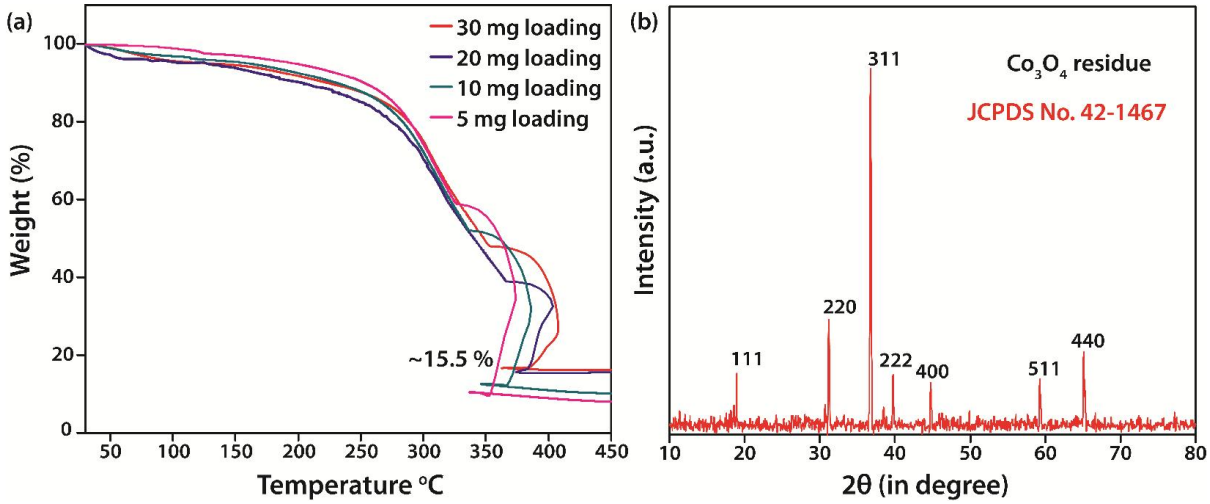

Figure 5A.5. *a) TGA profile of Co-TpBpy in O_2; b) PXRD of the residue left behind.*

5A.2.1.5. ^{13}C NMR spectral study

The ^{13}C NMR of TpBpy is inspected before and after the cobalt impregnation to check the impact of the chemical modification on the support matrix. The ^{13}C CP-MAS solid-state NMR spectra of both TpBpy and Co-TpBpy show carbonyl (C=O) carbon signals at δ 182.8 and 181.5 ppm respectively. The spectrum is found to remain largely unaffected after the chemical treatment, which indicates that the COF framework is undisturbed (**Figure 5A.6a**).

5A.2.1.6. Surface area analysis

The N_2 adsorption isotherm of the as synthesised TpBpy performed at 77 K shows the features of a reversible Type-IV adsorption isotherm. The analysis shows that the pristine COF possesses a very high BET surface area of 1600 m^2/g. The N_2 isotherm analysis after cobalt impregnation estimates that the COF retains a BET surface area of 450 m^2/g after the chemical modification (**Figure 5A.6b**).

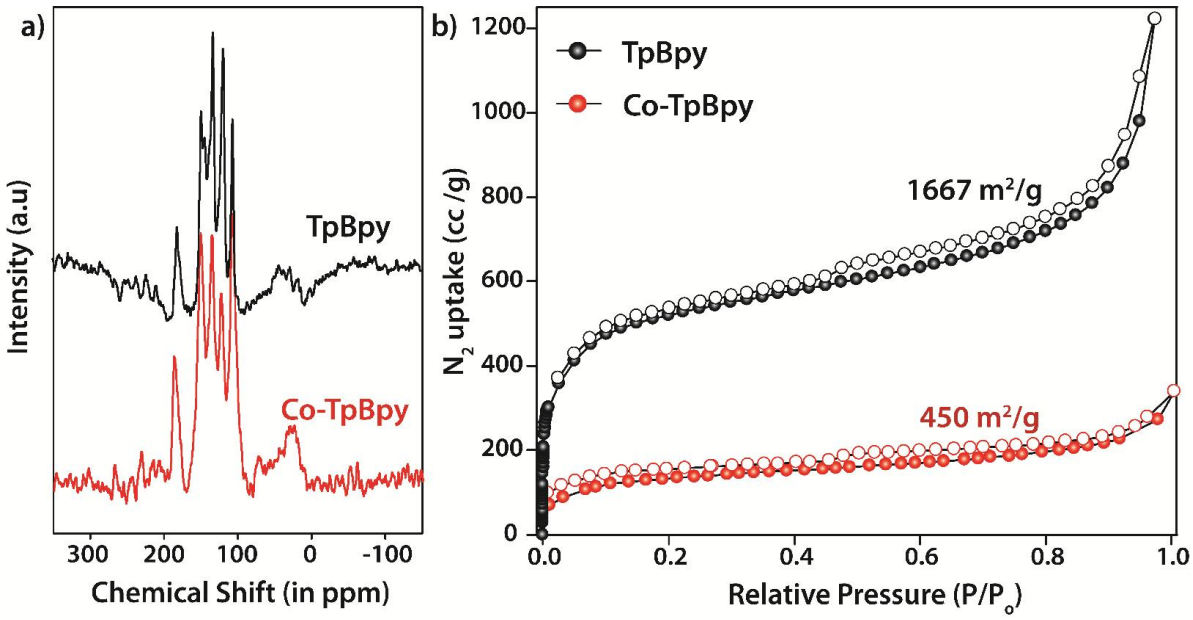

***Figure 5A.6**. Combined a) Solid State ^{13}C NMR spectra and b) N_2 adsorption isotherms of TpBpy before and after cobalt modification.*

5A.2.1.7. XPS spectral analysis

The survey scan XPS profile of pristine TpBpy highlights the presence of N, O and C elements only (**Figure 5A.7a**). The deconvoluted N 1s spectrum of TpBpy indicates the presence of two distinctive peaks, of which, 400.92 eV is associated with the secondary N and 399.82 eV corresponds to the pyridinic N in the TpBpy framework (**Figure 5A.7c,d**). [14] After cobalt coordination, the XPS spectrum of Co-TpBpy shows two broad sets of signals corresponding to core levels of cobalt ions ($2p_{3/2}$ at 781.7 eV and $2p_{1/2}$ at 797.1 eV). [15] The Co 2p spectrum clearly specifies the presence of the shake-up satellite signal verifying the existence of Co (II) ions in the matrix (**Figure 5A.7b**). Further, on cobalt modification, a noticeable shift in the binding energy from 399.82 to 400.04 eV is observed, which is associated with that of the pyridinic N (**Figure 5A.c,d**). However, no shift is observed in the position of the peak corresponding to that of secondary N (400.92 eV), which hints at the complexation of the cobalt ions to the TpBpy framework by means of its bipyridinic entities only. [15b] Besides it, a distinct shift in the Co 2p 3/2 binding energy (781.7 eV) compared to that of pure cobalt acetate (784.3 eV) also confirms the Co-N interaction between Co (II) and N in the TpBpy framework (**Figure 5A.7b**).

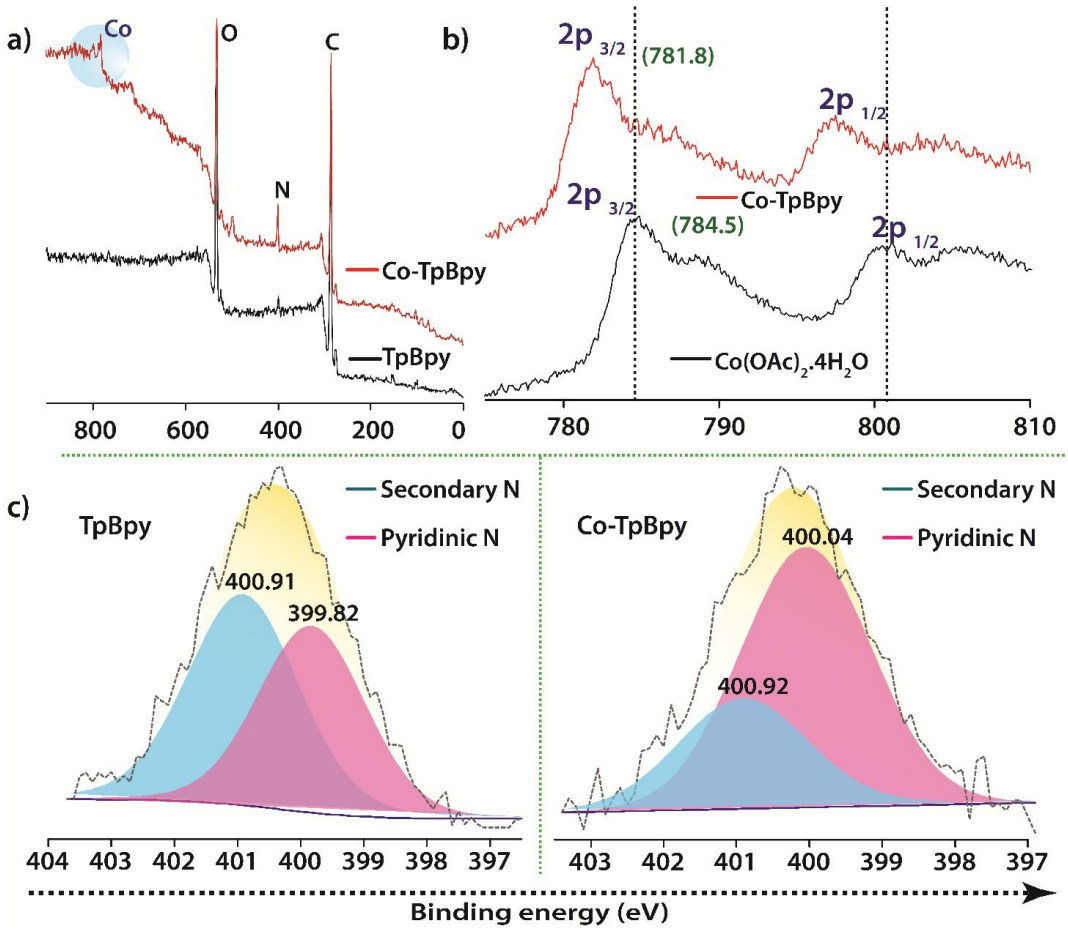

Figure 5A.7. *Comparative Co 2p XPS spectra of TpBpy COF before and after the cobalt modification.*

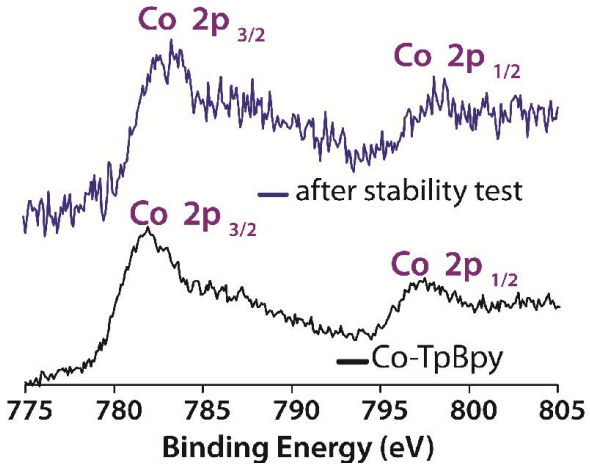

Figure 5A.8. *Co 2p XPS spectra recorded before and after the stability test.*

The Co 2p XPS spectra is also inspected post OER activity. The spectral inspection confirms that the oxidation state of the cobalt remains mostly unchanged after the tests

(**Figure 5A.8**). A slight shift in the Co 2p peak position is observed which is possibly due to the creation of tiny CoO_x realms during the extended water oxidation cycles. However, the broad shoulder in the spectra validates that most of the Co ions are in the Co (II) oxidation state.

5A.2.1.8. UV-Visible spectral analysis

The solid-state UV Visible spectra of TpBpy indicates the presence of peaks at 276 and 323 nm which corresponds to the bipyridinic π-π* and n- π* transitions, whereas the broad band at 520 nm signatures the existence of the delocalised π electron cloud in TpBpy. On complexation with cobalt ions, two intense absorption bands appear at 470 nm and 510 nm (which is found overlapping with the 520 nm TpBpy peak) (**Figure 5A.9b**). These bands correspond to the charge transfer transitions, usually observed in case of the Co (II)-bipyridine complexes. [16]

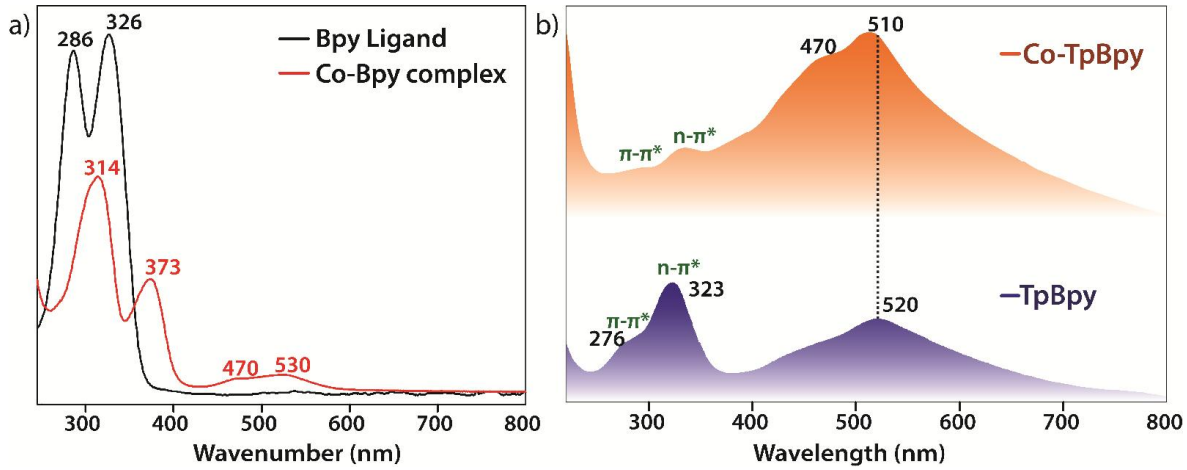

Figure 5A.9. *Comparative UV-Vis spectra of a) Bpy and Co (II)-Bpy complex; b) TpBpy and Co-TpBpy.*

5A.2.1.9. Estimation of the coverage of Co (II) per bipyridine unit

In order to estimate the coverage of Co^{2+} per bipyridine unit, the total percentage of Co^{2+} that can ideally coordinate to the TpBpy backbone is calculated based on the asymmetric unit of TpBpy (as it is difficult to calculate the molecular weight of an extended 2D framework like COF). It is important to note that the asymmetric unit of TpBpy ($C_8H_6N_2O_6$) contains one secondary N and one pyridinic N (blue) (**Figure 5A.10**).

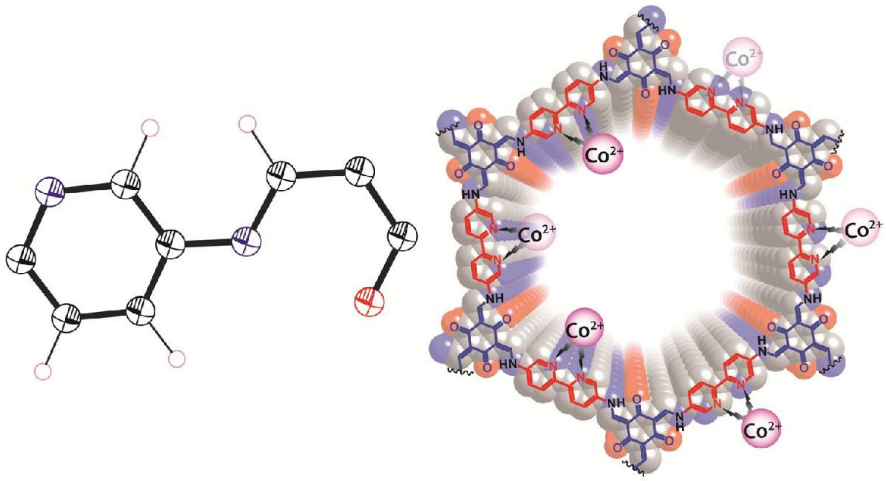

Figure 5A.10. *Asymmetric unit of TpBpy and eclipsed stacking model of TpBpy.*

The following calculations are made based on the information obtained from the FTIR spectra and XPS analysis, which indicate that the Co (II) ions bind only to the bipyridine units of the framework.

- One asymmetric unit of TpBpy contains one pyridine N. It is usually observed that in the presence of a chelating metal ion like Co^{2+}, the bipyridine unit resumes trans configuration resulting in 1:1 coordination with Co^{2+}.
- Likewise, in the present case, ideally one asymmetric unit (containing ½ bipyridine unit) could coordinate to ½ Co^{2+} ion ----------(1)
- The molecular weight of each asymmetric unit amounts to 146.05 g/mol. Therefore, ideally 100 g of TpBpy contains 0.684 moles of asymmetric units.
- Thus, 100 g of TpBpy could ideally coordinate to 0.684 /2 moles of Co^{2+} ions [----from (1)] *i.e.*, 100 g of TpBpy ideally coordinates to 20.15 g of Co^{2+} ions (molecular weight of Co taken as 58.93 g/mol).

Experimentally, the TGA plots as well as the ICP results indicate that TpBpy could uptake a maximum of about 12% Co^{2+} ions. Thus, on an average, it is observed that 60% (12/20) of the bipyridine units in TpBpy is coordinated to the Co^{2+} ions. From the simulated structure, it is observed that out of the six-bipyridine units, three face towards the pore and remaining three face away from it. In spite of several efforts, Co^{2+} coordinated monomer could not be crystallized and thus it is intricate to visualize the coordination of Co-bpy units within the COF. However, we believe that the coordination of Co $(OAc)_2$ to the

bipyridine unit supposedly instigates steric hindrance within the COF layers, which limits the coverage of Co^{2+} to 60% in the COF.

5A.2.2. Electrochemical characterizations

5A.2.2.1. Preparation of the working electrode

The electrochemical catalytic activity of Co-TpBpy is extensively studied using a three - electrode system with glassy carbon as the working electrode, Ag/AgCl (3M) as the reference electrode and a graphite rod as the counter electrode. Co-TpBpy and acetylene black (9 mg: 1 mg) are dispersed in isopropanol:water (3:2) to prepare the catalytic ink mixture. Subsequently, 10 µl of this mixture is coated onto the freshly polished glassy carbon electrode surface (geometrical area=0.196 cm^2) following which 5 µl of 0.5% Nafion binder solution is added. The electrode is dried at 60 ^oC for ~1 h. The electrochemical studies are performed at ambient temperature (298 K) using 0.1 M phosphate buffer solution (pH 7) and the electrode potentials are converted to the RHE scale using the relation E(RHE) = E(Ag/AgCl) + E^o (Ag/AgCl + 0.0591 ×7 (pH correction factor).

5A.2.2.2. Cyclic voltammetry (CV) analysis

The electrochemical analysis of Co-TpBpy is performed using Co-TpBpy coated glassy carbon (as working electrode) in 0.1 M aqueous phosphate buffer solution at pH 7.

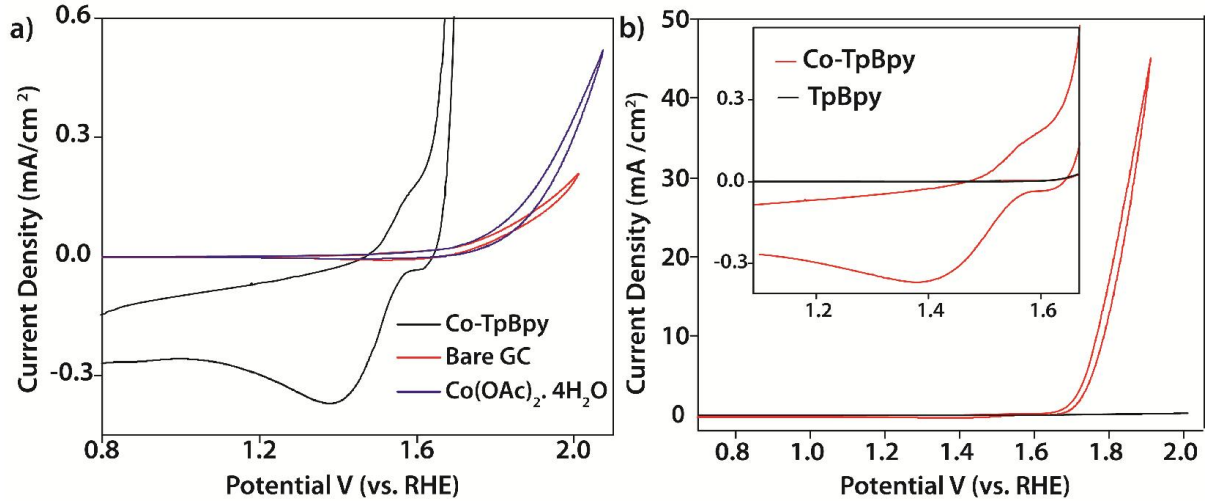

Figure 5A.11. *Comparative CV profiles of Co-TpBPy, bare glassy carbon electrode and $Co(OAc)_2.4H_2O$ salt solution in 0.1 M phosphate buffer solution.*

The cyclic voltammogram of Co-TpBpy clearly indicates the onset of an intense water oxidation activity at *ca*. 1.63 V (*vs*. RHE). The comparative CV profiles also show a marked difference in the OER activity of the cobalt modified TpBpy in comparison to that of the pristine unmodified TpBpy and bare glassy carbon electrode (**Figure 5A.11**). The CV profile of Co-TpBpy also indicates a characteristic redox couple at a peak potential of *ca*. 1.57 V *vs*. RHE, which verifies the involvement of the quasi-reversible $Co^{2+}/^{3+}$ couple in the water oxidizing activity.

5A.2.2.3. Linear Sweep Voltammetry (LSV) and Tafel slope study

The rotating disk electrode (RDE) measurement is carried out in order to understand the OER kinetics and stability of the catalyst. During the RDE experiment, the Co-TpBpy coated GC electrode is kept under a constant rotation rate of 1600 rpm. This ensures the preservation of a uniform ion concentration around the working electrode besides concurrently preventing the buildup of the evolving O_2 bubbles, the product of water oxidation activity. From the LSV analysis, it is observed that a minimum overpotential of 400 mV is needed to produce a current density of 1 mA/cm^2 (**Figure 5A.12a**). The catalytic performance of Co-TpBpy is found comparable with the other well-accepted Co-based OER catalysts. The LSV stability test from 0.6 to 1.8 V (vs. RHE) further denotes the remarkable cyclic stability of Co-TpBpy, wherein ~94 % of the OER current is observed to be retention after 1000 scans (**Figure 5A.12a**).

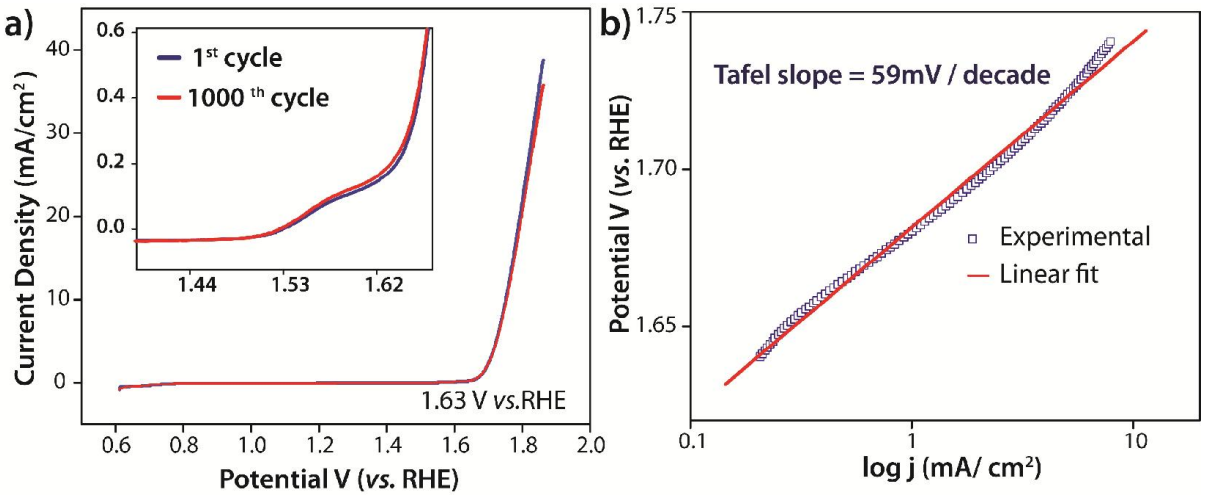

Figure 5A.12. *(a) LSV stability test profile of Co-TpBpy before and after 1000 cycles (inset: zoomed in LSV profile and (b) Tafel plot of Co-TpBpy at neutral pH.*

The Tafel slope is then determined to relate the OER kinetic current with the reaction overpotential. The plot is found to be linear with a corresponding slope of 59 mV/ decade (**Figure 5A.12b**). This indicates the possibility of reversible one-electron transfer mechanism being followed for oxidizing water in the present case. [17]

5A.2.2.4. Chronoamperometry study

The chronoamperometry measurement is also carried out to determine the long term operational stability of Co-TpBpy catalyst. On applying a constant potential of 1.74 V *vs.* RHE, a nearly constant anodic current of 15 ± 3 mA/cm^2 is obtained up to 24 h (**Figure 5A.13**). In the study, an initial increase in the OER current is observed, which indicates the stage of catalyst activation. It is important to note that during the OER activity, the working electrode surface is constantly covered with the non-conducting gas bubbles. This apparently blocks the active sites, eventually decreasing the current density, as observed in case of other gas evolution reactions. However, the high specific surface area of Co-TpBpy minimizes this detrimental effect, and at the end of 24 h of operation, just ~10% decrease in the current density is observed, which thereby explicates the high stability of the material.

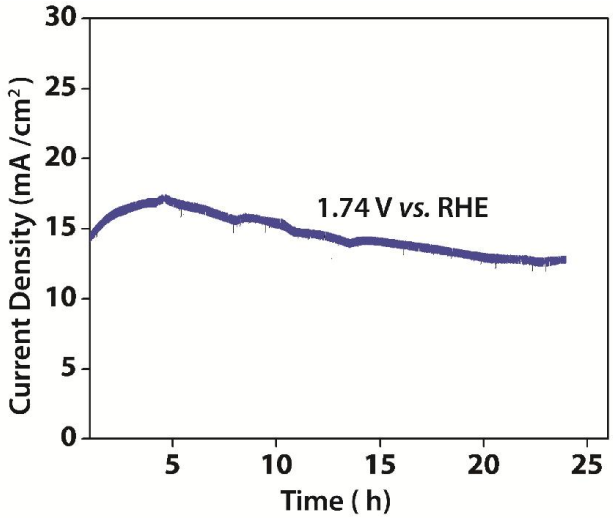

Figure 5A.13. *Chronoamperometric stability profile of Co-TpBpy at 1.74 V (vs. RHE).*

The post Inductive Coupled Plasma (ICP) analysis of electrolyte did not show any detectable cobalt traces, which preclude the possibility of Co (II) leaching from the catalyst during the course of its operation. Equally, the ICP test of Co-TpBpy indicates the retention of 10.5% of Co^{2+} content at the end of 24 h. The consistent water oxidation activity of Co-TpBpy can be mainly accredited to the stability instilled by the porous COF matrix. The high

surface nature helps in the easy passage of the evolving O_2 molecules and resists the catalyst leaching during the course of O_2 evolution.

5A.2.2.5. Estimation of the Electrochemical Assessable Surface Area (EASA) of the Co-TpBpy coated electrode

In each case, a 0.1 V potential window centered at the Open Circuit Voltage (OCV), with non-faradaic response is chosen and the potential is swept across it (positive to negative direction scan) at different scan rates. The double layer capacitance is then calculated by estimating the slope of the straight line part of the capacitive current *vs.* scan rate in each case, *i.e.*, bare GC and Co-TpBpy coated GC.[18] The double layer capacitance of the bare carbon electrode is calculated to be $C_a = 4.63\times10^{-6}$ F/cm^2 and that of Co-TpBpy coated GC was $C_b = 1.286\times10^{-5}$ F/cm^2. In order to determine the EASA of the Co-TpBpy coated GC, the $EASA_a$ of bare GC is first determined by running a CV with 1 mM solution of potassium ferricyanide $K_3[Fe(CN)_6]$ in 0.1 M pH 7 phosphate buffer solution (**Figure 5A.14**).

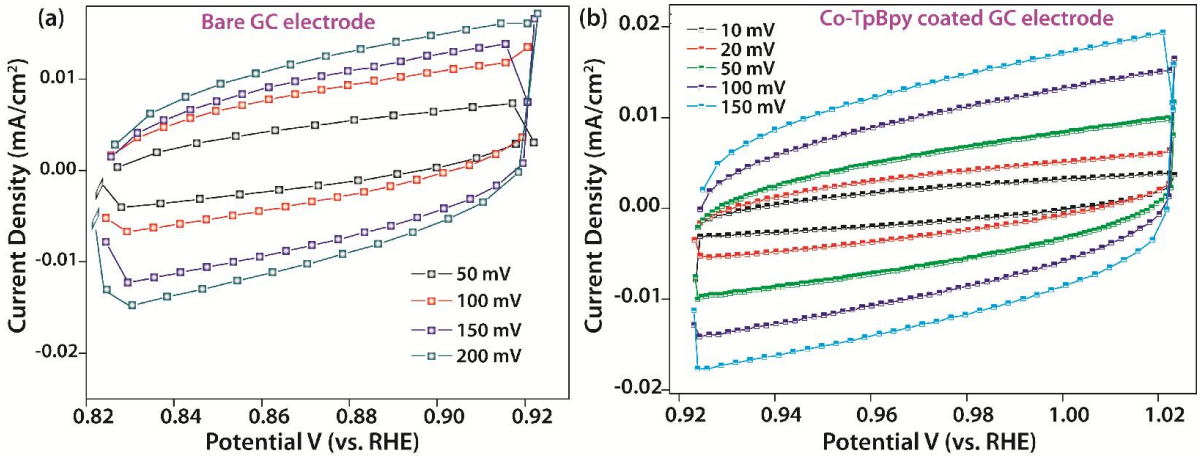

Figure 5A.14. *Cyclic voltammetry of (a) bare Glassy Carbon (GC) and (b) Co-TpBpy at different scan rates in the non-faradaic potential region.*

The slope of the i_p *vs.* (scan rate) $^{1/2}$ is used to determine the diffusion coefficient (D) (**Figure 5A.15**). The $EASA_b$ is further calculated using the Randles-Sevick equation: $i_p = 0.4463\ nFAC\ (nFvD/RT)^{1/2}$, where i_p = maximum current (in A); n = number of electrons transferred in the redox event; F =Faraday Constant in C/mol; D = diffusion coefficient in cm^2/s; C = concentration in mol/cm^3; ν = scan rate in V/s; R = gas constant in VC K^{-1} mol^{-1}; T = temperature in K.

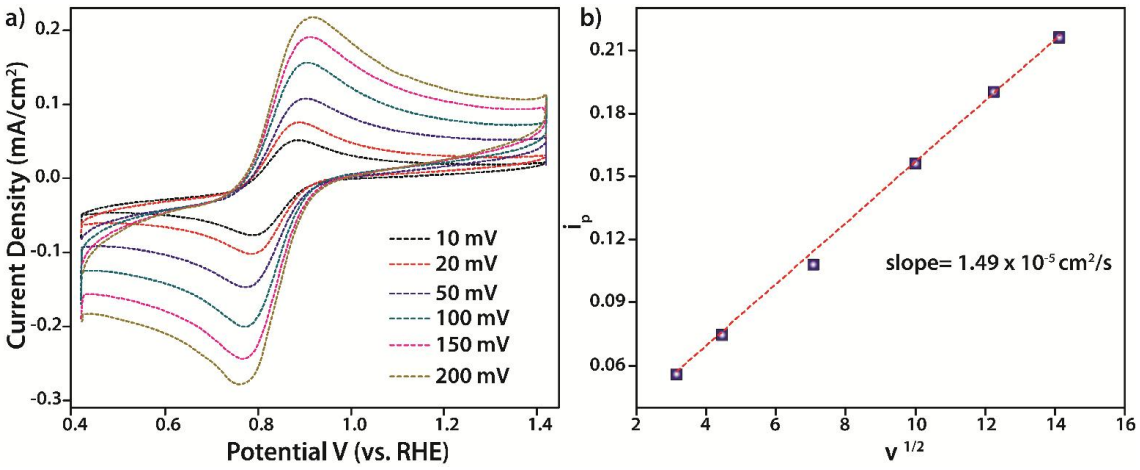

Figure 5A.15. *a) CV profiles of $Fe^{2+}/^{3+}$ couple at various scan rates in the phosphate buffer; b) plot of i_p vs. scan rate 0.1 M phosphate buffer solution.*

As capacitance, C = EASA × ($\varepsilon_r \times \varepsilon_0$ /d); wherein, ε_r is the dielectric constant of the electrolyte, ε_0 is the vacuum dielectric constant and d is the charge separation distance (double layer effective thickness). The $EASA_b$ is therefore calculated using the now known C_a, C_b and $EASA_a$ (0.1015 cm^2) values and is calculated to be 0.282 cm^2.

5A.2.2.6. Calculation of the Roughness Factor (R_f)

The roughness factor of Co-TpBpy catalyst is determined using the electrochemically accessible surface area ($EASA_b$) of Co-TpBpy. From the relation $EASA_b$ = Roughness factor × geometrical area (0.196 cm^2), the R_f is estimated to be 1.44. The $EASA_b$ is also similarly calculated at the end of 1000 stability cycle test (**Figure 5A.16**).

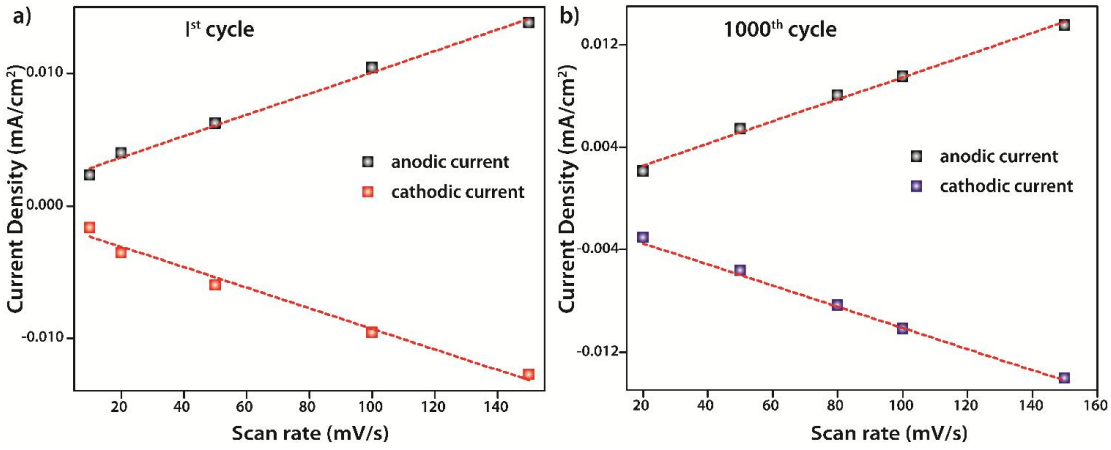

Figure 5A.16. *Plots of current density vs. scan rate of (a) 1st cycle and (b) 1000th cycle in 0.1 M phosphate buffer solution.*

The $EASA_b$ is found to be consistent even after the LSV cycling (0.286 cm^2). The roughness factor after the test is calculated as 1.46. The slight increase in the R_f value could be a result of the pore activation during the course of the O_2 evolution. However, the retention of the R_f value (1.46) after 1000 LSV cycles evidences the pronounced catalytic stability of the material.

5A.2.2.7. Calculation of Surface Coverage (τ_o) and number of active cobalt atoms/m^2 in Co-TpBpy

The active Co atoms/cm^2 on the Co-TpBpy coated GC surface is calculated by measuring the surface coverage (τ_o). The $Co^{2+}/^{3+}$ redox current (i) corresponding to different scan rates is measured **(Figure 5A.17)**. The surface coverage is eventually determined from the slope of the anodic peak current (i_p) *vs.* scan rate using the following equation: slope = $n^2F^2A\tau_o/4RT$, wherein, n is the number of electrons involved, F is the Faraday Constant in C/mol, A is the geometrical surface area (0.196 cm^2), τ_o is the surface coverage, R is the gas constant in VC K^{-1} mol^{-1} and T is the temperature in K.

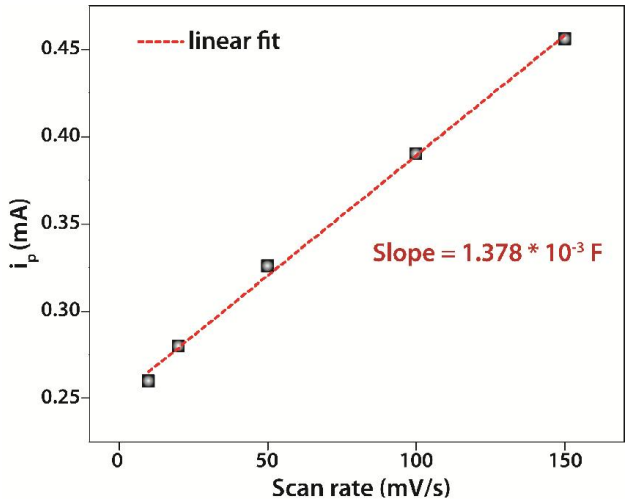

Figure 5A.17. *Plot of i_p versus scan rate.*

The surface coverage of the cobalt atoms is calculated to be 4.506×10^{15} cobalt atoms/cm^2, *i.e.*, 7.482 nmol/cm^2.

5A.2.2.8. Turn Over Frequency (TOF) calculation

The Turn Over Frequency (TOF) is calculated using the relation, TOF = [Current Density (1mA/cm^2) × Avogadro Constant]/[4 F× Roughness Factor × surface cobalt atoms/cm^2]. The TOF is found to be 0.23/s. It is important to note that the TOF value here is the lower limit of

the catalyst as it is calculated based on the number of surface-active Co atoms supposedly involved in the water oxidation reaction.

5A.2.2.9. Calculation of Faradaic Efficiency (ε) using Rotating Ring Disk Electrode (RRDE)study

The faradaic efficiency (ε) of Co-TpBpy for water oxidation reaction is measured by applying a current step from 1 to 15 mA/cm^2 to the Co-TpBpy coated GC disk electrode and then measuring the corresponding voltage. [19] The RRDE working electrode is kept at constant rotation of 1600 rotation per minute (rpm) throughout the study. The ring potential is set at a constant potential of 1.2 V *vs.* RHE throughout the study (**Figure 5A.18**). The collection efficiency (N) of the RRDE electrode is calculated using the ferrocene redox couple and is determined to be 0.37 in the present case.

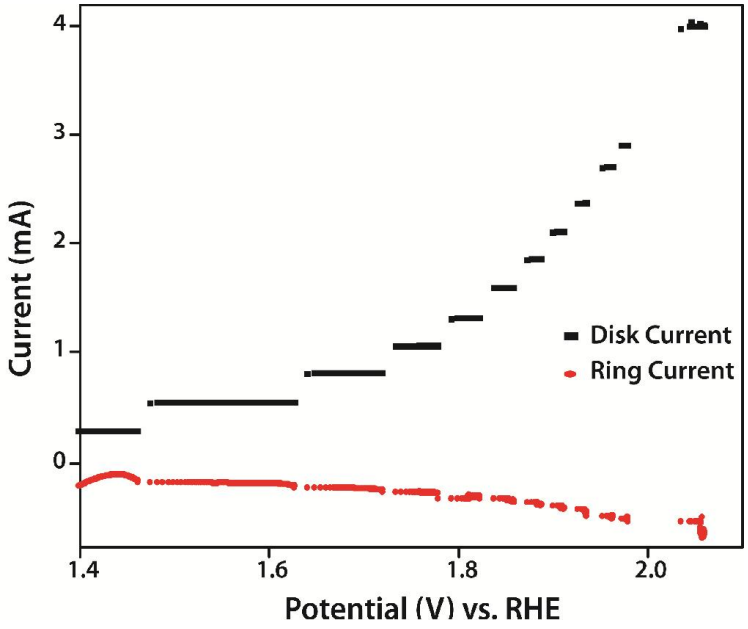

Figure 5A.18. *Rotating-ring disk electrode (RRDE) study for OER of Co-TpBpy, recorded in nitrogen saturated 0.1 M phosphate buffer solution at 1600 rpm.*

The Faradaic efficiency is then calculated using the equation, Faradaic efficiency (ε) = $2*I_r/I_d*N$ where, I_r is the ring current, I_d is 2.7 mA, which is the constant disk current for a 0.2646 cm^2 disk electrode to give a minimum current density of 10 mA/cm^2 and N is the collection efficiency (0.37).

The RRDE study indicates that the faradaic efficiency (ε) of Co-TpBpy is 0.95, which demonstrates the significance of Co-TpBpy as an efficient water oxidation catalyst.

5A.2.3. Gas chromatography studies

The quantification of the O_2 evolved during water oxidation reaction is carried out using three electrode system using glassy carbon (geometrical area= 0.07 cm^2) coated with Co-TpBpy (mixed with acetylene black, 9:1) as the working electrode, graphite rod as the counter electrode and Ag/AgCl (3M) as the reference electrode. A catalyst loading of 50 $\mu g/cm^2$ is maintained and the electrolyte used is 0.1 M phosphate buffer solution. The headspace of the electrolysis cell is purged with nitrogen gas (99.99%) prior to electrolysis. The water oxidation is carried out by applying a constant current density of 1 mA cm^{-2} for a period of 60 min. A portion of the gas mixture from the headspace of the electrochemical cell is directly injected into the Agilent 7890 B GC system (equipped with TCD). The increase in the peak area corresponding to the oxygen gas clearly indicates the O_2 evolution during the electrocatalytic reaction (**Figure 5A.19**).

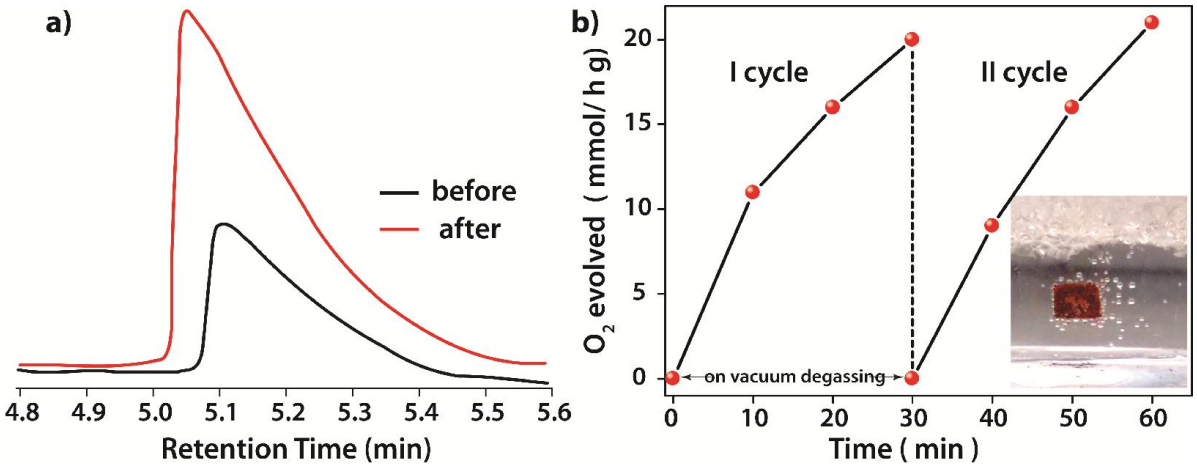

Figure 5A.19. *a) Gas chromatogram before and after the electrolysis and b) GC analysis of the evolved oxygen and evaluation of the cyclic stability.*

In order to further ascertain the catalytic stability, the headspace is evacuated and re-purged with high quality nitrogen gas. About two such consecutive evacuation-purging cycles are carried out to remove O_2 trace in the system. Then constant current density of 1 mA cm^{-2} is applied for a period of 60 min and the amount of O_2 evolved is monitored by sampling out the gas from the reaction vessel headspace after every 10 minutes. The cyclic stability is further confirmed by evacuating the headspace at the end of each OER cycle (**Figure 5A.19b**).

Part B

5B. CdS-COF composite as a visible light photocatalyst for hydrogen production from water

In the present state, fossil fuels and biomass fulfil most of the global energy demands ultimately contributing to the undesired CO_2 emission. This necessitates an immediate need to recognize cleaner and efficient energy substitutes. Water splitting is regarded as one of the most competent ways of conversion of the renewable solar energy into chemical energy in the form of cleaner hydrogen fuel. [5] At a power level of 1000 W/m^2, the solar energy incident on the earth's surface is theoretically sufficient to cover all human energy needs. Using suitable catalysts, this solar energy can be effectively used to split water, yielding fuels of a hydrogen-based economy. In this direction, a large number of H_2 producing photo catalysts are being reported. [20] However, in the current state of art, visible light (which constitutes a dominating *ca.* 46% of the solar spectrum) photocatalysts find poor mentioning. This is due to the limited availability of low band gap materials with inherent capacity to prevent electron-hole recombination in addition to the needed chemical stability. [21] Hence, there is a need for the development of visible light active catalysts with high photo-stability in order to realise a practical and large scale production of hydrogen from the solar energy. An effort in this regard has led to the growth of nanoparticles based photocatalysts which have proven to be prospective candidates for H_2 production, due to their tuneable size and band structure. [22] Among all, CdS systems have shown potential photocatalytic activity for hydrogen production due to their ability to absorb visible photons, except for their photo corrosive nature and quick agglomeration that decrease the conversion efficiency. [23] A smart way of stabilising these nanoparticles is loading them on nanosheets in order to enhance the photocatalytic activity. These sheet structures provide high surface area and abundant hetero-interface which effectively reduce the electron-hole recombination. However, most of such structures suffer from acute limitations like shielding effect in case of graphene, poor visible light absorption and low stability in case of TiO_2 sheets which render them practically less useful and demand precise optimisation of the systems before being put to use.[21] Till date, there exist few reports on use of highly porous materials like MOFs being used as photo sensitizers and substrates for loading of CdS nanoparticles resulting in an appreciable H_2

production. But, these systems cannot be extended to any operating conditions due to the limited stability of the MOFs in these conditions. [24]

In this perspective, covalent organic frameworks (COFs) seem to be an attractive option as substrates for nanoparticles synthesis owing their high stability in acidic and basic pH and high specific surface area.[1,25] Although the COFs are reported to be semiconductors with ability to show absorption in visible light, their potential as photocatalysts in particular for water splitting remains unexplored.[26] The second part of this chapter discusses the advantages of COF as a support for depositing CdS nanoparticles (**Figure 5B.1**). The two-dimensional framework of COF has an array of π clouds which helps in an efficient charge transfer thereby stabilising the nanoparticles and ultimately suppressing the rate of recombination. The synthesised CdS-COF composites show enhanced photocatalytic H_2 evolution. Upon addition of just 1 wt % of COF, a drastic tenfold increase in the H_2 production amounting to 1320 $\mu molh^{-1}g^{-1}$ is observed. The observed activity is 10 times higher than that of the bulk CdS and 55 times improved to that of the plain COF. The significant improvement in H_2 evolution of the composites over that of bulk CdS lies in the goodness of the structural features of COF like stability and π conjugation which imparts semiconductor character to it.

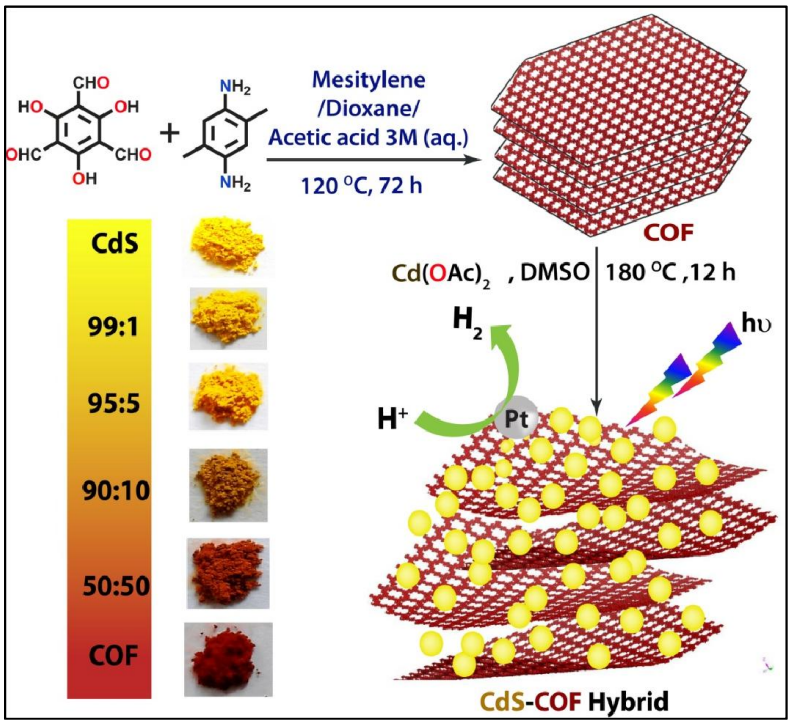

***Figure 5B.1**. Schematic representation of the synthesis of CdS-COF composite.*

5B.1. Experimental Section

5B.1.1. Synthesis of COF (TpPa2): The syntheses of COF is carried out in Schleck tube using Schiff-base reactions of 1,3,5-triformylphloroglucinol (63 mg, 0.3 mmol) with 2,5-dimethyl-p-phenylenediamine (61 mg, 0.45 mmol) respectively, in the presence of 3 M acetic acid (0.5 mL) using 1:1 mesitylene/dioxane (3 mL) solvent mixture. The reaction is performed at 120 ^{o}C for 72 h. The tube is allowed to cool down to RT and the product is recovered and washed with ethanol. The synthesized COF is dried at 60 ^{o}C for 12 h.

5B.1.2. Synthesis of CdS-COF composites: The CdS particle loaded COFs are hydrothermally synthesized, wherein different wt. % of the synthesized COF and 1.6 mmol of Cd $(OAc)_2 .2H_2O$ are dissolved in 160 mL of DMSO solvent. Different weight ratios of COF: CdS ranging from 0 to 50% (referred to COF proportion) are synthesised and named as CdS, CdS-COF (99:1), CdS-COF (95:5), CdS- COF (90:10), and CdS-COF (50:50), respectively. The solution is vigorously stirred and transferred into a Teflon-lined autoclave and heated at 180 ^{o}C for 12 h. The autoclave is then allowed to cool naturally to RT and the hybrid collected is washed with acetone followed by ethanol to remove the residual DMSO. The hybrid is dried at 60 ^{o}C for 12 h.

5B.2. Result and Discussion

5B.2.1. Material Characterization

5B.2.1.1. Electron microscopy analysis

The TEM images of TpPa 2 COF show sheet like structure, formed because of the π–π stacking of the COF layers. In absence of the support material (COF in this case), the CdS particle size is very large (>200 nm) and agglomeration of the particles is prominent (Figure **Figure 5B.2a**). On introduction of COF matrix, uniform distribution of the CdS nanoparticles results along with scaling down in their particle size with observable degree of exfoliation of COF (20–25 nm; **Figure 5B.2a**). The fringes with lattice spacing of 0.35 nm, corresponding to the (111) plane of cubic phase CdS nanoparticles, can be distinctly observed in the high-resolution TEM image of the CdS-COF (90:10) hybrid (**Figure 5B.2a**).

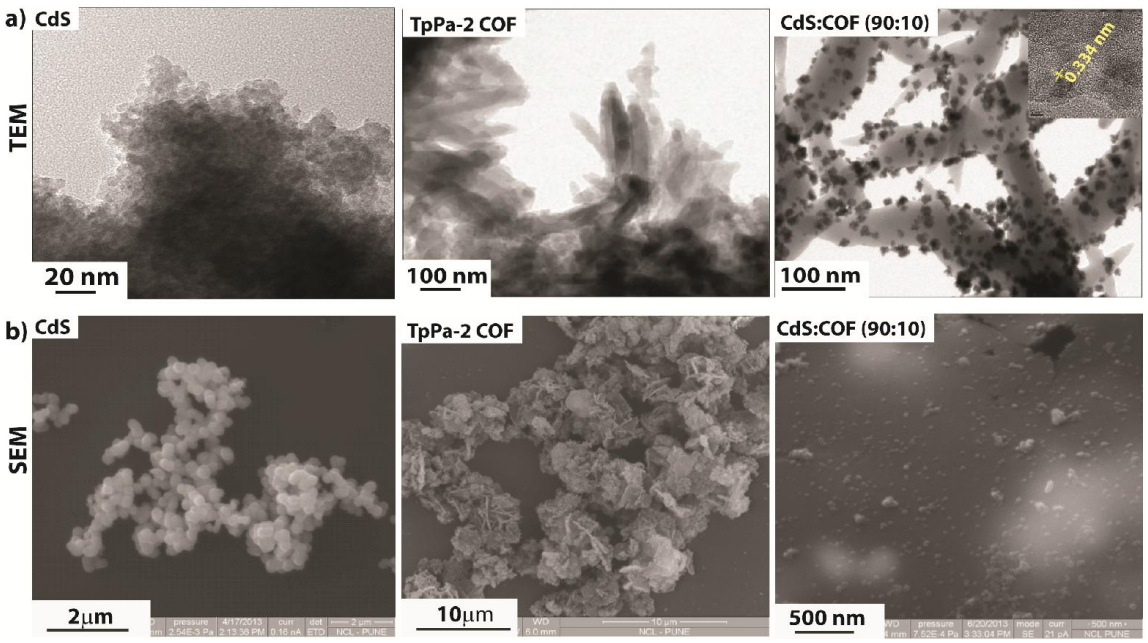

***Figure 5B.2**. a) Combined TEM and b) SEM images of bulk CdS, TpPa-2 COF and CdS-COF (90:10) hybrid.*

The SEM micrograph of COF further confirms the sheet like nature of COF, while the CdS-COF (90:10) hybrid shows well-distributed CdS nanoparticles on the TpPa-2 matrix (**Figure 5B.2b**). The loading of COF in CdS-COF is confirmed using EDX and CHNS analysis (**Table 5B.1**). The amount of C, Cd and S (in %) is found to be comparable with the amount of COF approximately used during the composite synthesis. The EDX analysis is carried at various spots on the hybrid surface to confirm the homogenous concentration of Cd and S content in the hybrid.

***Table 5B.1**. EDX and CHNS analysis results of COF and synthesised composites.*

	C (%)		Cd (%)	S (%)	
	EDX	**CHNS**	**EDX**	**EDX**	**CHNS**
CdS-COF (99:1)	2.7	2.1	75.98	19.69	19.3
CdS-COF (95:5)	6.2	5.4	70.50	19.34	19.8
CdS-COF (90:10)	9.0	7.2	67.42	19.41	19.2
CdS-COF (50:50)	49.9	47.3	29.14	9.20	8.3
COF	74.6	---	---	---	---

5B.2.1.2. PXRD analysis

The PXRD spectra of the synthesised CdS-COF composites predominantly show peaks corresponding to (111), (220), and (311) planes of the CdS nanoparticles. Interestingly, in the spectra, the diffraction peaks corresponding to the COF matrix could not be observed (**Figure 5B.3a**). This is probably due to the relatively lower amount and inherently poor diffraction intensity of COF in CdS-COF hybrid. It is worthy to note that unlike that of bulk CdS particles, the diffraction peaks of the composites are broader and less intense. This is a result of the decreased CdS particle size in the CdS-COF composite, as evident from the electron microscopic studies.

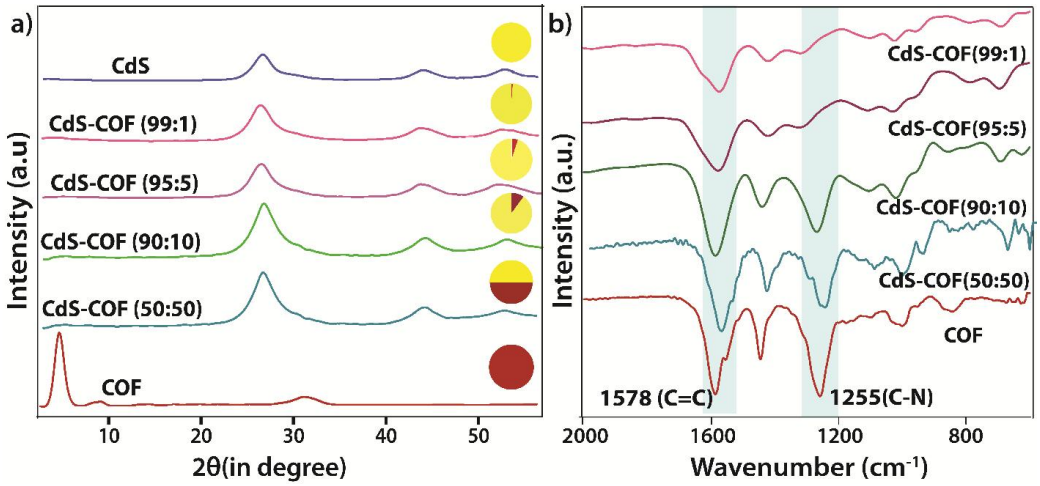

Figure 5B.3. *Combined a) PXRD and b) FTIR spectra of the synthesized composites along with bulk CdS and COF.*

5B.2.1.3. FTIR analysis

In contrast to the PXRD spectra, the comparative FTIR spectra of the composites show predominant resemblance to that of the COF matrix (**Figure 5B.3b**). The peaks corresponding to the characteristic C=C (1578 cm^{-1}) and C−N (1251 cm^{-1}) stretching of COF is observed in all the synthesised CdS-COF composites. Most importantly, the spectra remain the same after the composite formation. This indicates that COF is highly stable after the hydrothermal synthesis and in presence of the CdS particles deposited on its surface.

5B.2.1.4. Surface area analysis

The N_2 adsorption analysis of the bulk CdS indicates that it possesses a BET surface area of 93 m^2 g^{-1} (**Figure 5B.4a**). On synthesizing CdS on COF, the surface area of the hybrids is

found to gradually enhance with the increasing COF content (up to 280 $m^2 g^{-1}$). This behavior could be credited to the input from the COF support, which itself has a BET surface area of 866 $m^2 g^{-1}$ (**Figure 5B.4a**). The high specific surface area of the composites increases the number of catalytic sites besides promoting faster charge transport kinetics.

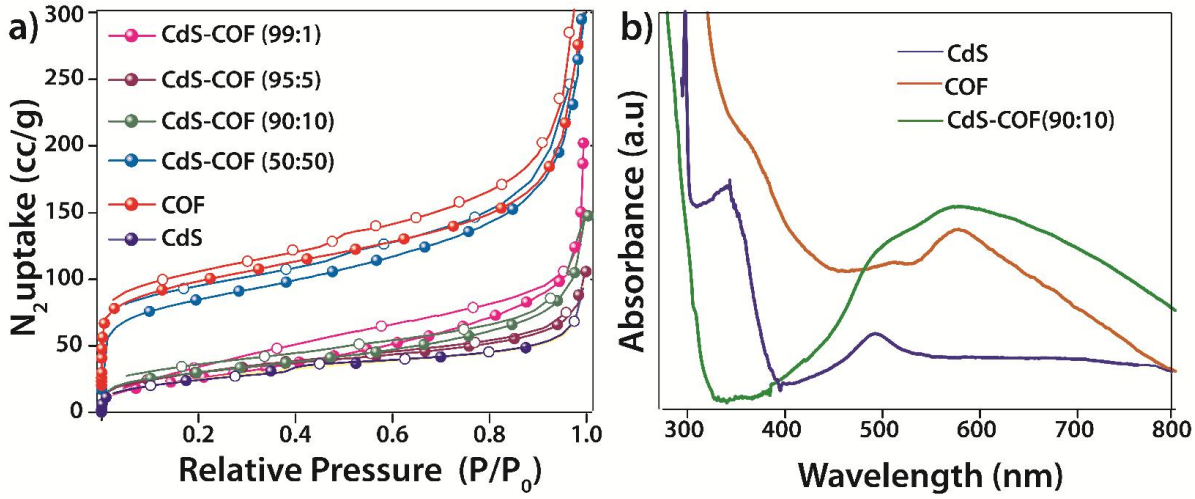

***Figure 5B.4**. Combined a) N_2 adsorption isotherms and b) UV-Visible DRS spectra of bulk CdS, pristine COF, and CdS-COF (90:10) hybrid.*

5B.2.1.5. UV-Visible spectral analysis

The UV/Vis spectrum of TpPa-2 shows a broad absorption band over the visible region (**Figure 5B.4b**), which verifies the superior visible absorption ability of the COF matrix and suggests its variable band nature. It can be observed that on introducing COF, the absorption rim of the CdS:COF (90:10) hybrid largely shifts towards the visible light region (>535 nm) when compared to that of the bulk CdS spectra. This was also evident from the change in the composite color (yellow to reddish brown) with addition of COF (**Figure 5B.4b**). The shift in the absorption spectra thereby confirms the enhanced visible light absorption ability of the synthesised CdS-COF hybrids.

5B.2.1.6. TGA analysis

The thermo gravimetric (TGA) analysis is carried out to determine the thermal stability of the hybrids (**Figure 5B.5**). The TpPa-2 COF is found to be thermally stable up to 350 ˚C, while the bulk CdS shows thermal stability up to 220 ˚C. Interestingly, the thermal strength of the

hybrids is found to increase with the COF content. This indicates the enhanced stability of CdS in the presence of the stable COF matrix.

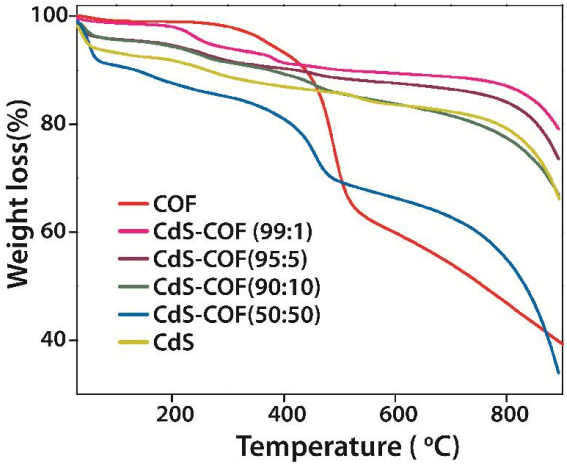

***Figure 5B.5**. Combined TGA profiles of bulk CdS, pristine COF and CdS-COF hybrids.*

5B.2.2. Photocatalytic study

5B.2.2.1. Gas chromatography experimental set-up

The glass reactor is initially ensured to be completely clean and 9 mL of deionized water is used each time. The experiments are carried out using 0.5 wt % Pt co-catalyst, lactic acid (sacrificial agent), and a 400 W xenon arc lamp with a UV cut-off filter ($\lambda = \geq 420$ nm) as a visible light source. Each time, a known amount of photocatalyst (30 mg) is used for the study. The reaction solution is continuously stirred to keep the entire mixture homogeneous. The whole assembly is thoroughly evacuated before irradiating the mixture using a Xenon light source. The reaction is carried out for 1 h after which the gas collected in it is analyzed using a GC equipped with molecular sieve 5A column and a TCD detector.

5B.2.2.2. Gas chromatography study

In order to examine the photocatalytic behaviour of the CdS-COF composites, the GC analysis of the evolving gases is carried out. The bare COF is observed to show very poor photocatalytic activity resulting in just 28 mmol h^{-1} g^{-1} of H_2 production. The poor activity of the bare COF could be attributed to its band gap (2.52 eV), which is adequately large to split water during band gap excitation, but small enough to wrap the entire visible-light spectrum. This makes them poor visible photon absorbers. In addition, the stacked nature of the COF further restricts the number of sheets being illuminated, which eventually decreases the

photocatalytic activity. On visible-light illumination, the bulk CdS shows moderate photocatalytic activity amounting to 128 mmol h^{-1} g^{-1} of hydrogen production (**Figure 5B.6a**). Surprisingly, on introducing mere 1 wt. % of COF, a striking increase in the photocatalytic activity amounting to 1320 mmol h^{-1} g^{-1} of hydrogen production is observed. This performance is notably ten times that of the bulk CdS (**Figure 5B.6b**).

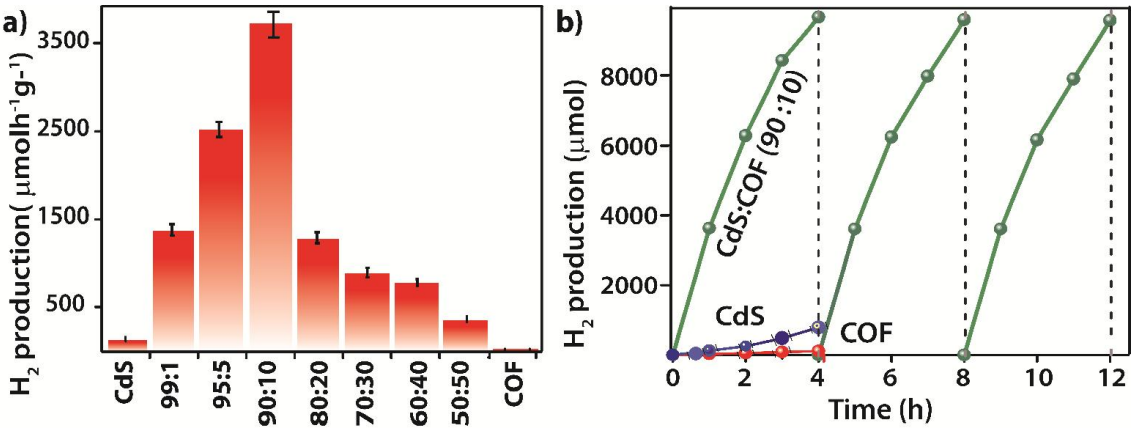

Figure 5B.6. *Comparison of the H_2 yield obtained in the present work; b) photocatalytic stability test.*

Of all, CdS-COF (90:10) is found to show the highest photocatalytic activity with 3678 μmol h^{-1} g^{-1} of constant H_2 production without any apparent decrease in the activity until three consecutive cycles with an apparent quantum yield reaching 4.2 % at 420 nm (**Figure 5B.6b**). The controlled experiment under dark conditions reveals negligible H_2 production, which confirms the role of illumination in effecting the catalytic activity. The photocatalytic activity is found to increase up to certain extent of COF addition (10 wt. %) and eventually decrease further.

5B.2.2.3. Quantum Efficiency

The quantum efficiency is calculated by following a procedure previously reported in the literature. The set-up has four LEDs (of 420 nm) that are positioned 1 cm away from the reactor along the four directions. The flux meter reading is noted (39 mW/cm^2).

$$\mathbf{Q.E} = \frac{\mathbf{Number\ of\ evolved\ H_2\ molecules\ \times 2}}{\mathbf{Number\ of\ incident\ photons}} \times \mathbf{100}$$

Using 39 mW/cm^2 as the power density, the quantum efficiency is calculated as 4.2% using the above equation.

Table 5B.2. *The H_2 production activity correlation with the BET surface area and weight percentage of COF.*

Sample	COF content (wt. %)	S_{BET} (m^2/g)	Activity (μmol/ h/ g)
Nano CdS	0	93	124
CdS – COF (99:1)	1.0	103	1320
CdS – COF (95:5)	5.0	107	2332
CdS – COF (90:10)	10	174	3677
CdS – COF (50:50)	50	280	162
bare COF	100	445	28

As the synthesised hybrids vary only in terms of the weight percentage of the COF added, this behavior is likely an outcome of the matrix shielding effect. After a threshold limit, the COF (which is a poor visible-light absorber) begins to drape the visible-light-active CdS nanoparticles. This eventually ceases the photocatalytic activity in the resulting hybrids, as they can now no longer absorb visible photons efficiently.

5B.2.3. Probable mechanism for the observed photocatalytic activity

5B.2.3.1. Mott Schottky (MS) experiment

To understand the nature of the coupling interfaces after composite making, the Mott-Schottky (MS) measurements are carried out using AC-impedance technique. The experiment is carried under dark conditions in actual hydrogen producing conditions as used for the photocatalytic experiments, *i.e*., in water-lactic acid-Pt solution. Prior to the measurements, the working electrode is prepared by making thin films of the materials under study on a fluorinated tin oxide (FTO) substrate using doctor blade method. The MS analysis reveals a flat band potential of -0.54 V (*vs*. NHE) for bulk CdS. The value is found to be higher than that of plain TpPa-2 (-0.45 V, *vs*. NHE). This implies that the bulk CdS has a higher lying Fermi level with respect to that of the COF. On the contrary, the best performing CdS:COF (90:10) composite is found to possess a flat band potential of -0.49 V *vs.* NHE (**Figure 5B.7a**). This indicates the formation of a new Fermi level between those of bulk CdS and TpPa-2 on the composite making. This suggests a high chance of transfer of photogenerated electrons from CdS to the COF matrix on illumination of visible light. [27b]

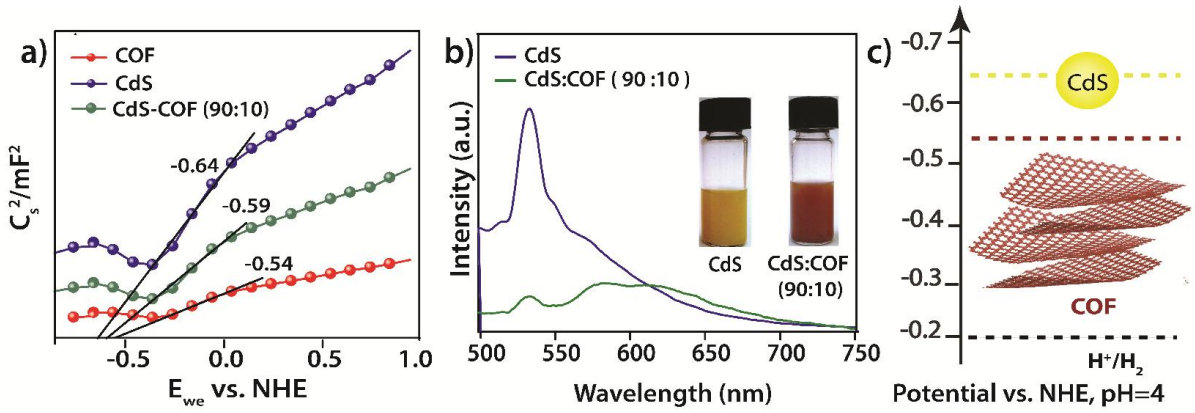

Figure 5B.7*. a) Combined MS plots, b) photoluminescence spectra of bulk CdS and CdS-COF (90:10) hybrid at 460 nm; c) schematic representation of the energy-level of the hybrid system.*

5B.2.3.2. Photoluminescence (PL) study

In conjunction with the MS study, the photoluminescence spectrum of CdS shows decrease in the PL peak intensity when compared to that of CdS:COF (90:10) (**Figure 5B.7b**). The decrease in the PL intensity is another typical feature of charge transfer from the CdS. This transfer is believed to efficiently suppress the recombination of the photogenerated e-hole pair in CdS, thereby increasing the longetivity of the photo activity. [27a]

Thus, from the MS and PL analysis, it is unstated that the presence of high surface area of COF apart from the abundantly available ordered two-dimensional hetero-interface, facilitates the stabilization of CdS photoelectrons onto the extended COF surface, which in turn decreases the chances of recombination of the generated electron-hole pair.

5.2. Conclusion

The first part of this chapter effectively highlights the utilization of a bipyridine unit enriched, chemically stable, crystalline COF, TpBpy, as a heterogeneous OER catalyst by coordinating active Co (II) ions into its high surface area framework. Co-TpBpy shows excellent stability with a low overpotential (400 mV at 1 mA /cm^2) even after 24 h of water oxidation activity in neutral medium. The cobalt modified TpBpy is also observed to display a high faradaic efficiency of 95 % and a consistent turn-over frequency (TOF) of 0.23/s at pH 7. It thereby pioneers a way for the synthesis and utilization of electrochemically active COFs as highly stable, molecularly tunable, heterogeneous catalysts for important reactions

involved in a variety of realizable energy devices such as water splitting, supercapacitors, batteries etc. The second part of the chapter explores the use of highly stable COFs for developing stable and efficient photocatalysts. A composite formation with TpPa-2 COF is observed to improve the stability of the photogenerated CdS electrons apart from suppressing the recombination of the as generated electron hole pair. This results in an amazingly high photocatalytic activity of the composite when compared to that of the bare CdS. It thereby demonstrates the authenticity of such highly stable COFs as effective substrates towards development of more efficient and stable visible light-active photo catalysts. Above all, this study highlights a successful amalgamation of the organic and inorganic entities within a hybrid with improvised activity.

5.3. References

[1](a)A.P.Cote, A.I. Benin, N. W. Ockwig, M.O'Keeffe, A.J. Matzger, O. M. Yaghi, *Science*. **2005**, *310*, 1166. (b) X.Feng, X.Ding, D.Jiang, *Chem. Soc. Rev.* **2012**, *41*, 6010. (c) E. L. Spitler, B. T. Koo, J. L. Novotney, J.W. Colson, F. J. Uribe Romo, G. D. Gutierrez, P. Clancy, W. R. Dichtel, *J. Am. Chem. Soc.* **2011**, *133*, 19416.

[2](a) S. Kandambeth, A. Mallick, B. Lukose, M. V. Mane, T. Heine, R. Banerjee, *J. Am. Chem. Soc.*, **2012**, *134*, 19524. (b) S. Kandambeth, D. B. Shinde, M. K. Panda, B. Lukose, T. Heine R. Banerjee, *Angew. Chem. Int. Ed*., **2013**, *125*, 13290. (c)D. B. Shinde, H. B. Aiyappa, M. Bhadra, B. P. Biswal, P. Wadge, S. Kandambeth, B. Garai, T.Kundu, S. Kurungot, R. Banerjee, *J. Mater. Chem. A*, **2016**, *4*, 2682.

[3] S. Berardi, S. Drouet, L. Francas, C. G. Surinach, M. Guttentag, C. Richmond, T. Stoll, A. Llobet, *Chem. Soc. Rev*., **2014**, *43*, 7501.

[4] D. Mullangi1, S. Nandi1, S. Shalini, S. Sreedhala, C. P. Vinod & R. Vaidhyanathan, *Scientific Reports*, **2015**, *5***,** 10876.

[5](a) D. G. Nocera, *Acc. Chem. Res.* **2012**, *45*, 767. (b) M. D. Karkas, O. Verho, E. V. Johnston, B. Akermark, *Chem. Rev.* **2014**, *114*, 11863. (c) S. Berardi, S. Drouet, L. Francas, C. G. Surinach, M. Guttentag, C. Richmond, T. Stoll, A. Llobet, *Chem. Soc. Rev.*, **2014**, *43*, 7501.

[6] V. M. Dhavale, S.S. Gaikwad, L.George, R. N. Devi, S. Kurungot, *Nanoscale*, **2014**,*6*, 13179.

[7](a)T. Reier, M. Oezaslan, P. Strasser, *ACS Catal.,* **2012**, *2*,1765.(b) K. Sardar, E. Petrucco, C. I. Hiley, J. D. B. Sharman, P. P. Wells, A. E. Russell, R. J. Kashtiban, J. Sloan, R. I. Walton, *Angew. Chem*. **2014**, *126*, 11140.

[8](a) Y. Surendranath, M. W. Kanan, D. G. Nocera, *J. Am. Chem. Soc*., **2010**, *132*, 16501. (b) J. B. Gerken, J. G. McAlpin, J. Y. C. Chen, M. L. Rigsby, W. H. Casey, R. D. Britt, S. S. Stahl, J. *Am. Chem. Soc*. **2011**, *133*, 14431.

[9](a) C. Zhang, M. Antonietti, T.P Fellinger, *Adv. Funct. Mater*. **2014**, *24*, 7655. (b) T. Zhou, D. Wang, S. C.K. Goh, J. Hong, J. Han, J. Mao, R. Xu, *Energy Environ. Sci.* **2015**, *8*, 526. (c) L. Wu, Q. Li, C. H. Wu, H. Zhu, A. M.Garcia, B. Shen, J. Guo, S. Sun, *J. Am. Chem. Soc.* **2015**, *137*, 7071.(d) G. Zhang, C. Huang, X. Wang*, small*, **2015**, *11*, 1215.

[10](a) J. D. Blakemore, R. H. Crabtree, G. W. Brudvig, *Chem. Rev.* **2015**, *115*, 12974. (b) S. W. Sheehan , J. M. Thomsen, U. Hintermair, R. H. Crabtree , G. W. Brudvig, C.A. Schmuttenmaer, *Nat. Comm*, **2015**, *6*, 1.

[11](a) Y. Surendranath, M. Dinca, D. G. Nocera, *J. Am. Chem. Soc.* **2009**, *131*, 2615. (b) S. Pintado, S.G. Ferron, E. C. E. Adan, J.R. G Mascaros, *J. Am. Chem. Soc.* **2013**, *135*, 13270.

[12]L. Francs, C. Richmond, P. G. Barros, N. Planas, S. Roeser, J. B. Buchholz, L. Escriche, X. Sala, A. Llobet, *Chem. Eur. J.* **2016,** *22*, 1.

[13] (a) X. Feng, X. Ding, D. Jiang, *Chem. Soc. Rev*., **2012**, *41*, 6010. (b) L. Stegbauer, K. Schwinghammer, B. V. Lotsch, *Chem. Sci.,* **2014**, *5*, 2789.

[14](a)T. Lukasczyk, K. Flechtner, L. R. Merte, N. Jux, F. Maier, J. M.Gottfried, H.-P. Steinruck, *J. Phys. Chem. C*, **2007**, *111*, 3090. (b) D. Huang, J. Lu, S. Li, Y. Luo, C. Zhao, B. Hu, M. Wang, Y. Shen, *Langmuir*, **2014**, *30*, 6990.

[15](a) S.Chandra, T.Kundu, K.Dey, M.Addicoat, T.Heine, R.Banerjee, *Chem. Mater*. **2016**, *28*, 1489. (b) T. D.M. Elko-Hansen, J. G. Ekerdt, *Chem.Mater.* **2014**, *26*, 2642.

[16](a) A. M. Lopez, M. Natali, E. Pizzolato, C. Chiorboli, M. Bonchio, A.Sartorel, F. Scandola, *Phys. Chem. Chem. Phys.,* **2014**, *16*, 12000. (b) Y. C Lin, Y. L Hsieh, Y. D Lin, C. H. Peng, *Macromolecules* **2014**, *47*, 7362.

[17](a)Y. Gorlin, T. F. Jaramillo, *J. Am. Chem. Soc*., **2010**, *132*, 13612. (b) A.Han, H. Chen, Z. Sun, J. Xu, P. Du, *Chem. Commun.*, **2015**, *51*, 11626.

[18](a) P. Manna, J. Debgupta, S. Bose, S. K. Das, *Angew. Chem. Int. Ed.* **2016**, *55*, 1. (b) A. J. Esswein, Y. Surendranath, S.Y. Reece, D. G. Nocera, *Energy Environ. Sci*. **2011**, *4*, 499. (c) F. Jiao, H. Frei, *Angew. Chem. Int. Ed.***2009**, *48*, 1841.

[19] (a) D. L. Ashford, B. D. Sherman, R. A. Binstead, J. L. Templeton, T. J. Meyer, *Angew. Chem.* **2015**, *127*, 1. (b) A. T. Swesi, J. Masud, M. Nath, *Energy Environ. Sci*. **2016**, *9*, 1771.

[20] (a) A. Fateeva, P. A. Chater, C. P. Ireland, A. A. Tahir, Y. Z. Khimyak, P. V. Wiper, J. R. Darwent, M. J. Rosseinsky, *Angew.Chem. Int. Ed*. **2012**, *51*, 7440. (b) Y. Horiuchi, T. Toyao, M. Saito, K. Mochizuki, M. Iwata, H. Higashimura, M. Anpo, M. Matsuoka, *J. Phys. Chem. C*, **2012**, *116*, 20848.

[21](a) Q. Li, B. Guo, J. Yu, J. Ran, B. Zhang, H. Yan, J. R. Gong, *J. Am. Chem. Soc.*, **2011**, *133*, 10878. (b). J. Zhang, Z. Zhu, Y. Tang, K. Müllen, X. Feng, *Adv. Mater*., **2014**,*26*, 734.

[22](a) B. Zhu, B. Lin, Y. Zhou, P. Sun, Q. Yao, Y. Chen. B. Gao, *J. Mater. Chem. A,* **2014**, *2*, 3819. (b) U. Maitra, U. Gupta, M. De, R. Datta, A. Govindaraj, C. N. R. Rao, *Angew. Chem. Int. Ed*., **2013**, *52*, 13057. (c) J. Zhang, J. Yu, Y. Zhang, Q. Li, J. R. Gong, *Nano Lett.*, **2011**, *11*, 4774. (d) H. N. Kim, T. W. Kim, I. Y. Kim, S. Hwang, *Adv. Funct. Mater.*, **2011**, *21*, 3111.

[23](a)Y. Zhang, N. Zhang, Z.Tang, Y.Xu, *Chem. Sci.*, **2012**, *3*, 2812. (b)(b) Q. Wang, J. Li, Y. Bai, J. Lian, H. Huang, Z. Li, Z. Lei, W. Shangguan, *Green Chem.,* **2014**,*16*, 2728. (c) P. Garg, S. Kumar, I. Choudhuri, A. Mahata, B. Pathak, *J. Phys. Chem. C*, **2016**, *120* , 7052.

[24] X. Hu, C. Sun, C Qin, X. Wang, H. Wang, E. Zhou, W. Li , Z. Su., *Chem. Commun.,* **2013**, *49*, 3564.

[25] P. Pachfule, S. Kandambeth, D. D. Diaz, R. Banerjee, *Chem. Commun*., **2014**, *50*, 3169.

[26](a) S. Wan, J. Guo, J. Kim, H. Ihee, D. Jiang, *Angew. Chem. Int. Ed.,* 2008, 120, 8958. (b)L. Stegbauer, K.Schwinghammer, B. V. Lotsch, *Chem. Sci.*, **2014**, *5*, 2789.

[27] (a) X. An, X. Yu, J. C. Yu, G. Zhang, *J. Mater. Chem. A*, **2013**, *1,* 5158. (b) Z. Sun, J. Guo, S. Zhu, L. Mao, J. Ma, D. Zhang, *Nanoscale*, **2014**, *6*, 2186.

Chapter 6

Metal Organic Framework (MOF)-derived porous carbons as electrode materials towards fabrication of energy devices*

This chapter discusses the role of metal organic frameworks (MOFs) as self-sacrificial templates for porous carbon synthesis. The first part of the chapter[#] reports an effective way of converting the less employed non-porous Zn-MOFs into more useful porous carbons. In the study, the self-sacrificial nature of MOFs has been exploited to convert non-porous MOFs into porous carbons without using any additional carbon source. The influence of ligands in the MOF architecture on the properties of carbons resulting from their direct carbonization is established. The as-synthesized MOF-derived carbons have been exclusively studied for gas adsorption properties and electrochemical applications. The second part of the chapter[# #] discusses a unique route through which the porous MOF-derived carbons are further activated for Oxygen Reduction Reaction (ORR) in PEMFCs. Herein, a MOF-derived carbon is used as a conductive matrix for anchoring heteroatoms, a feature known to improve the carbon's intrinsic activity towards ORR. The macro porosity of the MOF carbon is effectively used as a nitrogen reservoir for plugging nitrogen rich g-C_3N_4 units by means of *in situ* polymerization of the melamine. This route thereby opens a new conduit to design and develop metal-free electrodes with enhanced ORR activity and better mass diffusion characteristics optimal for PEMFC applications.

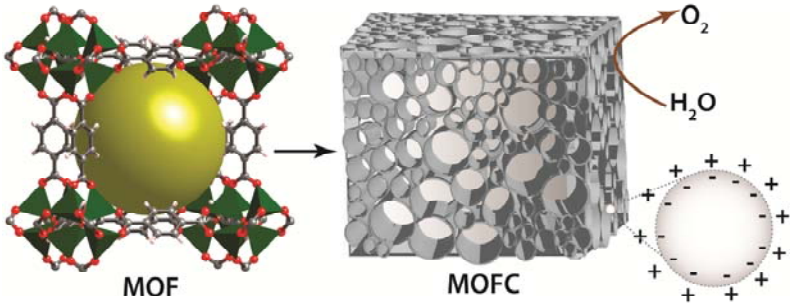

6.1. Introduction

The topical carbon research suggests that the nature of the carbon precursor primarily determines the properties of the resulting carbon. [1] Several hard inorganic templates *viz*., meso-structured silica, zeolites, alumina membranes, etc. impregnated with carbon precursors such as sucrose[2], furfuryl alcohol[3], phenol resins[4] etc. are being used for the synthesis of nanoporous carbons. A vigilant search for an ideal starting carbonizing material ends in one that could act as both template as well as a carbon precursor. This will not only abet the preservation of the original morphology but also facilitate predicting the nature of the resulting end carbon. Furthermore, the use of such self-dedicated template will also help evade the tedious post-synthetic procedures like removal of residual template materials from the carbon matrix, use of copious amounts of washing solvents and rigorous activation conditions to remove the residual solvent molecules and activate the pores before use.[5] Metal Organic Frameworks (MOFs) have recently gained scientific interest as contenders for deriving porous carbon structures owing to their tunable and permanent porosity, high stability and low framework density.[6] By the virtue of the metal ions and carbonaceous ligands already present in the framework, these structures are known to act as 'self-sacrificial templates' for carbon making.[7] Therefore, the synthesis of porous carbon by means of direct carbonization of MOFs has been a straightforward approach to synthesize nano structured carbons. Interestingly, most of these MOFs possess intrinsic porosity, which on carbonization are observed to result into spongy carbons with porosity comparable to that of the parent MOF.[8] This observation has often led to a notion that only porous MOFs potentially produce porous carbons. Hitherto, very few works defy this logic and in particular, the concept of conversion of non-porous MOFs to porous carbons could be found hardly worked on.

The first part of this chapter reports the synthesis of porous carbons by directly carbonizing non-porous Zn-based MOFs, without using any supplementary carbon precursor. It intends to provide an exclusive fundamental study on the pore characteristics and relative properties of the MOF-derived carbons. The porosity imbibed in the resulting carbons is related to the MOF's Zn/C ratio, which is further correlated with the microporosity and surface area of the resulting carbon. The capacitive behavior of the carbons has been assessed by using cyclic voltammetry and charge-discharge studies.

Part A

6A. Synthesis of Porous Carbons from Non-Porous MOFs: Study of the Influence of the MOF Ligand Characteristics on the Nature of the End Carbon

MOFs are crystalline, metal ion-ligand coordinated, long range ordered frameworks with exceptionally good stability, which make them potential, robust, sacrificial templates for carbon synthesis. [9] Interestingly, most of the MOF based carbon syntheses reportedly use an additional carbon source, which on heating results in the formation of *in situ* porous carbon with alongside decomposition of the MOF framework. However, recent findings show that MOFs do not need an additional carbon source due to the presence of organic linkers in its architecture. [10]

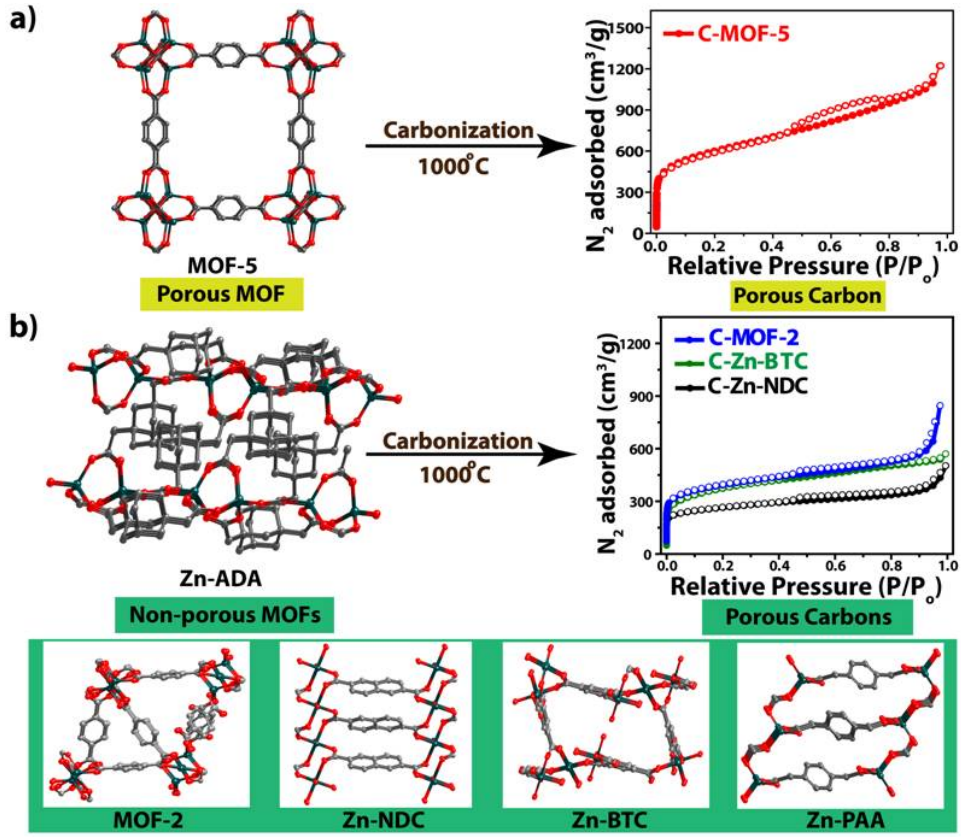

Figure 6A.1. *Schematic representation of the porous carbon synthesis from a) porous MOF and b) non-porous MOFs at 1000 °C with their N_2 adsorption isotherms. The non-porous MOF structures are shown inside the green frame. The solvent molecules in the MOF structures are omitted for clarity. (Color code: Zn: green, O: red, C: grey).*

The synthesis of porous carbon *via* carbonization of MOFs can be used as a shortest approach to obtain nano-structured carbons with improved surface area along with retention of exceptional stability as that of parent MOFs. However, it is equally important to note that there are numerous MOFs, which do not have any intrinsic porosity and are thus not potentially capable to be used for the routine porosity dependent applications like gas storage, gas separation etc. [11] However, as these architectures contain the needed organic content, they could still be potential self-sacrificial templates for carbon making. These results lead to an opinion that only porous MOFs are required to produce porous carbons. Hitherto, the concept based on the conversion of non-porous MOFs to porous carbon is not explicitly realized. It is well known that the property of a MOF depends on its constituting metal ions and ligands apart from their eventual self-assembly into long-range framework. However, during their carbonization, the influence of the MOF's ligand properties on the final carbon is not well understood. The effect of the nature of the pores on the gas uptake properties as well as energy storage behavior, *i.e.*, the capacitive nature, of such MOF-derived porous carbons could thus be of large interest. The first part of this chapter reports the synthesis of porous carbons from six Zn-based non-porous MOFs and demonstrates their application as potential electrode materials towards fabrication of supercapacitors (**Figure 6A.1**).

6A.1. Experimental Section

6A.1.1. Materials

1,4-Benzene dicarboxylic acid, 1,3,5-benzene tricarboxylic acid, 2,6-naphthalene dicarboxylic acid, 1,3-adamantanediacetic acid, 1,4-phenylenediacetic, $Zn(NO_3)_2.6H_2O$, $Zn(ClO_4)_2$ $.2H_2O$ used for the MOF synthesis were purchased from Sigma Aldrich Chemicals and used as received without further purifications. The solvents used like N,N-dimethyl formamide, N,N-diethyl formamide and methanol used for the synthesis of MOFs were purchased from Rankem and Avra Chemicals and used without distillation. HPLC grade dichloromethane and methanol used for the solvent exchange were purchased from Sigma Aldrich Chemicals and used as received.

6A.1.2. MOFs synthetic protocol

1. **MOF-5:** The standard procedure reported elsewhere was used for synthesizing MOF-5. In brief, 0.4 g of zinc nitrate hexahydrate and 0.1 g of terephthalic acid were added to a glass vial (15 ml capacity) containing 10 ml diethylformamide (DEF). The contents were

sonicated until a clear solution was obtained following which, the vials were heated at 90 °C for 3 days using a temperature controlled oven. The resulting transparent cubic crystals were later filtered and dried at 60 °C.

2. **MOF-2:** The standard procedure reported elsewhere was used for synthesizing MOF-2. In brief, 0.1 g of zinc nitrate hexahydrate and 0.4 g of terephthalic acid were dissolved in 10 ml DEF solution was heated at 90 °C for 3 days. The transparent crystals obtained were separated by filtration and dried at 60 °C.

3. **Zn-BTC:** The standard procedure reported elsewhere was used for synthesizing Zn-BTC. In brief, 0.66 g zinc acetate dihydrate and 0.42 g of 1, 3, 5 benzene tricarboxylic acid were dissolved in 8 ml DMSO solution and heated at 100 °C for 3 days. The whitish crystals obtained were later filtered and dried at 60 °C.

4. **Zn-NDC:** The standard procedure reported elsewhere was used for synthesizing Zn-NDC. A mixture of zinc nitrate hexahydrate, 2.6-naphthalene dicarboxylic acid dissolved in ethanol and water (1.5:1:60: 196) were treated under hydrothermal condition at 125 °C for 12 h using Teflon-lined steel autoclave. The transparent crystals obtained were later filtered and dried at 60 °C.

5. **Zn-PAA:** The standard procedure reported elsewhere with slight modification was used for synthesizing Zn-PAA. 0.17 g of zinc acetate dihydrate and 0.08 g of 1, 4, phenylene diacetic acid were added to 15 ml de-ionized water with pH adjusted to 5.0 using 1 mmol NaOH solution. The contents were then sealed and treated under hydrothermal conditions at 180 °C for 2 days.

6. **Zn-ADA:** 0.1 mmol of $Zn(ClO_4)_2$. $2H_2O$ and 0.1 mmol 1, 3 adamantane dicarboxylic acid were dissolved in DMF: CH_3OH (2:1) solvent mixture followed by heating at 90 °C for 3 days. The structure of the colorless, flower-like crystals obtained was confirmed by single crystal XRD. A PXRD spectrum was also recorded to confirm the purity of the bulk material (**Figure 6A.3**).

6A.1.3. Experimental and Refinement Details for Zn-ADA

A colorless plate-like Zn-ADA crystal (of dimension 0.34 × 0.29 × 0.12 mm^3) is taken in a 0.7 mm diameter nylon CryoLoops (Hampton Research) with Paraton-N (Hampton Research). The loop is mounted on a SMART APEX three-circle diffractometer. A total of 6407 reflections have been collected of which 6407 were unique and 4801 of these were greater than 2ó(*I*). The range of *è* was from 2.91 to 27.17º. All

non-hydrogen atoms are refined anisotropically. It should be noted that other supporting characterization data (*vide infra*) are consistent with the crystal structure (**Figure 6A.2**). The final full matrix least-squares refinement on F^2 converged to $R_1 = 0.0410$ ($F > 2\acute{o}F$)) and $wR_2 = 0.1231$ (all data) with GOF = 0.858.

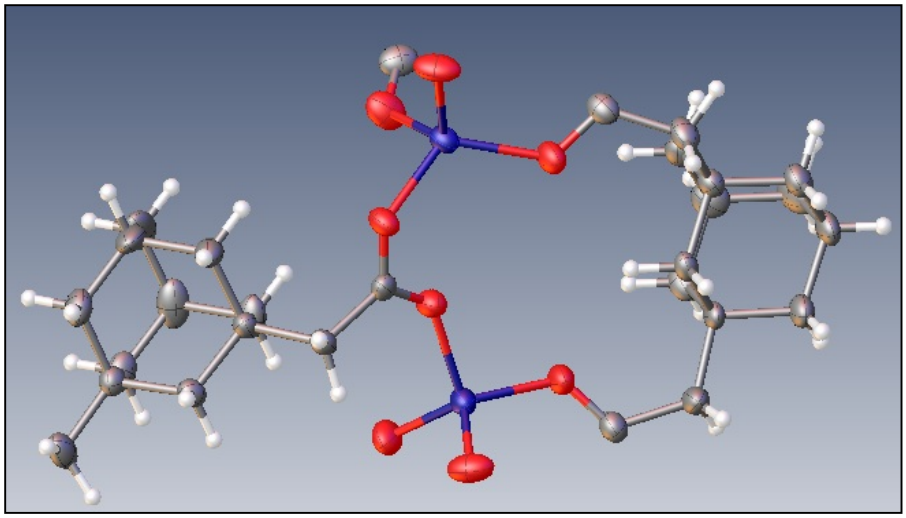

Figure 6A.2. *ORTEP diagram of Zn-ADA MOF.*

Table 6A.1. Crystal data and structure refinement for Zn-ADA MOF:

Empirical formula	$C_{28}\ H_{36}\ O_8\ Zn_2$
Formula weight	631.35
Temperature	293 (2) K
Wavelength	0.71073 Å
Crystal system	Monoclinic
Space group	$P2_1/c$
Unit cell dimensions	a = 14.3611(5) Å á = 90°
	b = 12.8622(4) Å â = 96.862(3)°
	c = 15.1403(5) Å ã = 90°
Volume	2776.62(15)
Z	4
Density (calculated)	1.510
Absorption coefficient	1.775
F(000)	1539

Crystal size	0.34 × 0.29 × 0.12 mm^3
Theta range for data collection	2.91 – 27.17
Index ranges	-19 <= h <= 19, -16 <= k <= 17, -20 <= l <= 19
Reflections collected	6407
Independent reflections	4801
Completeness to theta = 26.02°	98.4 %
Absorption correction	Semi-empirical from equivalents
Refinement method	Full-matrix least-squares on F^2
Data / restraints / parameters	6407 / 0/ 343
Goodness-of-fit on F^2	0.858
Final R indices [I>2sigma(I)]	R_1 = 0.0410, wR_2 = 0.1231
R indices (all data)	R_1 = 0.0608, wR_2 = 0.1472
Largest diff. peak and hole	0.413 and -0.471 e.$Å^{-3}$

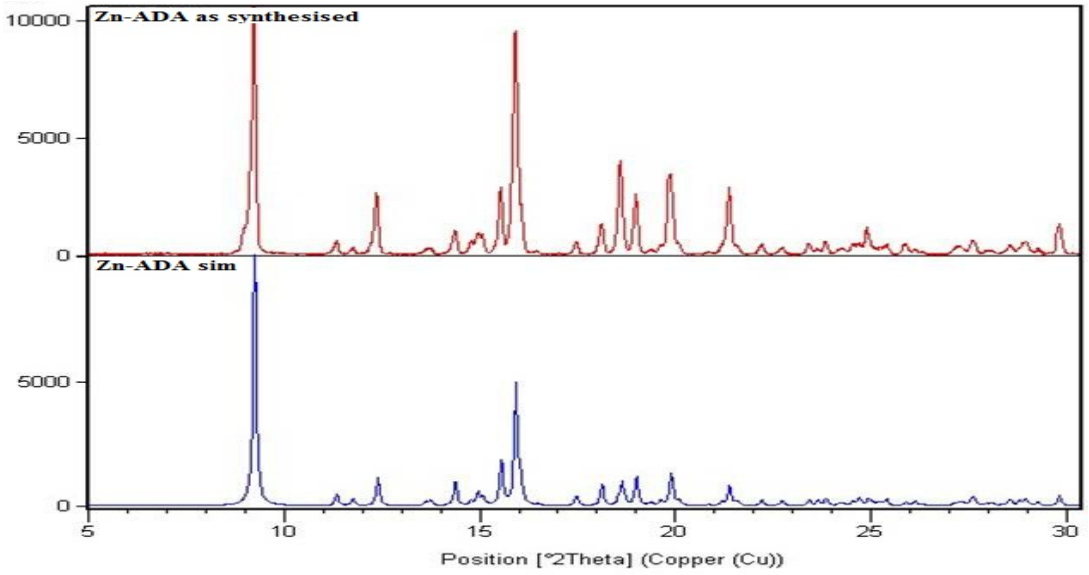

Figure 6A.3. *Simulated and experimental PXRD patterns of Zn-ADA.*

The bulk purity of the as synthesised Zn-ADA MOFs has been verified by comparing the simulated and the experimental PXRD patterns.

6A.1.4. Carbonization of Zn-MOFs

Five non-porous MOFs, *i.e.*, MOF-2 $[(H_2NEt_2)_2[Zn_3(BDC)_4]\cdot 3DEF]$,Zn-BTC $[Zn_3(BTC)_2(DMSO)_4]$, Zn-NDC $[Zn(NDC)(H_2O)]$, Zn-PAA $[Zn_2(PAA)_2]$ and Zn-ADA

along with the porous MOF-5[$Zn_4O(BDC)_3$] (for comparison) are chosen for the present study. In each case, MOF crystals are evenly spread inside an alumina boat and heated gradually till 1000 °C using a tube furnace under argon flow for 3 h at a ramp of 5 °C/min. After carbonization, the contents are allowed to cool naturally to room temperature.

6A.2. Result and Discussion

6A.2.1. Material Characterization

6A.2.1.1. Electron microscopic study

The Scanning Electron Microscopy (SEM) and Transmission Electron Microscopy (TEM) are used to study the effect of MOF porosity on the final carbon morphology.

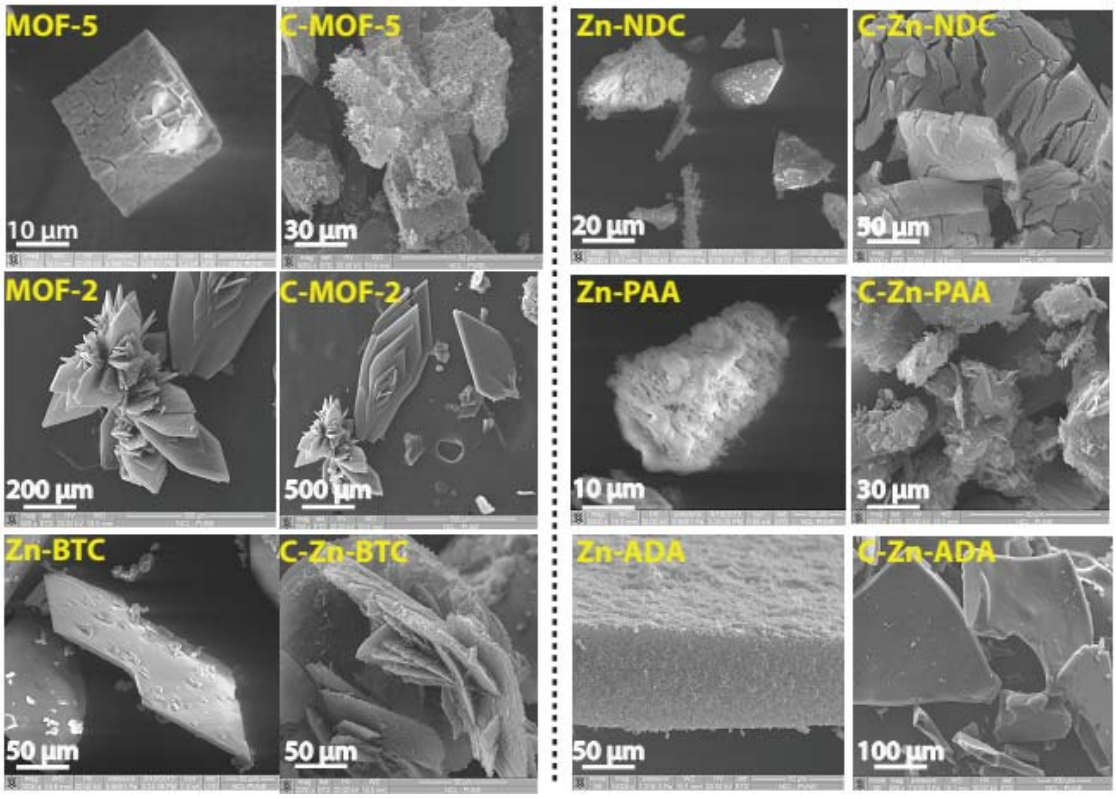

Figure 6A.4. *SEM images of the bare MOFs and corresponding MOF-derived carbons indicating the self-sacrificial of the synthesised MOFs except that of -Zn-ADA.*

The SEM analyses of the MOFs carbonized at 1000 °C indicate retention of the original MOF's morphology in all the MOF-derived carbons except that of C-Zn-ADA (**Figure 6A.4**). The MOFs containing aromatic linkers are observed to show better degree of rigidity during the carbonization (**Figure 6A.5**). On the other hand, this doesn't seem

to be the case of C-Zn-PAA and C-Zn-ADA, wherein 2D sheet phase is observed. The SEM images show that the MOF morphology is destroyed on thermal treatment at 1000 °C (e.g. Zn-PAA and Zn-ADA MOFs) (**Figure 6A.5c**).

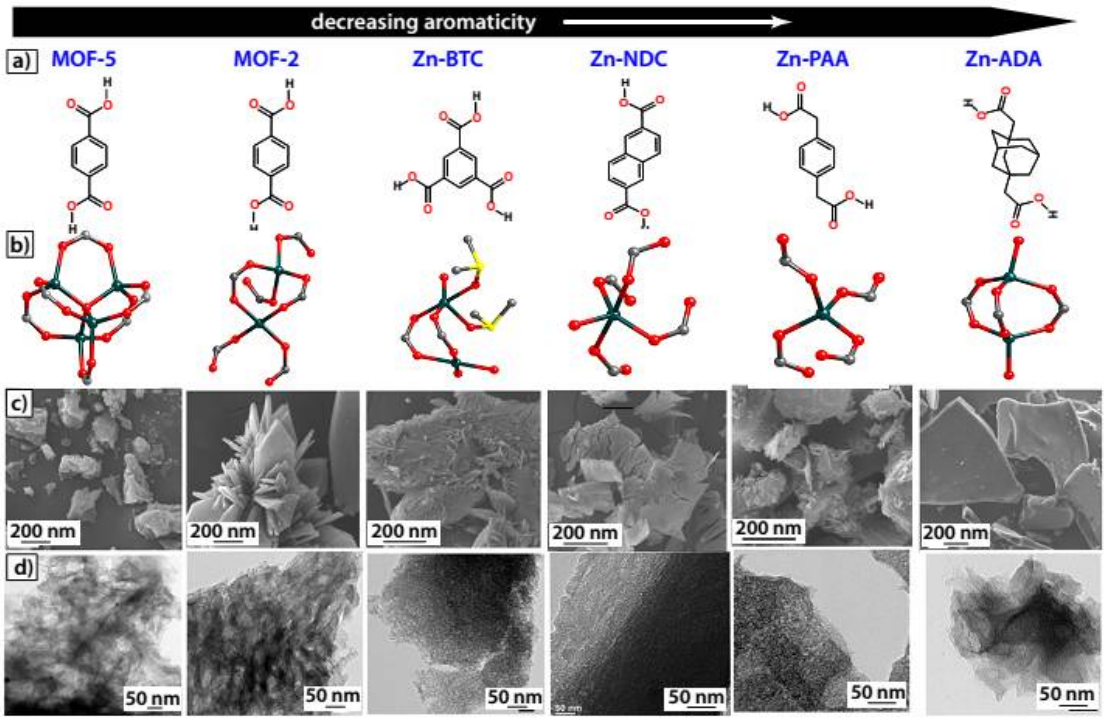

Figure 6A.5. *a)Chemical structure of the ligands used and b) the Secondary Binding Units (SBUs) of MOFs, c) SEM and d) TEM images of their corresponding porous carbons attained on directly carbonizing MOFs at 1000 °C. The constituting rigid/flexible ligands are placed based on the quantity of the sp^2/sp^3 type of carbons present in the ligand skeleton.*

In order to further verify this effect, the TEM analyses of all the carbons have been carried out. In comparison, C-MOF-5, C-MOF-2, C-Zn-NDC and C-Zn-BTC have much more prominent and larger sized pores than that of C-Zn-PAA and C-Zn-ADA. The high resolution TEM images clearly reveal the presence of well structured, periodic arranged carbon sheets with pores ranging from 5–10 nm in the carbon matrix of C-MOF-5, C-MOF-2, C-Zn-NDC and C-Zn-BTC (**Figure 6A.5d**). On the contrary, C-Zn-PAA and C-Zn-ADA are found to have less ordered, sheet–like arrangement in the carbon matrix. From the study, it is clear that the structural arrangement within the MOF architecture is a decisive factor for the development of ordered pores in the forming carbon. It is generally believed that, at very high temperature, the carbonizing structure

breaks down resulting in the loss of its intrinsic porosity.[12] However, these studies clearly specify the presence of pores along with the retention of original MOF morphology with few exceptions, thereby substantiating the role of these MOFs as the 'self-sacrificial' templates for the carbon synthesis.

6A.2.1.2. PXRD and Raman analysis

The PXRD spectra of the MOF-derived carbons have been recorded for a better understanding of the degree of crystallinity and graphitic nature of the obtained carbons. At *2θ* values of ~26 and ~44° , broad peaks observed in all of the spectra corresponds to the diffractions from (002) and (100) planes of the carbons, which indicate the existence of long range ordering in the matrix (**Figure 6A.6a**). The purity of the resulting nanoporous carbons is confirmed by the absence of peaks corresponding to ZnO, as Zinc (Zn) distills out of the system at ~907 ^{o}C (its boiling point), thereby leaving behind pure carbon.[13]

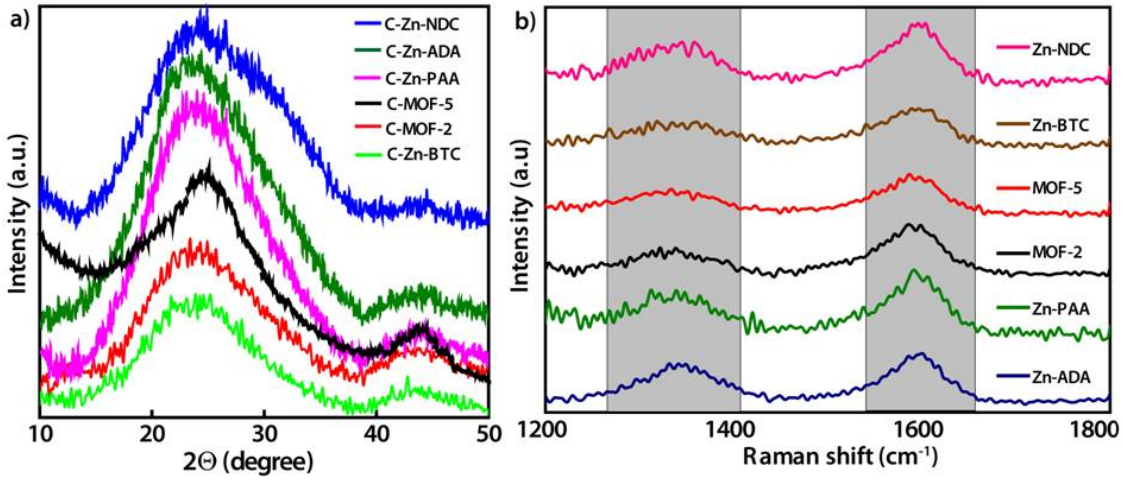

Figure 6A.6. *Combined (a) PXRD spectra and (b) Raman spectra of the as synthesised MOF-derived carbons.*

The MOF to carbon conversion is further confirmed using Raman analysis. The Raman spectra of all the carbons display two characteristic peaks, one at ~1330 cm^{-1} (corresponding to the disordered, or D band) and second at ~1580 cm^{-1} (corresponding to the graphitic, or G band), respectively (**Figure 6A.6b**). Thus both PXRD and Raman results consistently indicate the existence of graphitic domains in the carbon matrix.

6A.2.1.3. Surface area analysis and porosity study

The BET surface area study of the activated MOFs indicate that apart from MOF-5 [with a BET surface area ~2385 m^2/g], the rest of the MOFs have little/no porosity with surface area ranging between 20–65 m^2/g (**Figure 6A.7**).

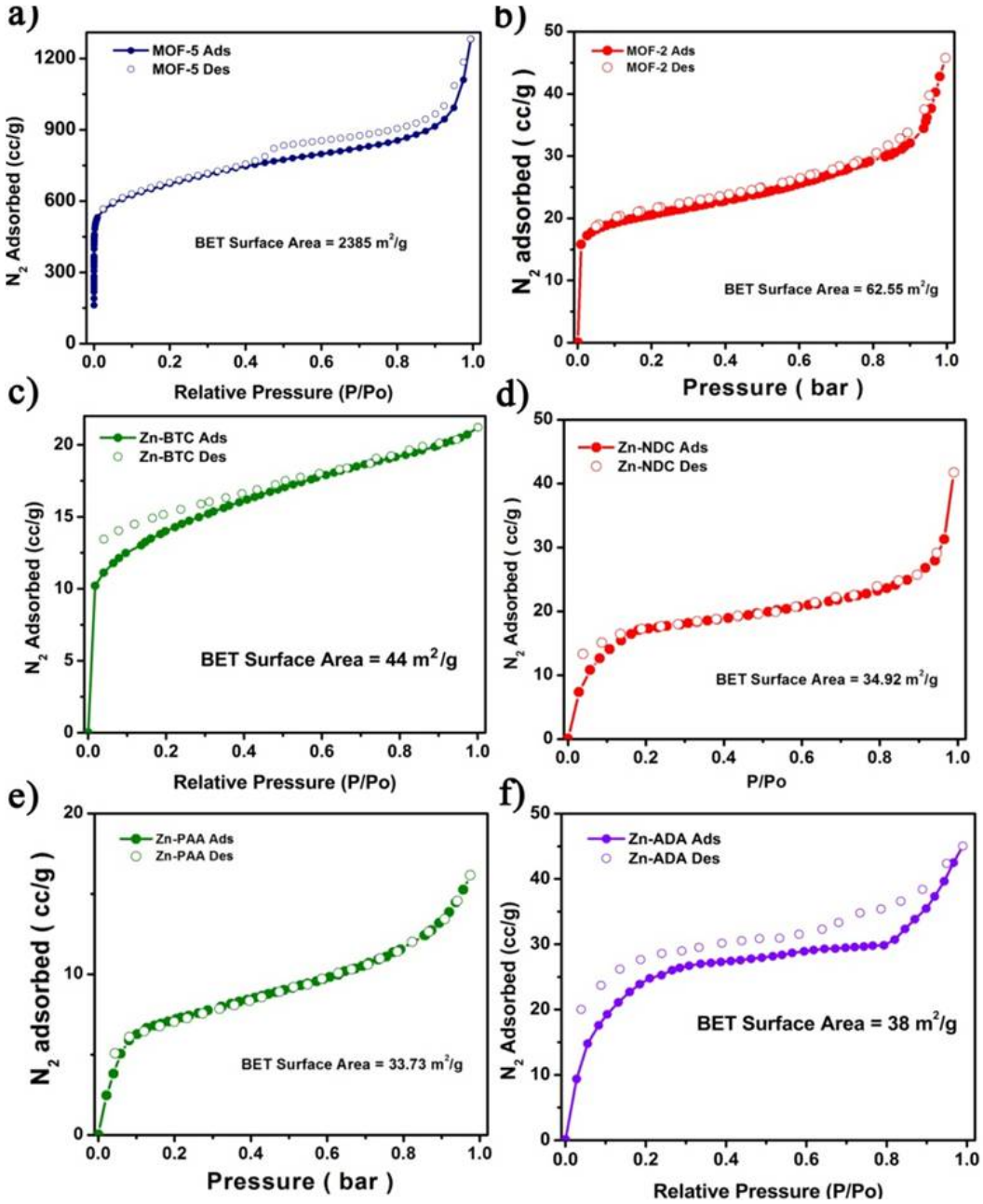

Figure 6A.7. *N_2 adsorption isotherms of the as syntheised porous MOF: a) MOF-5, non porous b) MOF-2, c) Zn-BTC, d) Zn-NDC, e) Zn-PAA and f) Zn-ADA MOFs.*

On carbonization, the gas adsorption profiles of the MOF-derived carbons show features characteristic of a Type-I isotherm without any hysteresis. This implies a dominating

microporous environment in the carbon matrix (**Figure 6A.8**). The BET surface areas have been calculated between a pressure range of 0.1–0.3 atm. The carbons obtained on carbonizing MOFs having rigid aromatic linkers (C-MOF-5, C-MOF-2, C-Zn-BTC and C-Zn-NDC) possess the BET surface areas of 2184, 1378, 1326 and 920 m^2/g respectively. Conversely, the surface areas of carbons obtained on carbonizing MOFs with flexible linkers (C-Zn-PAA and C-Zn-ADA) are found to be 495 and 513 m^2/g, respectively (**Figure 6A.8b**). This observation complies with the earlier reported phenomenon.[14] However, in the present study, it could be additionally observed that the linear relation between the Zn/C ratio and surface area holds good only in the case of MOFs constituting rigid ligands, *i.e.,* benzene derivatives like 1,4-BDC, 1,3,5-BTC, 2,6-NDC. However, the MOFs containing flexible ligands like 1, 3-ADA and 1, 4-PAA effect low surface area carbons and, therefore, do not fall in the linear regime (**Figure 6A.9**).

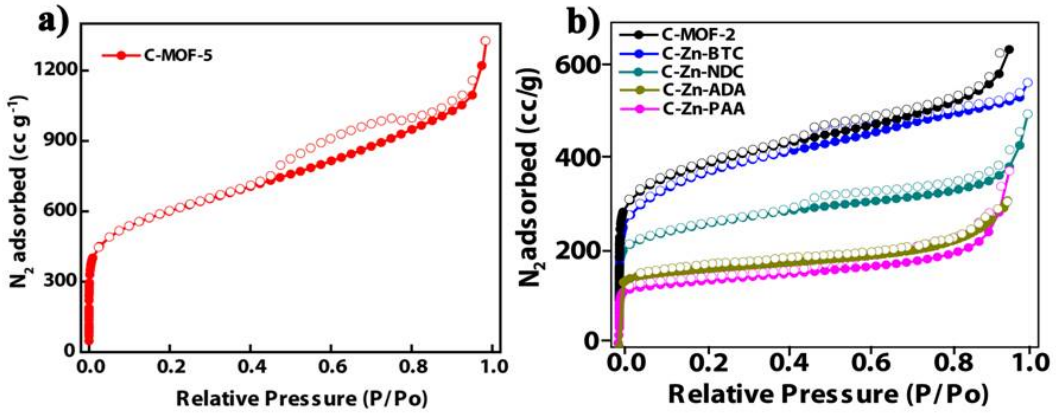

Figure 6A.8. *N_2 adsorption analyses of carbons obtained on direct carbonization of a) porous MOF and b) non-porous MOFs.*

A close observation reveals the chemical resemblance of the MOF's alicyclic linkers (the adamantane-based ligand) with the pitch-like compounds. This hints at the formation of a favourable mesophase intermediate state prior to the carbon formation.[15] In cases of C- MOF-2, C-Zn-NDC and C-Zn-BTC, the surface areas of the resulting carbons are nearly 22, 26 and 30 times, respectively, higher compared to their parent MOFs, while for C-Zn-PAA and C-Zn-ADA, 13 to 15 fold increase is observed. The surface area studies thereby reveal the influence of the presence of pure sp^3 (Zn-ADA) or sp^2 with some sp^3 (Zn-PAA) hybrid carbons in the MOF architecture.

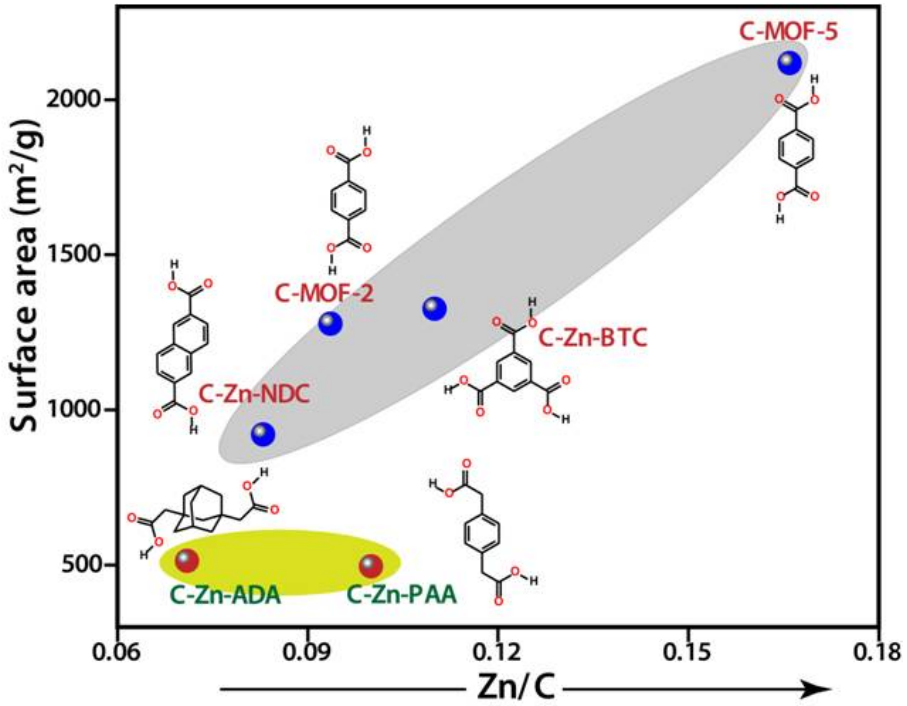

Figure 6A.9. *Plot indicating the relation between the MOF-derived carbon's surface area and the MOFs' Zn/C ratio.*

With increasing the sp^3 character (*i.e.,* with increasing ligand flexibility) the surface area of the resulting carbon is observed to decrease to a large extent, with regard to the carbons synthesized using MOFs with ligands having more sp^2 character (i.e., using rigid linkers) (**Figure 6A.9**).

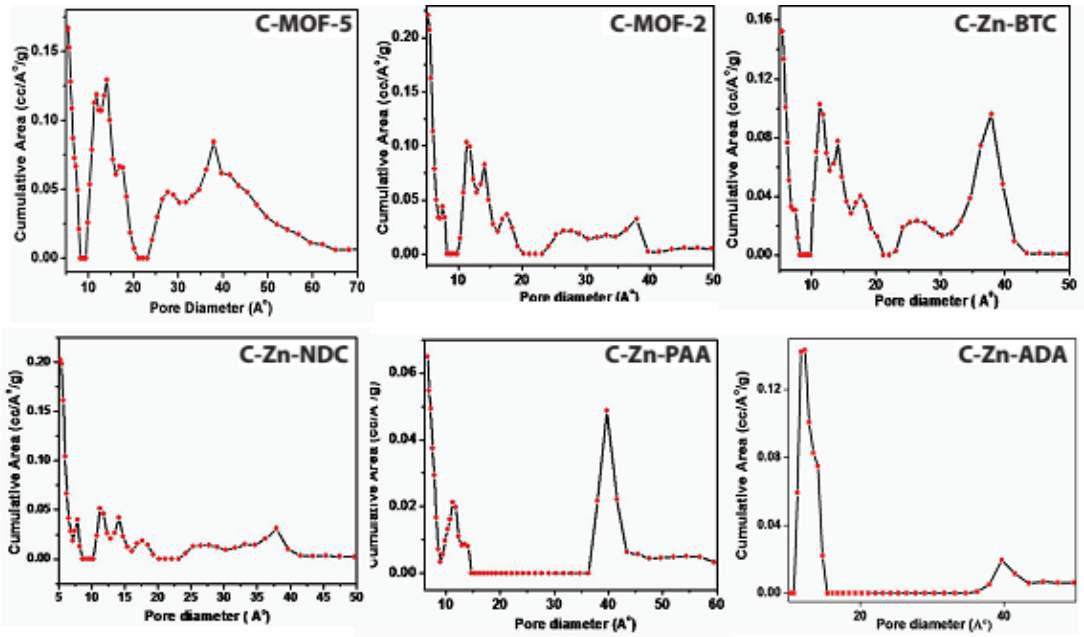

Figure 6A.10. *Pore size distribution plots the MOF-derived carbons.*

The study thereby implies that the linear relationship between the Zn/C ratio of MOF and surface area of the resulting carbon holds good only for the carbons obtained from the MOFs having rigid linkers.

6A.2.1.4. H_2 and CO_2 adsorption study

The H_2 and CO_2 adsorption properties of the carbons have been studied to understand the effect of the carbon microporosity on its adsorption properties. The H_2 (at 77 K) and CO_2 (at 273 K) adsorption isotherms illustrate characteristic Type–I isotherms without any hysteresis. As seen in (**Figure 6A.11**), H_2 uptake of C-MOF-5, C-MOF-2, C-Zn-NDC and C-Zn-BTC is 260, 223, 209 and 184 cc/g respectively, at 77 K and 1 atm pressure. Alternatively, C-Zn-PAA and C-Zn-ADA carbons are observed to adsorb 136 and 151 cc/g of H_2 at similar conditions (**Figure 6A.11a**).

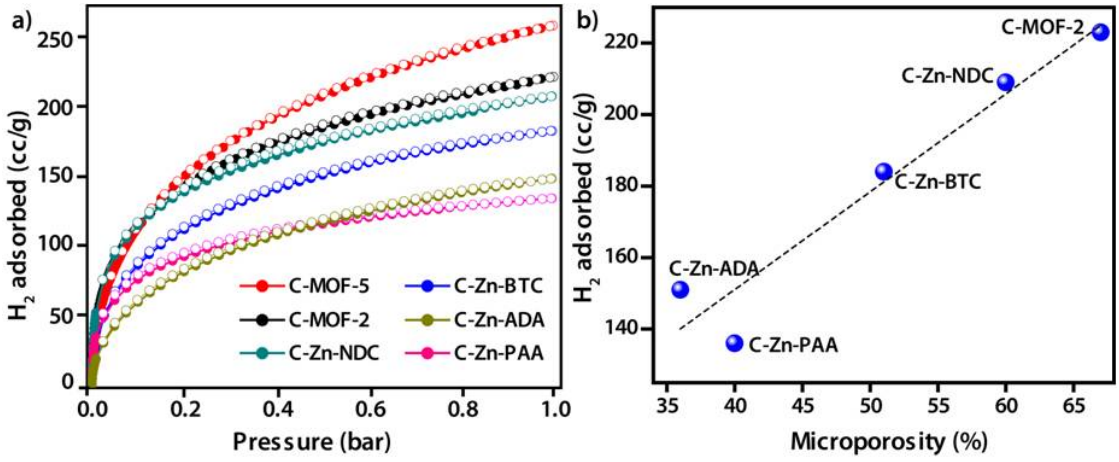

Figure 6A.11. *a) H_2 adsorption isotherms of the as synthesised MOF-derived carbons and b) plot of their H_2 uptake vs. % microporosity (obtained using the pore size distribution plots).*

It is well known that in a microporous solid, the adsorption potential increases with improved number of adsorption sites owing to the comparable pore size and kinetic diameter of the adsorbing gas molecules. [16]

The CO_2 adsorption study of C-MOF-5, C-MOF-2, C-Zn-NDC and C-Zn-BTC indicates 107, 100, 80 and 88 cc/g of CO_2 adsorption at 273 K and 1 atm pressure. Under similar conditions, C-Zn-PAA and C-Zn-ADA display only 95 and 73 cc/g of CO_2 adsorption (**Figure 6A.12**).The high rate of H_2 and CO_2 uptake is accounted to the substantial microporous nature of the carbons.

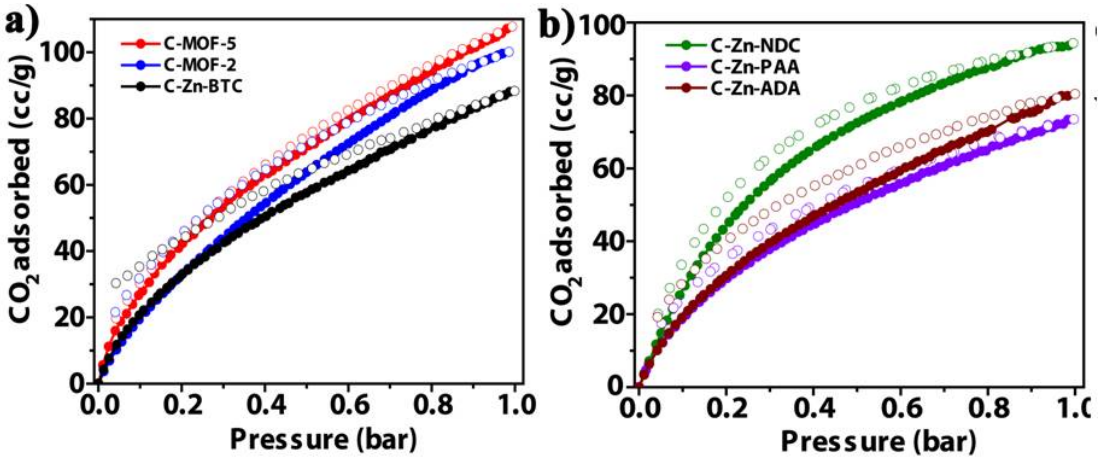

Figure 6A.12. *CO_2 uptake isotherms for porous a) C-MOF-5, C-MOF-2 and C-Zn-BTC and b) C-Zn-NDC, C-Zn-PAA and C-Zn-ADA collected at 273 K and 1 atm pressure.*

6A.2.2. Electrochemical study

The potential of the MOF-derived carbon as electrode materials for fabricating supercapacitor has been tested electrochemically. The electrochemical studies have been carried out by means of symmetric two-electrode cell assembly at 25 ˚C. *BioLogic* SP-300 Potentio-Galvanostat is used to carry out the cyclic voltammetry and galvanostatic charge-discharge tests in 1 M H_2SO_4 electrolyte. A potential window of 1.0 V is chosen to inspect the capacitive behavior of the carbon at various scan rates. The working electrode has been fabricated using the active material which consists of 85 % MOF-derived active carbon, 5 % PTFE (binder) and 10 % carbon black (used as conductive filler) onto a porous Toray® carbon paper (as catalyst support and current collector). A loading of 1 mg/cm^2 loading is maintained each time. The electrodes are dried at 60 °C overnight. Prior to their testing, they are soaked in the electrolyte solution for about 30 mins to ensure sufficient electrolyte infiltration into the electrode.

The cyclic voltammetry and charge-discharge measurements are carried out at a scan rate of 10 mV/s and different current densities (varying from 0.5 to 10 mA/cm^2). From **Figure 6A.13**, the specific capacitance at 1 A g^{-1} current density for C-MOF-2, C-MOF-5, C-Zn-BTC, C-Zn-NDC, C-Zn-PAA and C-Zn-ADA is calculated to be 170, 150, 134, 114, 110 and 95 F g^{-1}, respectively. The capacitance values calculated from the charge-discharge tests are in close agreement with those from the CV studies. The study clearly implies that the carbons show increased capacitance with increasing surface area (**Figure 6A.13a**). This validates the surface area-capacitance dependence concept in case of electrical double layer capacitor (EDLC), wherein, the ability of the carbon to amass

charges increases with increasing in the available surface area. [17] It also indicates the compatibility of the pore size of the carbons with that of the solvated ionic size.

The capacitance retention ability of the carbons is also studied to understand the amount of charge retained by the carbons despite the increasing limitations (diffusion and charge transfer resistance) with increasing current load. **Figure 6A.13b** indicates the capacitance retention plot with current density varying from 1 to 10 A/g. The carbons derived from MOFs with rigid linkers, *i.e.*, C-MOF-5,C-MOF-2, C-Zn-BTC and C-Zn-NDC, are observed to show capacitive retention of 79, 81, 84 and 80 %, respectively, while the one from MOFs with flexible linkers, i.e., C-Zn-PAA, and C-Zn-ADA show capacitance retention of 74 and 63 % respectively. The superior retention ability of carbons derived from MOF containing rigid linkers could be credited to the presence of ordered pores and comparatively higher mesoporous content. [18]

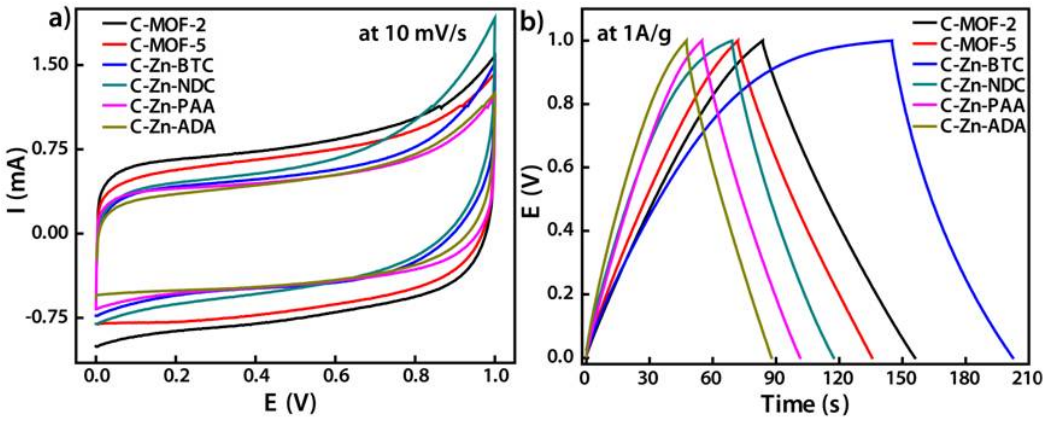

Figure 6A.13. *a) Cyclic voltammograms and b) charge-discharge profiles of C-MOF-2, C-MOF-5, C-Zn-BTC, C-Zn-NDC, C-Zn-PAA and C-Zn-ADA in 1M H_2SO_4*

The presence of hetero atoms like sulphur is known to perk up the wettability of the electrode surface and assist the electrode kinetics. [19] It is most likely that the lower retention in cases of carbons derived from flexible linkers, *i.e.,* C-Zn-PAA and C-Zn-ADA, due to the presence of smaller sized pores, which restricts rapid diffusion of ions. MOF-derived carbons have also been previously tested for their capacitive behavior. In the present work, of all the MOF-derived carbons, C-MOF-2 with a BET surface area of 1378 m^2/g is found to exhibit the highest capacitance of 170 F/g at 1 A/g current density (**Table 6A.2**).

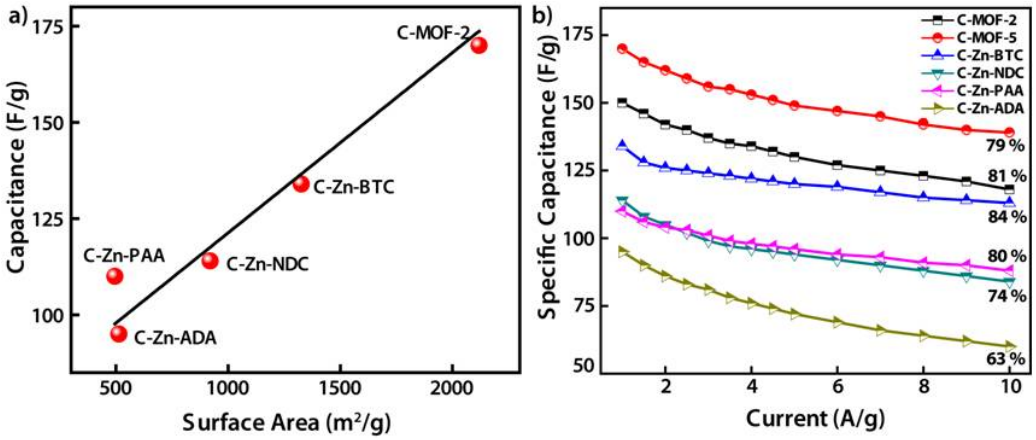

Figure 6A.14. *Plots indicating a) % specific capacitance retention ability at different current density values and b) variation of specific capacitance vs. surface area.*

The linear dependence of the specific capacitance with the surface area of the carbons can be explained based on the understanding of the role of micropores in facilitating the formation of double layer. Thus, an adequate balance in both micro and meso pore content is observed to render the surface area accessible for the formation of double layer at the electrode-electrolyte interface. [20]

Table 6A.2. *Summary of the MOF-derived carbons' pore parameters and their relative gas uptake and capacitance values as observed in the present study.*

Sample Name	BET Surface Area (m^2/g)	Zn/C Ratio	H_2 uptake (cc/g)	CO_2 uptake (cc/g)	Capacitance (F/g)
C-MOF-5	2119	0.167	260	107	150
C-MOF-2	1378	0.094	223	100	170
C-Zn-BTC	1326	0.1	184	88	134
C-Zn-NDC	920	0.115	209	80	114
C-Zn-PAA	495	0.084	136	95	110
C-Zn-ADA	513	0.072	151	73	95

Part B

6B. g-C_3N_4 modified MOF-derived carbon as an efficient metal-free ORR electrocatalyst

High surface area-hetero atom containing carbon materials have received significant attention due to their substantial application in energy fields, such as supercapacitors, fuel cells, lithium ion batteries etc.[21] These heteroatom doped carbon materials namely nitrogen doped graphene, nitrogen doped CNTs etc. have been explicitly tried as non-precious ORR catalysts in fuel cell systems, considering their additional CO tolerance and fuel selectivity under the PEMFC (Polymer Electrolyte Membrane Fuel Cell) operating conditions.[22] The nitrogen doping is thought to alter the electron density of the basal carbon, thereby creating the active sites obligatory for catalyzing ORR. However, the methods used for synthesizing these highly conductive nitrogen doped carbon often suffer from severe disadvantages *viz.*, use of toxic precursors, harsh acid post-treatment procedure, demand of specially designed equipments besides rigorous and trained handling etc.[5] Most importantly, despite being cumbersome, these methods still cannot precisely control the extent of heteroatom doping. In particular, the high temperature annealing treatment induces easy escape of the precursors during the course of the reaction. [23] This results in ineffective doping and minimizes the number of active sites. Thus, the challenge is to develop new generation electrocatalysts using an approach that could not only increase the ORR kinetics by creating more active sites, but also alongside maintain high surface area, a feature needed to facilitate faster mass transfer under the operating conditions. Through their inherent porosity and presence of high carbon content, MOFs have gained popularity as self-sacrificial templates to derive highly porous carbon structures. [7] The organic matter present in their robust architecture rules out the need for any supplementary carbon sources. [10] Interestingly, one of the as-synthesized carbons (derived from porous MOF-5), is observed to exhibit decent ORR activity under alkaline conditions. In order to improve its catalytic activity, the porous carbon derived from MOF is used to anchor nitrogen heteroatoms, a concept used to break the electro neutrality of carbons and in turn increase their catalytic activity. [24] Among the heteroatoms used for carbon doping, nitrogen (N), sulphur (S) and phosphorus (P) elements are often tried, owing to comparable atomic size with the basal carbon atoms. [25] Among the nitrogen precursors, due to its high N content, the graphitic carbon nitride (g-

C_3N_4) is extensively tried as an effective catalyst for numerous reactions, in particular, photo catalytic hydrogen generation, water splitting etc.[26] However, low surface area and poor electrical conductivity is believed to restrict the catalytic activity of the pristine g-C_3N_4.[27] The second part of this chapter thereby proposes one of the ways to overcome this limitation by incorporating g-C_3N_4 into a largely mesoporous, electrically conductive and ORR active MOF-derived carbon backbone in an attempt to create a superior catalyst for catalyzing ORR **(Figure 6B.1)**.

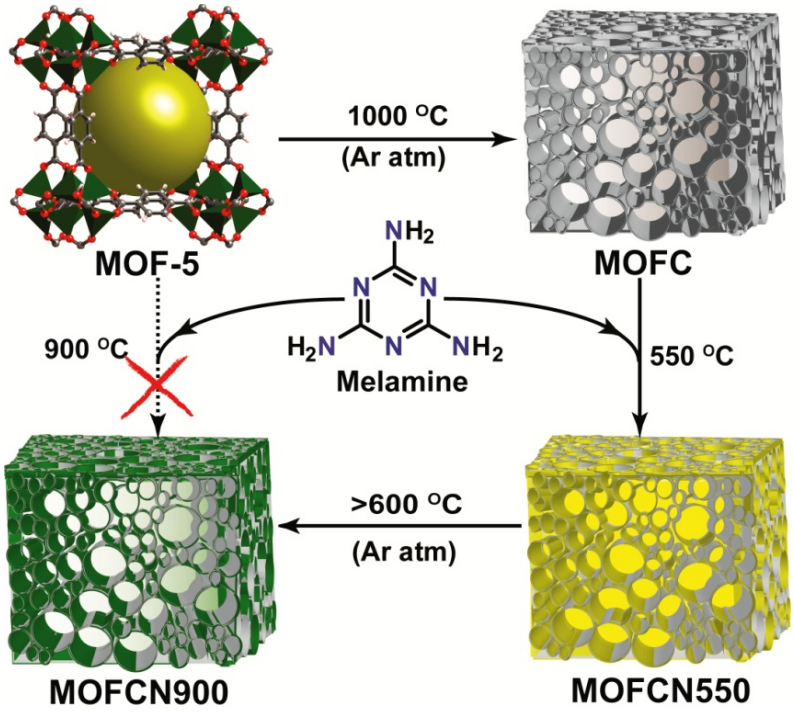

Figure 6B.1. *Schematic representation of the synthesis of N-doped porous carbon from g-C_3N_4 on impregnating melamine into the pores of MOF-5 derived carbon followed by the second carbonization at higher temperature (> 600 °C).*

6B.1. Experimental Section

6B.1.1. Materials

In the present work, the reagents namely melamine, potassium hydroxide (KOH), zinc nitrate hexahydrate, terephthalic acid and diethylformamide (DEF) are acquired from Sigma Aldrich. The solvents isopropyl alcohol (IPA) and ethanol are procured from Rankem Chemicals. The chemicals have been used as received without any additional purification.

6B.1.2. Synthesis of ORR active MOFCN catalysts

In the first approach followed, the as synthesized MOF-5 crystals are carbonized at 1000 °C in inert argon atmosphere for 3 h at a heating rate of 5 °C/min using an alumina boat. The resulting carbons are collected, washed in deionized water and finally dried overnight at 60 °C. The carbon, named MOFC, is further used for the melamine impregnation. A calculated amount of MOFC and melamine is ground together using mortar and pestle (mass ratio 1:3) to get a uniform mixture. The mixture dispersed in ethanol is further sonicated for 30 min using a bath type sonicator followed by 12 h stirring at room temperature until homogeneous mixture was obtained. The mixture is then heated to instigate solvent evaporation by stirring at 60 °C. The solid material as obtained is again fired at 550 ºC for 3 h under Ar atmosphere at a rate of 5 ºC/min. The final product, thereby named MOFCN550, is used for further studies. During the double heat treatment procedure followed, the as synthesized MOFCN550 composite is pyrolyzed at 800, 900 and 1000 °C temperatures each time. The samples there after obtained are referred as MOFCN800, MOFCN900 and MOFCN1000, respectively.

In the second approach followed, the nitrogen source melamine is directly impregnated into the MOF crystal matrix. Here the MOF-5 crystals and melamine precursors are dispersed in ethanol and stirred overnight. The mixture is then similarly pyrolysed under argon flow at 900 °C. The resulting sample is denoted as MOF5CN.

6B.2. Results and Discussion

6B.2.1. Material characterization

6B.2.1.1. Electron microscopic analysis

The imaging has been carried to study the morphology of the resulting carbons. The TEM image of MOFC indicates the presence of structured pores in the carbon matrix **(Figure 6B.2**). MOFCN550 shows the presence of slate like g-C_3N_4 particles within the carbon matrix (**Figure 6B.2b**). Conversely, the TEM image of the resulting MOFCN900 indicates the formation of microporous sheets and confirms the retention of the sheet morphology during the transformation of g-C_3N_4 into nitrogen doped porous carbon (**Figure 6B.2c**).

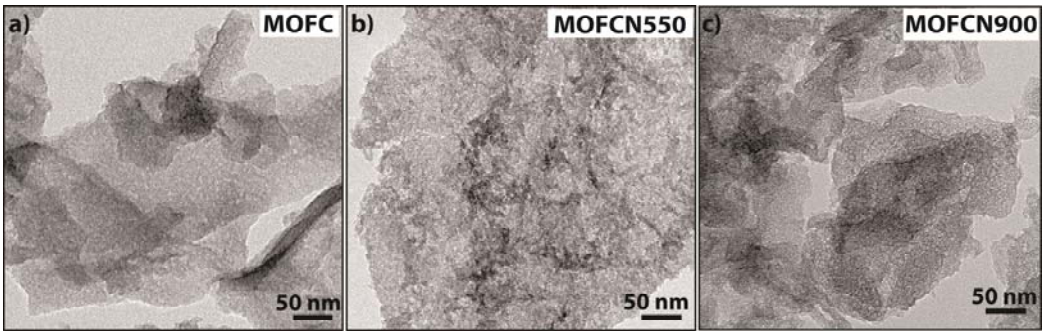

Figure 6B.2. *TEM images of a) MOFC, b) MOFCN550 and c) MOFCN900.*

The EDX analysis is also performed to analyze the elemental composition of the MOFC (**Figure 6B.3a**). The profile analysis evidently indicates the presence of C, O elements, without any traces of metal impurities. On the other hand, the EDX analysis of MOF5-CN indicates the presence of 1.2% nitrogen content with detectable Zn impurities, revealing the presence of the metal remains in the carbon matrix. However, after carbonization, the profile of the resulting electrocatalyst, *i.e*., MOFCN900, verifies the retention of the nitrogen element and removal of the metal residues from the carbon matrix (**Figure 6B.3b**). Through the EDX analysis a total of 7.18 % of nitrogen content is observed.

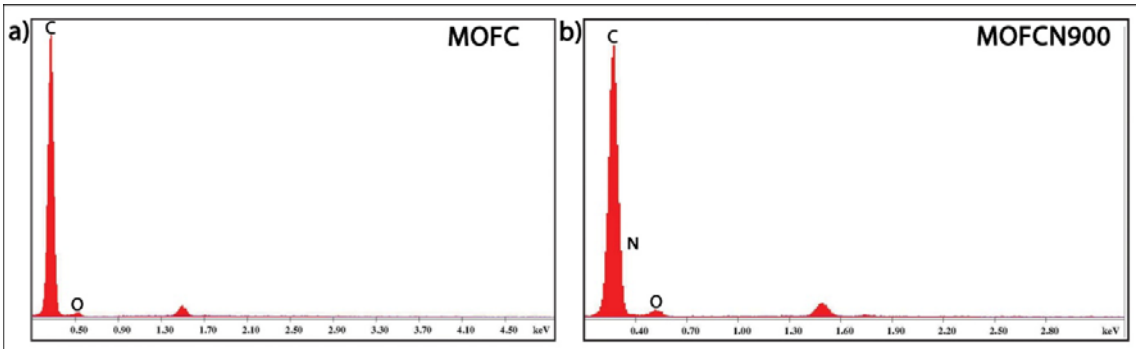

Figure 6B.3. *Energy dispersive X-ray (EDX) plots of MOFC and MOFCN900.*

6B.2.1.2. PXRD analysis

A strong diffraction peak at 27° in case of g-C_3N_4 corresponds to the interlayer stacking of the aromatic melamine units. The peaks corresponding to both g-C_3N_4 and MOFC could be observed in case of MOFCN550, which further confirms the melamine polymerization within the MOFC pores and its subsequent *in situ* formation of g-C_3N_4 at 550 °C. On annealing at higher temperatures, the spectra showed only one peak at 26.2°, indicating the breakdown of g-C_3N_4 moieties (**Figure 6B.4**).

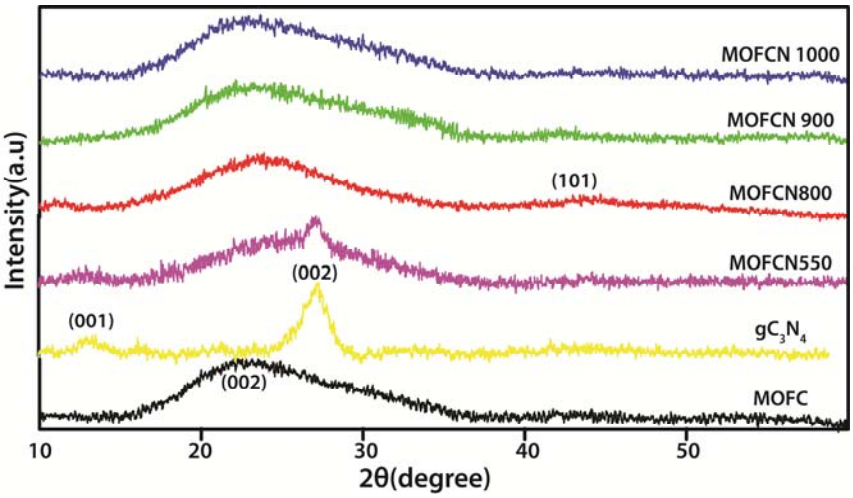

Figure 6B.4. *Combined PXRD spectra of the samples heated at different temperatures.*

The shift in the peak position indicates the probable intercalation of nitrogen atoms inside the carbon matrix, thereby confirming the successful introduction of the heteroatom into the carbon matrix. [28] On the other hand, the MOF5-CN spectrum shows peaks at 26° and 44°, similar to other carbons.

6B.2.1.3. FTIR and Thermogravimetric analysis of MOFCN550

The FTIR spectrum of the MOFCN550 has been recorded to determine the nature of functionalities present in it. The spectrum shows band at 810 corresponding to the C=N stretching frequency. The spectrum of MOFCN550 also indicates the presence of tri-s-triazine units at 1050–1600 cm^{-1}, which matches with that of the g-C_3N_4 (**Figure 6B.5a)**

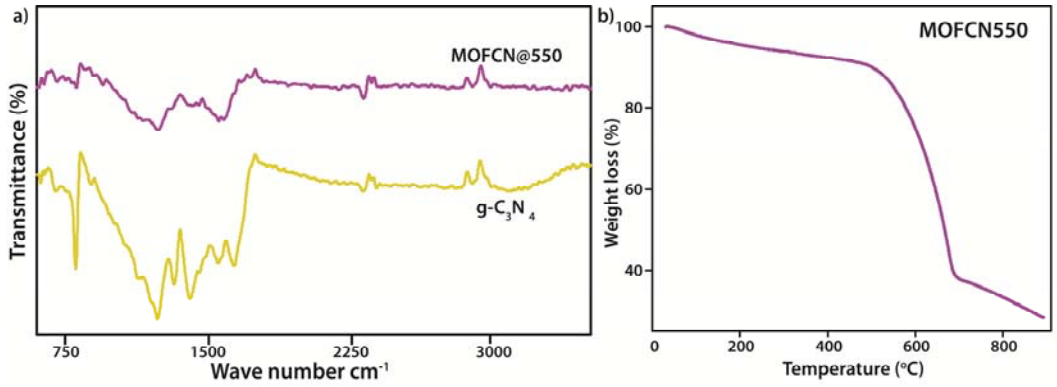

Figure 6B.5. *a) Comparative FTIR spectra of MOFCN550 and g-C_3N_4 and b) TGA curve of MOFCN550 in N_2 atm.*

The TGA analysis of the synthesised electrocatalysts has been carried out to determine their thermal stability. The thermo-gravimetric analysis of MOFCN550 reveals an initial weight loss at 70 ˚C, corresponding to the loss of the solvent molecules. This is

in turn followed by a major weight loss region from 600 to 900 °C, indicating the decomposition of the g-C_3N_4 units plugged inside the carbon pores which begins at around 550 ºC (**Figure 6B.5b**). On completion of the g-C_3N_4 decomposition, a total of 80 % weight loss is observed.

6B.2.1.4. Raman analysis

The Raman spectra of all the carbons show two characteristic peaks centered around ~1330 cm^{-1} (the disordered, or D band) and ~1580 cm^{-1} (the graphitic, or G band), respectively (**Figure 6B.6**).

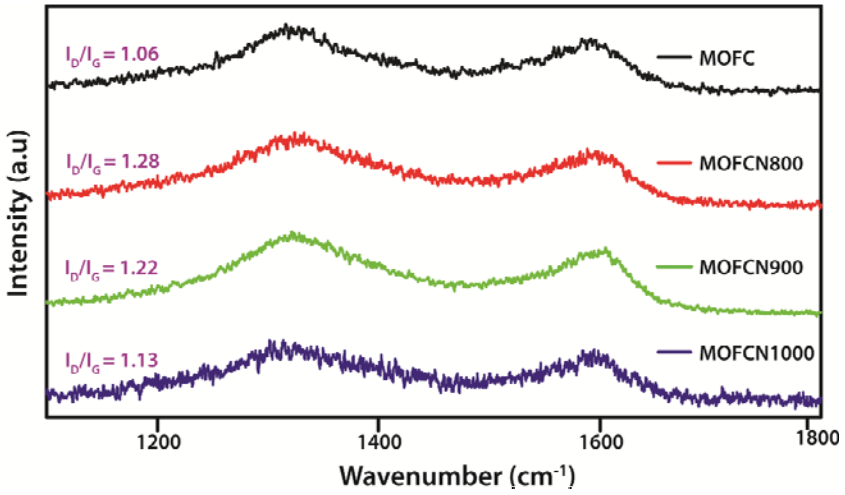

Figure 6B.6. *Combined Raman spectra of the prepared samples: MOFC, MOFCN800, MOFCN900 and MOFCN1000 respectively.*

On calculating the I_D/I_G ratios, it could be observed that MOFCN800 shows the highest I_D/I_G ratio of 1.28, followed by MOFCN900 (1.22) and MOFCN1000 (1.13). The study implies the effect of increasing carbonization temperature on graphitization. It is also noteworthy that with increase in temperature, the extent of nitrogen doping also decreases. Thus, an optimal carbonization temperature should be able to substantially graphitize carbon (in order to make it more conductive) and also allow sufficient retention of the dopants (in order to preserve its active sites).

6B.2.1.5. XPS analysis

In conjunction with the EDX analysis, the XPS spectral analysis also discloses a decline in the total nitrogen content with increasing the carbonization temperature. It is apparently observed that on increasing the temperature from 800 to 900 °C, the MOFCN800 shows a nitrogen content (8.26%) trailed by MOFCN900 (7.0 %) and MOFCN1000 (4.74 %). The study also verifies the conversion of pyridinic-N into

graphitic-N (**Figure 6B.7** and **Table 6B.1)** [29]. The ineffective heteroatom doping is supposedly caused by the rapid decomposition of g-C_3N_4 with increasing temperature.

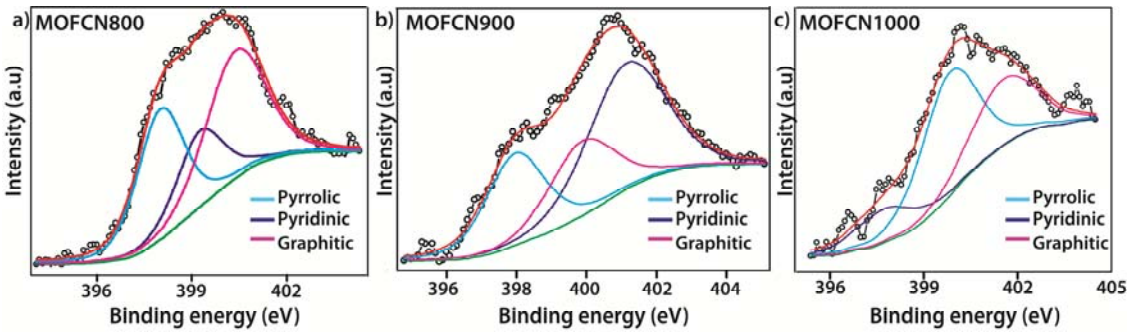

Figure 6B.7. *The deconvoluted XPS N1s spectra of MOFCN800, MOFCN900 and MOFCN1000, respectively.*

Table 6B.1. *Summary of the elemental composition of the prepared samples.*

Sample Name	Element	Atomic Percentage (%)	Graphitic	Pyridinic	Pyrrolic
MOFCN800	**C**	73.1			
	N	8.26	41.68	36.12	21.88
	O	18.0			
MOFCN900	**C**	83.09			
	N	7.0	47.53	27.97	24.48
	O	9.45			
MOFCN1000	**C**	80.73			
	N	4.74	25.6	12.46	62.1
	O	14.52			

6B.2.1.6. Surface area analysis

The surface area analysis of the MOF-derived carbons has been carried out to understand the effect of the post treatment procedures on the carbon porosity. The MOFC carbon (derived from MOF-5) has been observed to possess a BET surface area of 2184 m^2/g. The surface area of the MOFC is observed to drastically decrease on g-C_3N_4 assimilation, from 2184 to 276 m^2/g (**Figure 6B.8**). The abrupt decrease indicates the probable plugging of the g-C_3N_4 units inside the carbon pores. However, on carbonizing the MOFC-g-C_3N_4 composite at 900 ^oC, the surface area gets restored to 765 m^2/g. This

indicates that on decomposition of the g-C_3N_4 units, there is a revival of porosity in the carbon system.[28]

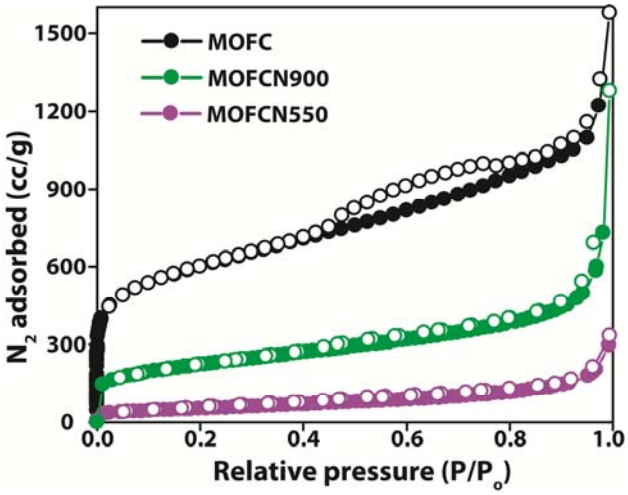

Figure 6B.8. *Comparative N_2 adsorption isotherms of MOFC, MOFCN550 and MOFCN900.*

6B.2.2. Electrochemical study

In order to verify the ORR activity of the post modified MOF-5 derived carbon, the electrochemical experiments are carried using a three-electrode system using Autolab PGSTAT 30 (Ecochemie). The Glassy carbon (GC) electrode (5 mm diameter) embedded in Teflon is used as the working, Ag/AgCl (saturated KCl) as the reference and high purity graphite rod as the counter electrodes correspondingly. Prior to the catalyst loading, the glassy carbon electrode is polished using 0.3 μm alumina slurry and then rinsed well with deionized water. The protocol used for sample is as follows: 1 ml of ethanol in water (3:2) solution is used to disperse 5 mg of the catalyst by sonication for 1 h. Once a homogenous ink is obtained, 10 μl of the aliquot is drop-casted on the GC electrode using a micro syringe. 3 μl of 0.1 % Nafion® binder ethanolic solution is subsequently coated onto the catalyst surface. In all the electrochemical studies, 0.1 M KOH is used as the electrolyte. The Rotating Ring Disk Electrode (RRDE) experiments are performed using a platinum ring disk electrode as a working electrode in a *BioLogic* VPM3 instrument. During the cyclic voltammetry and RDE experiments, highly pure (99.99%) O_2 and N_2 gases are used to achieve oxygen saturated and oxygen-free environments, respectively.

6B.2.2.1. Cyclic Voltammetry (CV) analysis

In the present work, the electrocatalyst coated GC electrode is initially dipped in 0.1 M KOH solution. The study begins with the saturation of the KOH electrolyte by bubbling N_2 gas into the solution. This displaces the oxygen molecules previously dissolved in the electrolyte. The resulting CV profile does not show any characteristic faradic peaks. However, on purging oxygen gas into the solution, a well defined cathodic peak appears which confirms the onset of the oxygen reduction reaction (**Figure 6B.9a**). A comparison of the CV profiles of all the synthesised electrocatalysts at 10 mV/s scan rate testifies the superior ORR activity of the MOFCN900 sample, in terms of both onset potential and current density (**Figure 6B.9b**).

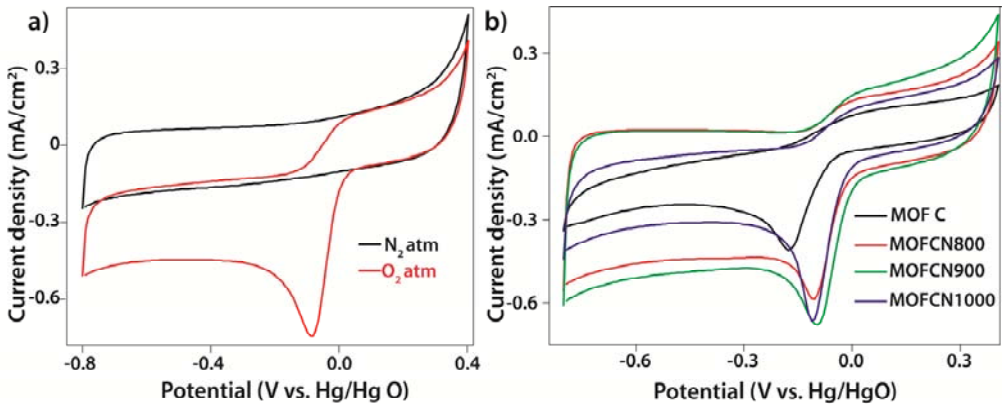

Figure 6B.9. *Cyclic voltammograms of a) in N_2 and O_2 saturated electrolyte and b) the MOF prepared electrocatalysts in 0.1 M KOH electrolyte, with a scan rate of 10 mV/s.*

6B.2.2.2. Linear Sweep Voltammetry (LSV)

On achieving O_2 saturation, the LSV studies have been carried out for a better estimation of the catalytic activity of the synthesised electrocatalysts. The study reveals the catalytic superiority of MOFC over the commercial Vulcan carbon with respect to both onset potential and the limiting current density ((**Figure 6B.10a**). This is mainly attributed to the high surface area and intrinsic porosity of MOFC, which is known to improve the mass transfer and facilitate rapid diffusion of the ions towards the catalytic sites. With the introduction of the heteroatoms into the carbon matrix, a notable shift in the ORR onset potential is observed, indicating an advance in the intrinsic activity of MOFC after N-doping (**Figure 6B.10**). In the study, the RDE experiments are carried out at 10 mV/s scan rate. The LSV study of MOFCN800 shows an onset potential of 0.0 V and a current density of 3.74 mA/cm^2, which is relatively higher than MOFC.

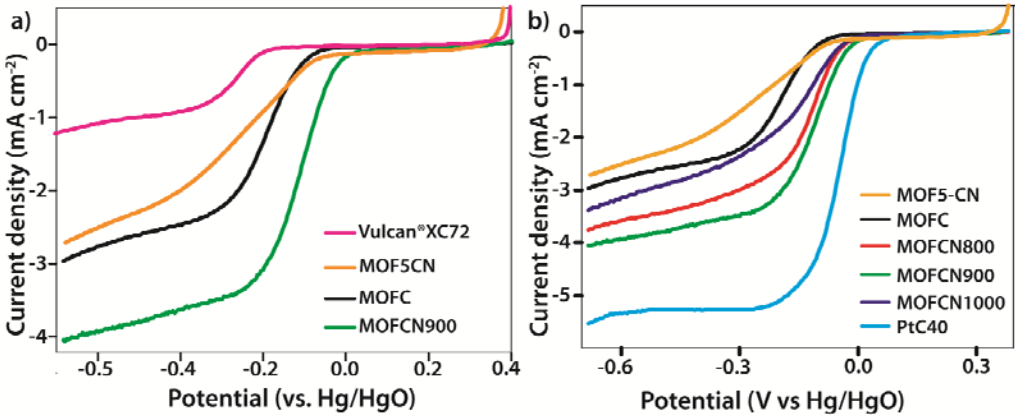

Figure 6B.10. *a) Comparative LSV plots of the homemade catalysts with the commercial Vulcan carbon and b) combined steady state polarization plots under O_2 saturated conditions in 0.1 M KOH at 10 mV/s scan rate and with electrode rotation of 1600 rpm.*

In case of MOFCN900, which is obtained on carbonization at 900 ˚C, the onset potential is observed to be positively shifted towards 0.035 V with an enhanced current density of 4.2 mA/cm^2. But with further increase in the carbonization temperature, the catalytic performance is found to abruptly decrease (**Figure 6B.10**). Thus among all the composites prepared, MOFCN900 is found to show the best electrochemical performance. This observation hints at the possible reduction in the catalytic sites, which in turn could be related to the decrease in the nitrogen content in the system, as found from the XPS and EDX analysis. The LSV comparison of MOFCN900 with 40 wt. % Pt/C catalyst verifies that the former fares comparably with the latter state-of-the-art catalyst by an overpotential difference of just 65 mV. The catalytic activity of MOFCN900 is also found to be better than most of the hetero atom doped carbon materials reported in the literature.[30] It is interesting to note that MOF5-CN as such is also found to be ORR active, with an onset at - 0.095 V. But the activity is far lesser than MOFCN900. The decrease in the catalytic activity ascertains the negative influence of the Zn impurities present in MOF5-CN, is believed to minimize the extent of nitrogen doping in the resulting carbon.

6B.2.2.3. K-L plot analysis and Rotating Ring Disc Electrode (RRDE) study

The reaction kinetics of the synthesised electrocatalysts is studied using the RRDE technique. Of all, the RRDE study of MOFCN900 indicates a low peroxide yield of 15% at -0.4 V (**Figure 6B.11a**). This also accounts for the basal carbon's enhanced activity and better ORR kinetics after nitrogen doping. The K-L plot analysis also indicates that

the reaction is mediated by an e^- transfer number of 3.12, which signifies that the reaction follows the desired 4 e^- pathway (**Figure 6B.11b**).

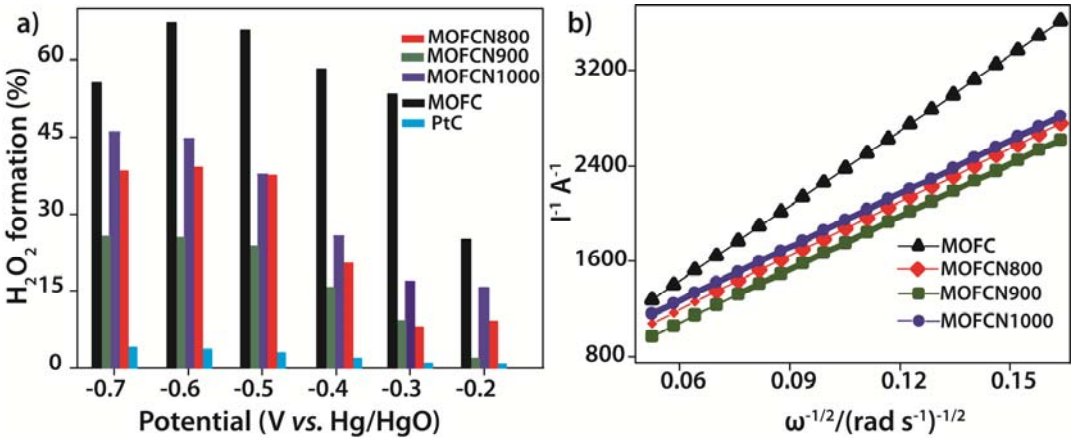

Figure 6B.11. *a) Bar graphs corresponding to the H_2O_2% formed using RRDE studies and b) K-L plots derived from the polarization studies.*

Thus, on observing the ORR performance of the current materials of interest, and as supported from the previous literature reports, it could be established that among all the nitrogen forms detected, the graphitic-N provides the chief active site for catalyzing ORR. [29] This study also verifies the fact that the performance of any ORR catalyst is largely decided by the amount of the doped nitrogen apart from the precise availability of the requisite nitrogen forms (primarily the graphitic and pyridinic N).

6B.2.2.4. Accelerated durability test (ADT) and Chronoamperometric study

ADT has been carried out to determine the electrochemical stability of the electrocatalysts. It is carried out by cycling the potential applied to the working electrode between -0.15 to 0.15 V for 1000 cycles. The materials under this study are the best performing MOFCN900 and the state-of-the-art 40 wt. % Pt/C catalysts. The LSV study after ADT clearly indicates that the 40 wt. % Pt/C experiences a negative potential shift of 40 mV (*vs.* Hg/HgO), while the degradation of the potential in case of the in-house metal-free catalyst (MOFCN900) is just 30 mV (**Figure 6B.12a**). The study thereby confirms the better electrochemical stability of the in-house MOFCN900 catalyst. Further, the chronoamperometric study is also carried out to determine the CO tolerance ability of the in-house MOFCN900 catalyst in comparison with the standard 40 wt. % Pt/C catalyst. Upon addition of CH_3OH, MOFCN900 doesn't show any change in the ORR current unlike that of the Pt catalyst, (**Figure 6B.12c**). This study thereby validates the high CO tolerance of the MOFCN900 catalyst.

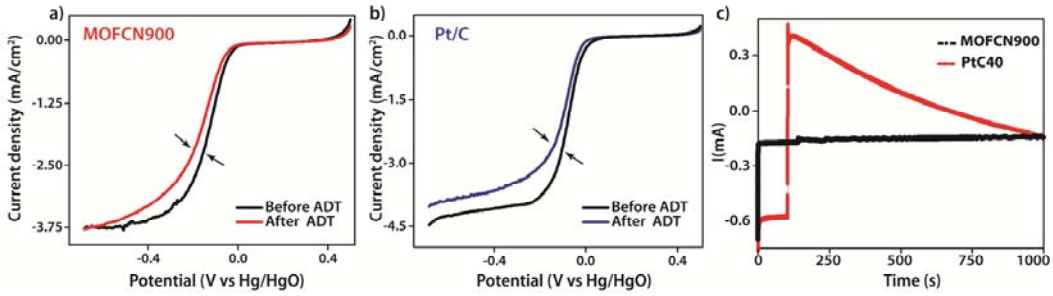

Figure 6B.12. *a) and b) Linear sweep voltammograms of (a) PtC40 and (b) MOFFCN900 before and after ADT at a rotation speed of 1600 rpm and a scan rate of 10 mV/ S; c) chrono amperometric responses on CH_3OH addition at 150 s.*

6.2. Conclusion

The carbon research implicitly indicates that the kind of template used and nature of the precursors selected along with the carbonizing time and temperature play a fundamental role in deciding the fate of the final carbons. The present chapter discusses the role of MOFs as self-sacrificial templates for synthesizing high surface area carbons with well-ordered pores The first part of the chapter illustrates the conversion of non-porous MOFs to porous carbons by way of direct carbonization without any added carbon source. In the study, an attempt is made to understand the influence of the nature of the MOF ligand on the end carbon porosity. The as-synthesized MOF-derived carbons have been exclusively considered for their gas adsorption properties and electrochemical functions. They are observed to display porosity-dependent H_2 uptake up to 260 cc/g, CO_2 uptake up to 107 cc/g at 273 K and 1 atm pressure and supercapacitance up to 170 F/g at 10 mV/s. The second part of the chapter discusses a new route of post-modifying the MOF-derived carbon towards development of a metal-free, hetero atom doped electrocatalyst with increased ORR activity and enhanced mass transport character. Herein, the macro porosity of the MOF-derived carbon is effectively utilized as a nitrogen reservoir through initial plugging of the g-C_3N_4 units *via in situ* polymerization of melamine. The developed electrocatalyst possesses high nitrogen content and shows high oxygen reduction activity, high fuel selectivity and superior durability when compared to that of the commercial Pt based catalysts. This route thus opens a new passageway for designing and developing metal-free fuel cell cathodes. These nitrogen-doped carbon composites have prospective applications in a range of renewable energy areas such as solar cells, metal-ion batteries etc.

6.3. References

[1] J. Lee, J. Kim, T. Hyeon, *Adv. Mater.* **2006**, *18*, 2073.

[2] (a) Z. G. Shi, Y.Q.Feng , L. Xu, S.L. Da, M. Zhang, *Carbon*, **2004**, *42* ,1677. (b) J. E. Hampsey, Q. Hu, L. Rice, J.Pang, Z. Wu and Y. Lu, *Chem. Commun.,* **2005**, 3606. (c) J. S. Yu, S. B. Yoon, G. S. Chai, *Carbon*, **2001**, *39*, 1421. (d) D. Yuan, X. Yuan, W. Zou, F. Zeng, X. Huang , S. Zhou, *J. Mater. Chem*., **2012**, *22*, 17820.

[3] (a) J. Lee, S. Han, T. Hyeon, *J.Mater.Chem.,* **2004**,*14*, 478. (b) K. P. Gierszal, T. Kim, R. Ryoo, M. Jaroniec, *J. Phys. Chem. B,* **2005**, *109*, 23263.(c) A. H. Lu, W. Schmidt, B. Spliethoff, F. Schüth, *Adv. Mater.*, **2003**, *15*, 1602. (d) P. Pachfule, B. P. Biswal, R. Banerjee, *Chem. Eur. J.*, **2012**, *18*, 11399.

[4] (a) X. Wang, C. Liang, S. Dai, *Langmuir*, **2008**, *24*, 7500.(b) R. Liu, Y. Shi, Y. Wan, Y. Meng, F. Zhang, D. Gu, Z. Chen, B. Tu, D. Zhao, *J. Am. Chem. Soc.*, **2006**, *128*, 11652.

[5] A. Olejniczak, M. Lezanska, J. Wloch,A. Kucinskaa, J. P. Lukaszewicza , *J. Mater. Chem. A*, **2013**, *1*, 8961.

[6] (a) W. Chaikittisilp, K. Ariga, Y. Yamauchi, *J. Mater. Chem. A*, **2013**, *1*, 14. (d) J. Hu, H. Wang, Q. Gao, H. Guo, *Carbon*, **2010**, *48*, 3599. (b) S. Ma, G. A. Goenaga, A.V. Call, D. J. Liu, *Chem. Eur. J.*, **2011**, *17*, 2063. (e) W. Cho, S. Park , M. Oh, *Chem. Commun.*, **2011**, *47*, 4138.

[7] W. Chaikittisilp, M. Hu, H. Wang, H. S. Huang, T. Fujita, K. C. W. Wu, L. C. Chen, Y. Yamauchi, K. Ariga, *Chem. Commun.*, **2011**, *47*, 8124.

[8] (a) P. Su, L. Jiang, J. Zhao, J. Yan, C. Li, Q. Yang, *Chem. Commun.*, **2012**, *48*, 8769.

[9] S. J. Yang, T. Kim, J. H. Im, Y. S. Kim, K. Lee, H. Jung, C. R. Park, *Chem. Mater.* **2012**, *24*, 464.

[10] (a) S.Lim, K. Suh, Y. Kim, M.Yoon, H. Park, D.N. Dybtsev, K. Kim, *Chem. Commun*., **2012**, *48*, 7447. (b) H.-L. Jiang, Q. Xu, *Chem. Commun*. **2011**, *47*, 3351. (c) H.L. Jiang, B.Liu, Y.Q. Lan, K. Kuratani, T. Akita, H. Shioyama, F. Zong, and Q. Xu, *J. Am. Chem. Soc.*, **2011**, *133* , 11854.

[11] (a) R. J. Kupplera, D. J. Timmonsb, Q. R. Fanga, J.R. Li, T. A. Makala, M.D. Younga, D. Yuana, D. Z.,W. Zhuanga, H.C. Zhoua, *Coordin.Chem.Rev.,* **2009**, *253*, 3042. (b)F. X. L. Xamena, A. Corma, H. Garcia, J. Phys. Chem. C, **2007**, *111*, 80. (c) S. B. Yoon, J. Y. Kim, J. S. Yu, *Chem. Commun.* **2001**,*5*,59. (d) H. L. Jiang,

B.Liu, Y. Q. Lan, K. Kuratani, T. Akita, H. Shioyama, F. Zong, Q. Xu , *J. Am. Chem. Soc.,* **2011**, *133*, 11854.

[12] H. Deng, S. Jin, L. Zhan, Y. Wang, S. Qiao, L. Tang, X. Liang, W. Qiao, L. Ling, *Mater. Lett.,* **2010**, *64*, 1187.

[13] S. Lim, K. Suh, Y. Kim, M.Yoon, H. Park, D.N. Dybtsev, K. Kim, *Chem. Commun.,* **2012**, *48*, 7447.

[14] (a) B. Liu, H. Shioyama, H. Jiang, X. Zhang, Q. Xu, *Carbon*, **2010**, *48*, 456. (b) B. Liu, H. Shioyama, T. Akita, Q. Xu, *J. Am. Chem. Soc*., **2008**, *130*, 5390.

[15] (a) K. S. Yang, Y. J. Yoon, M. S. Lee, W. J. Lee, J. H. Kim, *Carbon*, **2002**,*40,* 897. (b) K. Lenghausa, G. G. Qiaoa, D. H. Solomona, C. Gomezb, F. R. Reinoso, A. S. Escribano, *Carbon*, **2002**, *40*, 743. (c) A. Y. Jee, M. Lee, *Carbon*, **2009**, *47*, 2528. (d) Y. Gogotsi , S. Dimovski , J. A. Libera, *Carbon*, **2002**, *40*, 2263.

[16] (a) M. A. de la Casa-Lillo, F. Lamari-Darkrim, D. Cazorla-Amoros, A. Linares-Solano, *J. Phys. Chem. B*, **2002**, *106*, 10930. (b) M. Choi, R. Ryoo, J. Mater. Chem., 2007, 17, 4204. (c) H. Wang, Q. Gao, J. Hu, Z. Chen, *Carbon*, **2009**,*47*, 2259.

[17](a) A. G. Pandolfo, A.F. Hollenkamp, *J. Power Sources*, **2006**, *157*, 11. (d) E. Frackowiaka, F. Beguinb, *Carbon*, **2001**, *39*, 937.

[18](a) Y. Wen, G. Cao, J. Cheng, Y. Yang, *J. Electrochem. Soc*., **2005**, *152*, A1770. (b) Z. Wang, X. Zhang, X. Liu, M. Lv, K. Yang, J. Meng, *Carbon*, **2011**, *49*,161.

[19](a) W. Shen , W. Fan, *J. Mater. Chem. A*, **2013**, *1*, 999. (b) Y. El-Sayed , T. J. Bandosz, Langmuir, 2002, 18, 3213. (c) M. F. R. Pereira, S. F. Soares, J. J.M. Orfao, J. L. Figueiredo, *Carbon*, **2003**, *41*, 811.

[20] (a) C. Largeot, C. Portet, J. Chmiola, P. L. Taberna, Y. Gogotsi, P. Simon, *J. Am. Chem. Soc.,* **2008**, *130*, 2730.(b) Y. Xia, G. S. Walker, D. M. Grant, R. Mokaya, *J. Am. Chem. Soc*. ,**2009**, *131*, 16493.

[21] a) R. Liu, D. Wu, X. Feng, K. Müllen, *Angew. Chem., Int. Ed*. **2010**, *49***,** 2565. b) Z. Chen, D. Higgins, A. Yu, L. Zhang, J. Zhang, *Energy Environ. Sci*, **2011**, *4*, 3167. c) T. Palaniselvam, R. Kannan K.Sreekumar, *Chem. Commun*, **2011**, *47*, 2910. d) M. J. Ju, J. C. Kim, H.J. Choi, I. T. Choi, S. G. Kim, K. Lim, J. Ko, J.J. Lee, I.Y. Jeon, J.B Baek, H. K. Kim, *ACS Nano*, **2013**, *7* , 5243.

[22] a) Y.Tang, B. Allen, D. Kauffman, A. Star, *J. Am. Chem. Soc*. **2009**, *131***,** 13200.b) K.Gong, F. Du, Z. Xia, M.Dustock, L.Dai, *Science,* **2009**, *323*, 760.

[23] (a) X. Li, H. Wang, J. T. Robinson, H. Sanchez, G. Diankov, H. Dai, *J. Am. Chem. Soc.* **2009**, *131,* 15939. (b) H. Wang, T. Maiyalagan, X. Wang , *ACS Catal.* **2012**, *2*, 781.

[24](a)Y.Wang, Y.Shao, D.Matson, J.Li, Y.Lin, *ACS Nano,* **2010**,*4,* 1790. (b) T. Palaniselvam, B. P. Biswal, R. Banerjee, K. Sreekumar , *Chem. Eur. J.* **2013**, *19*, 9335.

[25](a) C. H. Choi, S. H. Park, S. I. Woo, *ACS Nano*, **2012**, *6*,7084. (b) S. Wang , E. Iyyamperumal, A. Roy, Y. Xue, D. Yu, L. Dai, *Angew. Chem.* **2011**, *123*, 11960.

[26] (a) Y. J .Zhang, T. Mori, J. H. Ye, *Sci. Adv. Mater,* **2012**, *4*, 282. b) X. Wang, K. Maeda, A. Thomas, K. Takanabe, G. Xin, J. M. Carlsson, K. Domen, M. Antonietti *Nat. Mater,* **2009**, *8,*76.

[27] (a) J. Li, Y. Zhang, X. Zhang, J. Han, Y. Wang, L. Gu, Z. Zhang, X. Wang, J. Jian, P. Xu, Bo Song , *Appl Mater Interfaces*, **2015**,*7*, 19626 (b) M. Kim, S. Hwang, J.-Sung Yu, *J. Mater. Chem*., **2007**, *17*, 1656.

[28] K. Parvez, S.Yang, Y. Hernandez, A. Winter, A. Turchanin, X.Feng, K. Mullen, *ACS Nano*, **2012**, *6,* 9541.

[29] L. Lai, J. R. Potts, D. Zhan, L. Wang, C. K. Poh, C. Tang, H. Gong, Z. Shen, J. Lin, R. S. Ruoff, *Energy Environ .Sci.*, **2012**, *5*, 7936.

[30] (a) S. A. Wohlgemuth, R. J. White, M. G. Willinger, M.M. Titiricia, M. Antoniettia, *Green Chem.,* **2012***, 14,* 1515. (b) Y. Zheng, Y. Jiao, J. Chen, J. Liu, J. Liang, A. Du, W. Zhang, Z. Zhu, S. C. Smith, M. Jaroniec, G. Q. Lu, S. Z. Qiao, *J. Am. Chem. Soc.* **2011***,* 133*,* 20116.

Chapter 7

Summary and Conclusions

This chapter presents an overview of the chief observations and conclusions presented in each of the chapters of the thesis. The chief focus of the present thesis is the excavation of the applications of porous polymeric materials namely MOF, COF, metallogel and their derivates as components for fabricating electrochemical energy devices *viz*., fuel cell, supercapacitor, water electrolyzer etc. Herein the porous materials are mainly utilized to improve the electrode-electrolyte interface, which is considered to be vital for improving the performance of any electrochemical system. The work showcases the ways in which porous materials are selectively functionalized and rendered competent to catalytically drive the energetically important reactions like water oxidation, hydrogen generation, oxygen reduction reaction etc. The enormous intrinsic porosity of the materials is utilized to allow facile movement of ions towards and away from the electrochemical interface. The highly stable porous skeleton is employed to load ion carriers and thereafter examined for their functioning as electrolyte materials at relatively drastic conditions compared to the conventional materials.

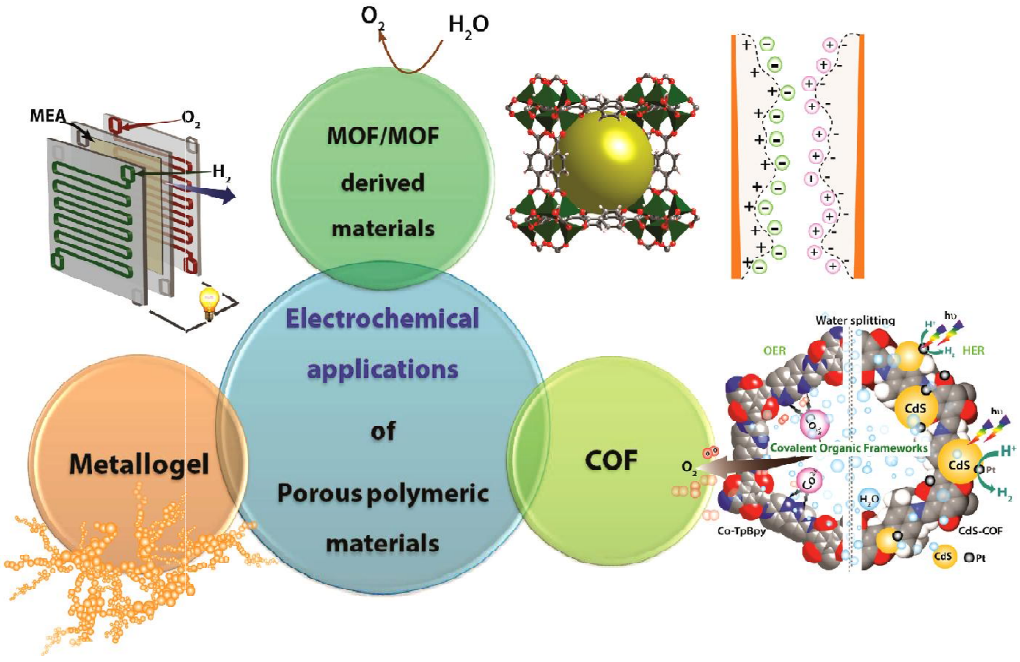

7.1. Summary

The chief spotlight of thesis is to excavate the electrochemical applications of porous polymeric materials namely metal organic gels, metal organic framework (MOF), covalent organic framework (COF) and their derivatives. It is observed that most of these polymeric materials are poor conductors of electrons. The work mainly demonstrates the ways in which protogenic groups can be incorporated within the porous framework and thereafter used as intrinsic/extrinsic ion conducting materials for energy devices such as fuel cells. In another instance, these materials are used as nanoreactors and made catalytically active *via* selective pore functionalization by anchoring coordinating moieties/ active nanoparticles and then tried as catalysts for energetic electrochemical reactions like OER, H_2 production from water etc. The work also highlights the use of robust porous frameworks like MOFs to obtain pure, microporous carbons that could be used for making electrodes of energy storage devices like supercapacitors. Lastly, the post modification of the MOF-derived carbon has been attempted to improve the electrocatalytic activity of the basal carbons towards oxygen reduction reaction activity in alkaline medium.

The major accomplishments of the thesis work are summarized below:

Fe-based coordination polymer gels as proton conductors and their typical transformation into Fe-metal organic frameworks

The sol-gel technique has been one of the renowned wet-chemical techniques used for improving the size of the crystals inorder to enable a clear-cut recognition of the molecular structures using X-Ray diffraction techniques. This technique has been useful in cases of growth of single crystals which does not have appropriate solvents for recrystallization. It is interesting to note that both MOFs and metallogels belong to the regime of supramolecular materials. Interestingly, there exist few examples of the fusion of the MOFs into polymeric gels. However, the conversion of metallogels into MOFs has been hardly observed. Herein, a simple and efficient conversion of Fe^{3+} based metallogels into Fe-MOFs by $PdCl_2$ mediated gel degradation is discussed. The conversion protocol involves a one pot-two step process for the bulk synthesis of large-sized single crystal Fe-MOFs, which are otherwise difficult to synthesize. Herein, we also introduce two novel MOF crystal structures, Fe-Pd-BTC-DEF (3-D) and Fe-BTC-NMF (2-D)

achieved *via* Fe-metallogel degradation. This procedure enables an effective utilization of the metallogel systems as reservoirs for furnishing the needed metal ions as well as organic linkers for *in situ* MOF formation. This also eliminates the need of routinely used inert gel matrix, which demands an external stimulus for the matrix removal and final recovery of the crystals.

The second part of the work presents a directed proposal for the synthesis of a proton conducting PEMFC solid electrolyte by immobilizing protogenic, phosphate ester based ligand *via* gelation with Fe^{3+} ion using high boiling solvent namely, DMF. The FNPA metallogel carries distinct proton conducting ability due to the presence of one-dimensional nanofibrillar structure, which favors proton propagation using minimum activation energy. The entrapment of such phosphoric acid derived ligand eliminates the need for loading any additional proton carrier molecules and also eradicates the problems of carrier leaching, a limitation of the present phosphoric acid doped polybenzimidazole (PBI) membranes. The Membrane Electrode Assembly (MEA) fabricated using the FNPA xerogel proves to be gas tight giving a maximum OCV of 1.02 V ± 0.02 at 120 ˚C. The *in situ* impedance measurements performed on the MEA shows that the FNPA xerogel is a potential PEMFC membrane material with a high anhydrous proton conductivity of 2.4×10^{-2} S/cm. For the first time, proton conducting ability of the FNPA metallogel is directly demonstrated *via* linear fuel cell polarization tests. A power density of 0.94 mW/cm^2 (at 0.6 V) validates the electrical circuit completion of the fuel cell. These studies undoubtedly prove the inherent ability of the gel materials to conduct protons at elevated temperature under dry conditions which is an immediate requisite for high temperature PEMFC's.

Covalent Organic Framework (COF) as prototype solid electrolyte in Proton Exchange Membrane Fuel Cells

Covalent organic frameworks (COFs) belong to the class of porous organic materials with immense potential to be applied in many fields such as gas adsorption and separation, catalysis, sensing etc. However, the synthesis of such stable COFs involves an arduous protocol, which makes their scaling up very difficult. On this aspect, lately, a simpler and greener mechanochemistry route is used to synthesize COFs with a near quantitative yield. However, such mechanochemically-synthesized COFs show poor porosity and crystallinity compared to their solvothermal counterparts thereby restricting their use as high surface area materials and making them unrealistic for any practical application. Hitherto, this feature could be taken

advantage of to employ them as gas separators owing to their poor porosity. By integrating proton conducting functionalities into such stable mechanosynthesized COFs, a unique way to utilize them as solid electrolytes in proton exchange membrane fuel cell is herein demonstrated. The mechanochemically synthesized COFs possess sufficiently high surface area thereby allowing a high amount of H_3PO_4 impregnation. Most importantly, the COF framework remains intact upon acid doping, thereby permitting a long time PEMFC operation. Owing to its poor porosity, the H_3PO_4 loaded mechanochemically synthesized COF is thereby found to outperform its solvothermal counterpart in its efficacy when operated under real fuel cell operating conditions. The mechanochemically synthesized COFs is found to inhibit fuel crossover and builds up a stable satisfying Open Circuit Voltage (OCV = 0.93 V at 50 °C), thereby establishing itself as an effective solid electrolyte material (showing proton conductivity of 1.4×10^{-2} S/cm) for PEMFCs, while the solvothermally synthesized COF proves unproductive under similar conditions. Interestingly, although the pristine COFs are found to exhibit negligible proton conductivity, on phosphoric acid loading, the COFs drastically show the onset of proton conducting activity at anhydrous conditions. This demonstration is thus believed to unfurl more avenues to employ such mechanochemically synthesized materials for energy applications such as ion conducting electrolytes for high temperature fuel cells and batteries.

Covalent Organic Framework (COF) as catalysts for water splitting half-cell reactions

The development of a stable, efficient Oxygen Evolution Reaction (OER) catalyst capable of oxidizing water is one of the premier challenges in the conversion of solar energy to electrical energy, owing to its poor kinetics. The development of an earth-abundant, stable catalyst operating at neutral conditions at low overpotential thus remains a deep-seated chemical challenge. The COF functionalized with the recognized critical structural motif for Oxygen Evolution Reaction (OER) is thereby tested for its water oxidation activity in neutral pH conditions. Herein, a bipyridine containing covalent organic framework (TpBpy) is utilized as a heterogeneous OER catalyst by way of engineering active Co (II) ions into its porous framework. The as obtained Co-TpBpy retains high accessible surface area (450 m^2/g) and shows exceptional stability even after 1000 cycles and 24 h of OER activity in phosphate buffer at neutral pH conditions with a low overpotential of 400 mV at 1 mA /cm^2 current density. The cobalt modified TpBpy is observed to display high faradaic efficiency of 95 % and turn-over frequency (TOF) of 0.19 /s at pH 7. The Co-TpBpy catalyst is observed to exhibit a Tafel slope

of ~ 60 mV, highly indicative of the one e^- [Co (II)/Co (III)] transfer kinetics involved in the production of oxygen from water in neutral solutions. The work demonstrates the material's exceptional stability towards water oxidation activity owing to its highly porous structure which assists the easy passage of the evolved O_2 molecules thereby improving their long term stability (up to 24 h) in neutral pH. The high water oxidation activity, consistent catalytic activity and strong durability of Co-TpBpy arise from the synergetic effect of the inherent porosity and presence of coordinating bipyridine units in the COF skeleton. This work thereby pioneers a way for the synthesis and utilization of electrochemically active COFs as highly stable, molecularly tunable, heterogeneous catalysts for important energetic reactions involved in a variety of energy devices such as water splitting, supercapacitors, batteries etc.

In the second part, a highly stable COF, TpPa-2 has been employed as a support for anchoring the CdS nanoparticles on account of its π conjugated, 2-D framework, which could possibly help in an efficient charge transfer thereby stabilising the nanoparticles. This hybrid is then used as photo catalyst for visible light driven H_2 production.Remarkably, on addition of just 1 wt% of COF, a drastic increase in the H_2 production with 1320 $\mu molh^{-1}g^{-1}$ is observed, which is about ten times higher compared to that of the pristine CdS. Among all the synthesized hybrids, CdS-COF (90:10) is found to display the highest photocatalytic activity with 3678 $\mu molh^{-1}g^{-1}$ of H_2 production. The photocatalytic activity is found to be consistent without any apparent decrease in the activity for the next three consecutive cycles with an apparent quantum yield of 4.2% at 420 nm. To validate the postulate, impedance measurements are also employed to carry out the Mott-Schottky (MS) study under dark conditions. The study hints at a high probability of the transfer of the as-generated photoelectrons triggered by illumination of visible light from CdS to the COF matrix. Thus the stable COF support is observed to improve the photo stability of the deposited CdS apart from effecting the recombination suppression, resulting in a remarkably high activity of the hybrid compared to that of the pristine CdS.

Metal Organic Framework (MOF)-derived porous carbons as electrode materials towards fabrication of energy devices

The carbon research highly implies that the type of template used and nature of the precursors selected along with the carbonizing time and temperature decides the fate of the final carbons. In this direction, the role of MOFs as self-sacrificial templates for synthesizing high surface area carbons with well-ordered pores is discussed. The first part illustrates the conversion of non-

porous MOFs to porous carbons by way of its direct carbonization without any added carbon source. In this study, an attempt is made to understand the influence of the nature of the MOF ligand on the end-carbon porosity. The study importantly reports the conversion of less employed non-porous MOFs to more useful porous carbons besides studying the influence of the ligands present in the MOF architecture on the properties of carbons resulting from their direct carbonization. They are also observed to display porosity-dependent H_2 uptake up to 260 cc/g, CO_2 uptake up to 107 cc/g at 273 K and 1 atm pressure and supercapacitance up to 170 F/g at 10 mV/s. This work therefore presents an exclusive fundamental study of the pore characteristics and the properties of the MOF-derived carbons.

The second part of the chapter discusses a new route of post-modifying the MOF-derived carbon towards development of a metal-free, hetero atom doped electrocatalyst with increased ORR activity and enhanced mass transport character. Herein, the macro porosity of the MOF-derived carbon is effectively utilized as a nitrogen reservoir through initial plugging of the g-C_3N_4 units *via in situ* polymerization of melamine. The as developed electrocatalyst possesses high nitrogen content and shows high oxygen reduction activity, high fuel selectivity besides superior durability when compared to that of the commercial Pt based ORR catalysts. This route thereby opens a new route for designing and developing metal-free fuel-cell cathodes. These nitrogen-doped carbon composites have prospective applications in a range of renewable energy areas such as solar cells, metal-ion batteries etc.

7.2. Future prospective

It is well understood that no single energy device can meet all the global power requirements. By 2030, an alarming 50% increase in the world's energy requirement is expected. Among all the energy systems, the electrochemical energy devices like batteries, supercapacitor, and fuel cell systems show promising signs of revolutionizing the future energy technology in terms of their cleaner, greener and safer ways of operation. However, most of these systems either fall short in terms of their energy density or power density. Thus efforts are on to synthesize and develop new materials inorder to improve the energy as well as power efficiency of the energy systems. The present thesis focuses on the synthesis and utilization of porous polymeric materials namely MOF, COF, metallogels and their derivatives for electrochemical applications. In Chapter-3, metallogels are successfully tried as proton conducting materials for proton exchange membrane

fuel cell. The xerogel pellets used for single cell fabrication reveal completion of the fuel cell circuit besides efficiently conducting protons at the real operating conditions. However, the material needs further thinning down inorder to improve the fuel cell performance. Thus fabricating a membrane using such metallogel materials could possibly help in the development of anhydrous ionic electrolytes, which is one of the prime requisites of a high temperature fuel cell. The Chapter-4 demonstrates the use of a chemically stable COF for loading acidic proton carriers. Although the resulting material is found to be an optimistic extrinsic proton conducting electrolyte for PEM fuel cell, the development of intrinsic proton conducting material is highly desirable as it would eliminate the risk of carrier leaching during the course of the fuel cell operation. In Chapter-5, the COF is pre-functionalized with coordinating units and then tried as water oxidation electrocatalyst after cobalt modification. Although the present activity seems to be in par with the analogous homogenous catalysts, the electrical conductivity of the system could be a major factor hindering its full scale electrochemical activity. Therefore an electrically conducting COF or at least a composite of the COF with a conducting material could be expected to be the next future line of this work wherein an improvement in the electrocatalytic activity is most likely. Lastly the Chapter-6 discusses the use of MOFs as 'self-sacrificial hard templates' for making porous carbons. The carbons derived from Zn-based MOFs are found to be containing pure carbon matrix owing to the reduction of ZnO in presence of hot carbon and thereby exhibit a typical electrical double layer nature. Thus it is more likely that the carbonization of other transition metal based MOFs like Mn-MOFs, Fe-MOFs, Co-MOFs could possibly result in formation of metal-oxide/C composites. This would presumably improve the energy density of the resulting supercapacitor, as now the pseudo capacitance of the metal oxide is more likely to add on to the double layer capacitance of the carbon matrix.

Patents and Publications

Patents filed

(1) N-doped porous carbon electrocatalyst and process for preparation thereof, **WO2015040638**.

(2) Phytic acid based metallogel and applications thereof, **WO2016024292**.

Journal Articles

(1) Cobalt modified Covalent Organic Framework as a robust water oxidation electrocatalyst

Harshitha Barike Aiyappa, Jayshri Thote, Digambar Balaji Shinde, Rahul Banerjee, and Sreekumar Kurungot, ***Chem. Mater.*, 2016**, *28*, 4375–4379.

(2) Constructing Covalent Organic Frameworks in Water *via* Dynamic Covalent Bonding

Jayshri Thote, **Harshitha Barike Aiyappa**, Raya Rahul Kumar, Sharath Kandambeth, Bishnu P. Biswal, Digambar Balaji Shinde, Neha Chaki Roy and Rahul Banerjee, ***IUCrJ,* 2016**, Accepted Article.

*** equal contribution**

(3) Multifunctional copper dimer: structure, band gap energy, catalysis, magnetism, oxygen reduction reaction and proton conductivity.

Debraj Sarkar, Purna Chandra Rao, **Harshitha Barike Aiyappa**, Sreekumar Kurungot, Sudip Mandal, Kothandaraman Ramanujam and Sukhendu Mandal, ***RSC Adv.***, **2016**,6, 37515-37521.

(4) Mechanochemically Synthesized Covalent Organic Framework as Proton-conducting Solid Electrolyte

Digambar Balaji Shinde, **Harshitha Barike Aiyappa***, Mohitosh Bhadra, Bishnu P. Biswal, Pritish Wadge, Sharath Kandambeth, Bikash Garai, Tanay Kundu, Sreekumar Kurungot and Rahul Banerjee, , ***J. Mater. Chem., A,* 2016**, 4, 2682-2690.

*** equal contribution**

(5) Fe (III) Phytate Metallogel as a Prototype Anhydrous, Intermediate Temperature Proton Conductor

Harshitha Barike Aiyappa, Subhadeep Saha, Pritish Wadge, Rahul Banerjee* and Sreekumar Kurungot*, ***Chem. Sci.***, **2015**, 6, 603-607.

(6). Phosphate Enriched Polyoxometalate Based Ionic Salts for Proton Conduction.

Chandan Dey, Tanay Kundu, **Harshitha Barike Aiyappa** and Rahul Banerjee, ***RSC Advances***, 2015, 5, 2333-2337.

(7) A Distinctive PdCl2 Mediated Transformation of Fe-based Metallogels into Metal Organic Frameworks.

Harshitha Barike Aiyappa, Subhadeep Saha, Bikash Garai, Jayashri Thote, Sreekumar Kurungot, and Rahul Banerjee, ***Cryst. Growth Des.,*** **2014**, 14, 3434-3437.

(8) Post modification of MOF derived carbon via g-C3N4 entrapment for efficient metal-free oxygen reduction reaction.

Sekar Pandiaraj*****, **Harshitha Barike Aiyappa***, Rahul Banerjee and Sreekumar Kurungot, ***Chem Commun.***, **2014**, 50, 3363-3366.

*** equal contribution**

(9) Covalent Organic Framework-CdS Hybrid as a Prototype Photocatalyst for Visible-Light-Driven Hydrogen Production.

Jayshri Thote*****, **Harshitha Barike Aiyappa***, Aparna Deshpande, David Díaz Díaz, Sreekumar Kurungot, and Rahul Banerjee, ***Chem Eur. J.,*** **2014**, 20,15961–15965.

*** equal contribution**

(10) Porous Carbons from Non-Porous MOFs: Influence of Ligand characteristics on Intrinsic Properties of End Carbon

Harshitha Barike Aiyappa, Pradip Pachfule, Rahul Banerjee, and Sreekumar Kurungot, ***Cryst. Growth Des.***, **2013**, *13*, 4195–4199.

(11) Efficient oxygen reduction electrocatalyst from graphene by simultaneously generating pores and nitrogen doped active sites.

Thangavelu Palaniselvam, **Harshitha Barike Aiyappa** and Sreekumar Kurungot, ***J. Mater. Chem.***, **2012**, 22, 23799-23805.

ERRATUM